Technischen Universität München
Max-Planck-Institut für extraterrestrische Physik
Garching bei München

Study of Long-lived Radioactive Sources in the Galaxy with INTEGRAL/SPI

Wei Wang

Vollst"andiger Abdruck der von der Fakultät für Physik der Technischen Universität München zur Erlangung des akademischen Grades eines

Doktors der Naturwissenschaften

genehmigten Dissertation.

Vorsitzender:		Univ.-Prof. Dr. Andrzej J. Buras
Prüfer:	1.	Hon.-Prof. Dr. Günther Hasinger
	2.	Univ.-Prof. Dr. Stephan Paul

Die Dissertation wurde am 30.08.2007 bei der Technischen Universität München eingereicht und durch die Fakultät für Physik am 27.09.2007 angenommen.

Physik-Department

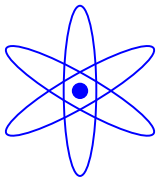

Doktorarbeit

Study of Long-lived Radioactive Sources in the Galaxy with INTEGRAL/SPI

Wei Wang

27 September, 2007

Technische Universität Müchen

Max-Planck-Institut für extraterrestrische Physik

Abstract

Two long-lived radioactive isotopes, ^{26}Al and ^{60}Fe in the Galaxy are studied with the high spectral resolution INTEGRAL spectrometer (SPI). ^{26}Al and ^{60}Fe have the similar half-life ($\sim$ million years) and astrophysical origins in the Galaxy. Their nucleosynthesis and ejection into the interstellar medium (ISM) are dominated by massive stars and the subsequent core-collapse supernova explosions. Detections of these isotopes provide evidence that nucleosynthesis is ongoing in the Galaxy. And their line shapes reflect the dynamics of the ejected isotopes in the interstellar medium and then probe properties of ISM. Observations of diffuse ^{26}Al and ^{60}Fe emission and their line shapes in the inner Galaxy and active nearby star-formation regions with SPI are main scientific objectives of this thesis.

With the four-year SPI data, we obtain the ^{26}Al spectrum for the inner Galaxy region ($|l| < 30^\circ$, $|b| < 10^\circ$) using model fittings with the different sky tracer models including ^{26}Al COMPTEL maps, HI, CO, EGRET sky survey maps, free electron density distribution models, the Robin young disk model, an exponential disk model, a homogenous disk model (constant along longitudes, exponential-like in latitudes, scale height 200 pc). The fitted parameters of derived ^{26}Al spectra from different distribution models: line centroid, flux and width, are well consistent with each other within error bars. Different sky distribution models do not affect ^{26}Al intensity and line shapes for the inner Galaxy. The measured ^{26}Al intensity for the inner Galaxy is $(3.0 \pm 0.2) \times 10^{-4}$ ph cm^{-2} s^{-1} rad^{-1} which is consistent with the COMPTEL results. The ^{26}Al line centroid is determined at 1809.0 ± 0.1 keV, which is higher than the laboratory value for the ^{26}Al line of 1808.65 ± 0.07 keV. The ^{26}Al line for the inner Galaxy show a narrow feature, with an intrinsic line width of 0.5 ± 0.4 keV. This ^{26}Al line width for the inner Galaxy is consistent with expectation of Galactic rotation (< 0.9 keV) and modest interstellar-medium turbulence (< 200 km s^{-1}) around the sources of ^{26}Al . Our results are consistent with the previous reports by HEAO-C and RHESSI, but a very broad line feature reported by GRIS is clearly ruled out by our present SPI result. Based on 3D distribution models of Galactic ^{26}Al , we can obtain a Galactic ^{26}Al mass of $(2.7 \pm 0.6)\ M_\odot$, where we have taken the distance of the Sun to the Galactic center $R_0 = 8.5$ kpc, which can be converted to a core-collapse supernova rate of 1.90 ± 0.95, corresponding to a star-formation rate (SFR) of $(3.8 \pm 1.9)\ M_\odot$ yr^{-1} in the Galaxy.

^{26}Al spectra along the Galactic plane ($|l| < 60^\circ$) can be obtained with SPI. ^{26}Al line centroid energy shifts along longitudes are detected as expected by Galactic rotation. The ^{26}Al line centroid for the Galactic center ($|l| < 5^\circ, |b| < 10^\circ$) is determined at $\sim$ 1808.66 keV, well consistent with the laboratory energy. Relative to the line centroid of

the Galactic center, ^{26}Al lines show a redshift of $\sim 0.1 - 0.2$ keV for positive longitudes ($5^\circ < l < 40^\circ$), and a blueshift of $\sim 0.5 - 0.9$ keV for negative longitudes ($-40^\circ < l < -5^\circ$). However, Galactic rotation predicts symmetric line energy shifts of $\pm(0.2 - 0.4)$ keV for positive and negative longitudes from our simulations assuming that Galactic ^{26}Al follows the free electron density distribution models based on pulsar dispersion measurements. Observed asymmetry of ^{26}Al line energy shifts with SPI cannot be explained only by Galactic rotation. Other effects not considered in simulations may contribute to this asymmetry: the Bar structure in the Galactic center; bulk motions of nearby ^{26}Al sources.

The ^{26}Al line width and intensity along the Galactic plane are also determined. ^{26}Al lines for different longitudes show the narrow line features except for the direction of $20^\circ < l < 40^\circ$. Possible broad line feature in this region may reflect the kinematics of nearby ^{26}Al sources in the Sagittarius arm. Brightness of ^{26}Al emission along the plane also show asymmetries: the 4th quadrant is brighter than the 1st quadrant, with the ^{26}Al flux ratio of ~ 1.3 for $|l| < 60^\circ$, and ~ 1.2 for $|l| < 30^\circ$. In simulations of ^{26}Al emission in the inner Galaxy, three different free electron density distribution models are adopted: all components ; all except the thick disk and the Galactic center ; only the thin disk and spiral arms. For two former models, no asymmetries of ^{26}Al intensity are expected. While for the third model, ^{26}Al intensity for the 4th quadrant obviously appear higher than that for the 1st quadrant, and the predicted ratio is consistent with the SPI observations. Therefore, we draw a conclusion that the free-electron density model of only the thin disk and spiral arms would reflect the real distribution of Galactic ^{26}Al .

We also derived ^{26}Al spectra along Galactic latitudes with the SPI data. Possible ^{26}Al emission for high latitudes ($|b| > 5^\circ$) should originate from local star-formation systems in the Gould Belt, while ^{26}Al in low latitudes ($|b| < 5^\circ$) would be dominated by the large-scale origin in the Galactic disk. ^{26}Al emission for low latitudes ($|b| < 5^\circ$) is significantly detected as expected. The ^{26}Al line for the disk shows a narrow feature. The asymmetry of ^{26}Al brightness for the 1st and 4th quadrants is also detected for the disk component. ^{26}Al line centroid energy shifts along the disk are evident, but the asymmetry of energy shifts is still inconsistent with the explanation of Galactic rotation. A large blueshift for the negative longitudes ($-40^\circ < l < -10^\circ$) may be also attributed to the contamination of nearby ^{26}Al sources. Weak ^{26}Al emission is detected in the positive latitude region of $5^\circ < b < 20^\circ$ with a blueshift of ~ 0.7 keV, but no ^{26}Al signal is detected in the negative latitude region $-20^\circ < b < -5^\circ$. Further analysis shows that ^{26}Al emission for $5^\circ < b < 20^\circ$ is contributed only by the negative longitude part, where the nearest active star formation region, the Sco-Cen OB association in the Gould belt is located.

Detections of ^{26}Al from nearby star-formation regions are the good probe for the massive star origin of Galactic ^{26}Al and kinematics of ^{26}Al ejecta in ISM. ^{26}Al spectra for three regions (Cygnus, Vela and Sco-Cen) are obtained with the present SPI observations. The reported ^{26}Al flux for the Cygnus region is $\sim (7.0 \pm 1.2) \times 10^{-5}$ph cm^{-2} s^{-1}

with a significance level of $\sim 6\sigma$. The ^{26}Al line for Cygnus appears a narrow feature, without line centroid shift. ^{26}Al emission for Vela is not significantly detected with SPI, with a measured flux of $(4.0 \pm 1.2) \times 10^{-5}$ph cm^{-2} s^{-1}. The ^{26}Al spectrum for Vela appears a broad line feature (intrinsic width of FWHM $\sim$ 2 keV), implying that supernova explosions and winds from Wolf-Rayet stars in Vela have strong effects on ISM near ^{26}Al sources. The Sco-Cen region would contribute to ^{26}Al emission toward high latitudes. We found a ^{26}Al line flux of $(6.3 \pm 2.0) \times 10^{-5}$ph cm^{-2} s^{-1}. The spectrum appears a narrow feature and has a large blueshift of $\sim$ 1.5 keV relative to the rest energy of the ^{26}Al line. This significant blueshift implies that ^{26}Al sources in Sco-Cen are dominated by the component of ^{26}Al ejecta with a bulk velocity of $\sim$ 200 km s^{-1} toward us.

Finally, we searched for the gamma-ray signal from the other long-lived radioactive isotope ^{60}Fe in the Galaxy with the 2.5 year SPI data. The detection of ^{60}Fe decay gamma-ray lines at both 1173 and 1333 keV from the Galaxy are reported with our measurements, with a significance of 4.9σ after combining two lines. The average ^{60}Fe line flux from the inner Galaxy region is $(4.4 \pm 0.9) \times 10^{-5}$ph cm^{-2} s^{-1} rad^{-1}. From the same observations and analysis procedure applied to ^{26}A, we find a flux ratio of ^{60}Fe/^{26}Al of (14.8 ± 6.0)%. The present theoretical predictions are still consistent with our result on the ratio of ^{60}Fe /^{26}Al . The ^{60}Fe signals are too weak to determine line shape details; it appears that a Gaussian with the width of the instrumental resolution can fit the data well, implying that broadening of ^{60}Fe lines from astrophysical processes is not significant. In order to investigate the variations over the Galaxy, we also search for ^{60}Fe emission from the Cygnus and Vela regions, and do not find ^{60}Fe signals.

Using more SPI data in future, we could improve spectral resolution of ^{26}Al in the inner Galaxy and ^{26}Al spectra along the plane, and then confirm ^{26}Al line shapes for Cygnus, Vela and Sco-Cen, further obtain ^{26}Al spectra from some other nearby star-formation regions, like Orion and Carina. For ^{60}Fe studies, the significance level of detections for the inner Galaxy will be pushed forwards again, and possible differences of ^{60}Fe signals for the 1st and 4th quadrants can be probed with more SPI data.

Contents

1 Introduction

Radioactivity was first discovered by the French physicist Henri Becquerel more than one century ago, when he observed the image of the photographic plate fogged by exposure to radiation from uranium salts, and then found that all uranium compounds and the metal self can emit "light" (Becquerel rays), with the intensity proportional to the amount of uranium, independent on its chemical composition [Becquerel, 1896]. Two year later, Pierre and Marie Curie coined the term "radioactive" for those elements which emitted Becquerel rays. In 1903, these three physicists shared the Nobel Prize in Physics, "in recognition of the extraordinary services they have rendered by their joint researches on the radiation phenomena discovered by Professor Henri Becquerel."

In 1899, Rutherford discovered that three different kinds of radiation are emitted in these radioactive substances, and firstly called these "alpha (α)", "beta (β)" and "gamma (γ)" rays [Rutherford, 1899]. In the later years, α rays were identified with the nuclei of helium [Rutherford, 1905], and β rays were electrons [Becquerel, 1900]. It took a long time until people realized that γ rays have all the properties of energetic electromagnetic radiation, now called high energy photons [Allen, 1911, Compton, 1929].

At present, we understand that radioactive decays are transitions between different states of atomic nuclei through electroweak interactions. Measurement of radioactive decays is an important tool of experimental physics. On Earth, radioactivity as a geological clock is widely used in the life and different scientific fields, e.g. the evolution of the Earth and the crust, biology, archeology, meteoritics. In the distant universe, radioactive decays can been studied by measuring γ-ray line spectra of celestial sources. The γ-ray lines can identify the individual isotope, and the abundance of these isotopes can be quantified with the measurement of γ-ray line intensity of the sky. In particular, γ-ray line photons are nearly transparent for the universe, with no absorption by the very dense molecular clouds and interstellar medium. So detections of these γ-ray lines are a powerful tool to study the cosmic abundance of radioactive isotopes, which is the original scientific motivation of this thesis. Cosmic radioactive isotopes are produced through stellar nucleosynthesis and supernovae (SNe), ejected into the interstellar medium by winds, and explosion processes (also see details in the reviews by Prantzos and Diehl 1996, Diehl and Timmes 1998).

1.1 Cosmic nucleosynthesis and nuclear astrophysics

The Universe is a huge factory of the elements. Just 3 minutes after the big bang, primordial nucleosynthesis occurred (original idea by Gamow 1946). The big bang nucleosynthesis (BBN) produces the present abundance of light elements: D (Deuterium), ^{3}He, ^{4}He, ^{7}Li. But the heavier elements (A>12) cannot be produced during BBN. Some light elements, e.g. B, Be and ^{6}Li, are produced by cosmic ray spallation processes. But the heavier elements are mainly produced by nucleosynthesis in stars (see details in a review by Wallerstein et al. 1997, and a good text book by Arnett 1996, also refer to the early excellent paper by Burbidge, Burbidge, Fowler, and Hoyle 1957).

Stars can produce the heavy elements through fusion processes due to the very high temperature in their interiors. Hydrogen burning is first triggered, and helium is produced through the $p-p$ chain and CNO cycle. Then helium burning follows in higher temperature, producing ^{12}C, and α captures can extend nucleosynthesis to ^{16}O, and ^{20}Ne, ^{24}Mg, etc., up to the very stable, double magic nucleus ^{40}Ca. Because experiments show that the ^{16}O(α, γ)^{20}Ne rate is very slow in stellar interiors, at present people generally believe that the formation of nuclei heavier than ^{16}O proceeds successfully by core carbon, neon, oxygen and silicon burning. After silicon burning, freed alphas, protons, and neutrons build nuclei up to the region of the most stable nuclei, the iron (e.g. ^{54}Fe, ^{56}Fe) abundance peak. If the buildup occurs rapidly, with increase of neutron excess, the dominant nucleus will be ^{56}Ni. The iron group nuclei are most stable in the nature, so the further fusion (burnings) stops. Massive stars (e.g. $M > 8M_{\odot}$) will end their life through supernova explosions. Supernova nucleosynthesis is the only origin of the heavier elements than the iron group. Due to the neutron rich environment in supernova explosions, the nucleosynthesis proceeds by neutron captures (rapid capture, called "*r-process*"; slow one "*s-process*"). The *r-processes* and *s-processes* could produce nearly all the heavy elements above the iron, e.g., ^{60}Fe and famous radioactive isotopes ^{235,238}U. Proton-rich isotopes are rare in the nature (e.g., ^{26}Al), they can be produced through proton captures in the proton-rich environment.

Stars produce the elements, and can ejected them to the interstellar medium (ISM) by stellar winds and supernova explosions. The interstellar medium would cool and collapse into dense clouds, and then form the new stars. Then a cosmic element cycle finishes, and a new one begins. Cosmic nucleosynthesis becomes the foundation of the life and the present human world.

Cosmic element abundance could be measured precisely by astronomical observations over a wide range of the electromagnetic spectrum, specially in the optical band nowadays. For example, the Hubble Space Telescope, and large-aperture earth-based telescopes have yields very high resolution spectra of stars, galaxies and interstellar medium. The high resolution spectral analyses can determine cosmic abundance of most elements and their isotopes. Anyway, optical, infrared, and ultraviolet observatories provide only a part of the information. Observations of gamma-ray lines from radioactive isotopes open a new window of observations and guide our understand-

ing of nucleosynthesis in stars. The observational constraints challenge theorists, and push them to do detailed calculations of stellar evolution and nucleosynthesis. At present, new astronomical observations, new nuclear experimental capabilities, and new computational power present an opportunity for an important advance in our knowledge of cosmic nucleosynthesis.

There are good news for modern nuclear astrophysics. (1) A wealth of new observations require detailed nuclear data for a credible explanation. (2) New accelerators and detection techniques provide an unprecedented and growing capability for providing the needed nuclear data. (3) Exponentially growing computational power makes it possible to include the resulting microphysics in simulations of stellar evolution and the sequence of events leading to novae, X-ray bursts, and supernova explosions. The enhanced programs for nuclear astrophysics, experimental and theoretical, will greatly advance our understanding of the cosmos.

1.2 Gamma-ray line astronomy

Detections of gamma-ray lines provide a special window to determine the cosmic abundance of radioactive isotopes. Radioactive isotopes are co-products with stable nuclei of nucleosynthesis. They are generally produced in stellar interiors, supernovae, novae, and interstellar medium. These radioactive isotopes decay with emission of characteristic gamma-ray lines. Measurements of these gamma-rays can relate to existence of their parent isotopes. Gamma-ray line emission can penetrate dense mass layers, so the detection of these lines are more direct than the measurements of photospheric or interstellar absorption or emission lines in the optical band. Observations of gamma-ray lines provide a possible tool to probe nucleosynthesis in early evolution stages of supernova and novae, when gamma-ray emission becomes transparent a few days after explosions.

Gamma-ray lines are also detected from nuclear excitation in astrophysics. Atomic nuclei in excited states are produced in energetic collisions in interstellar space and in the vicinity of compact objects. Typical excitation energies of atomic nuclei are in the MeV regime, prominent examples being the C first excited level at 4.4 MeV, or O at 6.1 MeV. In the outer regions of the Sun, such collisions occur prominently during solar flares. In interstellar space, cosmic ray interactions with ambient interstellar gas results in de-excitation gamma-ray lines. Near neutron stars, neutron capture line at 2.2 MeV or the redshifted one could be detected (e.g. see McConnell et al. 1997). This line can be very strong [Kuzhevskij, Kuznetsov, and Troitskaia, 1998] and was also detected in solar flares [Terekhov et al., 1993].

Radioactive isotopes have the different decay lifetimes. If the decay lifetime is too short, the emission site is not transparent for gamma-ray lines, we can not observe the emission. So only a small number of radioactive isotopes with a relative long lifetimes, are related to the gamma-ray line measurements of cosmic nucleosynthesis. We have

Table 1.1: Radioactive isotopes for gamma-ray line astronomy

isotopes	mean lifetimes	decay chain	γ-ray energy (keV)	sources
^{7}Be	77 d	$^{7}\mathrm{Be} \rightarrow {}^{7}\mathrm{Li}^{*}$	478	novae
^{22}Na	3.8 yr	$^{22}\mathrm{Na} \rightarrow {}^{22}\mathrm{Ne}^{*} + e^{+}$	1275	novae
^{26}Al	1.04×10^{6} yr	$^{26}\mathrm{Al} \rightarrow {}^{26}\mathrm{Mg}^{*} + e^{+}$	1809	SNe, novae, massive stars
^{44}Ti	89 yr	$^{44}\mathrm{Ti} \rightarrow {}^{44}\mathrm{Sc}^{*}$ $\rightarrow {}^{44}\mathrm{Ca}^{*} + e^{+}$	68, 78, 1157	SNe
^{56}Ni	111 d	$^{56}\mathrm{Ni} \rightarrow {}^{56}\mathrm{Co}^{*}$ $\rightarrow {}^{56}\mathrm{Fe}^{*}$	158, 812, 847, 1238	SNe
^{57}Co	390 d	$^{57}\mathrm{Co} \rightarrow {}^{57}\mathrm{Fe}^{*}$	122	SNe
^{60}Fe	2×10^{6} yr	$^{60}\mathrm{Fe} \rightarrow {}^{60}\mathrm{Co}^{*}$	59, 1173, 1333	SNe
e^{+}	$10^{4} - 10^{7}$ yr	$e^{+} + e^{-} \rightarrow \mathrm{Ps}$ $\rightarrow \gamma\gamma$	511, <511	SNe,pulsars, dark mater

listed these interested isotopes in Table 1.1. For long-lived radioactive isotopes, the emission from several or many nucleosynthesis events is superimposed, e.g. ^{26}Al and ^{60}Fe . Gamma-ray lines emissions from ^{26}Al and ^{60}Fe can probe the young source populations, and may correlate to the structure of the Galaxy, which are the targets studied in this thesis.

Gamma-ray line astronomy has been greatly developed in the last half century. The first gamma-ray line observations were from OSO-3, OSO-7 in 1960's, which revealed the strong 2.223 MeV line from solar flares [Brandt, 1969]. This line results from the formation of deuterium via the union of a neutron and proton; in a solar flare the neutrons appear as secondaries from interactions of high-energy ions accelerated in the flare process. And the field of gamma-ray line astronomy took great leaps forward with the HEAO C, the COS-B (1975-1982) and the Solar Maximum Mission (launched in 1980) satellites. The HEAO C first detected the 1809 keV line from radioactive ^{26}Al in the inner Galaxy [Mahoney et al., 1982]. In 1977, NASA announced plans to build a "great observatory" for gamma-ray astronomy. The Compton Gamma-Ray Observatory (CGRO) was designed to take advantage of the major advances in detector technology during the 1980s, and was launched in 1991. The COMPTEL telescope aboard CGRO first mapped the 1809 keV γ-ray line emission of the whole sky [Diehl et al., 1995a, Plüschke et al., 2001], and first detected the strong and broad ^{44}Ti line around 1157 keV from a young supernova remnant (SNR) Cas A [Iyudin et al., 1994]. The OSSE telescope aboard CGRO also firstly mapped the 511 keV annihilation line emission in the inner Galaxy [Purcell et al., 1997]. Currently, the main space-based gamma ray observatory is the *INTE*rnational *G*amma-*R*ay *A*strophysics *L*aboratory

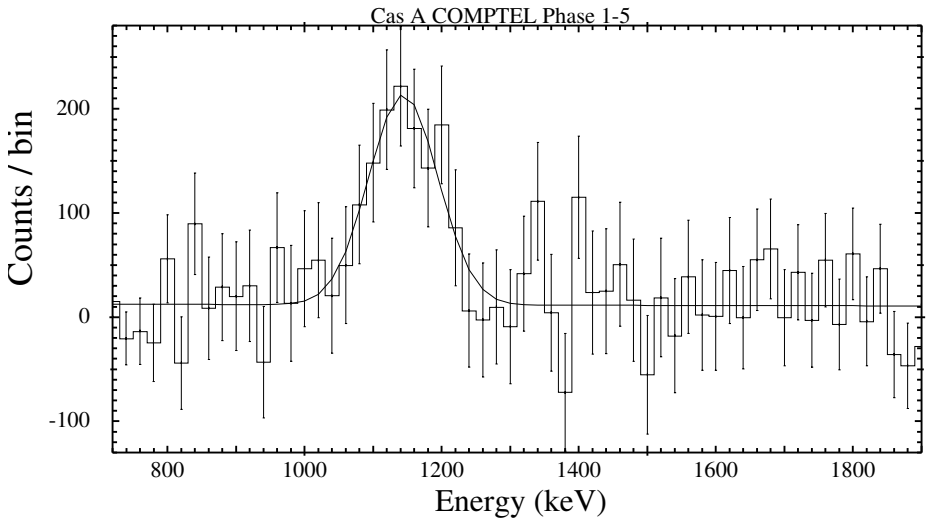

Figure 1.1: The spectrum of 1157 keV γ-ray line from Cas A discovered by COMPTEL (from Iyudin et al. 1997). The broad line feature suggests that the ejecta of ^{44}Ti have the velocities of $\sim$ 10000 km s^{-1}.

(INTEGRAL). The spectrometer aboard INTEGRAL (SPI) provides the high spectral resolution enough to resolve astrophysical lines and allow spectroscopy in the regime of gamma-rays. The progress and present results of two important long-lived radioactive isotopes, ^{26}Al and ^{60}Fe will be discussed in more details in the following. Here, we first briefly present the recent detections of gamma-ray lines from the other two interesting isotopes: ^{44}Ti and positrons (e^-e^+ annihilations).

1.3 ^{44}Ti

^{44}Ti is a short-lived radioactive isotopes with a mean life of 89 years. In theories, the most plausible cosmic environment for production of ^{44}Ti is the α-rich freeze-out from high-temperature burning near the nuclear statistical equilibrium (see Woosley et al. 1973; Arnett 1996). The required high values for the entropy may be found in core-collapse supernovae. So it is believed that core-collapse supernovae dominate the production of radioactive ^{44}Ti, which should be visible in gamma-rays in a few centuries. ^{44}Ti decay is believed to be the only source of the stable isotope ^{44}Ca. ^{44}Ti gamma-rays reflect the current rate of supernovae due to its short decay time scale, so the present detections should be directly related to the current population of massive stars. There are three γ-ray lines which can be used to detect the decay of ^{44}Ti: the 68 and 78 keV lines from the ^{44}Sc de-excitation cascade and the 1157 keV line as ^{44}Ca decays to its stable ground state.

Supernova observations have demonstrate that these events are the origin of ^{44}Ti

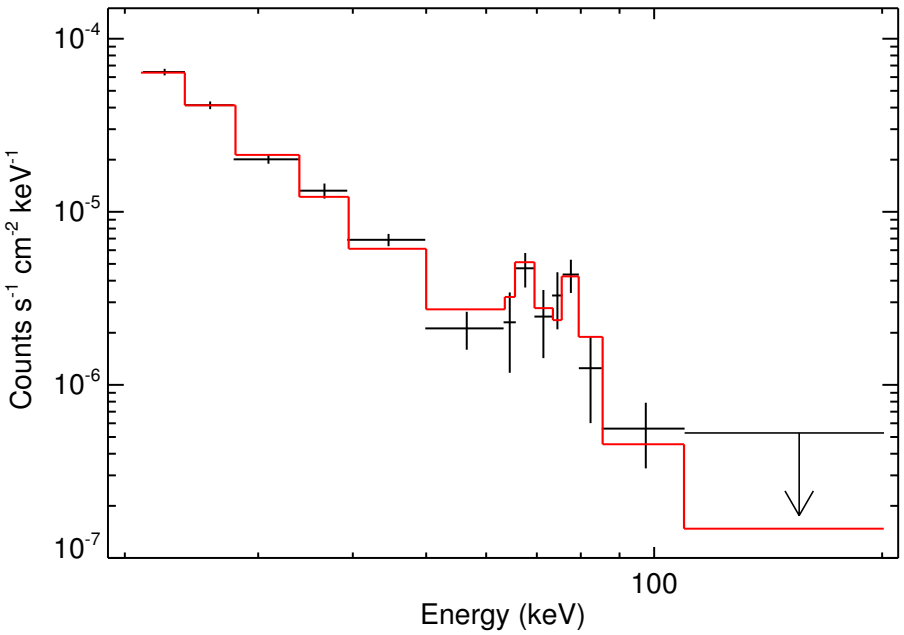

Figure 1.2: The spectrum of Cas A from INTEGRAL/IBIS and the best-fit model (solid red line, from Renaud et al. 2006). The two lines at positions of 67.8 ± 1.6 and 77.4 ± 1.4 keV are clearly detected, and identified as the signature of ^{44}Ti.

production. The 1157 keV γ-ray line following ^{44}Ti decay has been detected in the 340-year old Galactic SNR Cas A with COMPTEL (see Figure 1.1, Iyudin et al. 1994; Schönfelder et al. 2000). COMPTEL's survey [Dupraz et al., 1997, Iyudin et al., 1999] have resulted in another candidate source, the so-called Vela junior SNR (GRO J0852-4642, Iyudin et al. 1998). Yet Cas A seems to be the only source with the established ^{44}Ti detections. The two low-energy lines at 68 and 78 keV from Cas A have also been clearly detected by Beppo-SAX [Vink et al., 2001], and confirmed by INTEGRAL/IBIS (Figure 1.2, Renaud et al. 2006) and INTEGRAL/SPI (Martin et al. 2007, in preparation). And INTEGRAL's inner-Galaxy survey with the IBIS did not reveal a new source in this region [Renaud et al., 2004, 2006]. Furthermore, SN 1987A's late light curve, observed in details over more than 15 years, appears powered by a similar amount of $(0.2 - 2) \times 10^{-4} M_{\odot}$ ^{44}Ti, from modelling of radioactive energy deposition and photon transport in the SNR [Woosley et al., 1989, Fransson and Kozma, 2002].

^{44}Ti lives long enough so that it should have been detected from several recent Galactic supernovae if these occur at a rate of ~ 2 per century; but with the exception of Cas A (Iyudin et al. 1994; Renaud et al. 2004, 2006), no other SNRs have been detected yet. Analysis of COMPTEL data supported a 5σ detection of Cas A at $(4.2 \pm 0.9) \times 10^{-5}$ photon cm^{-2} s^{-1} in the 1157 keV line (Iyudin et al. 1997), implying $\sim 2.4 \times 10^{-4} M_{\odot}$ of ^{44}Ti. Measurements of the 68 and 78 keV lines by

Beppo-SAX, IBIS and SPI aboard INTEGRAL also suggested the ejected ^{44}Ti mass of $\sim (1.0-2.5)\times 10^{-4}M_{\odot}$. However, solar metallicity Type II and Type Ib supernova models indicate $\sim (3-6)\times 10^{-5}M_{\odot}$ yields of ^{44}Ti (e.g. Woosley & Weaver 1995; Thielemann et al. 1996; Rauscher et al. 2002; Limongi & Chieffi 2003). This leaves the ^{44}Ti observations from Cas A as a puzzle. Theorists then suggested that asymmetries in the supernova explosion mechanism could drive an enhancement of ^{44}Ti in the ejecta (e.g. Nagataki et al. 1997; Maeda & Nomoto 2003). Figure 1.3 has shown the comparison between the observation limit of ^{44}Ti in Cas A and the predictions of different supernova explosion models on the ejected masses of ^{44}Ti and ^{56}Ni. The standard supernova models with symmetrical explosions [Rauscher et al., 2002, Limongi and Chieffi, 2003] predicted a lower amount of ^{44}Ti, cannot explain the case of Cas A; non-spherical models seemed to resolve the ^{44}Ti puzzle in Cas A [Maeda and Nomoto, 2003]. So Cas A may be a special case in the Galactic supernovae, e.g., possibly an asymmetrical Type Ib supernova explosion.

1.4 511 keV emission from electron-positron annihilation

Positrons with a low energy around a few tens of eV, could either annihilate directly with electrons or form positronium by charge exchange or radiative capture [Bussard, Ramaty, and Drachman, 1979]. The annihilations produce the 511 keV line and positronium continuum below the energy of 511 keV.

Positrons will lose their energy mainly through via Coulomb interactions with the interstellar medium. The energy loss timescale of Coulomb interactions in the medium τ_c depends on the positron energy, the medium density, and the degree of ionization. For the positrons with energy around 1-100 MeV, the Coulomb interaction cooling timescale is estimated as $\tau_c \sim 10^5 n^{-1}$ yr (within a factor of 2, Wang et al. 2006), and n is the medium number density in units of cm^{-3}. And the medium in the Galaxy is quite complicated. Then the energy loss timescales could vary from $\tau_c \sim 10^3$ yr in the molecular clouds ($n > 10^2$cm^{-2}), $\tau_c \sim 10^5$ yr for the typical warm interstellar medium ($n \sim 1$cm^{-2}), and $\tau_c > 10^7$ yr for the hot gas ($n \sim 10^{-2}$cm^{-2}).

The potential positron sources include: neutron stars or black holes [Lingenfelter and Ramaty, 1983]; ^{56}Co β-decays in supernova remnants [Ellison, Jones, and Ramaty, 1990]; other radioactive nuclei (e.g. ^{26}Al) formed by nucleosynthesis in supernova, nova, red giants, and Wolf-Rayet stars [Ramaty et al., 1979]; cosmic ray interactions with the interstellar medium [Kozlovsky et al., 1987]; pair production by gamma-ray photons interacting with starlight photons in the interstellar medium [Mastichiadis, Protheroe, and Stephen, 1991] and pulsars and pulsar winds [Sturrock, 1971, Chi, Cheng, and Young, 1996], probably gamma-ray bursts (GRB, Lingenfelter and Hueter 1984).

Since the first detection [Johnson and Haymes, 1973] and subsequent identification [Leventhal et al., 1978] of the Galactic 511 keV annihilation line, the origin of the galactic positrons has become a lively topic of scientific debate. The first result of the

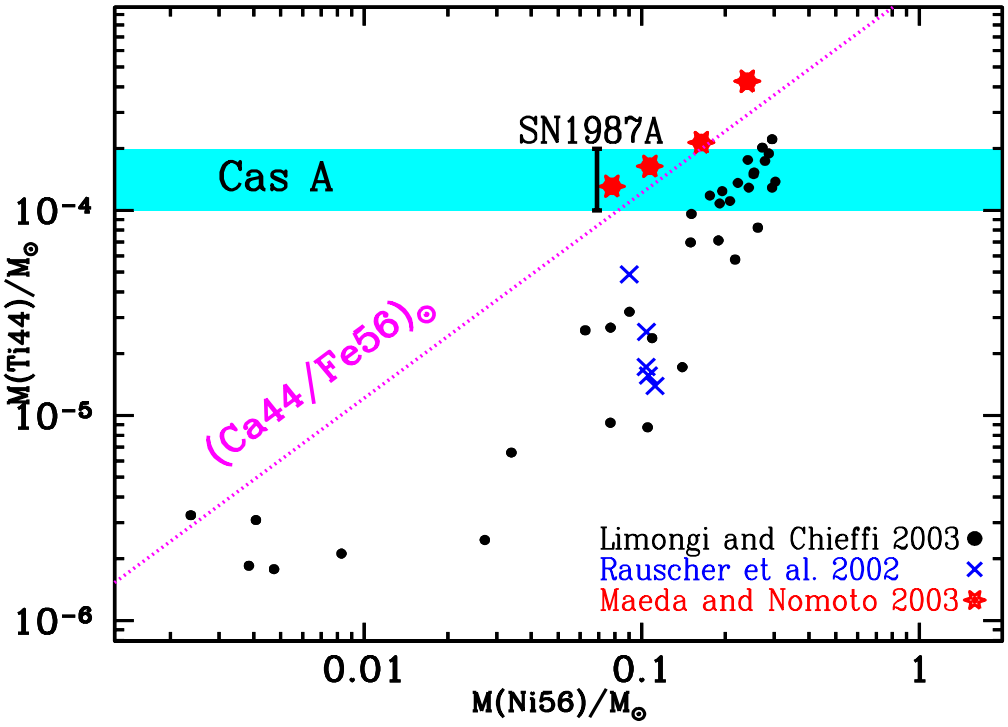

Figure 1.3: Yield of ^{44}Ti vs yield of ^{56}Ni, from models and observations (from Diehl et al. 2006b). Model results are from Limongi and Chieffi (2003, filled dots, with large variations in yields due to variations in both stellar mass - from 15 to 35 $M_\odot$ - and explosion energy), Rauscher et al. (2002, crosses, for stars in the 15 to 25 $M_\odot$ range and explosion energies of 10^{51} ergs) and Maeda and Nomoto (2003, asterisks); the latter concern axisymmetric explosions in 25 and 40 $M_\odot$ stars, producing high ^{44}Ti/^{56}Ni ratios. ^{44}Ti detected in Cas A appears as a horizontal shaded band (assuming that its decay rate has not been affected by ionisation in the Cas A remnant, otherwise its abundance should be lower). The amount of ^{44}Ti in SN1987A is derived from its late optical lightcurve. The diagonal dotted line indicates the solar ratio of the corresponding stable isotopes (^{44}Ca/ ^{56}Fe)$_\odot$ [Prantzos, 2004].

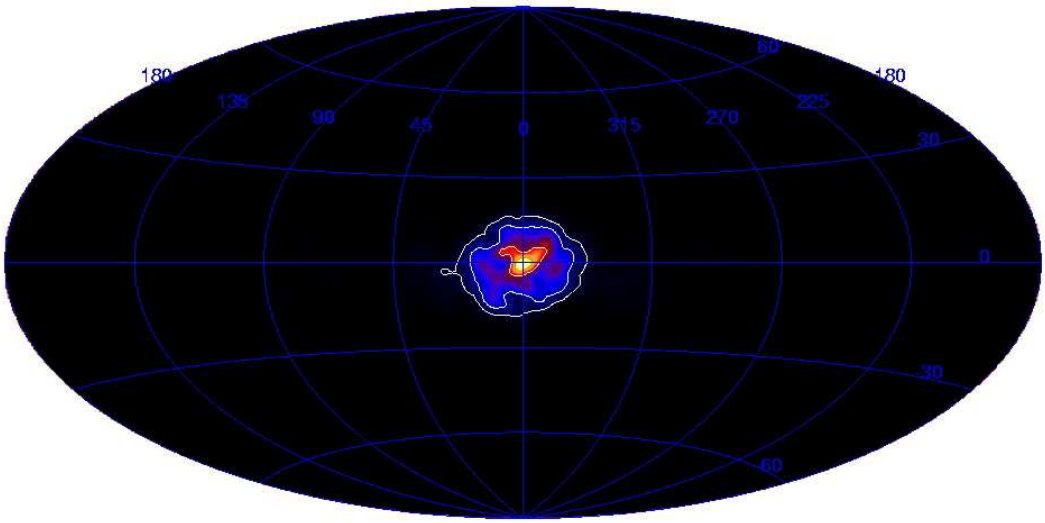

Figure 1.4: All-sky distribution of 511 keV line emission observed by INTEGRAL/SPI (from Knödlseder et al. 2005).

511 keV emission morphology was obtained by OSSE aboard CGRO [Purcell et al., 1997, Cheng et al., 1997, Milne et al., 2000, 2001], and observations were restricted to the inner Galaxy. With the launch of INTEGRAL satellite, one of the prime instruments, SPI allows the detailed studies of positron annihilation features, combining high-resolution spectroscopy ($R \sim 250$ at 511 keV) with relatively good angular resolution (2.5° FWHM). The recent SPI results based on two-year data firstly presented an all-sky map of 511 keV electron-positron annihilation emission [Knödlseder et al., 2005]. The spatial distribution of 511 keV line emission appears centered on the Galactic center (GC, bulge component, with radius of $6^\circ - 8^\circ$), with no or weak contribution from a disk component (see Figure 1.4; Teegarden et al. 2005, Knödlseder et al. 2005) [1], and no evidence for additional point-like 511 keV line emission down to a flux limit of 1.4×10^{-4}ph cm^{-2} s^{-1}. The high-resolution spectral analyses show a strong 511 keV line with a positronium continuum (Figure 1.5), suggesting that the dominant fraction of positrons ($\sim$ 94%) form positronium before annihilation [Churazov et al., 2005, Jean et al., 2006]. The high luminosity of 511 keV emission with a positronium continuum component suggests that the positron injection rate is up to 10^{43} e^+s^{-1} within $\sim 6^\circ$ of the Galactic center.

In the present viewpoints, the bulge-dominated morphology of the 511 keV line may indicate that the positron source population could be an old stellar population. However, some candidate positron sources, like supernovae, ^{26}Al sources, pulsars, cosmic ray interactions, show a disk-like distribution. The low-mass X-ray binaries (LMXBs)

[1] Recently, the significant disk component from 511 keV line emission was reported from near 4-year SPI observations (Weidenspointner et al. 2007 in preparation).

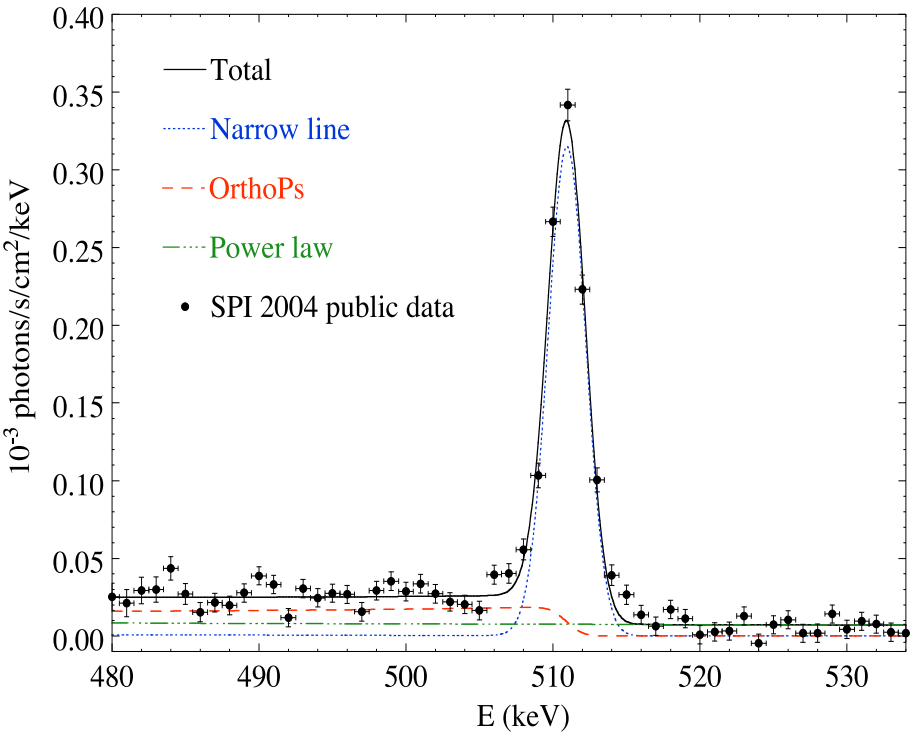

Figure 1.5: Fit of the spectrum measured by SPI with contributions from a Gaussian line, an ortho-positronium continuum and a power-law Galactic continuum (from Jean et al. 2006). A single Gaussian does not give a good fit to the flux measured in the wings of the line.

and Type Ia supernovae could be the candidate positron sources, but they may not produce the enough positron injection rate in the Galactic center. As a result, Cassé et al. [2004] argues that normal supernova explosion in the GC cannot contribute to the required positrons, but hypernovae (Type Ic supernovae/gamma-ray bursts) in the Galactic center may be possible sources of galactic positrons. In addition, annihilations of light dark matter particles into $e^{\pm}$ pairs [Boehm et al., 2004] have also been suggested as the potential origin of the 511 keV line in the GC. Cheng et al. [2006] also proposed that the continuous capture of stars by the supermassive black hole at Sgr A* could explain the morphology and intensity of the $e^{\pm}$ annihilation line. But these scenarios may require turbulent diffusion processes which are able to diffuse the positrons over the galactic bulge within the positron lifetime ($\sim 10^4 - 10^7$ yr). It is also suggested that a millisecond pulsar (MSP) population exists in the Galactic center [Wang et al., 2005a, Wang, 2006], and positrons from winds of these millisecond pulsars can provide enough positron injection rate [Wang et al., 2006].

1.4.1 Positrons from millisecond pulsars in the Galactic center

Millisecond pulsars are old pulsars which could have been members of binary systems and been recycled to millisecond periods, having formed from low mass X-ray binaries in which the neutron stars accreted sufficient matter from either white dwarf, evolved main sequence star or giant donor companions. The current population of these rapidly rotating neutron stars may either be single (having evaporated its companion) or have remained in a binary system. In observations, they distribute in two populations: the Galactic field (1/3) and globular clusters (2/3, see details in Wang 2006).

One motivation for a millisecond population in the Galactic center comes from the GeV spectrum toward the Galactic center detected by EGRET on board the Compton GRO [Mayer-Hasselwander et al., 1998]. The photon spectrum can be well represented by a broken power law with a break energy at ~ 2 GeV (see Figure 1.6). Some models, e.g. gamma-rays related to the massive black hole, inverse Compton scattering, and mesonic decay resulting from cosmic rays, are difficult to produce the hard gamma-ray spectrum with a sharp turnover at a few GeV. However, the gamma-ray spectrum toward the Galactic center is similar with the gamma-ray spectrum emitted by middle-aged pulsars (e.g. Vela and Geminga) and millisecond pulsars (Wang et al. 2005). In Figure 1.6, we can see that the superposed spectrum of 6000 MSPs could significantly contribute to the observed GeV spectrum (Wang et al. 2005). Wang (2006) also suggested that non-thermal X-ray emission from pulsar wind nebulae of these MSPs can contribute to weak unidentified X-ray sources discovered by deep Chandra X-ray surveys of the Galactic center (a field of $17' \times 17'$, Muno et al. 2003).

Firstly, we will argue that millisecond pulsars would dominate the pulsar population in the Galactic center region. The birth rate of normal pulsars in the Milky Way is about 1/150 yr (Arzoumanian, Chernoff, & Cordes 2002). As the mass in the inner 20

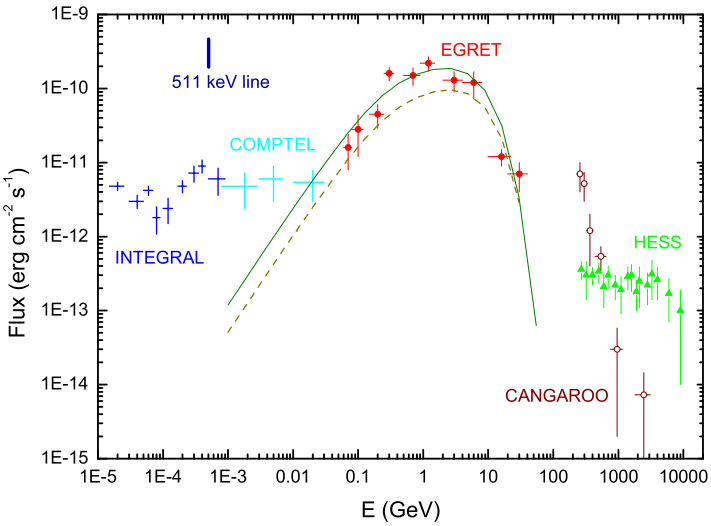

Figure 1.6: The diffuse gamma-ray spectrum in the Galactic center region within 1.5° and the 511 keV line emission within 6° (from Wang 2006). The solid and dashed lines are the simulated spectra of 6000 MSPs according to the different period and magnetic field distributions in globular clusters and the Galactic field respectively.

pc of the Galactic center is $\sim 10^8 M_\odot$ [Launhardt et al., 2002], the birth rate of normal pulsars in this region is only 10^{-3} of that in the entire Milky Way, or $\sim 1/150\,000$ yr. We note that the rate may be increased to as high as $\sim 1/15000$ yr in this region if the star formation rate in the nuclear bulge was higher than in the Galactic field over last $10^7 - 10^8$ yr (see Pfahl et al. 2002). Few normal pulsars are likely to remain in the Galactic center region since only a fraction ($\sim 40\%$) of normal pulsars in the low velocity component of the pulsar birth velocity distribution [Arzoumanian et al., 2002] would remain within the 20 pc region of the Galactic center studied by Muno et al. (2003) on timescales of $\sim 10^5$ yrs. The number of gamma-ray mature pulsars is not higher than 10 according to the birth rate of pulsars in the Galactic center. So normal pulsars are not likely to be a major contributor.

On the other hand, there may exist a population of old neutron stars with low space velocities which have not escaped the Galactic center [Belczynski and Taam, 2004]. Such neutron stars could have been members of binary systems and been recycled to millisecond periods, having formed from low mass X-ray binaries in which the neutron stars accreted sufficient matter from either white dwarf, evolved main sequence star or giant donor companions. The current population of these millisecond pulsars may either be single or have remained in a binary system. The binary population synthesis in the Galactic center (Taam 2005, private communication) shows more than 200 MSPs are produced through recycle scenario and stay in the Muno's region.

Millisecond pulsars as the positron sources

We consider that the electron-positron pair production occurs in the pulsar outer-magnetospheric region in MSPs.

It has been proposed that there is a strong multipole magnetic field near the stellar surface, although a global dipole magnetic field gives a good description of the magnetic field far from the star [Ruderman and Sutherland, 1975, Ruderman, 1991]. The typical radius of curvature l of the local magnetic field is on the order of the crust thickness of the star (i.e. $l \sim 10^5$ cm), which is much less than the dipole radius of curvature of dipole field component near stellar surface. The relation between the local multipole magnetic field and dipole field can be given by [Zhang and Cheng, 2003]

$$B_s \simeq B_d (\frac{R}{l})^3, \tag{1.1}$$

where B_d is the dipole magnetic field of a pulsar, R is the radius of neutron stars. For MSPs, typically $B_d \sim 10^8 - 10^9$ G, $B_s \sim 10^{11} - 10^{12}$ G which is much lower than the quantum critical magnetic field $B_q \sim 4.4 \times 10^{13}$ G, so pair cascades are also efficient in the local multipole field.

The pair production mechanism is a synchrotron photon cascade in a strong magnetic field. Photons will be converted into $e^\pm$ pairs in the local magnetic field when their energy satisfies (Ruderman & Sutherland 1975)

$$E \geq E_{\rm crit} \equiv \frac{2 m_e c^2}{15} \frac{B_q}{B_d} (\frac{R}{l})^{-3}. \tag{1.2}$$

The primary $e^{\pm}$ from the outer-gap have the energy $E_p = \gamma_p m_e c^2 = 5.7 \times 10^{12} P^{1/3}$ eV, so generally, the energies of primary curvature photons and secondary synchrotron photons are higher than $E_{\rm crit}$, a photon-electron cascade will start and develop until this condition fails. At the end of a cascade, each incoming primary electron-positron can produce, on average,

$$N_{e^{\pm}} = \frac{E_p}{E_{\rm crit}} = 1.9 \times 10^3 B_{d,9} P^{1/3} (\frac{R}{l})^3, \tag{1.3}$$

and then the total pair production rate can be estimated as

$$\dot{N}_{e^{\pm}} = f \dot{N} N_{e^{\pm}} = 2 \times 10^{33} f B_{d,9}^{10/7} P^{-8/21} (\frac{R}{l})^{30/7} {\rm s}^{-1}, \tag{1.4}$$

where $f \simeq 5.5 P^{26/21} B_{12}^{-4/7}$ is the fraction size of the outer gap, and

$$\dot{N} = 2.7 \times 10^{27} P^{-2} B_{d,9} (\frac{R}{l})^3 {\rm s}^{-1} \tag{1.5}$$

is the primary electron-positrons passing through the polar gap [Goldreich and Julian, 1969]. Taking the typical parameters $P = 3$ ms, $B_d = 3 \times 10^8$ G, the positron injection rate for a MSP: $\dot{N}_{e^{\pm}} \sim 5 \times 10^{37} e^+ {\rm s}^{-1}$ (Wang et al. 2006).

Since these pairs are created close to the stellar surface and the field lines are converging, only a small fraction may keep moving toward the star and annihilate on the stellar surface. Ho [1986] showed that the loss cone for these pairs will approach $\pi/2$, in other words, most pairs will be reflected by the magnetic mirroring effect and then move toward the light cylinder. These particles will flow out with the pulsar wind and be accelerated by the low-frequency electro-magnetic wave.

Then how many MSPs in the region of annihilation emissions? Figure 1.6 has shown that 6000 MSPs can contribute to gamma-rays with 1.5°, and the diffuse 511 keV emission have a size $\sim 6^\circ$. We do not know the distribution of MSPs in the GC, so we just scale the number of MSPs by $6000 \times (6^\circ/1.5^\circ)^2 \sim 10^5$, where we assume the number density of MSPs may be distributed as $\rho_{MSP} \propto r_c^{-1}$, where r_c is the scaling size of the GC. Then a total positron injection rate from the millisecond pulsar population is $\sim 5 \times 10^{42}$ e^+ ${\rm s}^{-1}$ which is consistent with the present observational constraints. What's more, our scenario of a millisecond pulsar population as possible positron sources in the GC has some advantages to explain the diffuse morphology of 511 keV line emissions without the problem of the strong turbulent diffusion which is required to diffuse all these positrons to a few hundred pc.

There are many possible positron sources at present. Thus, how could we distinguish the model of a millisecond pulsar population from other models? Firstly, we can estimate the typical spatial diffusion scale of positrons in the magnetic field of the GC, which is given by $\lambda_{diff} \sim (r_L c t)^{1/2}$ (Wang et al. 2006), where $r_L \approx E_e/eB$ is the Larmor radius, E_e is the energy of positrons, $B \sim 10^{-5}$ G is the average magnetic field in the GC [LaRosa et al., 2005]. The average cooling time t of positrons in the

GC is $\sim 10^6$ years, so the characteristic diffusion scale is about 1 pc. Because of the low angular resolution of SPI/INTEGRAL (about 2 degrees), we can assume that the positrons annihilate in the local region as their sources, i.e. the millisecond pulsars.

Therefore, we predict that the spatial intensity distribution of the annihilation lines should follow the spatial distribution of MSPs if a millisecond population exists in the GC. We could assume the spatial distribution of MSPs should follow the mass distribution of the GC though we do not know how well they follow each other. But because the proper motion velocity of MSPs is relatively low, we could reasonably assume that the two distributions are quite close to each other. Then if the positron sources originate in the MSP population, the 511 keV annihilation line intensity would follow the mass (e.g. stars) distribution of the Galactic center region. If the positrons originate from supernovae or hypernovae, the 511 keV line emssion could follow the distribution of massive stars and dense molecular clouds. For the light dark matter scenario, the annihilation emissions may correlate to the dark matter density profile. Discrimination of these possible correlations may be tested in the future high resolution observations.

1.5 All-sky observations of ^{26}Al by CGRO/COMPTEL

The 1809 keV gamma-ray line from radioactive ^{26}Al with its decay time of 1 million years can be used as the tracer of the recent nucleosynthesis activity in the Galaxy. Ramaty and Lingenfelter [1979] first predicted the 1809 keV γ-ray line flux of $\sim 10^{-4}$ph cm^{-2} s^{-1} rad^{-1} from the inner Galaxy, combining the solar ^{27}Al abundance with an estimate of the isotope ratio ^{26}Al /^{27}Al ($\sim 10^{-5}$) from supernovae.

The 1809 keV γ-ray line emission was first detected with the Ge spectrometer on the HEAO-C spacecraft (Mahoney et al. 1982). This detection was confirmed by the measurement of Galactic transits through the field of view by the NaI spectrometer on the SMM spacecraft [Share et al., 1985]. The following balloon-borne experiments measured the intensity of the ^{26}Al emission and derived some information on its angular distribution (see von Ballmoos et al. 1987, Schoenfelder and Varendorff 1991, Durouchoux et al. 1993, Prantzos and Diehl 1996). And the ^{26}Al fluxes derived from these different measurements depend on the assumed Galactic distribution of ^{26}Al line emission. For example, they found $(1.1 - 4.6) \times 10^{-4}$ph cm^{-2} s^{-1} for a point source at the Galactic center, and $(3.9 - 5.4) \times 10^{-4}$ph cm^{-2} s^{-1} from the inner Galaxy for a flat supernova model. So mapping the 1809 keV γ-ray line emission of the Galaxy can provide insight into the nature of ^{26}Al sources, and precise determination of the ^{26}Al flux.

The COMPTEL imaging telescope aboard the Compton Observatory performed the first survey of ^{26}Al γ-ray line emission in the whole Galaxy. COMPTEL covered the energy range of 1 – 30 MeV, with an energy resolution of 140 keV (FWHM) around 1809 keV and an angular resolution of 3.8° (see Schoenfelder et al. 1993). COMPTEL

has the enough sensitivity to study the origin of ^{26}Al .

Diehl et al. (1995a) analyzed the first-year COMPTEL survey data, which has covered the whole Galactic plane. They applied two image-generation algorithms to the COMPTEL data: the *Maximum Likelihood* method [de Boer and et. al., 1991, Bloemen et al., 1994] which convolves a point source in the data space with the 3-dimensional point-spread function (PSF), testing for the statistical significance of the point-source hypothesis throughout the sky; the *Maximum Entropy* method (Strong et al. 1991; Strong 2003) which extracts a 1809 keV sky image, using the 3-D PSF, by maximizing the overall image entropy (i.e. minimizing its new information content) until satisfactory agreement with the data is achieved. These two methods yield the maps of 1809 keV emission along the Galactic plane with structured emission over a wide longitude range and a marked asymmetry relative to the Galactic center. The smooth intensity distribution expected from the nova origin cannot reconcile the data. Overlays of the ^{26}Al emission map with the positions of supernova remnants and Wolf-Rayet (WR) stars in the Galaxy suggest that the large-scale structure of ^{26}Al emission in the Galaxy may be contributed to massive stars. And the Vela region (the Vela SNR) shows evidence for a single identified close-by ^{26}Al source [Diehl et al., 1995b]. So the first ^{26}Al emission map of the Galactic Plane favors the dominant ^{26}Al origin from massive stars, presumedly core-collapse supernovae or Wolf-Rayet stars.

The first 1809 keV all-sky map was presented based on the first three years of COMPTEL observations [Oberlack et al., 1996]. This image was also based on the maximum entropy deconvolution method [Strong and et. al., 1991, Strong, 2003] applying an adjacent energy background model to the individual observation periods. The all-sky map confirmed the non-local character of the detected ^{26}Al emission in the first Galactic plane survey (Diehl et al. 1995a). Later, this feature was confirmed in the 5-year COMPTEL image [Oberlack, 1997]. Most of the ^{26}Al emission is attributed to young, massive stars and star-formation regions.

Knödlseder et al. [1999a] introduced a multi-resolution regularized expectation maximization algorithm (MREM) using a wavelet filtering for noise suppression, and applied it to the COMPTEL data. The MREM images are much less structured than the maximum entropy maps, but the previously reported main emission features can be confirmed. The MREM approach may be somewhat conservative with respect to image structures, whereas the maximum entropy images may still include artifacts.

Based on the 9-year COMPTEL observations (from the launch of CGRO in spring 1991 to the end of the mission, early summer 2001), Plüschke et al. (2001) obtained 1809 keV all sky maps with two imaging methods: the Maximum Entropy method and MREM. The background was also modelled on the basis of an adjacent energy approach. Both image reconstructions (see Figures 1.7 and 1.8) show an extended Galactic ridge emission mostly concentrated towards the Galactic center region ($-30^\circ < l < 30^\circ$), plus an emission feature in the Cygnus region, and a low-intensity ridge along the Carina and Vela regions. These features confirm the previously reported emission structures. In addition, the maximum entropy image shows some low-intensity fea-

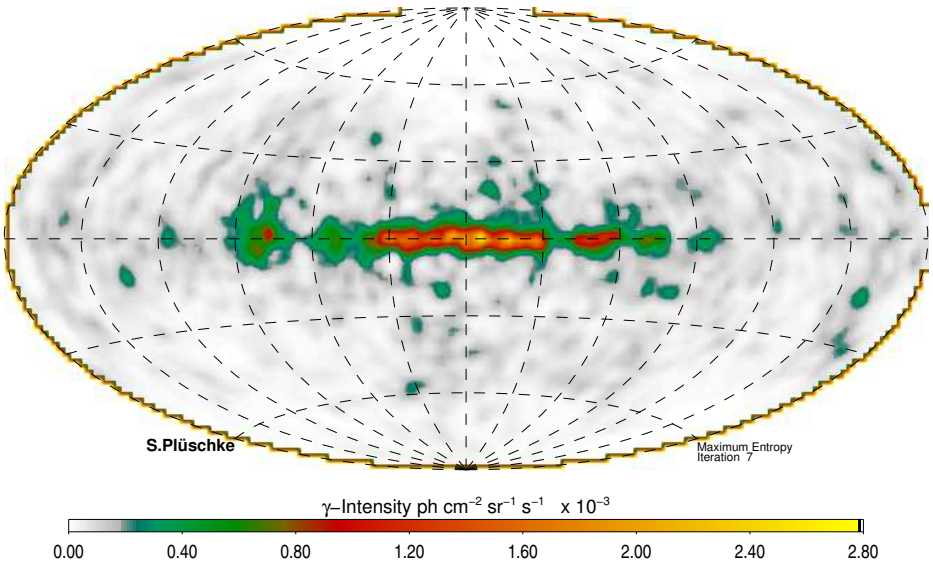

Figure 1.7: The maximum-entropy all-sky image of the Galactic 1809 keV line emission observed with COMPTEL over 9 years (from Plüschke 2001).

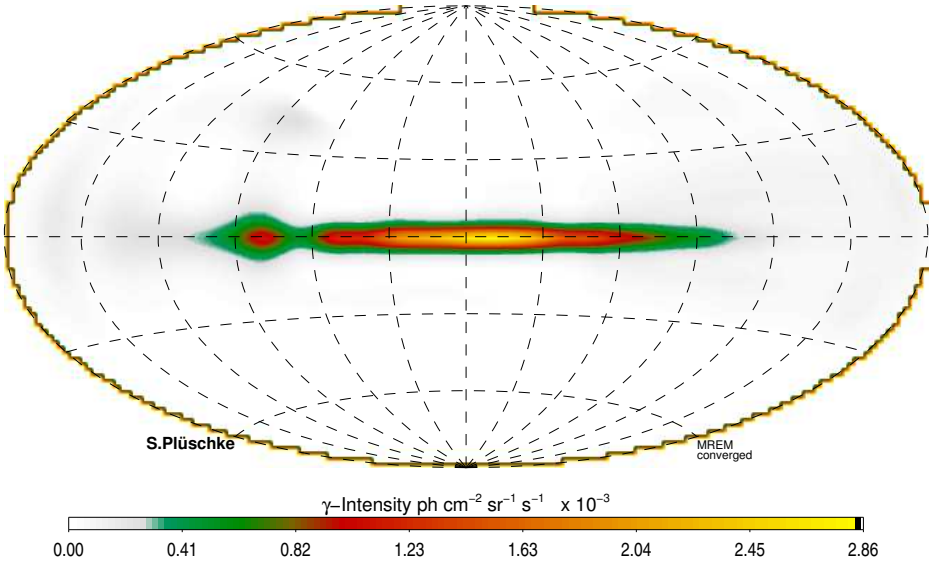

Figure 1.8: The MREM all-sky image of the Galactic 1809 keV line emission observed by COMPTEL over 9 years (from Plüschke 2001).

tures in the longitude range between 110° and 270°, e.g. the Orion region (Figure 1.7). Near the Galactic center region, the image shows a possible emission from the nearby Sco-Cen region. Also at latitudes beyond ±30°, some of these low-intensity structures are visible, which may be artifacts, subject to further studies.

In summary, from the all-sky ^{26}Al emission image by COMPTEL, the observed 1809 keV γ-ray line is ascribed to the radioactive decay of ^{26}Al in the interstellar medium. ^{26}Al has been found to be predominantly synthesized in massive stars and their subsequent core-collapse supernovae. Furthermore, ^{26}Al flux enhancements are detected aligned with regions of recent star formation, such as apparently observed in the Cygnus and Vela regions.

1.6 The origin of ^{26}Al in the Galaxy

^{26}Al is an unstable nucleus, produced almost exclusively by proton capture on ^{25}Mg in a sufficiently hot environment [Woosley, 1986], mainly destroyed by the β^+ decay into ^{26}Al since the competing destruction process, i.e., the ^{26}Al $(p,\gamma)^{27}$Si reaction, becomes efficient for $T > 5 \times 10^7$ K, and the end of central the H burning barely reaches such a temperature (see the reaction chains shown in Figure 1.9). In addition, the ^{26}Al freshly synthesized must be ejected into the interstellar medium before it is destroyed *in situ*. So its synthesis occurs, essentially in three different specific environments: i.e., the core H burning, the C and Ne convective shells, and the explosive Ne burning. For the hydrostatic nucleosynthesis in the core of stars with convective envelopes, the fresh ^{26}Al requires to be convected away from the hot inner burning region sufficiently fast to prevent destruction, and ejected by strong stellar winds. ^{26}Al can be also produced by nuclear reactions of low-energy heavy cosmic rays in the interstellar medium [Clayton, 1994].

The present theoretical knowledge of ^{26}Al origin in the Galaxy will be presented as follows (see more details in Prantzos & Diehl 1996). Here, we discuss five possible origins of ^{26}Al separately: core-collapse supernovae; Wolf-Rayet stars; novae; asymptotic giant branch (AGB) stars; and cosmic-ray nuclear reactions in the interstellar medium.

1.6.1 Core collapse supernovae

Massive stars (e.g. $M > 8M_\odot$) end up as core-collapse supernovae (Type II and Type Ib/c events). Thirty years ago, it has been suggested that ^{26}Al is created in core-collapse supernovae [Ramaty and Lingenfelter, 1977, Arnett, 1977]. Explosive ^{26}Al nucleosynthesis is triggered by the shock wave in the Ne burning shell (Woosley & Weaver 1980) and ^{26}Al production can be enhanced by neutrino-induced nuclear reactions [Woosley et al., 1990].

Significant ^{26}Al production occurs in the late pre-supernova phases, when ^{26}Al synthesized in the C/Ne convective shell is located close enough to the iron core that is

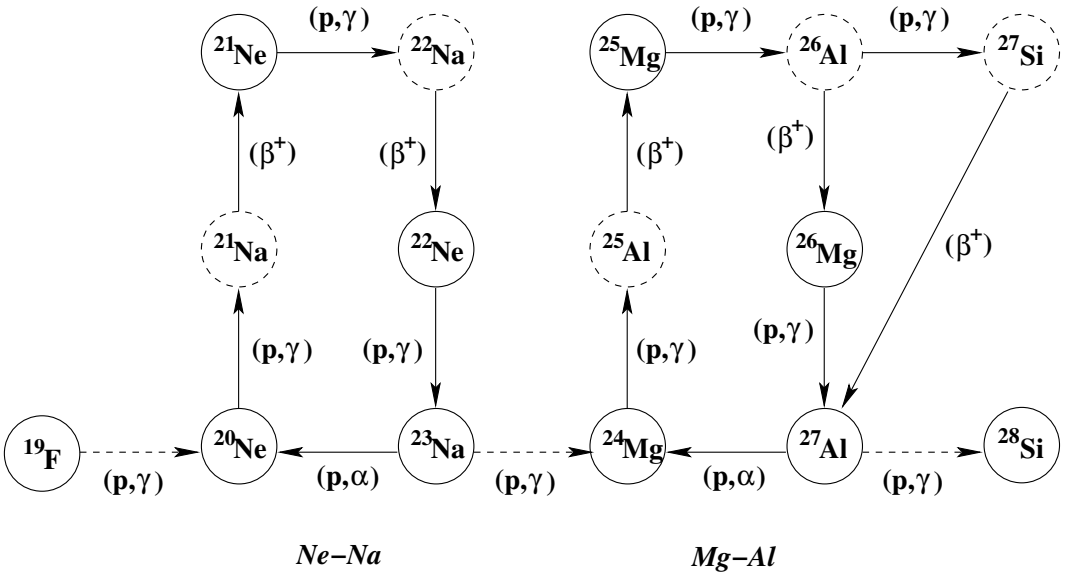

Figure 1.9: Reactions of the Ne-Na and Mg-Al chains. Unstable isotopes are denoted by dashed circles (from Rolfs and Rodney 1994).

partially destroyed by the passage of the shock wave. As for the C shell, its typical temperature [$\log(T) < 9.08$] does not allow in general a substantial production of ^{26}Al . But after the central Si burning, the strong contraction and heating of the inner core that precedes the final gravitational collapse, induces a strong temperature increase of the C-burning shell [$\log(T) \sim 9.255$]. If at this stage, such a burning occurs in an efficiently convective shell, a substantial amount of ^{26}Al is produced. ^{25}Mg that enters in the ^{26}Al production comes directly from the initial CNO abundance, and protons are mainly produced by the ^{12}C(^{12}C,p)^{23}Na and the ^{23}Na(α, p)^{26}Mg processes. Contrary to variation in C burning, ^{26}Al is always produced by Ne burning both in the center and the shell. A substantial amount of ^{25}Mg is left unburned in the C shell, protons needed to activate the ^{25}Mg(p, γ)^{26}Al reaction mainly come from the ^{23}Na(α, p)^{26}Mg. And the most effective proton poison is the ^{23}Na(p, α)^{20}Ne. In radiative environment the ^{26}Al *equilibrium* abundance depends on the local balance between production and destruction, so that only the presence of an efficient convective shell could act as a preservation buffer. Since most of stars do not reach the onset of the explosion with an efficient Ne convective shell, in general only small equilibrium abundance of ^{26}Al located with the radiative Ne burning shell is present at the beginning of the core collapse. There are exceptions for $14M_{\odot}$ and $15M_{\odot}$ models (see triangles in Figure 1.10). Stars within this mass interval are characterized by the lack of a C convective shell. At the end of the central Si burning, A Ne convective shell forms very close to the region where is was previously efficient in a C convective shell. During the last strong

contraction of the core, such a Ne convective shell penetrates a C-rich region with the consequence of producing a huge amount of ^{26}Al . In general, the larger the mass, the lager amount of ^{26}Al that survives the explosion (Woosley & Weaver 1995; Rauscher et al. 2002; Limongi & Chieffi 2006). The triangles in Figure 1.9 show the ^{26}Al yield produced in C/Ne convective shells that survived to the explosion as a function of the initial mass.

^{26}Al is produced during explosion at a typical temperature of the order of $\sim$ 2.3 billion degrees. Such a condition occurs within the C convective shell and the main process that controls its production is also the ^{25}Mg$(p,\gamma)^{26}$Al process, while its destruction is now controlled, roughly parithetically by the (n,p) and (n,α) processes. The ^{25}Mg now comes mainly from the (n,γ) capture on ^{24}mg, this isotope being a primary outcome of the C and Ne burning. The neutron density that enters in both the production and destruction of ^{26}Al is determined by the competition among several processes. The main neutron producers are (α,n) captures on ^{26}Mg, ^{25}Mg, ^{21}Ne, and ^{29}Si, plus the (p,n) capture on ^{28}Al, while the main neutron poisons are the (n,γ) captures on ^{24}Mg, ^{16}O, and ^{20}Ne. The proton density is determined by the competition between the production via the (α,p) captures on ^{20}Ne, ^{24}Mg, ^{23}Na, and destruction via the (p,γ) captures on ^{26}Mg, ^{20}Ne, ^{24}Mg, ^{27}Al and ^{25}Mg, plus the (p,n) reaction on ^{28}Al. In Figure 1.10, squares present the contribution of the explosive burning to the synthesis of ^{26}Al .

The explosive ^{26}Al yield is generally a little higher than pre-supernova production with the different initial masses (Limongi & Chieffi 2006, see Figure 1.10). But different models may have different predictions, e.g., the explosive ^{26}Al is low compared to pre-supernova production for stars with masses higher than $35M_{\odot}$ [Weaver and Woosley, 1993]. Typically, the ^{26}Al yields from core-collapse supernovae range from $2\times10^{-5}-5\times10^{-4}M_{\odot}$ with initial star masses of $12-120M_{\odot}$ (Limongi and Chieffi 2006, also see Figure 1.10).

1.6.2 Wolf-Rayet stars

Hydrostatic core H burning in the main sequence stars can produce large amounts of ^{26}Al . At central H exhaustion, the ^{26}Al is located in the He core and in the region of variable H left behind by the receding convective core. Since the He burning easily and quickly destroys the ^{26}Al (via the (n,α) and (n,p) reactions), the amount of ^{26}Al synthesized by central H burning and possible preserved up to the explosion is just the one located in the H-rich layers plus the one locked in the fraction of the He core that would not be affected by the He burning. If the dredge-up and the mass-loss were not effective, ^{26}Al would mostly decay before it could be ejected by the explosion. These two phenomena: dredge-up and mass-loss, may anticipate such ejection at earlier times and then increase the amount of ^{26}Al ejected into the interstellar medium.

Stars with masses between $10-35M_{\odot}$ will undergo a dredge-up episode that does not enter into the He core, and the mass-loss is weak. Since the He convective shell

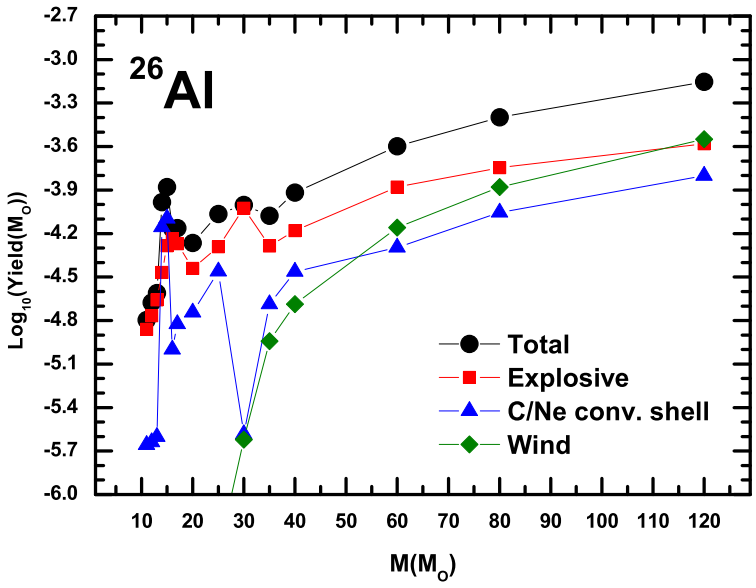

Figure 1.10: ^{26}Al yields in different processes (C/Ne convective shells, explosion, winds in the WR star phase) as a function of the initial stellar mass (from recent calculations by Limongi and Chieffi 2006).

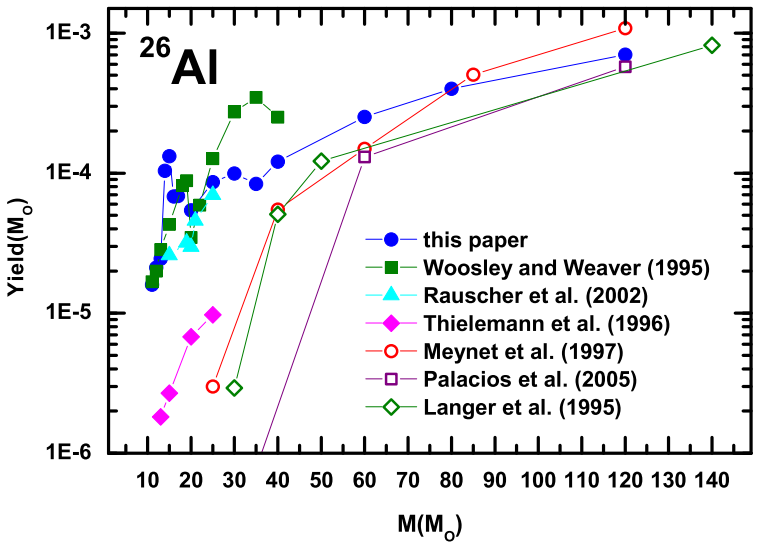

Figure 1.11: Comparison among the ^{26}Al yields as a function of the initial mass derived by different work in the last ten years (the data points of solid circles are taken from Limongi and Chieffi 2006). See more details in the text.

extends almost up to the base of the H burning shell, only a tiny amount of ^{26}Al which is present in the region of variable H left by the receding H convective core and engulfed in the convective envelope, would be ejected into the interstellar medium. Stars more massive than 35 $M_{\odot}$ do not show dredge-up episodes, but the mass-loss is so strong that a substantial fraction of the He core is ejected through stellar winds, i.e., the Wolf-Rayet phase [van der Hucht et al., 1988]. For the Wolf-Rayet stars, a large amount of ^{26}Al present in the He core is thus preserved from the destruction and ejected into the interstellar medium. So the main ^{26}Al production in the ISM before supernova explosions comes from the stellar winds of Wolf-Rayet stars.

The larger amount of ^{26}Al is produced with the higher initial masses of the Wolf-Rayet stars (Figure 1.10). The average yield of ^{26}Al production during the Wolf-Rayet phase ranges from $1 \times 10^{-5} - 3 \times 10^{-4} M_{\odot}$ for with initial star masses of $35 - 120 M_{\odot}$ [Limongi and Chieffi, 2006, Palacios et al., 2005].

From the all-sky survey of 1809 keV emission by COMPTEL (Plüschke et al. 2001, also see §1.3), the ^{26}Al in the interstellar medium is predominantly synthesized in massive stars, through the strong stellar winds of Wolf-Rayet stars and core-collapse supernova explosions. The total ^{26}Al yields due to the two processes have been calculated by different authors. Figure 1.11 displays the comparison among the ^{26}Al yields with a function of an initial mass by the different works (e.g., Limongi and Chieffi 2006;

Woosley and Weaver 1995; Langer et al. 1995; Meynet et al. 1997; Thielemann et al. 1996; Rauscher et al. 2002; Palacios et al. 2005). The average ^{26}Al yields provided by various work range from $(0.3-30)\times10^{-5}M_{\odot}$ for $10-35$ $M_{\odot}$ stars, and from $(1-10)\times10^{-4}$ $M_{\odot}$ for stars above 35 $M_{\odot}$. The calculations of the total ^{26}Al yield would be directly compared with the observational limits. Knödlseder [1999] argued that most of ^{26}Al in the Galaxy comes from WR stars, and the study of ^{26}Al in the Cygnus region is a way to resolve this argument.

1.6.3 Novae

^{26}Al production requires moderate peak temperatures, e.g., $T_{\rm peak} < 2\times10^{8}$ K, and a fast decline from maximum temperature [Ward and Fowler, 1980]. These conditions are commonly achieved in nova outbursts. In 1980s, one-zone model calculations of explosive H-burning nucleosynthesis with solar or CNO-enhanced envelopes [Hillebrandt and Thielemann, 1982, Wiescher et al., 1986] suggested that classical novae might produce sufficient amounts of ^{26}Al to account for some of the observed meteoritic anomalies but would not represent major Galactic sources. New calculations on the basis of ONeMg white dwarf stars [Weiss and Truran, 1990, Nofar, Shaviv, and Starrfield, 1991] produced large amounts of long-lived radioactive nuclei, such as ^{22}Na and ^{26}Al , concluding that the ONe novae might be important sources of the Galactic ^{26}Al . According to Nofar, Shaviv & Starrfield (1991), no ^{26}Al production occurs for models with $T_{\rm peak} > 2.7\times10^{8}$ K. But some calculations refute this result [Politano et al., 1995, Starrfield et al., 1993], demonstrating the crucial role played by convection to carry some ^{26}Al to the outer, cooler layers of the envelop, where its destruction through proton captures is prevented. Furthermore, the production of ^{26}Al by novae is very sensitive to the initial composition of the envelope and to the nuclear reaction rates adopted. ONe novae should be more important ^{26}Al sources than CO novae, because seed nuclei for the Ne-Na and Mg-Al cycles (see Figure 1.9) are almost absent in CO novae. For the same reason, the amount of ^{26}Al synthesized in ONe novae depends on the initial composition of the white dwarf core. Some improvements in the nuclear reaction rates since Caughlan and Fowler [1988] would lead to a lower ^{26}Al production. Recent hydrodynamic calculations of nova outbursts [Jose, Hernanz, and Coc, 1997] predict that the ejected ^{26}Al mass by ONe novae ranges from $(0.3-1.7)\times10^{-8}$ $M_{\odot}$ considering various white dwarf masses and accretion rates.

The amount of ^{26}Al ejected into the interstellar medium by ONe novae decreases as the mass of the underlying white dwarf increases [Jose et al., 1997]. So the low-mass white dwarfs are most likely candidates for ^{26}Al production, with the higher ^{26}Al production and higher ejected mass. But white dwarfs lower than $\sim 1.1M_{\odot}$ are expected to be CO white dwarf, which are unable to produce important quantities of ^{26}Al . Then the maximum ejection mass of ^{26}Al by one ONe nova event would be $\sim 2\times10^{-8}M_{\odot}$. The predicted contribution of nova outbursts to the Galactic ^{26}Al ranges $(0.1-0.4)$ $M_{\odot}$, which is small compared with the present observational limits

($M_{\rm gal}(^{26}{\rm Al}) \sim 2\ M_\odot$) derived by COMPTEL measurements [Diehl et al., 1995a] and INTEGRAL/SPI [Diehl et al., 2006a]. Hence, novae represent important ^{26}Al sources in the Galaxy, but cannot be the dominant ones, which is consistent with the accepted hypothesis of young populations as major sources of the Galactic ^{26}Al (see §1.3).

1.6.4 Asymptotic Giant Branch (AGB) stars

The intermediate-mass stars ($1.5 \leq M/M_\odot \leq 6$) can evolve through a thermally-pulsing phase with the strong stellar wind, so-called asymptotic giant branch (AGB) stars. AGB stars are characterized by two burning shells, one of helium, and one of hydrogen, and by a deep convective envelope extending from above the H-burning shell up to the surface. ^{26}Al could be produced in three sites of AGB stars: the H-burning shell via Mg-Al chain; the He-burning shell via α-capture on ^{22}Ne, and at the base of the convective envelope in the most massive AGB stars that experience H-burning. In AGB stars, ^{26}Al is efficiently produced by H-burning, but destruction by n-capture reaction during the interpulse and pulse phases become increasingly more efficient [Mowlavi and Meynet, 2000].

The ejected ^{26}Al masses by AGB stars depend on the temperature which directly relates to the initial mass, and initial composition. Recent calculations show that the low mass AGB stars ($< 4M_\odot$) cannot significantly contribute to ^{26}Al production [Mowlavi and Meynet, 2000, Karakas and Lattanzio, 2003]. The AGB star with masses of $4 - 6M_\odot$ can yield ^{26}Al in the regime of $(0.2 - 8) \times 10^{-8}\ M_\odot$ (Karakas & Lattanzio 2003). The AGB stars with lower metallicity produce a higher amount of ^{26}Al . The rough estimation of the contribution by AGB stars to the Galactic ^{26}Al varies from $0.01 - 0.4\ M_\odot$ (Mowlavi & Meynet 2000). Though the large uncertainties exist for the prediction of ^{26}Al by AGB stars, AGB stars cannot be the main ^{26}Al sources in the Galaxy. But the AGB stars could be best candidates to explain the inferred ^{26}Al /^{27}Al ratios ranging from $\sim 10^{-4} - 10^{-2}$ observed in meteoritic grains. As an interesting science, models predict a higher amount of ^{26}Al ($\sim (1 - 2) \times 10^{-7}\ M_\odot$, Mowlavi & Meynet 2000) around planetary nebulae, which could be possible candidates for direct ^{26}Al detection in future.

1.6.5 Interactions of cosmic rays with the interstellar medium

The interactions of accelerated particles with ambient matter can produce a variety of gamma-ray lines following the de-excitation of excited nuclei in both the ambient matter and the accelerated particles. Nuclear reaction of low energy heavy cosmic-ray particles have been proposed as another ^{26}Al source process [Clayton, 1994]. Based on the COMPTEL measurement of excited ^{12}C in the Orion molecular cloud complex [Bloemen et al., 1994], Clayton (1994) suggested that this could be an efficient ^{26}Al source process. The cross sections for the ^{26}Mg(H,n)^{26}Al and ^{28}Si(H,ppn)^{26}Al reactions are of the similar magnitude as the one for the ^{12}C(H,p)^{*12}C reaction. Therefore, the

estimation for the Orion region of active star formation corresponds to an ^{26}Al yield of $\sim 10^{-4}\ M_{\odot}$.

The Galactic ^{26}Al yield is quite uncertain, depending on the fractions of molecular clouds irradiated by low-energy cosmic rays. And the absence of substantial Galactic plane 4.4 MeV emission due to ^{12}C de-excitation suggests that this process is probably negligible as a Galactic ^{26}Al source [Ramaty, 1996].

1.7 The origin of ^{60}Fe

The radioactive isotope ^{60}Fe is believed to be synthesized through successive neutron captures on Fe isotopes (e.g., ^{56}Fe) in a neutron-rich environment inside He shells in AGB stars (^{60}Fe is stored in white dwarfs and cannot be ejected), and massive stars, before or during their final evolution to core collapse supernovae (see Figure 1.11). ^{60}Fe can be also synthesized in Type Ia SNe [Woosley, 1997]. It is also destroyed by the ^{60}Fe (n, γ) process. Since its closest parent, ^{59}Fe is unstable, the ^{59}Fe(n, γ) process must compete with the ^{59}Fe(γ^{-}) decay to produce an appreciate amount of ^{60}Fe .

1.7.1 Massive stars

A neutron-rich environment in massive stars is required to produce ^{60}Fe . And a temperature of the order of 2 billion degrees represents an upper limit for the synthesis of ^{60}Fe because above this temperature the (γ, n) and the (γ, p) photon disintegrations of both ^{59}Fe and ^{60}Fe become tremendously efficient. Such an occurrence limits a possible ^{60}Fe production to the He, C, Ne shell burning phases.

In He burning, the main neutron donor is the ^{22}Ne$(\alpha, n)^{25}$Mg process, and a temperature of the order of 4×10^8 K would be required to reach the threshold neutron density of $3 \times 10^{10}\ n\ \mathrm{cm}^{-3}$. In central He burning, the temperature remains below 3×10^8 K, so that the neutron density never exceeds $10^7\ n\ \mathrm{cm}^{-3}$, and no appreciable production of ^{60}Fe occurs. In shell He burning, the temperature could raise to and above 4×10^8 K, then a large amount of ^{60}Fe may be synthesized. For the stars with masses below 40 $M_{\odot}$, the temperature at base of the He convective shell never raises enough to make the ^{59}Fe(n, γ) process competitive with respect to the ^{59}Fe(β^{-}) decay, so no ^{60}Fe is synthesized in these stars. Such feature holds up to the first mass that becomes a WR star, which experiences such strong mass loss that it first loses all H-rich envelope and then continues eroding the He core up to the moment of the core collapse. In these stars, the He convective shell forms within the region of variable He abundance, then a problem arises of whether the Schwarzschild criterion or the Ledoux one is used to determine if a convective region forms. In Figure 1.13, The solid and open circles refer to the amount of ejected ^{60}Fe for two different choices of the stability criterion in the He convective shell, i.e., the Schwarzschild and the Ledoux criteria, respectively. C burning behaves similarly to the He burning. The neutron donor is the ^{22}Ne$(\alpha, n)^{25}$Mg

process, with α-particles provided by the $^{12}C(^{12}C,\alpha)^{20}Ne$ reaction. In C shell burning, the high temperature ($> 10^9$ K) allows a large production of α-particles which translates into a high neutron density and hence a large yield of ^{60}Fe . C convective shell could produce a conspicuous amount of ^{60}Fe in stars of the initial mass below 40 $M_\odot$. Ne burning may produce ^{60}Fe , but the lack of an extended and stable convective shell lasting up to the explosion prevents the build up of a significant amount of ^{60}Fe . The average yield of ejected ^{60}Fe in convective shells varies from $10^{-6} - 7 \times 10^{-4}$ $M_\odot$, increasing with the initial mass from 11 -120 $M_\odot$ [Limongi and Chieffi, 2006]. Calculations by Limongi & Chieffi (2006) also suggested the dominant yield of ^{60}Fe in massive stars above 40 $M_\odot$ comes from the He convective shell burning, which sensitively depends on the mass-loss rate. Models with a strong mass-loss rate [Langer, 1989] would reduce the ^{60}Fe production during the WR phases into a level of $\sim 10^{-5}$ $M_\odot$ (see Figure 1.13).

1.7.2 Supernovae

The last episode of synthesis of ^{60}Fe occurs when the blast wave crosses the mantle of the star on its way out during the core-collapse supernova explosions. The peak temperature is of the order of 2.2×10^9 K, and hence roughly in the same region where the explosive synthesis of ^{26}Al occurs. The average yield of ^{60}Fe in explosion varies from 10^{-5} $M_\odot$ (initial mass region of $11 - 50$ $M_\odot$) to 4×10^{-5} $M_\odot$ ($50 - 120$ $M_\odot$).

Figure 1.12 shows the total amount of ejected ^{60}Fe as a function of the initial stellar masses (from 11 -120 $M_\odot$) calculated by Limongi and Chieffi [2006]. The results by the previous work (initial masses from 12 -40 $M_\odot$, Woosley & Weaver 1995; Rauscher et al. 2002) are also presented for a comparison. In the initial mass range < 40 $M_\odot$, the ^{60}Fe yield by Rauscher (2002) are significantly larger than the yields by both Woosley & Weaver (1995) and Limongi & Chieffi (2006). In Figure 1.12, the solid and open circles are obtained by adopting the mass-loss rate by Nugis and Lamers [2000]; the stars are obtained by taking the rate by Langer [1989]. The mass-loss rate proposed by Langer [1989] is much stronger than the Nugis and Lamers [2000] one. With adopting a stronger mass-loss rate, they have significantly reduce the ^{60}Fe production during the WR phases with the initial masses above 40 $M_\odot$.

In addition, ^{60}Fe could also be produced in substantial amounts by rare subtypes of SN Ia [Woosley, 1997], which would then be point sources of ^{60}Fe gamma-rays. The average yield of ^{60}Fe in SN Ia is $(1 - 5) \times 10^{-3}$ $M_\odot$ depending on models. The ^{60}Fe per event is typically 100 times greater in a high-density white dwarf explosion than in a Type II supernova. With an event rate 10^{-4} yr^{-1}, the composite signal here comes from $\sim$ 100 point sources. A single source at 10 kpc that made 0.005 $M_\odot$ of ^{60}Fe would be visible for several million years at a flux level of 10^{-7} ph cm^{-2} s^{-1}. However, this is well beyond the capability of present gamma-ray telescopes.

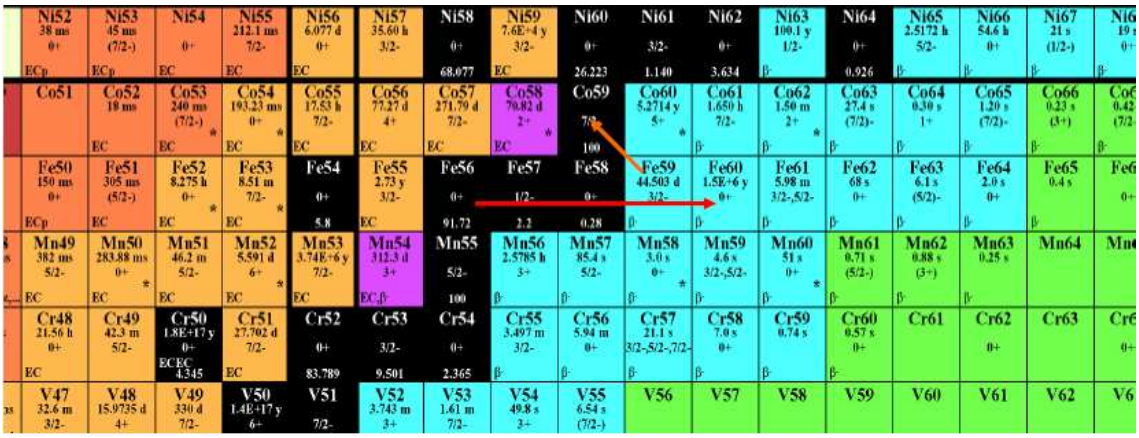

Figure 1.12: The caption of ^{60}Fe produced by neutron capture processes of iron isotopes e.g., ^{56}Fe, and ^{59}Fe β-decay will generate a leak in the ^{60}Fe production.

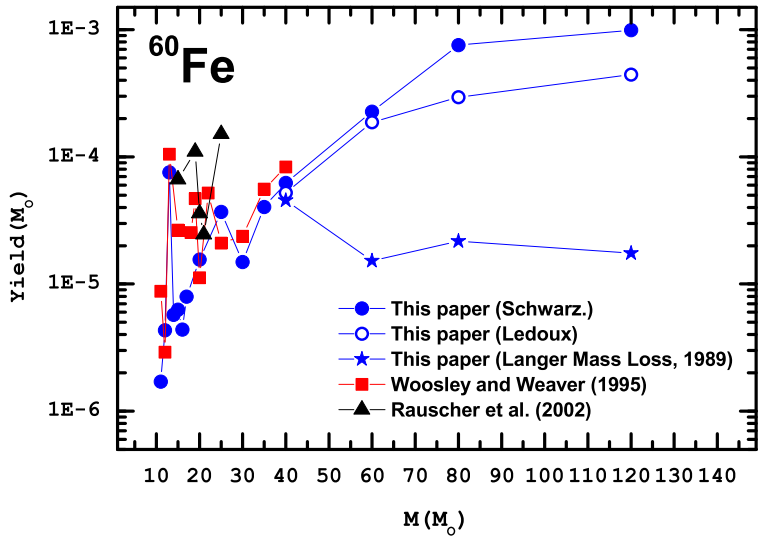

Figure 1.13: Comparison among the ^{60}Fe yields as a function of the initial stellar mass provided by various authors (from Limongi & Chieffi 2006). The solid and open circles refer to the amount of ejected ^{60}Fe for two different choices of the stability criterion in the He convective shell, i.e., the Schwarzschild and the Ledoux criteria, respectively. The stars represent the amount of ejected ^{60}Fe obtained by adopting the Langer [1989] mass-loss rate for massive stars (WR stars of masses from 40 - 120 $M_{\odot}$). Solid squares and triangles are the results from Woosley and Weaver [1995] and Rauscher et al. [2002] in the initial mass range of 12 - 40 $M_{\odot}$.

1.8 The INTEGRAL spectrometer (SPI)

The *INTE*rnational *G*amma-*R*ay *A*strophysics *L*aboratory (INTEGRAL) is an European (ESA) Gamma-Ray Observatory Satellite Mission for the study of cosmic gamma-ray sources in the keV to MeV energy range [Winkler et al., 2003]. INTEGRAL was successfully launched from Baikonur Cosmodrome (Kazakhstan) on October 17, 2002 using a Proton rocket provided by the Russian Space Agency. The INTEGRAL orbit is eccentric, with an apogee of 153 000 km, a perigee of 9000 km, and a 3 day period [Jensen et al., 2003].

The scientific objectives of INTEGRAL concentrate on:

(1) stellar nucleosynthesis via detection, cartography and fine spectroscopy of sources (nearby SNRs) and structures (Galactic disk) emitting radioactive gamma-ray lines such as those of ^{44}Ti, ^{26}Al , ^{60}Fe and the 511 keV positron annihilation line;
(2) compact objects such as pulsars, neutron stars and black holes in binaries, and massive black holes in the centers of active galactic nuclei;
(3) gamma-ray burst studies using fast detection and precise localization at the arcmin level to trigger afterglow studies.

The Principal Investigators (PI's) and Mission Scientists for INTEGRAL together with representatives of the participating agencies constitute the INTEGRAL Science Working Team (ISWT). All PI teams, providing the payload and data center, consist of large international collaborations from scientific institutes from almost all 14 ESA member states, USA, Russia, Czech Republic and Poland.

INTEGRAL was conceived from its initial study phase in 1989 as an observatory-type mission [Winkler et al., 2003]. Most of the total observing time ($\sim$ 70%) is awarded as the General Programme to the scientific community at large. Proposals for observations are selected on their scientific merit only by a single Time Allocation Committee (TAC). These selected observations are the base of the general programme. As a return to those scientific collaborations and individual scientists who contributed to the development, design and procurement of INTEGRAL and who are represented in the INTEGRAL Science Working Team (ISWT), a portion of the total scientific observing time, the guaranteed time, will be used for their Core Programme observations. INTEGRAL data are not automatically Public. Within one year, the data belong to the PI of the observation.

Two main instruments are on board INTEGRAL(see Figure 1.14): the INTEGRAL imager (IBIS) with an angular resolution of 12′, allowing for source localization with arcmin precise with a field of view of $9^\circ \times 9^\circ$ [Ubertini et al., 2003]; the INTEGRAL spectrometer (SPI) with an energy resolution of 2.5 keV at 1.3 MeV and angular resolution of 2.5° within a field of view of $16^\circ \times 16^\circ$. Two small monitors are included in the payload: JEM-X composed of two identical X-ray telescopes that provide comple-

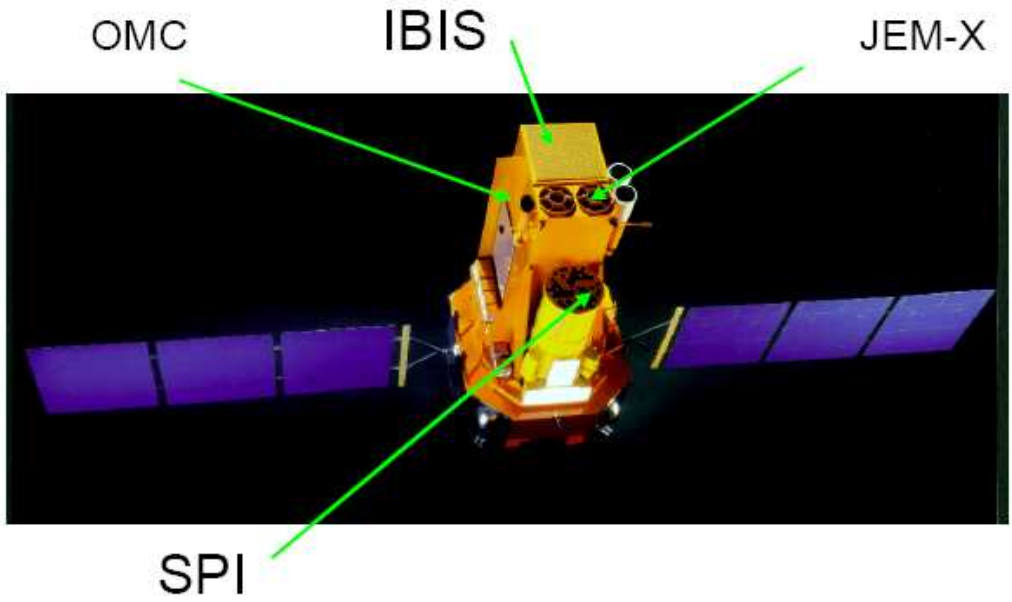

Figure 1.14: The four main instruments aboard INTEGRAL: the imager IBIS; the spectrometer SPI; the X-ray monitor JEM-X; and the optical camera OMC.

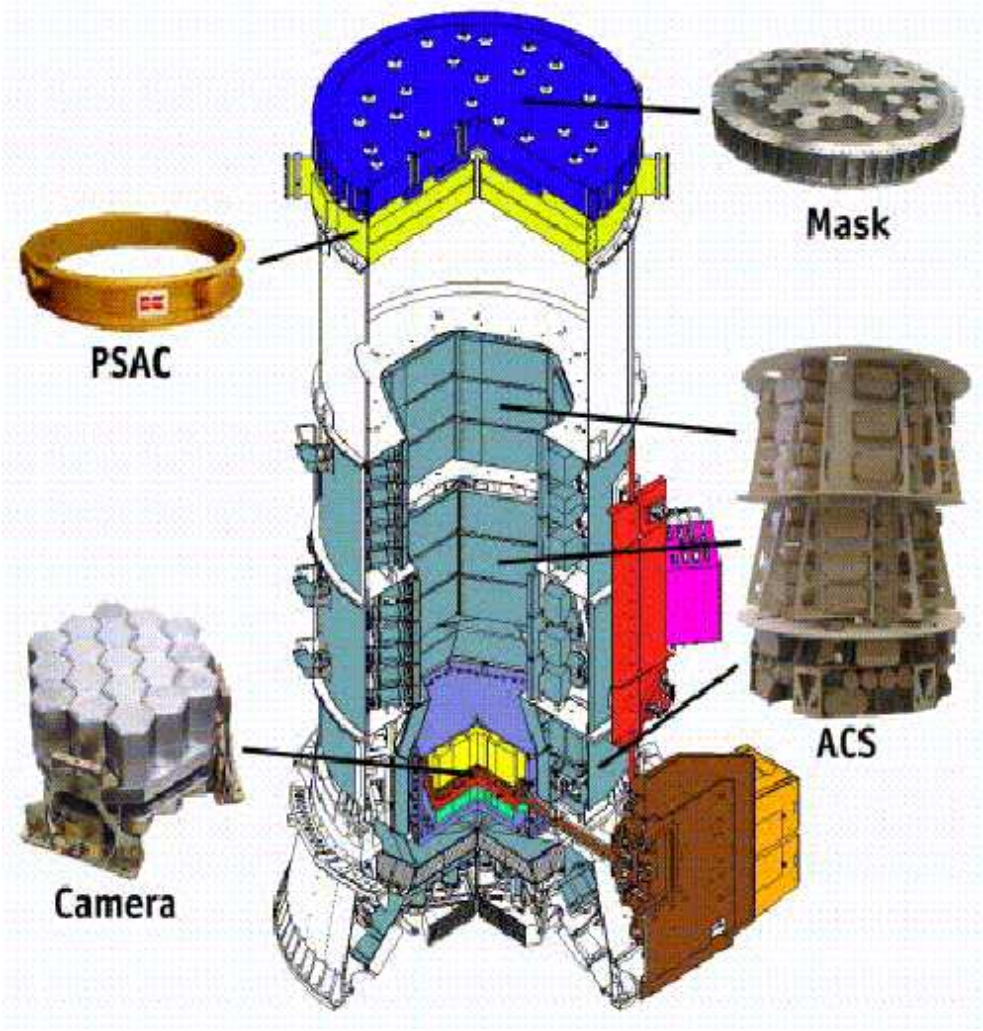

Figure 1.15: A brief cut-away view of the SPI instrument. The coded mask, plastic scintillator anticoincidence subassembly (PSAC), Ge camera and ACS subsystems are highlighted.

Table 1.2: Key parameters of the INTEGRAL spectrometer SPI

Parameter	Value
Energy range	18 keV – 8 MeV
Detector	19 Ge detectors, cooled at 85 K
Detector area	500 cm^2
Field of view (fully coded)	16° (corner to corner)
Spectral resolution (FWHM)	3 keV at 1.8 MeV
Angular resolution (FWHM)	2.5° (point sources)
Continuum sensitivity (3σ, 10^6s	5.5×10^{-6}ph cm^{-2} s^{-1} keV^{-1} at 100 keV
Line sensitivity (ph cm^{-2} s^{-1}, 3σ, 10^6s	3.3×10^{-5} at 100 keV, 2.4×10^{-5} at 1 MeV
Source location (radius)	$\leq 1.3°$ (depending on S/N)
Absolute timing accuracy (3σ)	$\leq 200\mu$s
Mass	1309 kg
Power (max/average)	385 W / 110 W

mentary data from 1 to 15 keV; OMC, an optical camera (Winkler et al. 2003).

Here, we only provide a brief description of the spectrometer SPI. (Figure 1.15, see more details in Vedrenne et al. 2003; Roques et al. 2003). SPI consists of the following main subsystems [Vedrenne et al., 2003]:

(1) the camera, composed of 19 high purity germanium detectors (GeD) and their associated electronics;
(2) a two-stage cooling system: the passive stage cools the cryostat housing and the preamplifiers to 215 K; the active stage cools the Ge array down to 85 – 90 K;
(3) a pulse shape discrimination system which allows discrimination between single and multi-site interactions in one Ge detector;
(4) an active anticoincidence shield (ACS) made of 91 $Bi_3Ge_4O_{12}$ (BGO) crystal blocks and a plastic scintillator anticoincidence subassembly (PSAC);
(5) a digital front-end electronics (DFEE) providing the SPI internal timing, the various (anti)coincidence functions, and the primary data encoding;
(6) a coded mask which allows imaging of the sky.

A summary of key instrument parameters of SPI is presented in Table 1.2 (also see Vedrenne et al. 2003).

At present, SPI has been functioning well for four years. Observations and science analyses of SPI data will be presented in details in Chapter 2. Ge detectors allow for high spectral resolution of $\sim$ 2.5 keV at 1 MeV, suitable for astrophysical studies of individual gamma-ray lines and their shapes, e.g. the 511 keV line, γ-ray lines from

radioactivities of ^{44}Ti, ^{26}Al and ^{60}Fe .

2 Data analyses of INTEGRAL/SPI at MPE

The SPI spectrometer on aboard INTEGRAL features a camera system with 19 Ge detectors, imaging photons through a tungsten coded mask. Though background is reduced by an anticoincidence detector system surrounding them, the background dominates the overall gamma-ray signals.

The coded mask casts a shadow onto the camera plane, effectively occulting approximately 50% of the camera area for a point source in the sky. Variation of the camera pointing around the source direction in a dither pattern is used to collect a database of shadowgrams which can be deconvolved to find the source location also in the presence of a large background signal. Though SPI supports γ-ray imaging, it has been optimized for γ-ray line spectroscopy with a high energy resolution ($\sim$ 2.5 keV at 1 MeV, Attié et al. 2003, Roques et al. 2003). In this thesis, we also concentrate on the spectroscopy analysis of the SPI data, with studies of γ-ray lines from cosmic radioactivity of ^{26}Al and ^{60}Fe in the Galaxy.

Calibration campaigns of the spectrometer SPI have been performed before launch in order to determine the instrument characteristics, such as the effective detection area, the spectral resolution and the angular resolution [Attié et al., 2003]. Absolute determination of the effective area has been obtained from simulations and measurements. At 1 MeV, the effective area is 65 cm^2 for a point source on the optical axis, the spectral resolution $\sim$2.3 keV. The angular resolution is better than 2.5° and the source separation capability about 1°. Temperature dependant parameters will require permanent in-flight calibration. Neutron or spallation induced background lines will be used as tracers to extract the background component of some lines of astrophysical interest.

The INTEGRAL Science Data Center (ISDC) provides the basic infrastructure for science analysis [Courvoisier et al., 2003], i.e., an organized archive of the data, and the associated software tools to prepare, execute, and view data analysis steps. The ISDC infrastructure was prepared in a most instrument-independent way, and instrument-specific algorithms were isolated in "instrument-specific software" modules. Standard analysis has been prepared at ISDC through scripts which perform a pipeline of processing tasks, starting from the pointing set definition, and routinely ending in images and/or point source spectra, through e.g., the SPIROS software [Skinner and Connell, 2003]. Such analysis will adequately address point sources with continuum spectra within the inner field of view. And γ-ray line spectral analysis and diffuse emission would have less well-conditioned analysis problems. The general description of the SPI data analysis methods and algorithms at ISDC was presented in Diehl et al. [2003a].

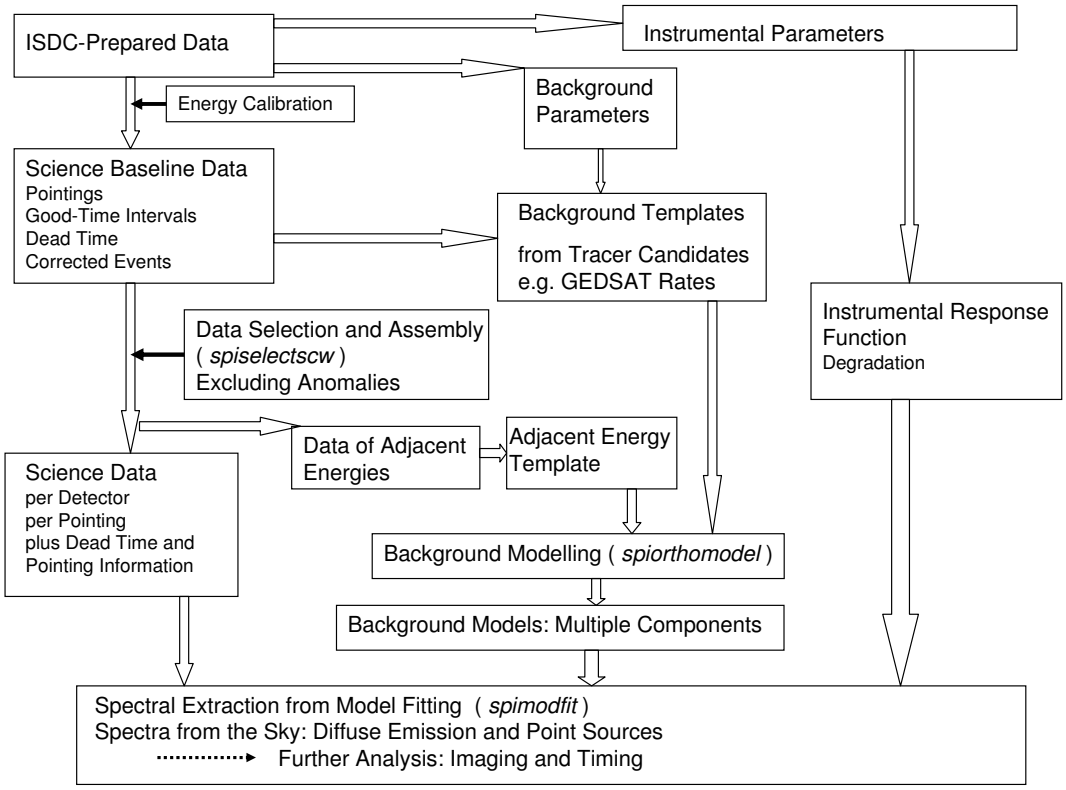

Figure 2.1: Scheme for the SPI data analysis software system developed at MPE.

In this chapter, we will give an overview of the SPI data analysis software system developed at Max-Planck-Institut für extraterrestrische Physik (MPE, Figure 2.1). This analysis system has been optimized to study individual γ-ray lines and diffuse emission components from large observation sets covering four years of data.

The data analysis steps are (also see Figure 2.1):

(1) Assembly of data selected to be free of contamination by, e.g., solar-flare events.

(2) Modelling the instrumental background over the full time period of observations using the full INTEGRAL database.

(3) Fitting the measured data in narrow energy bins with the background model and a model of celestial gamma-ray emission, folded through the instrumental response into the data space of the measurement; the fitted amplitude of the celestial model per energy bin then comprises the spectrum of observed sky emission.

(4) Deriving line parameters of the celestial signal including point sources and diffuse emission.

In the following, we will discuss in details the analysis steps and their implementation in the corresponding software utilities within MPE's INTEGRAL/SPI data analysis system. Firstly, we will introduce the observations with SPI.

2.1 INTEGRAL/SPI observations

INTEGRAL/SPI is a spectrometer devoted to the sky observation in the 18 keV – 8 MeV energy range using 19 Ge detectors (GeD). The performance of the cryogenic system is nominal and allows to cool the 19 kg of Ge down to 85 K with a comfortable margin. The energy resolution of the whole Ge camera is $\sim$ 2.5 keV at 1 MeV [Roques et al., 2003, Attié et al., 2003]. However, this resolution degrades with time due to cosmic particle irradiation in space. And the instrument is periodically shut off for a few days while annealing (by heating from cryogenic temperatures to 100°C) is applied to the detectors to restore the energy resolution (i.e. Figure 2.2) by heating of the cosmic-ray-induced defects [Roques et al., 2003, Leleux et al., 2003]. The success of annealing high depends on the initial damage and on the annealing temperature and duration. SPI Ge detectors are heated by four resistors glued on the Ge detector array support. From energy resolution evolution with time in Figure 2.2, specially the changes after each annealing, the recovery looks nearly perfect. The annealing capability of SPI is a constraint on the design of the camera but necessary to ensure good performance for a long lifetime mission ($>$ 5 years).

Primary γ-ray signals are gamma-ray interactions in the 19 Ge detector modules of the camera, translated in detector signal amplitude, shape and relative time among detector units. Triggers of just one of the 19 detectors are called *single events* (SE, *pseudo-detector* IDs 0 – 18), with three subclasses distinguished (in *pseudo-detector* IDs 85 – 141), depending on the success of the pulse shape determination. A basic event message holds detector-ID, trigger time, signal amplitude, and measured pulse shape informa-

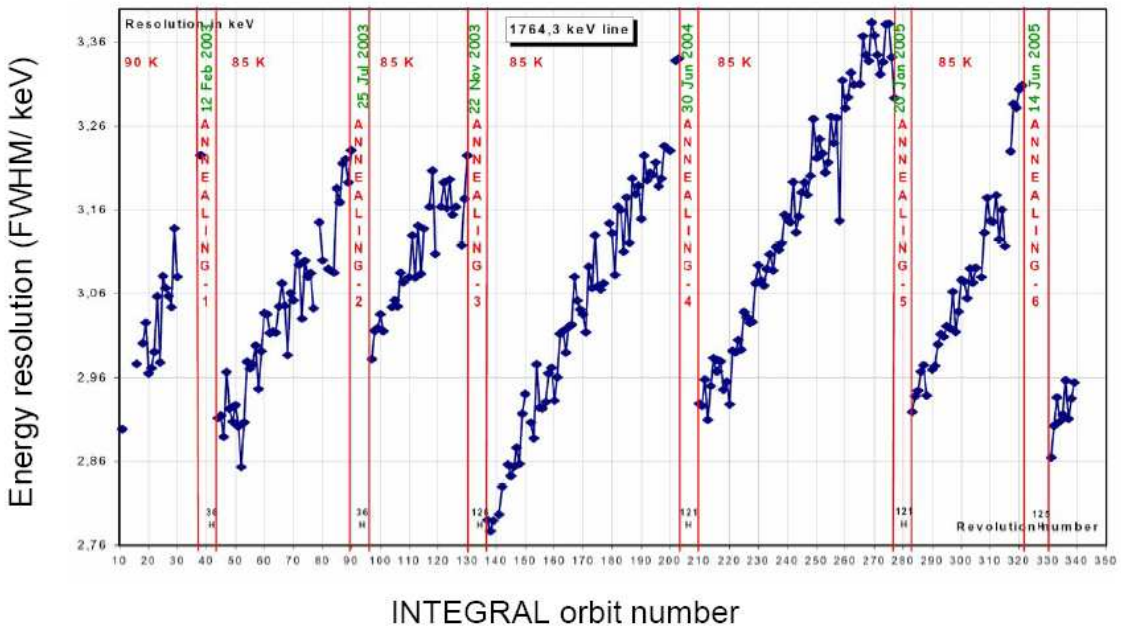

Figure 2.2: Energy resolution evolution with time in units of the INTEGRAL revolution (3 days) around 1800 keV, and six annealing processes are noted with dates and durations in units of hours. This energy resolution is determined from the spectrum for each detector individually and then averaged over all 19 detectors.

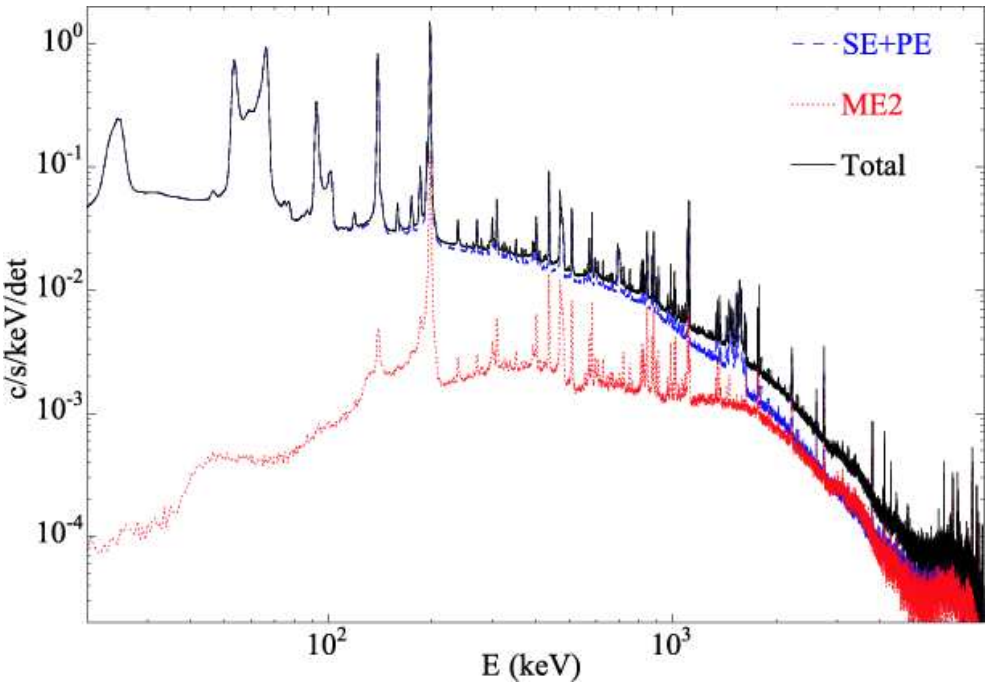

Figure 2.3: Averaged SPI raw spectrum dominated by background and instrumental lines [Weidenspointner et al., 2003]. Single GeD event (SE+PE) and double detector event (ME2) spectra are shown separately (from Jean et al. 2003).

tion. If the pulse shapes are derived, these are then called *pulse-shape-discrimination events* (PE). Detector triggers which occur simultaneously in more than one of the 19 detectors within a coincidence interval of 350 ns are called *multiple events* (ME, *pseudo-detector* IDs 19 – 84). They may arise from an interaction cascade of a single primary photon. A subclass, double Ge detector events (ME2, *pseudo-detector* IDs 19–60) trigger two Ge detector elements. For ME, the identifiers of detectors involved and all pulse heights are transmitted together with the relative arrival times in detectors. These multiples effectively constitute *virtual detector modules*, which can be used together with 19 real detectors for improved sensitivity and angular resolution at higher energies. The count ratio of ME to SE rises with increasing energies, being $\simeq$ 40% at 2 MeV (see Figure 2.3).

All events are processed by the digital front end electronics (DFEE, Vedrenne et al. 2003). This system provides event timing with 102.4μs accuracy, event rejection using the ACS veto signal. The events are also counted and the dead time is permanently monitored. The data processing electronics (DPE) receives from the DFEE all the data needed for such onboard analysis prior to telemetry to ground. Figure 2.4 shows the distribution of 19 GeDs and the non-saturating non-vetoed counts ($<$ 8 MeV).

The number of detectors in the array is too small to achieve good imaging perfor-

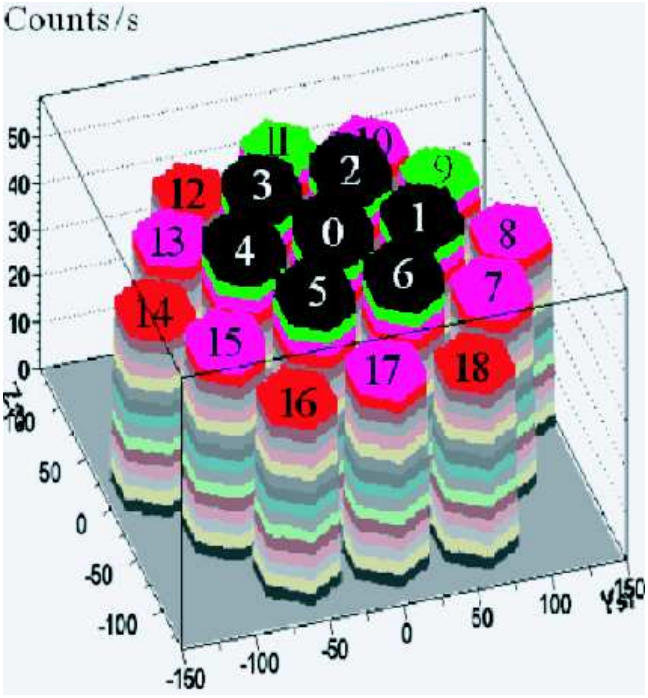

Figure 2.4: Distribution of 19 GeDs and the non-saturating, non-vetoed Ge counts on the SPI camera (from Roques et al. 2003, vertical axis in counts/s, Ysi and Zsi axis = positions of the detectors in mm, detector numbers marked on the plot). The outer detectors show less counts, since Compton scattered photons may escape into the BGO crystal shield and activate a veto signal, which suppresses the event.

mance from a single pointing, so successive images of the same field of view are taken with slightly different pointing angles. This is the *dithering* strategy which is used for both SPI and IBIS aboard INTEGRAL [Vedrenne et al., 2003]. At intervals of typically 30 minutes, the spacecraft is reoriented using inertial wheels to follow a prescribed dithering pattern. This strategy allows the sources to be separated from the background, which is particularly difficult due to the low level of the source signal (e.g., ^{26}Al emission in the Galaxy, few percent of the background). It also minimizes the effects of the small variations of the background which occur despite the choice of an eccentric orbit outside the radiation belts.

The SPI data are pre-processed using the ISDC standard analysis software (OSA) up to the level of event housekeeping into spectra and the corresponding assembly of pointing and livetime information. The present version is OSA 6.0 which was published in December 2006. The energy calibration is performed using instrumental background lines with known energies [Weidenspointner et al., 2003]. This is a critical operation for γ-ray line studies (sub-keV accuracy), for continuum studies, a standard

calibration (about 1 keV accuracy) is quite adequate. Various energy binnings can be used depending on the available statistics as a function of energy. After the failure of detector 2 at the INTEGRAL Julian Date (starts at 1 Jan 2000) 1434, the remaining 18 detectors were used; and after the failure of detector 17 at the Julian Date 1659, the remaining 17 detectors were used (see Figure 2.4).

2.2 Data selection and assembly

We test data quality per each 'science window' (typically a time interval of $\sim$ 30 minutes corresponding to one pointing), applying selection limits to 'science housekeeping' parameters such as the count rates in several onboard radiation detectors, instrument status codes, data ownership, and orbit phase (utility *spiselectscw*). We employ the INTEGRAL Radiation Environment Monitor (IREM; Hajdas et al. 2003), the SPI plastic scintillator anticoincidence counter (PSAC), and the rate of saturating events in SPI's Ge detectors (from events depositing > 8 MeV in a detector; hereafter referred to as GEDSAT rates) to exclude solar-flare events and other erratic background increases. We exclude data where the GEDSAT rates fall below 50 counts/s and exceed 10^5 counts/s to reject anomalies. Regular perigee background increases are additionally eliminated through a 0.05–0.95 window on orbital phase in order to exclude orbit phases near the Earth's radiation belts. From the selected events, spectra are accumulated per each detector and pointing, and together with dead time and pointing information assembled into the analysis database.

In studies, we establish databases both for SE (detector IDs 0–18) and ME (detector IDs 19 – 84). For γ-ray line studies, e.g., ^{26}Al and ^{60}Fe , the selected data are in spectral ranges with 0.5 keV or 1 keV bin size (depending on the scientific objectives) in $\sim 20 - 30$ keV bands around each of the γ-ray lines for science analysis, and also include data adjacent to the lines for determination of instrumental background (see below). These processes will be repeated in the following chapters for the different studies. For example, in ^{26}Al studies (see Chapter 3), we use the SE data in the spectral range of 1785 – 1826 keV with 0.5 keV bin size for the line analysis; for the background modelling from the adjacent continuum, we make use of 1785 – 1802 keV plus 1815 - 1826 keV, which have been combined into one energy bin. At present, SPI has accumulated 4 years of data. We will use all these data from the INTEGRAL core program (focusing on the survey of the inner Galaxy), data with rights (PI ownerships) residing within the MPE group, and public data available in March 2007. The exposure map of the selected data (for a sample of ^{26}Al studies) has been shown in Figure 2.5.

2.3 Background modelling

SPI spectra are dominated by the intense background radiation characteristic (see Figure 2.3) of space platforms undergoing cosmic-ray (CR) bombardment. Much of this

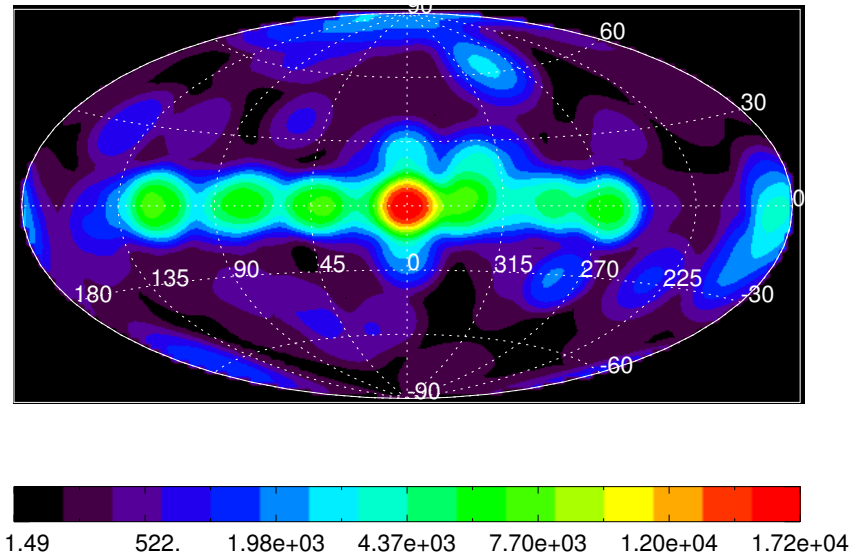

Figure 2.5: Exposure map of the all sky for the ^{26}Al data selected from 4-year SPI observations (from orbits 43 – 525). The database covers the whole sky with 23701 pointings, equivalent to a total deadtime-corrected exposure time of 47 Ms. The observations concentrate on the Galactic Plane, specially in the Galactic center, the inner Galaxy region, Cas A, Cygnus, and Carina-Vela regions.

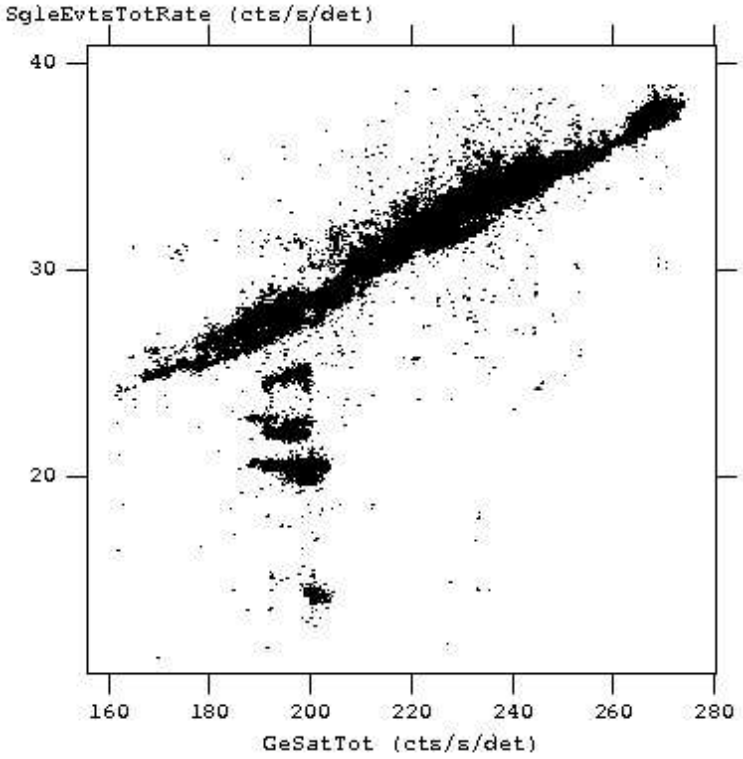

Figure 2.6: Total rates of single events for 19 Ge detectors (SgleEvtsTotRate) versus total rates of GEDSAT rates (GeSatTot).

radiation is prompt, resulting directly from CR impacts, whose variation with time ought to follow that of the incident CR flux. Other components arise from radioactive isotopes produced by the CR impacts, whose decay lifetimes are long compared to the coincidence window of the detector-anticoincidence electronics. Radioactive isotopes will increase in abundance until CR production balances β-decay. A time series of their γ-ray emission will be the convolution of the time behavior of the prompt CR source with an exponential decrease from decay (an exponential function e^{-t/τ_0}, where τ_0 is the isotope's decay time. Local radioactivity in the spacecraft and instruments themselves thus will generate both broad continuum background emission and narrow gamma-ray lines from long-lived radioactive isotopes. Varying with energy, background components may exhibit complex time variability due to their origins from more than one physical source.

We derive models for the background contribution per energy bin and pointing in each detector from comparisons to presumed 'tracers' of background; for these, we use independent contemporaneous measurements aboard INTEGRAL (Diehl et al. 2006c, and see Halloin et al. 2007 in preparation, also background model studies by

Sizun et al. 2007 in preparation). Comparing different candidate tracers to observed background variations, we find the best tracer(s) of background for each energy band. Candidate tracers with high statistical precision are the rates measured in SPI's plastic scintillator anticoincidence detector, the rate of saturated events in the BGO shield, the detector-by-detector GEDSAT rates (from events depositing >8 MeV in a Ge detector, reflecting the variability and effects of cosmic rays on detectors, also see Figure 2.6), and Ge-detector rates integrated over rather wide energy bands (for better statistical precision).

A correlation between total rates of single events for 19 Ge detectors and total rates of GEDSAT rates is shown in Figure 2.6. So the GEDSAT rates are good tracers to variability of background dominated in SPI raw spectra. For our analysis, we make use of the GEDSAT rates tracing the prompt CR activation to the γ-ray lines.

Each such tracer is regarded as a 'template' for time variability of background. By normalizing such a template to the set of counts per detector spectrum (i.e. per pointing), a background model can be constructed, which is applicable to the analysis data set of spectra. We construct our background model from two components, one derived from adjacent energy bands, and an additional component modelling instrumental line contributions.

Thus, in a first step, the detector-by-detector count rates in the continuum bands are fitted by the GEDSAT time series (a tracer for time variability of background in the adjacent continuum bands, Figure 2.6) to construct an 'adjacent-energies' background template.

Other background templates which are used for modelling instrumental line contributions come from the radioactive background line components in the energy bands in the individual science analysis. Generally, the GEDSAT tracer is taken as an important background component tracer for the instrumental line features which blend into the celestial γ-ray line signals (see above). This additional background component tracer is enough for the ^{26}Al studies (see Chapters 3 & 4). For studies of the ^{60}Fe lines, other radioactive background line component tracers may been needed, which will be discussed in Chapter 5.

Then, the set of detector-by-detector spectra per pointing in 0.5 or 1 keV bins covering the $\sim$ 20 keV intervals around and including the γ-ray lines are fitted to the sum of the adjacent continuum template, plus a GEDSAT template, or/and plus additional radioactivity templates for special important radioactive background lines, to capture any additional prompt background.

The adjacent continuum template is taken as the prime background tracer. And then we remove the information of this prime tracer from other candidate tracers through orthogonalization. So that we orthogonalize the different background model components for an improved convergence of the fitting (utility *spiorthomodel*, also see §2.2 of Diehl et al. 2006c). This step ensures that each higher-order background component carries new and independent information.

Thus we generate a background model for our actual set of spectra, which is con-

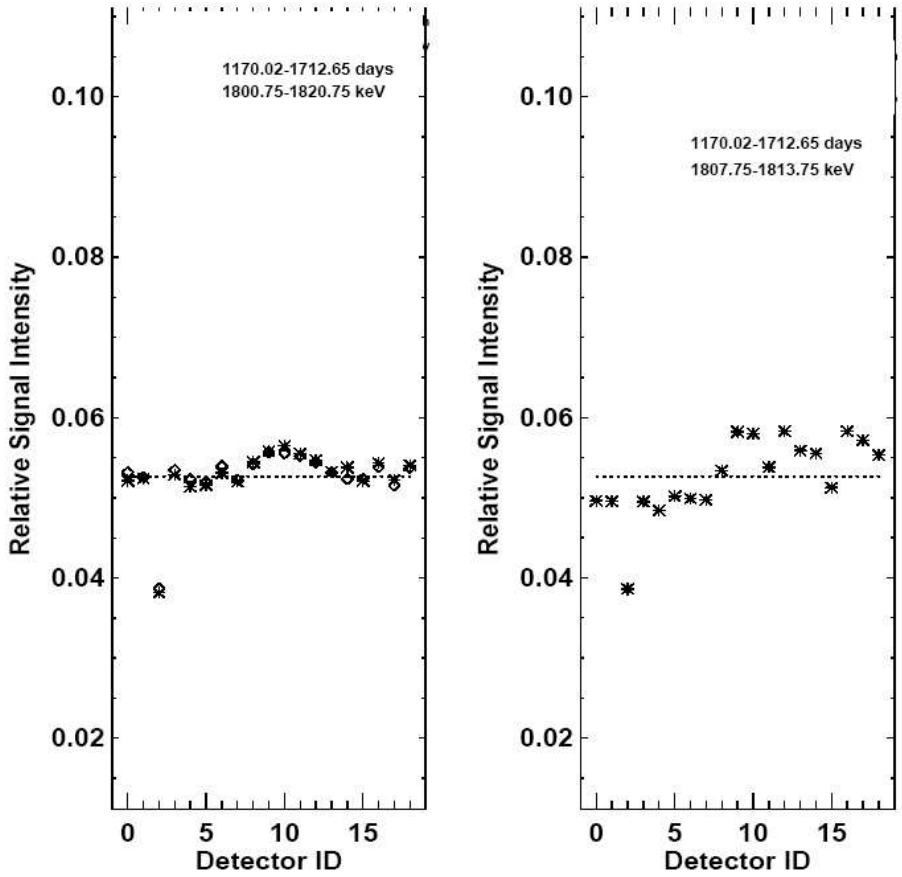

Figure 2.7: Detector ratios around the ^{26}Al energy band (1800 – 1820 keV): relative intensities of 19 detectors (see Figure 2.4) for the continuum (left) and for the 1810 keV line feature (right).

strained in its variability by the various background tracers. Contributions of celestial gamma-ray events are small, their variability is intrinsically different due to the coded-mask modulation of the background model supplemented by dithering, and thus is expected only to affect global normalization, but not the variability with time.

As we know, the counts vary with detectors. This detector ratio also changes with energies and spectral features. Figure 2.7 displays the detector ratios around the ^{26}Al energy band. The ratio in the continuum band (1800 – 1820 keV) is quite different from the ratio in the line feature (1807 – 1813 keV). This behavior should be taken into account in the background modelling in the ^{26}Al and ^{60}Fe line studies, specially for the high-resolution spectroscopy of strong γ-ray lines.

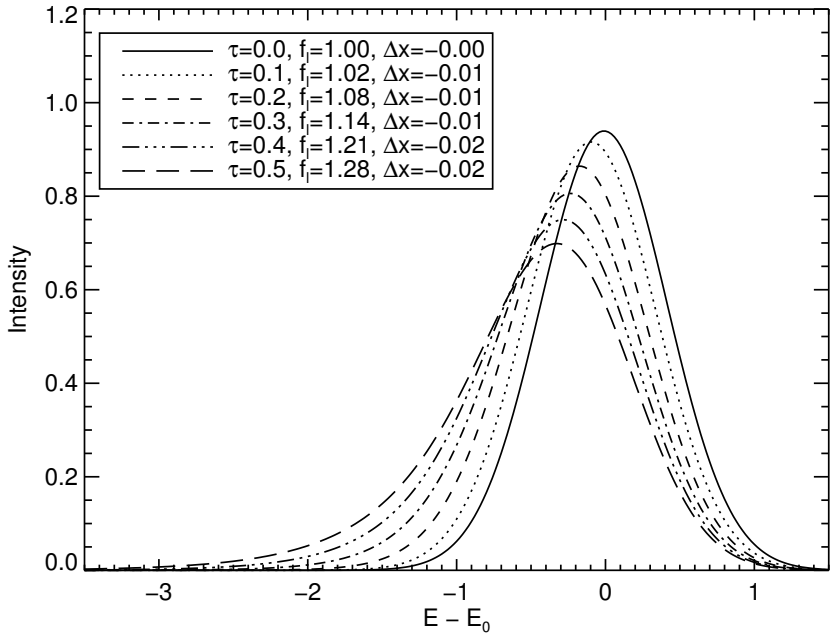

Figure 2.8: Line shape function (Gaussian plus a truncated exponential) used to model the degradation behavior of SPI's instrumental lines as changes of τ values (from Kretschmer 2007), which keeps the shape of the underlying Gaussian constant at a full width at half maximum of 1 energy unit and a peak intensity of one intensity unit. Line width (f_1) increases and the shift (Δx) moves towards lower energies with increasing degradation parameter τ.

2.4 Spectral response of SPI

The SPI instrumental response is based on extensive Monte Carlo simulations and parameterization [Sturner et al., 2003]. This has been tested on the Crab in-flight calibration observations and shown to be reliable to better than 20% in absolute flux at the current state of the analysis [Attié et al., 2003].

Since our aim is to derive the high-resolution spectroscopy of γ-ray lines, e.g., from ^{26}Al and ^{60}Fe , we need to study properties of the spectral response of SPI Ge detectors, which mainly relate to the instrumental background lines in SPI raw data spectra (Weidenspointner et al. 2003, see Figure 2.3). An ideal semiconductor detector would produce instrumental lines with Gaussian shapes. However, the GeD performance degrades with the damages created within the crystal by incident radiation (mainly protons and neutrons). In space, the cosmic particle flux is high enough to produce substantial degradation of the GeDs over a few months. This energy resolution of the GeDs thus evolves with time (see Figure 2.2) and a continuous monitoring of the

resolution is required to analyze properly the SPI data.

The instrumental line shape variations due to degradation of the GeDs are determined during the mission by fitting a specific spectral response to instrumental lines. This spectral response function consists of a Gaussian shape which characterizes each particular detector's intrinsic spectral resolution, and a one-side exponential function extending from the peak of the Gaussian towards lower energies (Kretschmer 2007, see Figure 2.8), which characterizes the pulse height losses due to detector degradation through the degradation width τ [Kretschmer, 2007]:

$$s_i = s_0 \int_0^\infty \left(\frac{1}{\sqrt{2\pi}\sigma} e^{-\frac{E_i+E-E_0}{2\sigma^2}} \cdot \frac{1}{\tau} e^{-\frac{E}{\tau}}\right) \mathrm{d}E, \tag{2.1}$$

where s_i is the amplitude per energy bin E_i, E_0 is the photopeak line energy, and σ the instrumental resolution of the Ge detectors. By fitting many calibration lines over the SPI energy range, the time-variable degradation can be determined. Figure 2.9 presents the time evolution of full width at half maximum of SPI instrumental background lines in four different energy ranges caused by the time-variable degradation effect. We will take this time-variable spectral response directly into account in the instrumental response in our model fitting and spectra determination (next section).

Degradation belongs to the long lifetime variation of spectral response (months). Gain variations with the GeD temperature in a short time scales ($<$ 1 orbit) have been also found [Lang, 2006]. In one INTEGRAL orbit, the changes (small, $\sim$ 0.2%) of E_{peak} (instrumental background lines) correlate to the detector temperature. This temperature correction has not yet been applied to energy calibration of SPI [Lang, 2006], and would improve spectral resolution.

2.5 Extracting spectra from the sky: diffuse emission and point sources

We obtain the sky information by using a model-fitting program which fits the data to a linear combination of input astronomical sky maps and point sources, together with background components. The fit is performed by the maximum-likelihood function based on Poissonion statistics with one parameter per component and energy range [Strong, 2003, Strong et al., 2003]. Hence the time-dependence of the background is explicitly determined from the data themselves on the assumption of constant detector ratios. The early implementation of such a model fitting (*spidiffit*) has been applied for diffuse continuum studies [Strong et al., 2003], and ^{26}Al line studies [Diehl et al., 2003b]from the inner Galaxy region using the early SPI data.

In the present updated program *spimodfit* (for more details of methods, see Strong et al. 2005), we similarly combine background models with spatial models for sky emission to fit our data, allowing for more powerful adjustments of fit parameters for background and sky intensities. The *spimodfit* output FITS files contain, per energy bin,

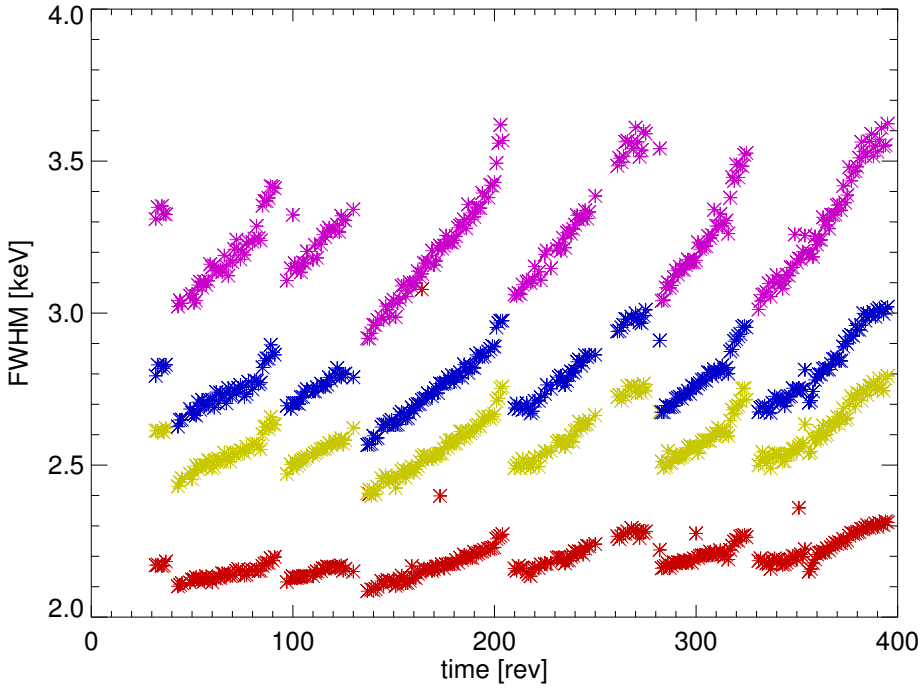

Figure 2.9: Time variations of full width at half maximum of SPI instrumental background lines in four different energy ranges due to degradation (from Kretschmer 2007, from bottom to top): 415 – 460 keV, 860 – 930 keV, 1060 – 1175 keV, 1740 – 1820 keV..

the fitted parameter values with uncertainties, the covariance matrices, and the fitted model components. The counts per energy bin, per detector, and per pointing are fitted to the background model described in §2.3 and the assumed sky maps of celestial emission plus a source catalogue as convolved into the domain of spectra per detector, energy bin, and pointing through the pointing sequence and the instrumental response:

$$D_{e,d,p} = \sum_{m,n} \sum_{j=1}^{k_1} A^{j,m,n}_{e,d,p} \beta^j_s I^{m,n}_j + \sum_{h=1}^{k_2} A^h_{e,d,p}(m,n) \beta^h_c S_h(m,n) + \sum_t \sum_{i=1}^{k_3} \beta^i_{b,t} B^i_{e,d,p} + \delta_{e,d,p}, \quad (2.2)$$

where *e,d,p* are indices for data space dimensions: energy, detector, pointing; *m,n* indices for the sky dimensions (galactic longitude, latitude); A is the instrument response matrix, I is the intensity per pixel on the sky, $S(m,n)$ is the input source catalogue (point sources). k_1 is the number of input sky maps; k_2 is the number of point sources in the catalogue; k_3 is the number of background components. Coefficients β_s for the sky map intensity (constant in time), β_c for the input point sources (time dependent where required, e.g., transient sources) and $\beta_{b,t}$ (time dependent) for different background intensities are derived (see §2.3; different normalizations allowed for each camera configuration of 19/18/17 functional detector elements due to failure of two Ge detectors). And the amplitude β_s comprises the resultant spectra of the signal from the sky (diffuse emission), β_c the spectra of the input point sources. δ is the count residue after the fitting. Generally, a good fit will lead to residuals being statistically distributed around zero (see examples in Chapters 3 & 5 after model fittings of ^{26}Al and ^{60}Fe data).

3 ^{26}Al emission and line shapes in the Galaxy

^{26}Al is the first cosmic radioactivity ever detected with gamma-ray detectors [Mahoney et al., 1982, Prantzos and Diehl, 1996]. It is unstable isotope to positron emission (82%) or to electron capture (15%), with a mean lifetime of 1.04 Myr. ^{26}Al can first decay into an excited state of ^{26}Mg, which de-excites into the Mg ground state by emitting gamma-ray photons with the characteristic energy of 1808.66 keV (see Figure 3.1).

The detailed studies of 1809 keV line emission from the Galactic ^{26}Al is the one of the main design goals of the INTEGRAL mission. As described in §1.3, the COMPTEL imaging of the ^{26}Al line from all sky suggested ^{26}Al emission extends along the Galactic plane, then ^{26}Al nucleosynthesis is a common Galactic phenomenon rather than local to the solar system [Plüschke et al., 2001]. The structure of this emission, alignments of emission maxima with spiral-arm tangent, and comparisons with tracers of candidate ^{26}Al sources, all have pointed to the conclusion that massive stars dominate ^{26}Al nucleosynthesis [Chen et al., 1995, Diehl et al., 1995a, Knödlseder et al., 1999b, Knödlseder, 1999].

SPI is a high resolution spectrometer with energy resolution of 3 keV (FWHM) at 1809 keV, which is expected to reveal more information about the ^{26}Al sources and their location through Doppler broadening and shift (^{26}Al line shapes), induced from Galactic rotation and dynamics of the ejected ^{26}Al as it propagates in the interstellar medium around the sources. So the spectral analysis would provide new and important astrophysics on ^{26}Al studies, beyond what could be learned only from the imaging of the COMPTEL all-sky survey.

In this Chapter, we will concentrate on studying the large-scale spectral characteristics of ^{26}Al emission along the Galactic Plane. The main goal is to measure the ^{26}Al line shapes in the inner Galaxy and different regions along the Galactic plane, and to globally probe the effect of Galactic rotation on the ^{26}Al line broadening and shift (a detailed study of the inner Galaxy region is also presented in Kretschmer 2007). The ^{26}Al line width would relate to the environment of the interstellar medium. Then measurements of the line width could provide the information of ISM around ^{26}Al sources: just normal interstellar turbulence (narrow line), or existence of supernova, stellar wind bubbles (broad line).

In spectral studies, the ^{26}Al spectrum from the model fitting of SPI data could depend on the input sky map (see §2.5). For a consistent check, we will compare different tracer maps of ^{26}Al source candidates, and their effects on the derived spectrum, spe-

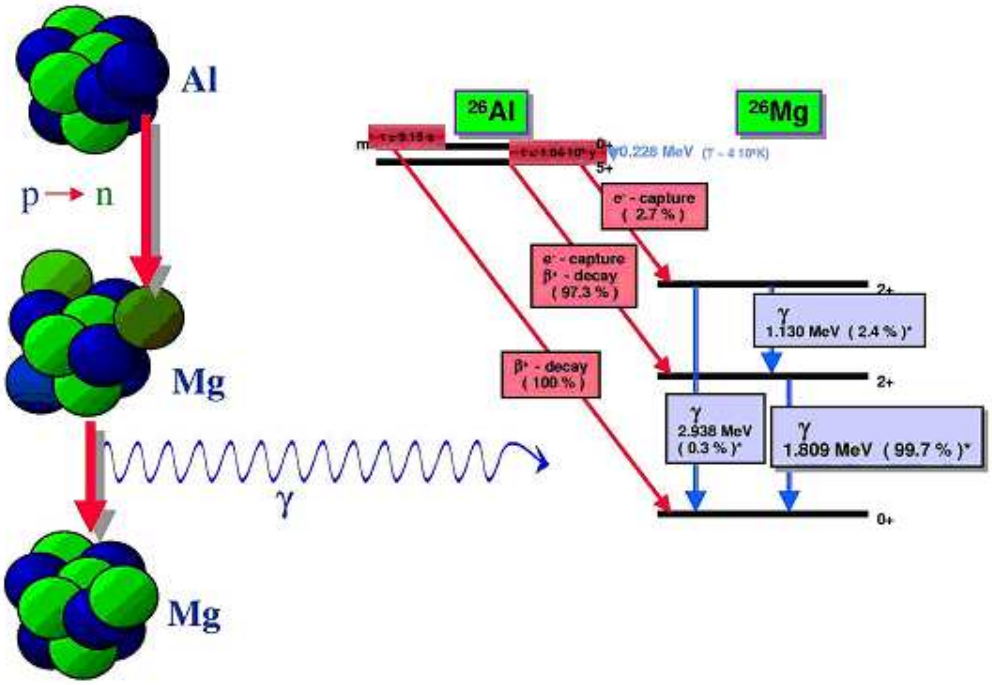

Figure 3.1: The decay chain of the radioactive isotope ^{26}Al . ^{26}Al decays with a characteristic lifetime of 1.04 Myr into an excited state of ^{26}Mg, then de-excites into the Mg ground state by emitting γ-ray lines with the energies of 1809 keV (99.7%) and 2.936 keV (0.3%).

cially on the ^{26}Al flux.

3.1 Data preparation and analysis

In ^{26}Al line studies (Chapters 3 & 4), we establish a SE database using the 4-year SPI observations, from the INTEGRAL orbit 43 – 525, which covers the whole sky with 23701 pointings, equivalent to a total deadtime-corrected exposure time of 47 Ms (see the exposure map in Figure 2.4). The selected data include a database in the spectral range of 1785 – 1826 keV with 0.5 keV bin size for the line analysis, and a database for the background modelling from the adjacent continuum. A raw data spectrum around the ^{26}Al line (1750 – 1830 keV) is presented in Figure 3.2 . Three instrumental line features dominate the raw spectrum: 1764 keV (^{205}Bi), 1779 keV (^{28}Al), and 1809.4 keV, a complex feature including ^{22}Na (1808.7 keV) with ^{56}Mn (1810.9 keV).

For the background modelling from the adjacent continuum, we make use of 1785 – 1802 keV plus 1815 - 1826 keV, which have been combined into one energy bin. As presented in §2.3, the detector-by-detector count rates in the the continuum band are fitted by the GEDSAT time series to construct an 'adjacent-energies' background template for the ^{26}Al line. And the GEDSAT rates can be used to trace the prompt CR activation to the instrumental lines. Then the set of detector-by-detector spectra per pointing in 0.5 bins covering the $\sim$ 10 keV intervals around and including the ^{26}Al line (1785 – 1826 keV) are fitted to the sum of adjacent continuum template, plus a GEDSAT template. Thus, we generate a background model for our actual set of spectra for the science analysis.

Then the model fittings are made for the SE database of ^{26}Al line. Since in the sky region we studied, i.e., $-120^\circ < l < 120^\circ$, $-30^\circ < b < 30^\circ$, SPI cannot detect and resolve any point sources in our narrow energy bands for γ-ray studies (including ^{26}Al and ^{60}Fe lines), we do not need to input the point-source catalogue for the model fittings. So only two components are used to fit the data: diffuse emission with input sky maps plus the background model, then Equation 2.2 can be simplified as follows:

$$D_{e,d,p} = \sum_{m,n} \sum_{j=1}^{k_1} A_{e,d,p}^{j,m,n} \beta_s^j I_j^{m,n} + \sum_t \sum_{i=1}^{k_2} \beta_{b,t}^i B_{e,d,p}^i + \delta_{e,d,p}, \tag{3.1}$$

where k_1 is the number of input sky maps; k_2 is the number of background components.

We use the sky intensity distribution of ^{26}Al from 9-year COMPTEL observations (maximum entropy map as a standard sky model, Plüschke et al. 2001) as the standard sky model in the model fittings. And different ^{26}Al emission tracer models or maps are also applied in fittings. We will compare the effect of these different sky models on the ^{26}Al line shape and intensity in §3.4. The residuals after the model fitting are shown in Figure 3.3 (residuals with the time) and Figure 3.4 (with the energies). The reduced χ^2 values around 1.0 confirm that the present background model is adequate.

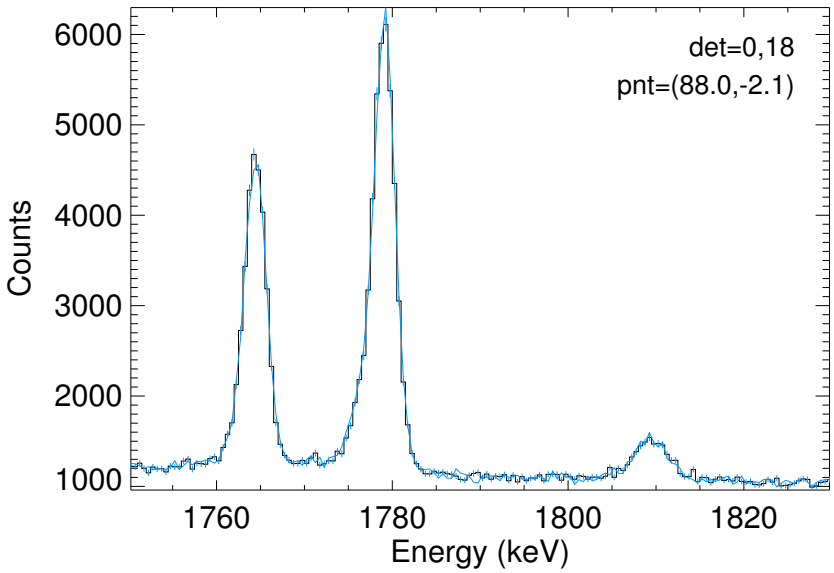

Figure 3.2: Raw data spectra around the energies of the ^{26}Al line in one-INTEGRAL-orbit observations (3 days), representing the instrumental lines and continuum background. Line origins are radioactivities excited by cosmic bombardment, e.g., ^{205}Bi (1764 keV), ^{28}Al (1779 keV), and ^{22}Na (1808.7 keV) with ^{56}Mn (1810.9 keV) for the composite feature (1809.4 keV) underlying the ^{26}Al line [Weidenspointner et al., 2003]. Fitting these instrumental lines, we typically find instrumental widths of three lines (keV): 1764/3.1, 1779/3.2, 1809/4.2, respectively. The intensity of instrumental feature at 1809 keV is typically $\sim$ 12% of the instrumental line at 1779 keV.

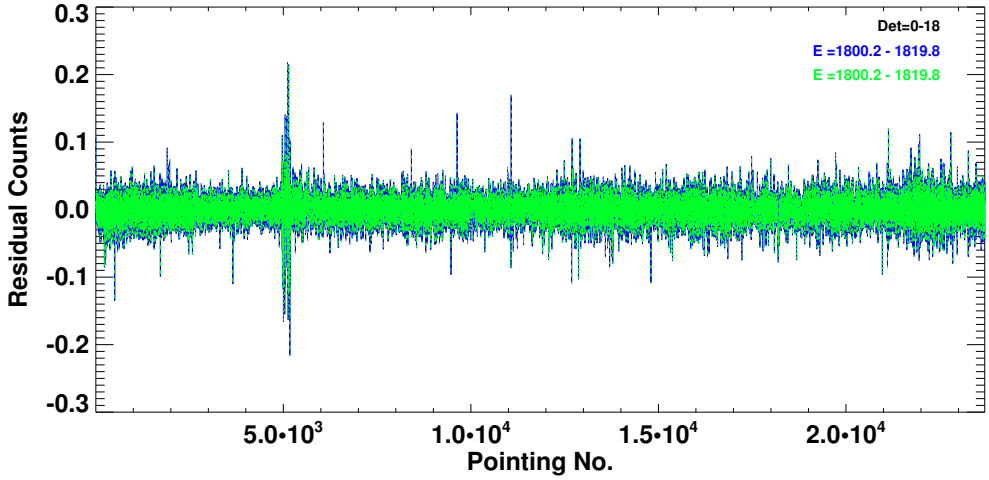

Figure 3.3: Residuals versus time (pointings, per 30 min) after model fitting for the SE database (in units of counts s^{-1}). Residuals around zero confirm that our background models are adequate, with $\chi^2/d.o.f. = 0.958$ (450315 *d.o.f.*) in model fittings.

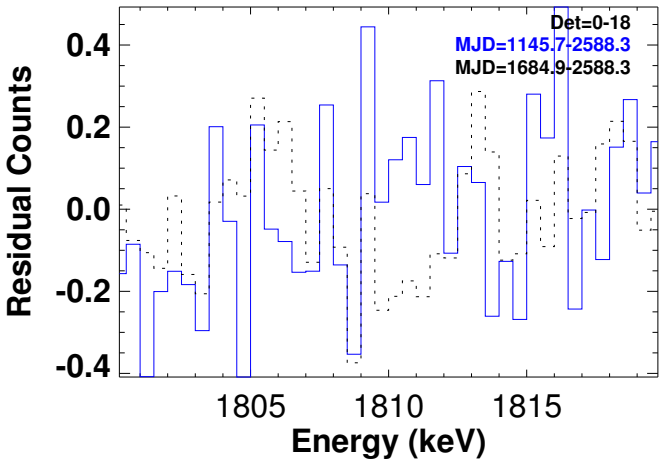

Figure 3.4: Residuals of counts versus energies after model fitting for the SE database (in units of counts s^{-1} keV^{-1}). Reduced χ^2 changes with energies: from 0.82 around off-line energies at 1800 and 1820 keV, to 0.95 – 1.05 in the line energy band. The solid line represents residuals for the whole data (e.g., Julian Date 1146 – 2588), and the dashed line for the late-time data (Julian Date 1685 – 2588).

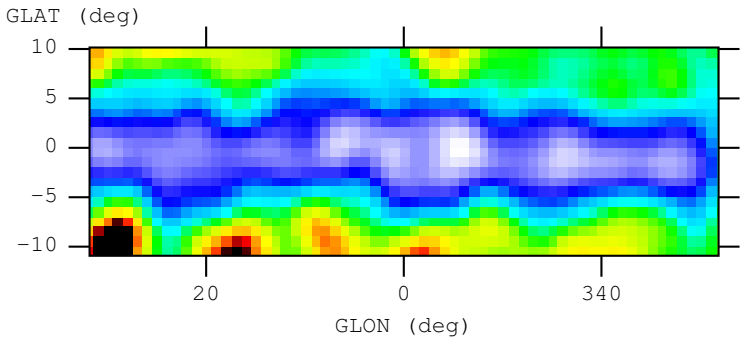

Figure 3.5: The COMPTEL maximum entropy ^{26}Al map [Plüschke et al., 2001] (hereafter COMPTEL MaxEnt) for the inner Galaxy as the input sky model in the model fitting.

3.2 ^{26}Al emission and line shapes in the inner Galaxy

The large-scale spectral feature of ^{26}Al emission in the inner Galaxy (e.g., $-30^\circ < l < 30^\circ$, $-10^\circ < b < 10^\circ$) is important to study the recent star-formation activity in the Galaxy and the properties of the interstellar medium near the ^{26}Al sources. By fitting our set of observations at 0.5 keV wide energy binning with the sky intensity distribution of ^{26}Al (maximum entropy image by COMPTEL, see Figure 3.5) together with the background model, we obtain the spectrum for ^{26}Al emission from the inner Galaxy shown in Figure 3.6. The ^{26}Al line is detected at $\sim 30\sigma$ significance. The line component above the linear component of our spectral fit determines the intensity of observed ^{26}Al . The upper one in Figure 3.6 show the Gaussian fit of the spectrum, the obtained width 3.09 ± 0.15 is consistent with the instrumental width $\sim$ 3.1 keV near 1.8 MeV. This fit implies the ^{26}Al line in the inner Galaxy would be intrinsically narrow. We also fit the adjacent continuum with the flat index, and this continuum is near zero, which is expected from the adjacent background modelling. And the diffuse gamma-ray background continuum in the inner Galaxy is $\sim 2 \times 10^{-6}$ ph cm^{-2} s^{-1}rad^{-1} keV^{-1} in the energy band of 1 – 2 MeV [Strong et al., 1999], which is also consistent with the continuum fitting.

The derived ^{26}Al intensity has been normalized to the region of $-30^\circ < l < 30^\circ$, $-10^\circ < b < 10^\circ$ (i.e. the flux in the inner radian). Then the total ^{26}Al gamma-ray flux of the Gaussian fit as determined for the inner Galaxy region is $(2.96 \pm 0.19) \times 10^{-4}$ ph cm^{-2} s^{-1} rad^{-1}. This is consistent with the COMPTEL imaging-analysis value of $(2.8 \pm 0.4) \times 10^{-4}$ ph cm^{-2} s^{-1} rad^{-1} [Oberlack, 1997, Plüschke, 2001] and the value from the previous analysis of the SPI data, $(3.3 \pm 0.4) \times 10^{-4}$ ph cm^{-2} s^{-1} rad^{-1} [Diehl et al., 2006c].

Due to the high significance ($\sim 30\sigma$) of the detection of ^{26}Al line in the whole inner Galaxy, we also try to derive the astrophysical width by fitting the instrumental-line-

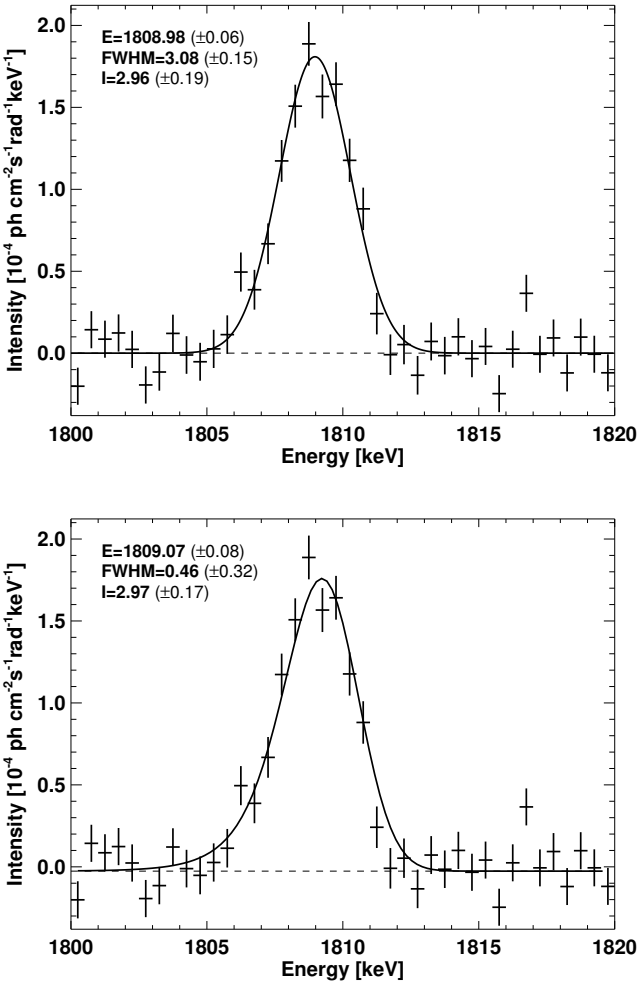

Figure 3.6: Spectrum derived from sky model fitting using the COMPTEL ^{26}Al Maximum Entropy image. The upper figure shows the ^{26}Al spectrum with a Gaussian fit, obtaining a Gaussian width of $\sim$ 3.08 keV which is consistent with the instrumental line width around 1.8 MeV. The lower figure shows the spectrum with a fit using the shape of the instrumental resolution as it results from cosmic-ray degradation and annealings during the time of our measurement (see Figure 2.9), convolved with a Gaussian, to obtain the intrinsic ^{26}Al line width ($\sim$ 0.46 keV). Both two fits demonstrate that the line is intrinsically narrow. Derived fluxes are consistent with each other. Fluxes are quoted in units of 10^{-4} ph cm^{-2} s^{-1}rad^{-1}. The ^{26}Al line centroid energy is determined at 1808.98 ± 0.06 keV from the Gaussian fit and 1809.07 ± 0.08 keV from the instrumental-response-convolved fit, which is a little higher than the laboratory value for the ^{26}Al line of 1808.65 ± 0.07 keV [Firestone and Ekström, 2004].

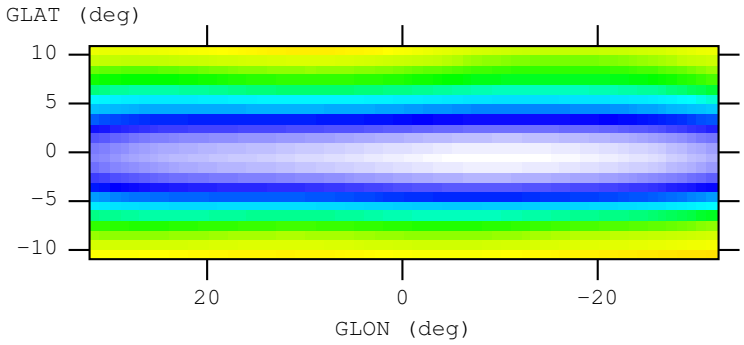

Figure 3.7: The COMPTEL MREM ^{26}Al map [Plüschke et al., 2001] for the inner Galaxy as the input sky model in the model fitting.

shape response function with time due to degradation (e.g., Figure 2.9) convolved with the ^{26}Al spectrum. In fitting non-analytical spectral shapes to our spectra, such as our time-integrated instrumental-response line shape convolved with intrinsically-broadened ^{26}Al emission, gradient-driven fit algorithms are inadequate, in particular when we aim to determine a parameter like the intrinsic ^{26}Al width, which is convolved with the instrumental line profile before being compared to our flux values per energy bin. The probability distribution in this case is very asymmetric, but we wish to perform quantitative statistical analysis of our findings. This is not possible with tools that inherently assume symmetric and smooth probability distributions for parameter fluctuations. We make use of the Monte Carlo Markov Chain (MCMC) method, pre-processed by simulated annealing (also see discussions in Kretschmer 2007, Diehl et al. 2006c).

We fit the effective accumulated instrumental line shape, convolved with a Gaussian for the celestial ^{26}Al line broadening, to our spectrum. The fitted parameters are the line centroid, the intrinsic width of celestial ^{26}Al , the intensity of the line, and two parameters for the underlying continuum. The intrinsic line width also appears to be rather small, 0.46 ± 0.32 keV (the below one in Figure 3.6). The derived width value is consistent with the early results by SPI [Diehl et al., 2004, 2006c]. And the line centroid energy and ^{26}Al line flux are still consistent with the results from the Gaussian fit.

The ^{26}Al line centroid energy from the inner Galaxy ($|l| < 30^\circ$, $|b| < 10^\circ$) is determined at 1808.98 ± 0.06 keV from the Gaussian fit and 1809.07 ± 0.08 keV from the instrumental-response-convolved fit. Even after considering the system error of 0.1 keV, the measured centroid energy is a little higher than the laboratory value for the ^{26}Al line of 1808.65 ± 0.07 keV [Firestone and Ekström, 2004]. The effect of this blueshift will discussed in more details in following sections.

According to Eq. 3.1, our model fitting depends on the input sky model. For a test, we also derive the spectrum after the fit using the COMPTEL MREM ^{26}Al map

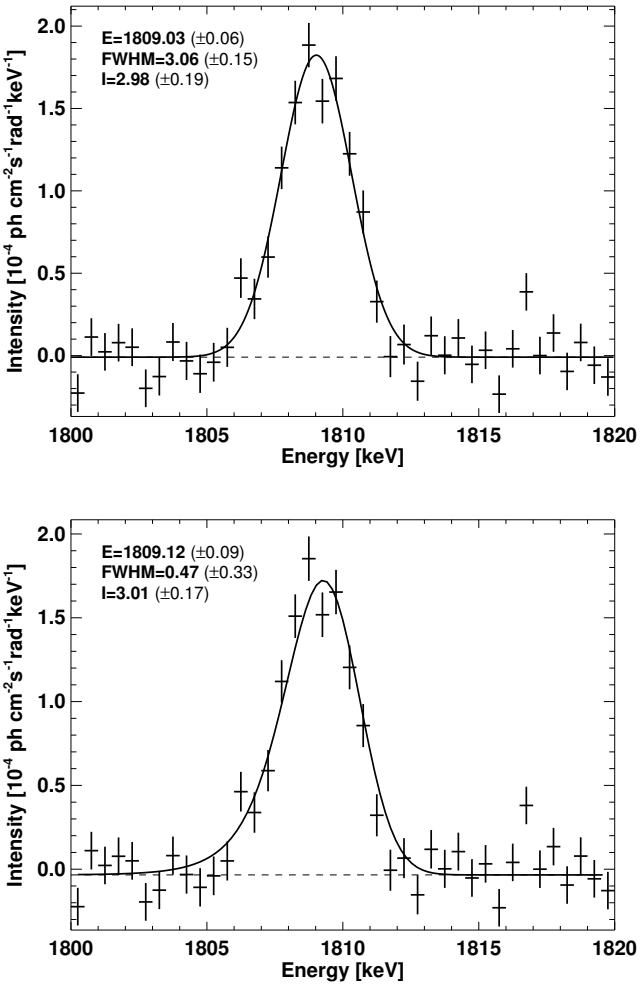

Figure 3.8: Spectrum derived from sky model fitting using the COMPTEL ^{26}Al MREM image. Similar to Figure 3.6, the upper figure shows the ^{26}Al spectrum with a Gaussian fit, and the below one shows the spectrum with a fit to derive the intrinsic width. The results of two fits are consistent with each other, narrow ^{26}Al lines, energy centroids, a same level of ^{26}Al line fluxes, and also consistent with the results in Figure 3.6.

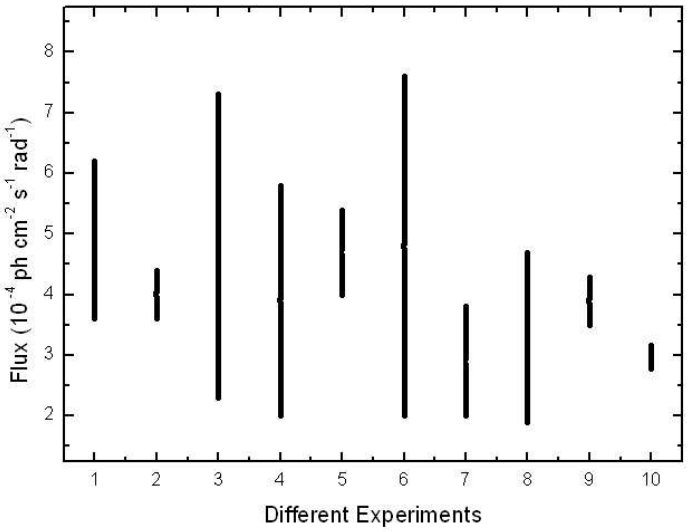

Figure 3.9: Reported ^{26}Al line flux values from the inner Galaxy for ten different experiments: (1) HEAO-C [Mahoney et al., 1984]; (2) SMM [Share et al., 1985]; (3) MPE balloon [von Ballmoos et al., 1987]; (4) Bell-Sandia [MacCallum et al., 1987]; (5) GRIS [Teegarden et al., 1991]; (6) HEXAGONE [Durouchoux et al., 1993]; (7) COMPTEL [Plüschke, 2001]; (8) OSSE [Harris et al., 1997]; (9) RHESSI [Smith, 2004b]; (10) SPI (this work).

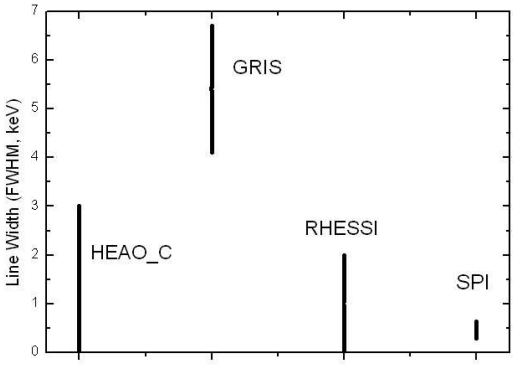

Figure 3.10: Reports on the constraints of the ^{26}Al line width from different experiments (1 σ error bars): HEAO-C [Mahoney et al., 1984], GRIS [Naya et al., 1996], RHESSI [Smith, 2003] and SPI.

(Figure 3.7). The ^{26}Al spectrum is shown in Figure 3.8. Since these two maps are quite similar with each other, the consistent results are expected. Further comparison among the different tracer maps of ^{26}Al sources for the inner Galaxy will be presented and discussed in §3.3.

Since the first detection of ^{26}Al emission from the inner Galaxy by HEAO-C [Mahoney et al., 1982], up to now, there are ten different experiments which have reported the ^{26}Al flux values from the inner Galaxy. We collected these values which are plotted in Figure 3.9. The SPI result has obtained the most significant report, which is consistent with the results by COMPTEL [Oberlack, 1997, Plüschke, 2001]and OSSE [Harris et al., 1997], and a little lower than the recent result by RHESSI [Smith, 2004b]. The ^{26}Al flux in the inner Galaxy is $\sim 3 \times 10^{-4}$ ph cm^{-2} s^{-1} rad^{-1}.

Several experiments have also reported the width values of the ^{26}Al line (see Figure 3.10). The results obtained by HEAO-C [Mahoney et al., 1984], RHESSI [Smith, 2003] and SPI suggested the intrinsic narrow line feature for the inner Galaxy. GRIS [Naya et al., 1996] reported a very broad line with a width $\sim$ 5.4 keV, which is inconsistent with the other measurements, and is clearly ruled out by our present result.

3.3 Astrophysical origins of ^{26}Al line width

A line broadening of $\sim$ 0.5 keV from our line-shape constraints corresponds to thermal Doppler velocities of $\sim$ 60 km s^{-1}. Astrophysical origins of ^{26}Al line width may come from two effects: random motions in the interstellar medium [Chen et al., 1997] and Galactic differential rotation [Kretschmer et al., 2003].

The typical turbulent velocities in ISM are around tens of km s^{-1}. If ejected ^{26}Al is mixed with the normal ISM in the time scale of Myr into an equilibrium ISM state, the ^{26}Al line is expected to be intrinsically narrow. In wind bubbles nearby massive stars and supernova remnants, ISM velocities would reach a high value range. A line broadening effect could be observed if a large fraction of ISM resides in connected bubbles or other unusual circumstances [Chen et al., 1997].

How much line broadening from ISM is plausible? Significant broadening is expected from the apparent existence of major interstellar cavities in the regions of massive-star clusters [Oey, 1996], and from the ejection kinematics of these presumed ^{26}Al sources, i.e. winds and supernovae. WR wind velocities are 1200 km s-1 [Vink and de Koter, 2005] or higher (Plüschke 2001), and models for ejection of ^{26}Al by core-collapse supernovae predict velocities in a similar range [Herant and Woosley, 1994]. Here sources may not yet have obtained a long-term equilibrium with their surrounding ISM, and ^{26}Al may thus be preferentially decaying from its initial and fast phase, rather than already being slowed down to normal ISM velocities in the 10 km s^{-1} range. Chen et al. (1997) also suggested that a high fraction of ^{26}Al bring deposited into high-speed grains near the ^{26}Al sources could produce significantly broad line features. The broadening could also be a result of re-acceleration of dust grains by interstellar shocks in the neighbourhood of the ^{26}Al source, allowing them to maintain a high velocity over the ^{26}Al decay time scale [Sturner and Naya, 1999]. Therefore, it will be interesting to test with SPI on INTEGRAL whether we can observe such effects for localized regions of ^{26}Al emission.

If our constraints on large-scale integrated broadening of the ^{26}Al line from the inner Galaxy can be interpreted in terms of interstellar-medium characteristics, the intrinsic width from ISM turbulence would be $\sim$ 0.5 keV, even considering a 2σ upper limit of 1.2 keV. This corresponds to 150 km s^{-1} for a 2σ limit on ISM velocities, well within the acceptable range. Therefore we conclude that, within uncertainties, the average velocities of decaying ^{26}Al in the Galaxy are probably not in excess of typical values for the ISM near massive stars.

In the inner Galaxy, Galactic differential rotation alone can lead to Doppler shifts and line broadening. Kretschmer et al. (2003) have simulated the ^{26}Al line shape diagnostics in the inner Galaxy due to the Galactic rotation effect. They adopted a three-dimensional model for the space density of free electrons as our parent distribution for ^{26}Al sources in the Galaxy derived by Taylor & Cordes (1993) from pulsar dispersion measure observations. The Doppler shifts due to Galactic rotation can then be determined from the Galactic rotation curve. In simulations, they used the results obtained by Olling and Merrifield [2000] from fitting radial velocity measurements with a five-component mass model of the Galaxy, consisting of a stellar bulge, a stellar disc, two gas disks (HI, H_2) and a dark-matter halo. Superimposed on Galactic rotation is the motion of freshly synthesized radioactive material due to the parental supernova explosion or the ejecting Wolf-Rayet star wind and its slowed-down motion in the ISM before decay, $\sim 10^6$ yr. Finally their results pronounced the line centroid

shifts of $\sim$ 0.25 keV towards longitudes $\pm 30^{\circ}$ [Kretschmer et al., 2003]; a possible line broadening of up to 1 keV had been estimated if integrated over this inner region of the Galaxy. A real measurement would yield a line width that is lower than the width obtained for the entire inner Galaxy (Kretschmer et al. 2003). Our present line-shape constraints are also consistent with Galactic-rotation effects.

So we believe that the measured line width of ^{26}Al from the inner Galaxy is consistent with Galactic rotation and modest interstellar-medium turbulence around the sources of ^{26}Al . We thus confirm earlier results obtained by HEAO-C(Smith 2003), RHESSI (Mahoney et al. 1982), and SPI on INTEGRAL (Diehl et al. 2006c). This is reassuring that neither the suppression of deceleration of ^{26}Al before decay in large, kpc-sized cavities around its sources nor other exotic explanations [Chen et al., 1997] are required to account for a large broadening of the ^{26}Al line.

3.4 Comparison of the different tracer maps of ^{26}Al sources in the Galaxy

The all-sky imaging in the 1.8 MeV gamma-ray line from ^{26}Al obtained by the 9-year COMPTEL observations [Plüschke et al., 2001] shows that ^{26}Al emission extends all along the plane of the Galaxy. The irregular structure of the emission, alignments of emission maximum with spiral-arm tangent points to the conclusion that massive stars dominate ^{26}Al nucleosynthesis. Comparisons of tracers of candidate ^{26}Al sources have also been a good probe of the origin of ^{26}Al production [Chen et al., 1995, Knödlseder et al., 1999b]. Knödlseder [1999] revealed a close correlation between 53 GHz microwave free-free emission and ^{26}Al γ-ray line emission. While microwave free-free emission arises from ionized interstellar medium, they argued that massive stars ($> 20\ M_{\odot}$) are at the origin of Galactic ^{26}Al .

In this section, we will compare the different tracers of ^{26}Al sources in the Galaxy. All the tracer maps except the maximum entropy and MREM ^{26}Al maps by COMPTEL are presented in Figure 3.11. Brief descriptions on these tracer maps are shown here as followed:

An exponential disk model: scale radius 4 kpc, scale height 180 pc (hereafter Exp Disk);

An artificially created homogenous disk model : constant brightness along longitudes, exponential-like in latitudes with scale height 200 pc (hereafter Homo Disk);

The HI survey map (21cm, Dickey and Lockman 1990) from the Leiden/Dwingeloo Survey;

The CO survey map (Dame et al. 1987, Strong et al. 1988), from a composite of the 5-year data of the Columbia 1.2 m telescopes in New York City and on Cerro Tololo in Chile, probing the distribution of molecular clouds in the Galaxy;

The IRAS 12μm survey map (Wheelock et al. 1991);

The radio 408 MHz survey map (Haslam et al. 1995) from the Parkes survey;

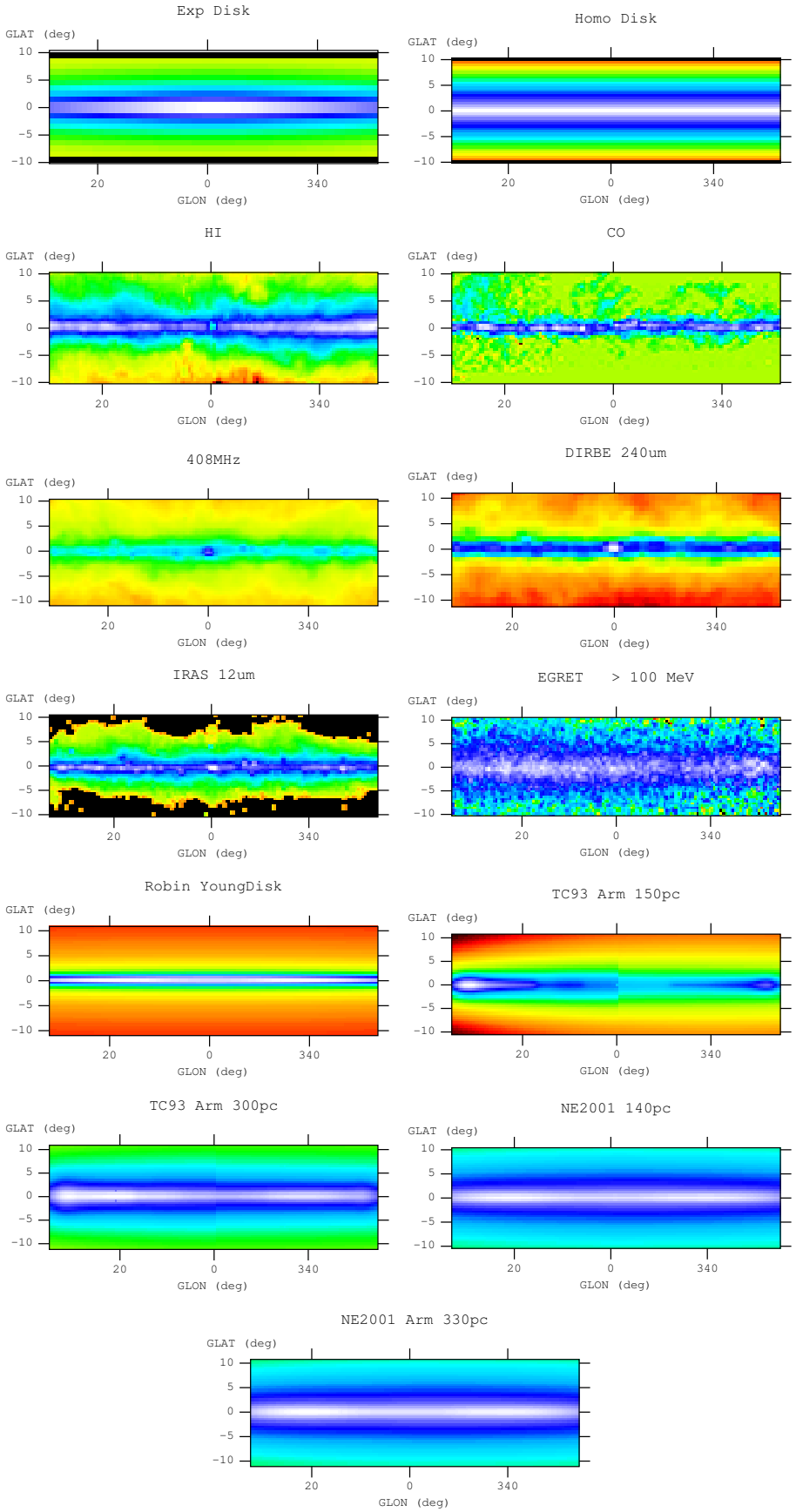

Figure 3.11: The different tracer maps of ^{26}Al sources in the inner Galaxy used in our model fittings.

The DIRBE/COBE 240μm survey map from the 4-year observations [Bennett et al., 1996];

The EGRET ($>$ 100 MeV) survey map (from Hunter et al. 1997);

A young disk model (from Robin et al. 2003, scale height 125 pc);

The free electron spiral arm model from pulsar dispersion measurements (from Taylor and Cordes 1993, scale height 150 pc, hereafter TC93 150pc);

The free electron spiral arm model (from Taylor and Cordes 1993, scale height 300 pc, hereafter TC93 300pc);

The recent free electron model from pulsar dispersion measurements (from Cordes and Lazio 2002, no thick disk, scale height 140 pc, hereafter NE2001 140pc);

The recent free electron spiral arm model from pulsar dispersion measurements (from Cordes and Lazio 2002, scale height 330 pc, hereafter NE2001 330pc);

In our model fittings, the output results should depend on the input sky models. Since ^{26}Al is dominated by massive star origin, all selected tracer models may reflect the distribution of the present star formation and massive star in the Galaxy. If some scientifically implausible sky distribution models (e.g., a point source at $l = 20^\circ$, a bulge model or a COMPTEL ^{26}Al map zeroed in the Galactic Plane, $|b| < 10^\circ$) are taken in model fittings, then no significant ^{26}Al signal could be detected. We carried out the separate model fittings using a sky model of each tracer map presented in Figure 3.11, and obtained the ^{26}Al spectra with these different tracer maps. These spectra have been displayed in Figures 3.12 and 3.13. For a complete comparison among these tracer maps for ^{26}Al sources, we have presented the ^{26}Al line centroids, fluxes and width values obtained from the different tracers including the COMPTEL MaxEnt and MREM maps in Table 3.1.

All the fitted parameters of the ^{26}Al line: line centroid, flux and width, using different tracer maps, are consistent with each other within error bars. The line centroid is at $\sim$ 1809 keV, with a little blueshift relative to the laboratory value. The line width values are $\sim$ 0.5 keV for all fittings. ^{26}Al line in the inner Galaxy is intrinsically narrow, with the origin of Galactic rotation and normal interstellar medium velocities. The ^{26}Al line flux in the inner Galaxy varies a little with the different sky models: a little lower flux obtained using the exponential disk model; for the free-electron distribution models including both TC93 and NE2001, higher fluxes obtained using the models with larger scale height values. The derived ^{26}Al flux in the inner Galaxy is $(3.0 \pm 0.2) \times 10^{-4}$ ph cm^{-2} s^{-1}rad^{-1}. This demonstrates that the derived ^{26}Al spectrum does not depend on details of the input sky as long as the main characteristics of the ^{26}Al sky are represented by these tracers.

3.5 ^{26}Al mass

Flux values in the ^{26}Al line as determined for geometrical source distribution models allow for a direct conversion in the Galaxy, because the 3D space distribution is known

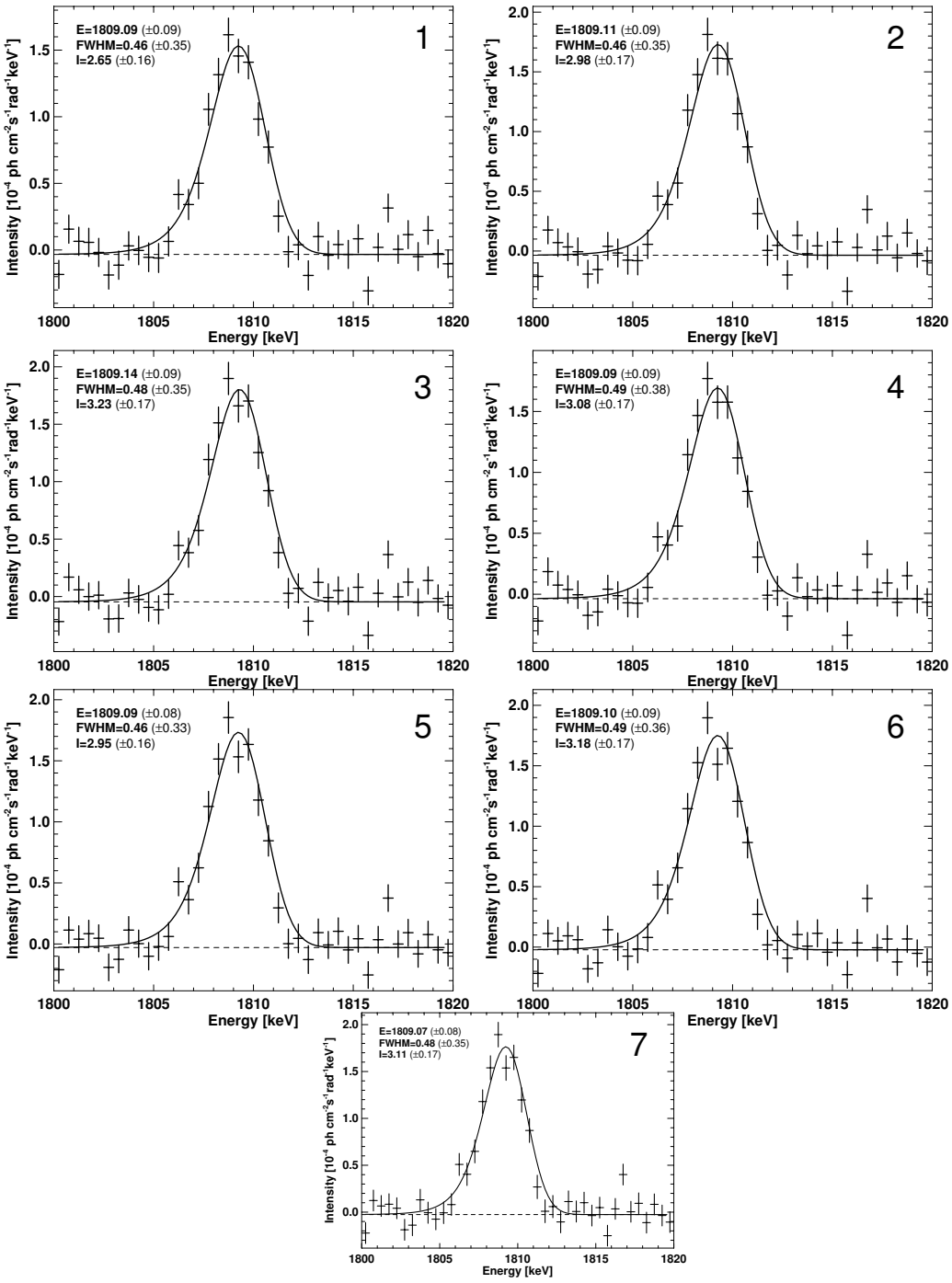

Figure 3.12: ^{26}Al spectra derived from sky model fittings using different tracer maps: 1. Exp Disk; 2. Homo Disk; 3. HI; 4. CO; 5. 408 MHz; 6. DIRBE 240μm; 7. IRAS 12μm.

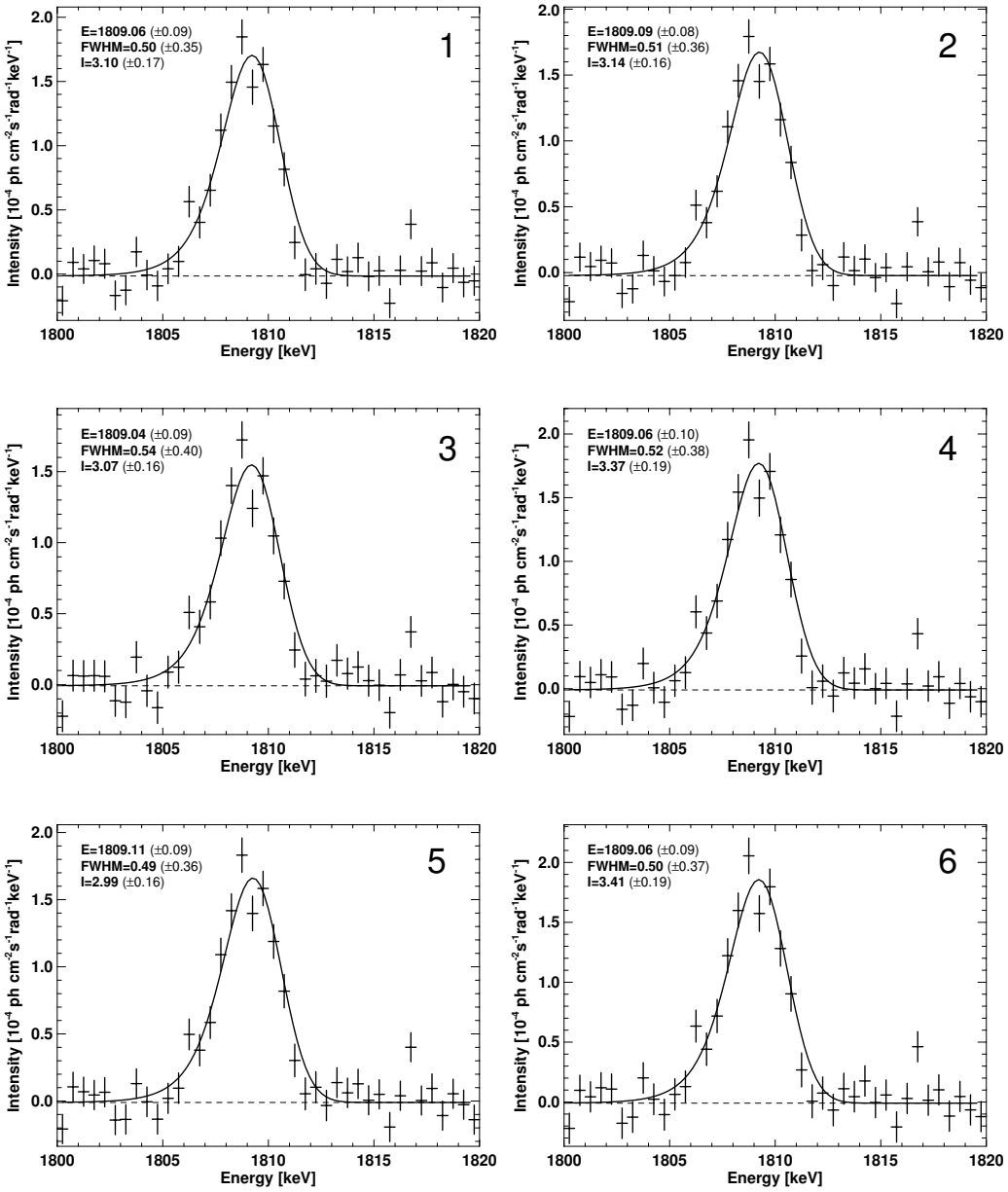

Figure 3.13: ^{26}Al spectra derived from sky model fittings using different tracer maps (continued): 1. EGRET (> 100 MeV); 2. Robin young disk; 3. TC93 150 pc; 4. TC93 300 pc; 5. NE2001 140 pc; 6. NE2001 330 pc.

Table 3.1: ^{26}Al line results for different sky distribution models

Sky model	Line centroid (keV)	^{26}Al flux (10^{-4} ph cm^{-2} s^{-1}rad^{-1})	Width (keV)
COMPTEL MaxEnt	1809.07 ± 0.08	2.97 ± 0.17	0.46 ± 0.32
COMPTEL MREM	1809.12 ± 0.09	3.01 ± 0.17	0.47 ± 0.33
Exp Disk	1809.09 ± 0.09	2.65 ± 0.16	0.46 ± 0.35
Homo Disk	1809.11 ± 0.09	2.98 ± 0.17	0.46 ± 0.35
HI	1809.14 ± 0.09	3.23 ± 0.17	0.48 ± 0.35
CO	1809.09 ± 0.09	3.08 ± 0.17	0.49 ± 0.38
408MHz	1809.09 ± 0.08	2.95 ± 0.16	0.46 ± 0.33
DIRBE 240μm	1809.10 ± 0.09	3.18 ± 0.17	0.49 ± 0.36
IRAS 12μm	1809.07 ± 0.08	3.11 ± 0.17	0.48 ± 0.35
EGRET ($>$ 100MeV)	1809.06 ± 0.09	3.10 ± 0.17	0.50 ± 0.35
Robin young disk	1809.09 ± 0.08	3.14 ± 0.16	0.51 ± 0.36
TC93 150pc	1809.04 ± 0.09	3.07 ± 0.16	0.54 ± 0.40
TC93 300pc	1809.06 ± 0.10	3.37 ± 0.19	0.52 ± 0.38
NE2001 140pc	1809.11 ± 0.09	2.99 ± 0.16	0.49 ± 0.36
NE2001 330pc	1809.06 ± 0.09	3.41 ± 0.19	0.50 ± 0.37

and can be integrated in terms of ^{26}Al mass. Normalization is obtained by standardizing the model projected sky brightness (for the inner Galaxy: $-30^\circ < l < 30^\circ$, $-10^\circ < b < 10^\circ$), and the brightness fit of respective model to our data (e.g. Table 3.1).

From comparisons of a large family of models across all wavelength regions (from radio to gamma-rays) and plausible parameter ranges in §3.3, models for the gas disk of the Galaxy [Robin et al., 2003], of warm dust emission based on the IRAS measurements [Wheelock et al., 1991] and the DIRBE/COBE observations [Bennett et al., 1996], and free electron distribution inferred from pulsar dispersion measurements [Taylor and Cordes, 1993, Cordes and Lazio, 2002] , have been identified as the most plausible ones (see Knödlseder et al. 1999b).

For conversion to ^{26}Al mass, we normalize the total integrated ^{26}Al luminosity of the geometrical models to the line-of-sight integrated flux fitted to our data. Due to very different distribution of ^{26}Al in these models, the dispersion of derived ^{26}Al amounts for the entire Galaxy is larger than the inner-Galaxy flux variations. We used the sky models (e.g., the exponential disk model, the Robin young disk model, the IR dust geometrical representation, and the free electron based models), and the average ^{26}Al mass is $(2.7 \pm 0.6)\ M_\odot$ including the ^{26}Al flux and source distribution uncertainties.

We also use the mass of interstellar gas in the Galaxy ($4.95 \times 10^9\ M_\odot$, Robin et al. 2003) and recently-updated standard abundances (log N_{Al}=6.40 by number, normalized to log N_H=12, Asplund et al. 2005) to determine the interstellar mass of Al, and

thus obtain an isotopic ratio ^{26}Al /^{27}Al of $\sim 8.1 \times 10^{-6}$. This ^{26}Al /^{27}Al ratio is about one order of magnitude lower than the value in the solar nebula $\sim 5 \times 10^{-5}$. It seems plausible from continued production of Al since the birth of the solar systems 4.6 Gyr ago, and from several other hints for special enrichment of the solar nebula at birth from a nearby nucleosynthesis source [Wasserburg et al., 1998, Goswami et al., 2001], or from locally-produced ^{26}Al enrichments made possibly by the jet outflows in the early stage of solar-nebula accretion onto the central Sun [Gounelle et al., 2006].

Radioactive ^{26}Al is produced and dispersed throughout the Galaxy at various sites of nucleosynthesis, and decays with a mean life of $\tau \sim 10^6$ yrs. This process is dominated by ejected matter from core collapse supernovae and their preceding winds during the Wolf-Rayet stage (see §1.6). Then ^{26}Al flux and derived ^{26}Al mass can be used to estimate the star formation rate (SFR) in the Galaxy. The relatively long mean life in comparison to the time between supernovae ($\sim$ 30 – 50 yrs) implies that a very large number of events contributes to a steady state abundance, which in turn results in a diffuse glow of the Galaxy in the 1.8 MeV gamma-ray line from the decay of ^{26}Al .

We can converse observed total gamma-ray line flux for ^{26}Al to the corresponding supernova rate (SNRate), and consequently to the average star formation rate. The main advantage of this method is the lack of extinction corrections in the gamma-ray band, so that we can see the full disk of the Galaxy and are not limited to a small sampling volume around the Sun, e.g., methods based on star counts. It is also worthy to note that averaging over a few million years implies a large number of events, which provides a better statistical ensemble in comparison to other methods in which the tracers have a much shorter observational lifetime and often very significant selection effects and highly uncertain evolution corrections (pulsars, radio supernova remnants, historic SN record, HII regions, see Diehl et al. 2006a).

The ^{26}Al method relates the observed line flux to the steady state equilibrium mass of ^{26}Al in the Galaxy via a spatial distribution model. Since the observed map at 1.8 MeV indicates that massive stars are the dominant contributors to this radioactive species in the ISM, we go beyond a simple axis-symmetric model, and include spiral structure of our Sbc-type Milky Way. The dynamic evolution of the injected ^{26}Al should also be accounted for, as stellar winds and explosive outflows cause the density distribution to be more extended than what one would infer from the known spatial distribution of massive stars. The resulting density map is somewhat uncertain; but perhaps the largest source of potential error is the overall scale of the Galaxy: The official IAU distance of the Sun to the Galactic center is 8.5 kpc, but a recent review of measurements does indicate values as small as 7 kpc [Reid, 1993]. Flux scales as the inverse square of distance, therefore such a global reduction in size of the Galaxy would decrease the inferred mass of ^{26}Al by $\sim$ 34%.

The amount of ^{26}Al is maintained in steady state by a core-collapse supernova rate via $M_{\rm eq} = SNRate \cdot \tau \cdot Y$, where the rate is measured in events per year, τ is the mean life of ^{26}Al , and Y is the IMF-averaged ^{26}Al yield in units of $M_\odot$ per supernova. The yield in this context must include the explosive yields from the supernova model as

well as any ^{26}Al ejected in the Wolf-Rayet wind phase. Yields are moderated by the steep initial mass function (IMF), $\xi \propto m^{-\alpha}$, in our relevant mass range 10–120 $M_\odot$. We use the Miller-Scalo IMF ($\xi \propto m^{-2.7}$) for this higher-mass range [Miller and Scalo, 1979], supported by a wide range of astronomical constraints. Y is obtained from the high-mass initial mass function (IMF) and the nucleosynthesis yields of models (see §1.6). The resulting ^{26}Al yield per massive star is $(1.4 \pm 0.7) \times 10^{-4}$ $M_\odot$ based on various published yields as a function of progenitor mass (see §1.6). The corresponding supernova rate is $SNRate = 1.90 \pm 0.95$ events per century (this does not include type Ia supernovae, which have been found to be negligible sources of ^{26}Al). The resulting range of one to three core collapses per century coincides with the recent values obtained from on a survey of local O3-B2 dwarfs [Reed, 2005], extrapolated to the Galaxy as whole with spatial distribution models, and the study of the luminosity function of OB associations [McKee and Williams, 1997].

The conversion from core-collapse supernova rate, which assumes that all stars more massive than ten solar masses end their lives as supernovae [Heger et al., 2003], is given by $SFR = SNRate \cdot < m > \cdot f_{\rm SN}^{-1}$, where $< m >$ is the average stellar mass in a star formation event, and is the fraction of all stars that become supernovae. Stars are predominantly formed in clusters with a quasi-universal IMF (narrowly distributed about the canonical Salpeter power law, Kroupa 2002, Weidner and Kroupa 2005), but that the integrated galaxial initial mass function (IGIMF) must be steeper than the canonical IMF. A steeper IGIMF implies a reduced supernova fraction in general, and implies a dependence on galaxy mass and the much less established cluster mass distribution function. It is thus possible that the true SFR could be significantly larger than the rate derived from the canonical IMF. We report a SFR based on the conversion choice made by McKee and Williams (1997): $SFR = 1.96 SNRate$. With an average stellar mass of $< m >= 0.51$ $M_\odot$ and $f_{\rm SN}^{-1} = 2.6 \times 10^{-3}$, we find $SFR = (3.8 \pm 1.9)$ $M_\odot$ yr^{-1}, which agrees with the value derived from the luminosity functions of OB associations [McKee and Williams, 1997].

3.6 ^{26}Al line shapes for the different longitudes along the Galactic Plane

The 9-year COMPTEL imaging of ^{26}Al line emission has suggested the structures or different brightness along the plane of the inner Galaxy (both for the maximum entropy and MREM images, see Figures 3.5 and 3.7). COMPTEL could provide the image details of ^{26}Al in the Galaxy, but spectral information is poor. SPI has the high spectral resolution around 1.8 MeV, which provide us a chance to probe the ^{26}Al line shapes in the different regions along the Galactic plane.

^{26}Al mainly originates in massive stars, which should correlate to star-formation complexes in the Galaxy (Figure 3.14). Star-formation complexes are distributed in spiral-arm structures. So from the sight at the Sun, the ^{26}Al emission would appear

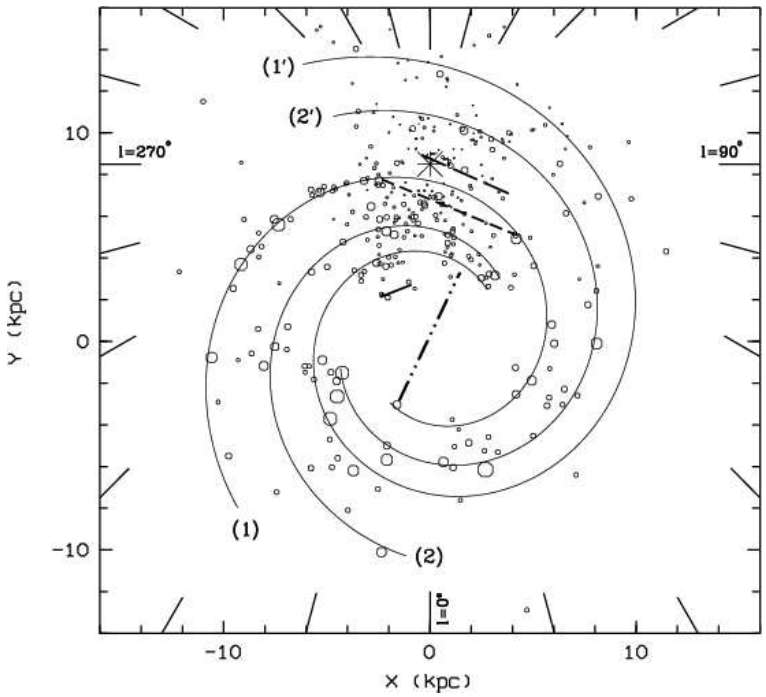

Figure 3.14: Distribution of the ^{26}Al candidate sources: star-formation complexes in the Galaxy [Russeil, 2003]. The Sun position is given by the large star symbol. The four-spiral-arm model is adopted to fit the all complexes: 1: Sagittarius-Carina arm, 2: Scutum-Crux arm, 1′: Norma-Cygnus arm and 2′: Perseus arm. The picture also sketches the local arm feature (long dashed line), the bar orientation and length (dashed-dot-dot line) from Englmaier and Gerhard 1999, the expected departure from a logarithmic spiral arm observed for the Sagittarius-Carina arm (short dashed line) and finally a feature certainly linked to the three-kpc arm (solid line).

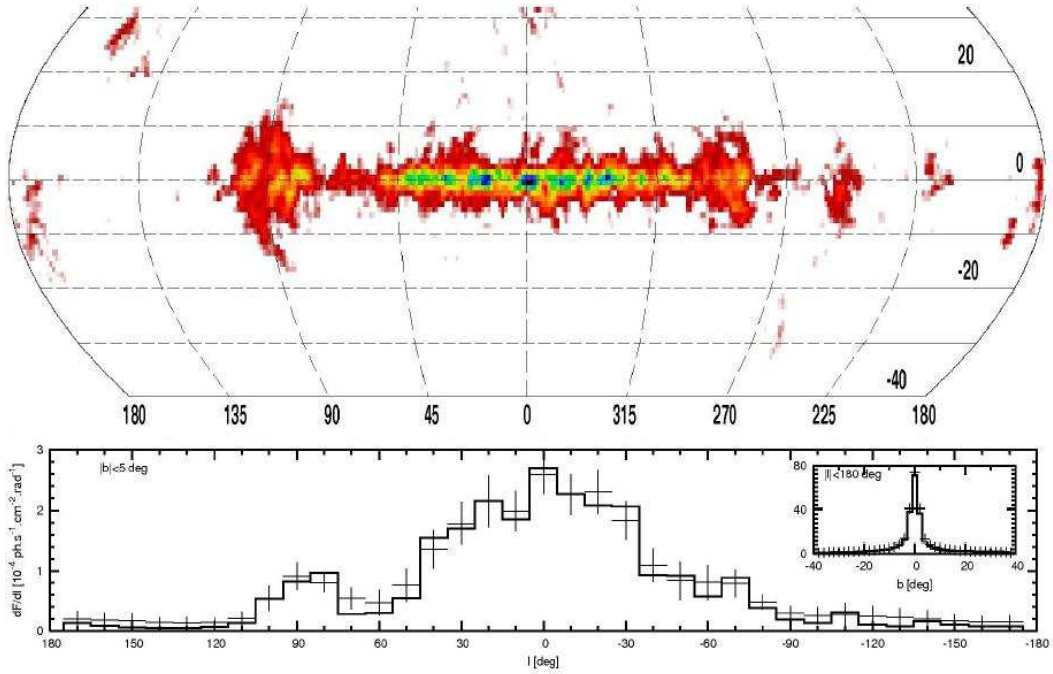

Figure 3.15: The all-sky imaging of ^{26}Al emission (1805 – 1811 keV) with 3-year SPI data (up) and the ^{26}Al intensity distribution along the longitudes (down) and intensity profile along the latitudes (small box). This image confirms extended ^{26}Al emission along the inner-Galaxy ridge, the bright ^{26}Al emission from the Cygnus region. And the 4th quadrant is slightly brighter than the 1st one (from Halloin et al. 2007, in preparation).

brighter in the direction of the spiral arms. For the Galactic center region, star formation should be active in the last million years, molecular clouds, and many SNRs have been discovered in the Galactic center [LaRosa et al., 2000]. In the Galactic center, a bar structure lying inside has been suggested [Englmaier and Gerhard, 1999, Gerhard, 2002]. Figure 3.14 also shows a hint of the presence of the local arm, possibly belonging to the nearest parts of the Sagittarius-Carina arm . A large number of star-formation complexes exist near the Sun, which would contribute to observed ^{26}Al emission toward these directions. But the number and space density of ^{26}Al near the Sun are probably lower than that in spiral arms. We do not know the distance information of ^{26}Al sources only from the ^{26}Al line brightness in the sky, but detailed studies of the line shapes, e.g. line centroids and widths, possibly probe the geometrical distribution of Galactic ^{26}Al which may locate in distant regions toward the Galactic center region and large-scale spiral arms, or the local star-formation regions (< 1 kpc).

3.6.1 Differences in the 1st and 4th quadrants

The three-year SPI observations also have obtained an all-sky ^{26}Al map (Figure 3.15, Halloin et al. 2007, in preparation), using SPI's coded-mask imaging at a limiting spatial resolution of $\sim 2.7^\circ$ at energies of 1.8 MeV (compared with COMPTEL, $\sim 3.8^\circ$). The basic characteristic ^{26}Al emission features are confirmed: ^{26}Al emission extends along the Galactic plane, prominent emission from the Cygnus region, and brightness asymmetries for the left and right parts of the Galactic plane, the fourth Galactic quadrant being brighter than the first one (lower part in Figure 3.15).

In this section, we will probe the asymmetries in a different way. We will directly derive the ^{26}Al line spectra in the regions of both the 1st and 4th Galactic quadrants. So the ^{26}Al line fluxes, line centroids and widths in the two quadrants can be studies together. The model fittings are carried out using separate sky maps covering the each sky region. A homogenous disk model (see Figure 3.11, $-60^\circ < l < 60^\circ$, $-10^\circ < b < 10^\circ$, scale height 200 pc) is used here to avoid the bias of maps in model fittings along the Galactic plane.

We first split this sky model into two sub-maps (the 1st quadrant $0^\circ < l < 60^\circ$, and the 4th quadrant $-60^\circ < l < 0^\circ$), and apply the model fitting using these two maps to determine the ^{26}Al spectra from both the 1st and 4th quadrants simultaneously. Two output spectra are displayed in Figure 3.16, and a Gaussian fit is applied to determine the ^{26}Al line shapes and fluxes. Both spectra show energy shifts relative to the centroid energy of ^{26}Al line in the laboratory, 1808.66 keV: a minor redshift 0.12 ± 0.10 in the 1st quadrant and a significant blueshift 0.54 ± 0.07 in the 4th quadrant. Both the spectra have width values near the value of the instrumental line width, implying that ^{26}Al emissions in these two regions are also the narrow lines. The ^{26}Al flux from the 4th quadrant is higher than that from the 1st quadrant, with the flux ratio of ~ 1.3.

We can further split the sky model into small longitude degree bins along the plane. Figure 3.17 shows ^{26}Al spectra in four segments along the Galactic plane: (1) $0^\circ < l < 30^\circ$, (2) $30^\circ < l < 60^\circ$, (3) $-30^\circ < l < 0^\circ$, and (4) $-60^\circ < l < -30^\circ$. The energy shifts of the ^{26}Al line are detected in the regions (1) and (3) along the plane. The inner region ($-30^\circ < l < 30^\circ$) is much brighter than two outside regions. The 1st quadrant brighter than the 4th quadrant is also confirmed: the region (3) is brighter than the region (1), with a flux ratio of ~ 1.2, and (4) is brighter than (2).

We also carried out model fittings using six sub-maps with 20 degree bin along the Galactic longitude, and obtained six ^{26}Al spectra from these regions (Figure 3.18): (1) $0^\circ < l < 20^\circ$, (2) $20^\circ < l < 40^\circ$, (3) $40^\circ < l < 60^\circ$, (4) $-20^\circ < l < 0^\circ$, (5) $-40^\circ < l < -20^\circ$, (6) $-60^\circ < l < -40^\circ$. The ^{26}Al line spectra can be still detected significantly for the inner Galaxy part ($-40^\circ < l < 40^\circ$, $> 6\sigma$ for each 20° bin region). For the two outside regions ($40^\circ < l < 60^\circ$ and $-60^\circ < l < -40^\circ$), ^{26}Al is detected with a lower significance level of $< 4\sigma$. This may be due to that the ^{26}Al fluxes in two outside regions are intrinsically low and the exposure time for the region is limited relative to the center region. For the four regions in the inner Galaxy, ^{26}Al line energy shifts are

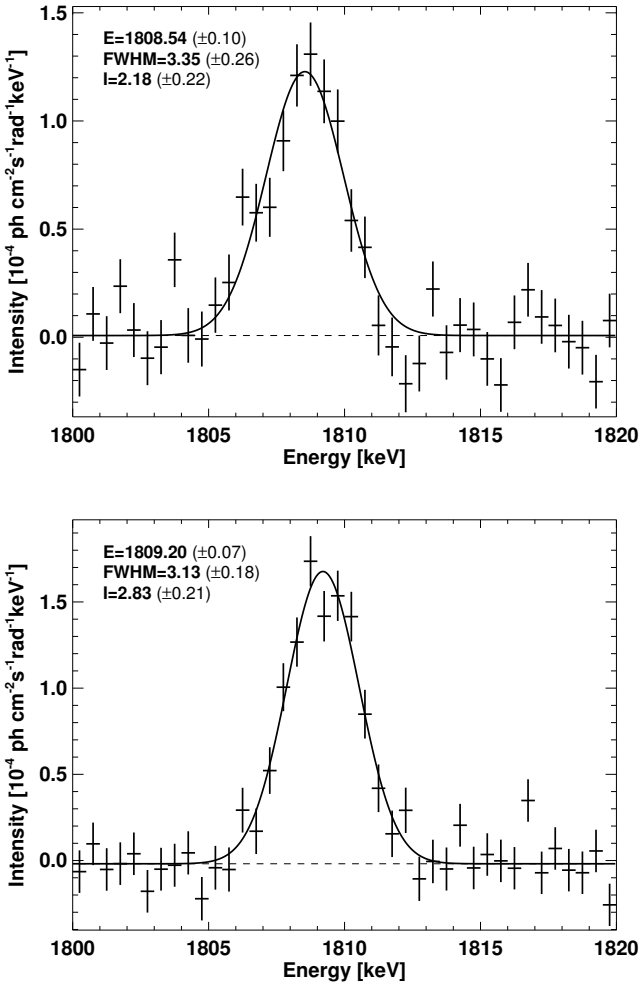

Figure 3.16: ^{26}Al spectra in two segments (upper $0^\circ < l < 60^\circ$, and down $-60^\circ < l < 0^\circ$ of the Galactic Plane derived from the model fitting using the two homogenous disk models. The spectra are fitted with Gaussian profiles. Two spectra show the energy shifts relative to the centroid energy of ^{26}Al line in the laboratory, 1808.66 keV: a minor redshift in the 1st quadrant and a significant blueshift in the 4th quadrant. Both the spectra have width values near the value of the instrumental line width, implying that ^{26}Al emissions in these two regions are also the narrow lines. And the ^{26}Al flux from the 4th quadrant a little higher than that from the 1st quadrant, the flux ratio is ~ 1.3.

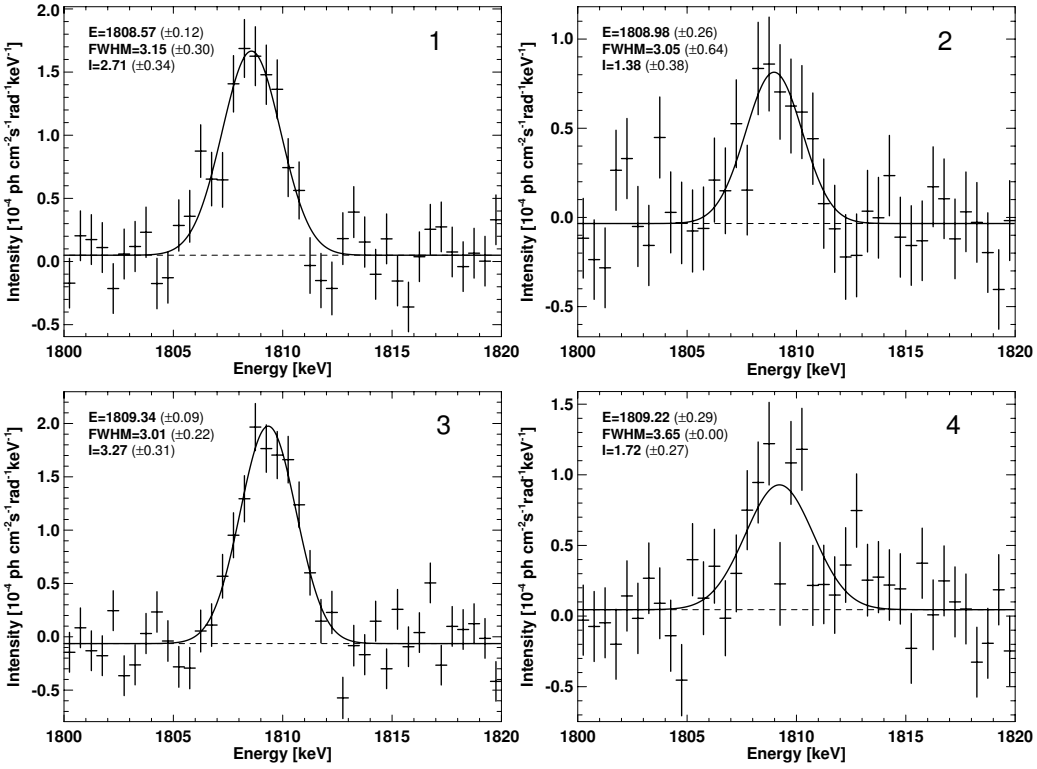

Figure 3.17: ^{26}Al spectra in four segments along the Galactic plane: 1. $1.0° < l < 30°$, 2. $30° < l < 60°$, 3. $-30° < l < 0°$, 4. $-60° < l < -30°$.

also observed. The region (5) appears brightest in the Galaxy. While the ^{26}Al line in the region (2) shows a broad feature, with a Gaussian width of FWHM$\sim 3.87 \pm 0.91$ keV. This possible broad feature is quite interesting and important to the origin of ^{26}Al toward this direction, i.e., the Sagittarius arm. The broad ^{26}Al line can not originate from the Galactic rotation (< 100 km s^{-1}, see Kretschmer et al. 2003). Then this broad line should be due to very high turbulent velocities ($\sim 300 \pm 200$ km s^{-1}) of ISM in the star-formation regions toward Sagittarius (also see complex structures toward this direction in Figure 3.14). Uncertainties are still large, thus the broad ^{26}Al line toward the Sagittarius arm need further studies.

^{26}Al emission from the four 20°-bin regions of the inner Galaxy is quite significant. As a check, we apply the model fitting using eight 10°-bin sub-maps in the inner region of $-40^\circ < l < 40^\circ$, and obtain the eight ^{26}Al spectra along the inner Galactic plane which are shown in Figure 3.19 and 3.20. The detections of the ^{26}Al line in each region is not significant ($< 3\sigma$) except the region of $-40^\circ < l < -30^\circ$. A Gaussian profile with a free parameter for the line width cannot give a good fit to the spectra. While a Gaussian line with an instrumental line width ($\sim$ 3.06 keV around 1.8 MeV) can fit the derived spectra relatively well with a reduced χ^2 around 1. ^{26}Al line emission in the region of $-40^\circ < l < -30^\circ$ is still significant ($\sim 6\sigma$) and appears brightest along the Galactic plane. Because of the wide field view of SPI ($\sim 16^\circ \times 16^\circ$), if two adjacent sub-maps (scales smaller than the field view) are used to fit SPI data, gamma-ray counts in one pointing (the time unit in fitting) can affect both the regions of two sub-maps simultaneously. Therefore, the model fitting with too many sub-maps covering relatively smaller regions ($< 16^\circ$) would contain some contaminations of fittings in adjacent sub-maps: a possible anti-correlation of the fitted coefficients in off-line spectra for adjacent maps (see examples in Figure 3.19 and 3.20). Hence, the model fitting may have difficulty to determine the ^{26}Al spectra with high significance using several adjacent small sub-maps (scales $< 16^\circ$). To study ^{26}Al emission in small intervals with SPI data more accurately, other approaches are still needed (see one approach for our test in §3.6.3).

3.6.2 Revisiting Galactic rotation effect

Galactic differential rotation can result in not only the broadening of ^{26}Al line but also the shifts of the line centroid energy due to the Doppler effect [Gehrels and Chen, 1996, Kretschmer et al., 2003]. Assuming a people looks through the Galaxy above the plane (e.g. the picture of spiral-arm structures in Figure 3.14), the Galaxy rotates in the clock direction, so that Galactic rotation would induce the ^{26}Al line centroid energy redshifts in the 1st quadrant and blueshifts in the 4th quadrant. The Galactic rotation curve can be been determined from observations of various objects (HI, CO, HII, Brand and Blitz 1993).

The angular distribution of ^{26}Al emission on the sky correlates well with tracers of ionization, such H_α and free-free emission. Adopting a three-dimensional model for

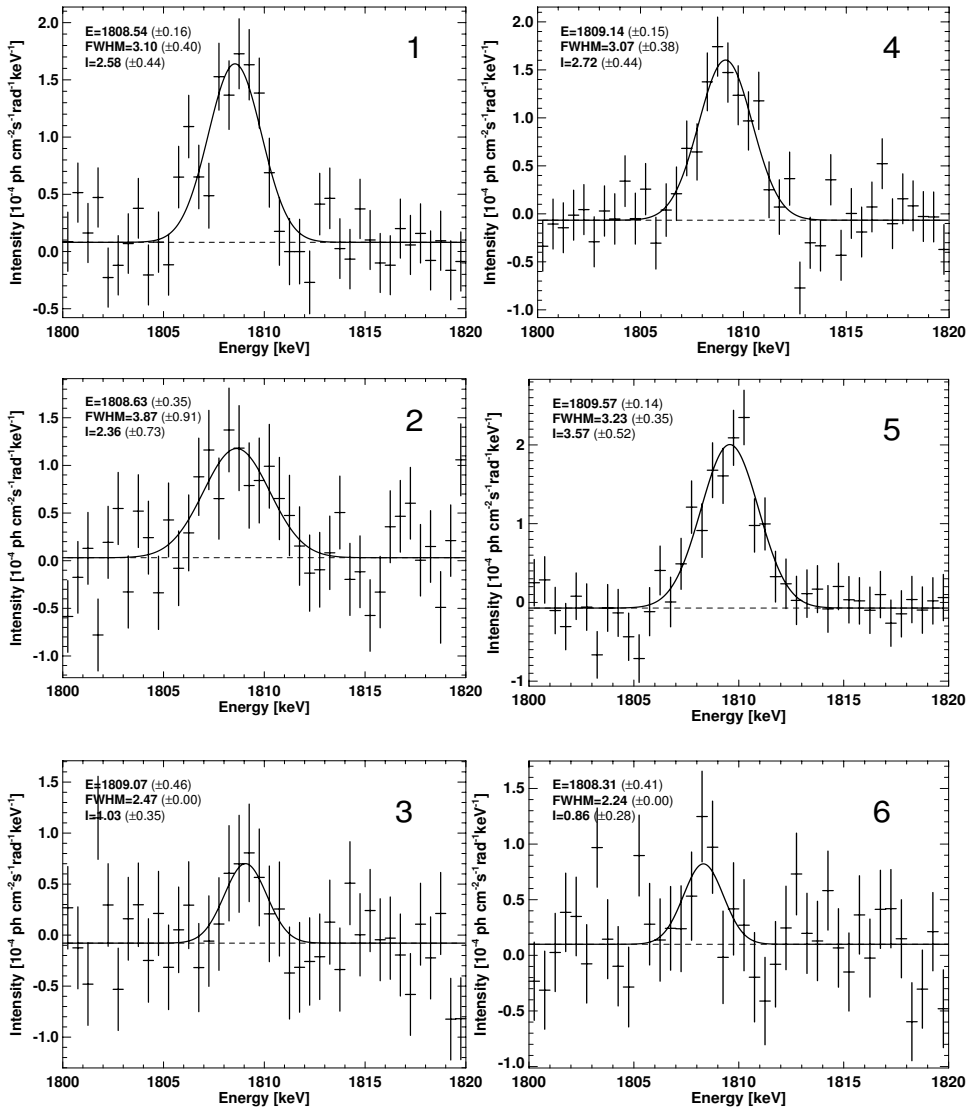

Figure 3.18: ^{26}Al spectra in six segments along the Galactic plane: 1. $1.0^\circ < l < 20^\circ$, 2. $20^\circ < l < 40^\circ$, 3. $40^\circ < l < 60^\circ$, 4. $-20^\circ < l < 0^\circ$, 5. $-40^\circ < l < -20^\circ$, 6. $-60^\circ < l < -40^\circ$. Small longitude degree bin (20°) makes the detections of ^{26}Al not significant in the regions of $40^\circ < l < 60^\circ$ and $-60^\circ < l < -40^\circ$.

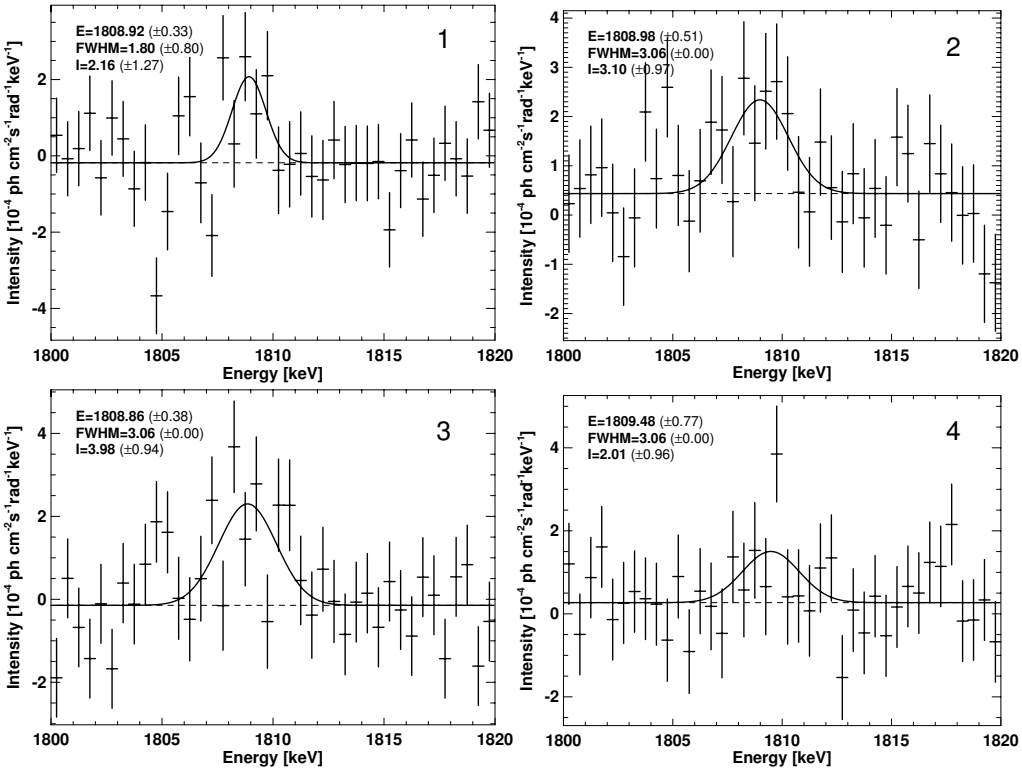

Figure 3.19: ^{26}Al spectra in four regions of the inner Galaxy: 1. $1.0^\circ < l < 10^\circ$, 2. $10^\circ < l < 20^\circ$, 3. $-10^\circ < l < 0^\circ$, 4. $-20^\circ < l < -10^\circ$.

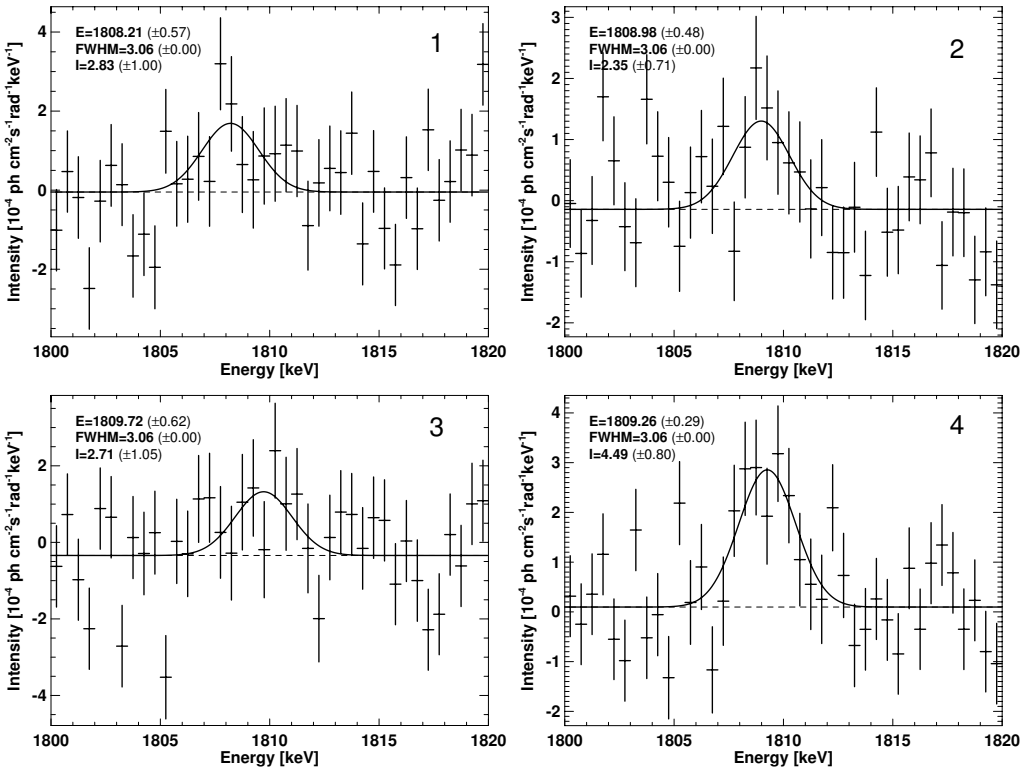

Figure 3.20: ^{26}Al spectra in four regions of the inner Galaxy (continued): 1. $20^\circ < l < 30^\circ$, 2. $30^\circ < l < 40^\circ$, 3. $-30^\circ < l < -20^\circ$, 4. $-40^\circ < l < -30^\circ$.

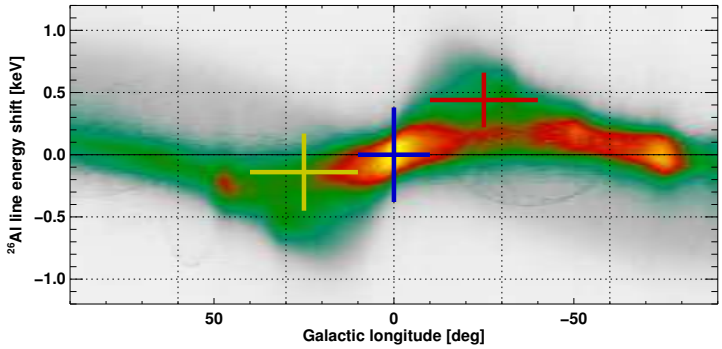

Figure 3.21: ^{26}Al line position shifts with different viewing directions along the inner Galactic plane derived from the 1.5-year SPI data [Diehl et al., 2006a]. Galactic rotation will shift the observed ^{26}Al line energy due to the Doppler effect, to appear blueshifted at negative longitudes and redshifted at positive longitudes. Colour scales are expectations of ^{26}Al line positions and intensity modelled from the Galactic rotation curve and a three-dimensional distribution of ^{26}Al sources [Kretschmer et al., 2003]. They used the central Galactic region ($-10^\circ < l < 10^\circ$) as a reference (fitted line energy 1808.72 keV) and found centroid energy shifts of -0.14 keV ($10^\circ < l < 40^\circ$) and +0.44 keV ($-40^\circ < l < -10^\circ$), respectively. So they concluded that the measurements are consistent with the Galactic rotation expectations of ± 0.3 keV in models though the error bars are very large.

the space density of free electrons [Taylor and Cordes, 1993] s the parent distribution for ^{26}Al sources in the Galaxy, the Doppler shifts of ^{26}Al line due to Galactic rotation have been modelled using the fitted Galactic rotation curve (Kretschmer et al. 2003, also see §3.2). Typically, the models expect Doppler shifts of 0.25 keV, varying by $\sim$ 0.05 keV with assumptions about inner-Galaxy rotation and spatial source distribution, for the integrated longitude ranges $10^\circ < l < 40^\circ$ and $-40^\circ < l < -10^\circ$ (see simulated profiles in Figure 3.21).

We first studied the Doppler shifts of ^{26}Al line due to Galactic rotation with the 1.5-year SPI data (Diehl et al. 2006). For extraction of Doppler shifts from SPI observations, we adopted a symmetric source distribution in the inner Galaxy in the form of an exponential disk (in Figure 3.11, scale radius 4 kpc, scale height 180 pc). A symmetric model avoids bias from uncertainties of spatial distribution details, and this exponential disk model is also plausible because spiral structure is insignificant in the inner Galaxy below $\sim 35^\circ$. Then we split this model into three longitude intervals ($-40^\circ < l < -10^\circ$, $-10^\circ < l < 10^\circ$, $10^\circ < l < 40^\circ$), and simultaneously derived the spectra for three segments using the model fitting. The results are plotted as crosses in Figure 3.21. Using the central Galactic region ($-10^\circ < l < 10^\circ$) as a reference (fitted line energy 1808.72 keV), we found centroid energy shifts of -0.14 keV ($10^\circ < l < 40^\circ$) and +0.44 keV ($-40^\circ < l < -10^\circ$), respectively. Though the error bars for the line positions are very large, we concluded that the results of the line energy shifts are consistent with the Galactic rotation effect [Diehl et al., 2006a].

Here, we revisit the ^{26}Al line energy shifts due to Galactic rotation with four-year SPI data. A new sky model are applied here in the model fitting. We have created a homogenous disk model (Figure 3.11, scale height 200 pc) to avoid the structures along the Galactic plane. The exponential disk model may be not good enough, because we have found that ^{26}Al emission is not weak from longitudes $|l| > 30\circ$ (see ^{26}Al spectra in Figure 3.20).

We split a homogenous disk model map into three intervals ($-10^\circ < b < 10^\circ$): $-40^\circ < l < -10^\circ$, $-10^\circ < l < 10^\circ$, $10^\circ < l < 40^\circ$. Then we derive the spectra for three segments simultaneously using model fitting, which can be compared with the early SPI results [Diehl et al., 2006a]. Three derived spectra are presented in Figure 3.22. The line centroid position shifts are clearly observed along the three longitude intervals. The ^{26}Al line centroid energy from the central interval $-10^\circ < l < 10^\circ$ is $1808.82 \pm 0.11(\mathrm{stat}) \pm 0.1(\mathrm{sys})$ keV with a minor blueshift, though it would be consistent with the laboratory value considering the error bars. For a comparison, similar to the previous SPI work [Diehl et al., 2006a], we use the central Galactic region ($-10^\circ < l < 10^\circ$) as a reference (fitted line energy 1808.82 keV) and find centroid energy shifts of -0.16 ± 0.13 keV ($10^\circ < l < 40^\circ$) and $+0.62 \pm 0.09$ keV ($-40^\circ < l < -10^\circ$), respectively. The line energy shifts have been plotted in Figure 3.23. The redshift of $\sim$ 0.16 keV in the positive longitude interval is lower than the prediction of $\sim$ 0.3 keV, but is still consistent with the Galactic rotation explanation. The blueshift of $\sim$ 0.62 keV in negative interval is quite significant, even concluding the error bars, this blueshift

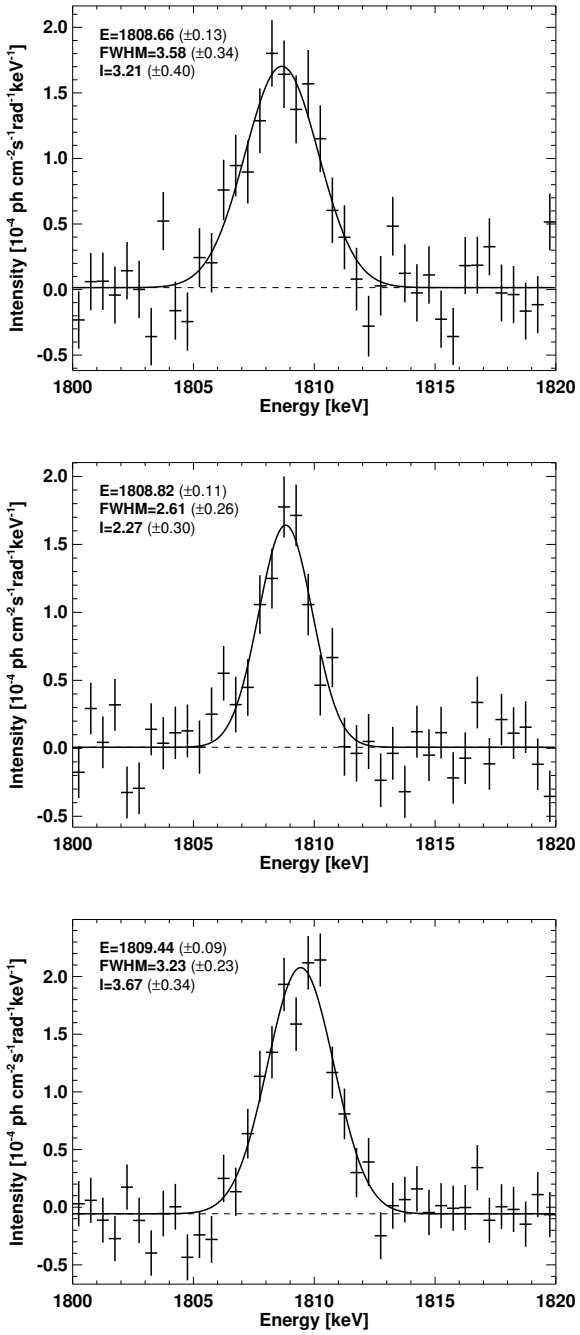

Figure 3.22: ^{26}Al spectra of three segments along the Galactic plane derived from the model fitting using three sub-maps ($-10^\circ < b < 10^\circ$): $10^\circ < l < 40^\circ$ (top), $-10^\circ < l < 10^\circ$ (middle), $-40^\circ < l < -10^\circ$ (down). Energy shifts of the ^{26}Al line centroid are observed along the plane.

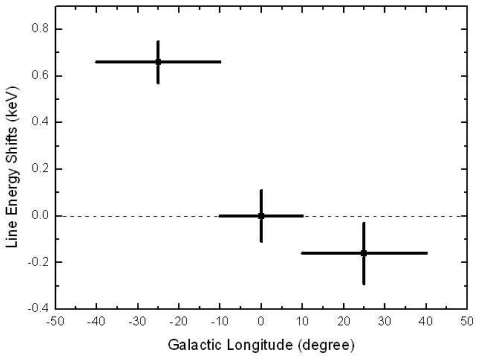

Figure 3.23: ^{26}Al line energy shifts along the Galactic plane. Similar to the previous SPI work [Diehl et al., 2006a], here the line centroid of the ^{26}Al spectrum from the region of $-10^\circ < l < 10^\circ$, $-10^\circ < b < 10^\circ$ has been set to be zero.

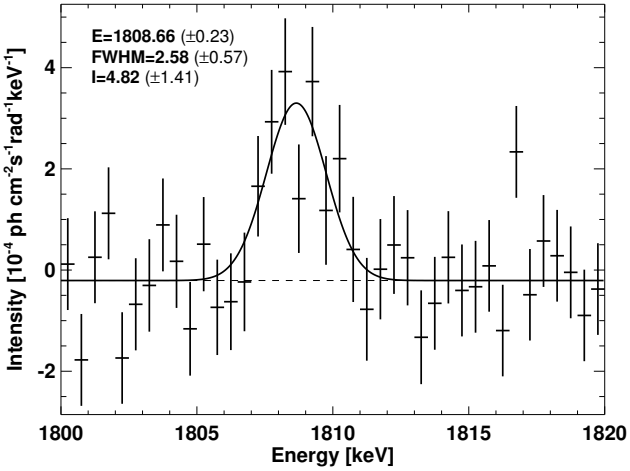

Figure 3.24: ^{26}Al spectrum from the Galactic center ($-5^\circ < l < 5^\circ$, $-10^\circ < b < 10^\circ$) derived from model fitting. The determined line centroid energy is consistent with the laboratory value.

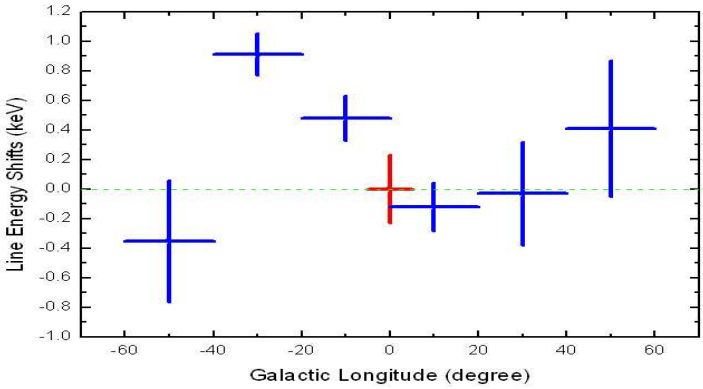

Figure 3.25: ^{26}Al line energy shifts along the Galactic plane ($-60^\circ < l < 60^\circ$, with longitude bin of 20°, fitted ^{26}Al spectra from Figure 3.18) relative to the line centroid of the ^{26}Al spectrum (fitted energy 1808.66 keV, see Figure 3.24) from the Galactic center region of $-5^\circ < l < 5^\circ$, $-10^\circ < b < 10^\circ$ which is set to be zero.

cannot be explained by the present Galactic rotation models [Kretschmer et al., 2003, Kretschmer, 2007].

We have used the ^{26}Al line centroid energy for the region $-10^\circ < l < 10^\circ, -10^\circ < b < 10^\circ$ as a reference to study the Galactic rotation effect. But we have found the centroid also has a minor blueshift relative to the laboratory value. For studies of the Galactic rotation effect on the ^{26}Al line energy shifts, we are unhappy for this systematic shift as a reference.

With more SPI data analyzed here, we can obtain the ^{26}Al spectrum the Galactic center region ($-5^\circ < l < 5^\circ, -10^\circ < b < 10^\circ$) using model fitting. The detection of ^{26}Al in the Galactic center is still significant ($> 4\sigma$). The line centroid energy is determined at 1808.66 keV is well consistent with the laboratory value. So we use the ^{26}Al line spectrum for the Galactic center (centroid energy of 1808.66 keV) as a reference to study line energy shifts for the 1st and 4th quadrants. Furthermore, we used the ^{26}Al spectra derived from 6 segments in 20° longitude bins along the plane (Figure 3.18). ^{26}Al line energy shifts along longitudes are plotted in Figure 3.25.

In positive longitudes of $\sim 0^\circ - 40^\circ$, the redshift in energy is $\sim 0.1 \pm 0.2$ keV, lower than the expectation of 0.2 – 0.5 keV for this longitude interval from Galactic rotation. Considering the uncertainties of measured line positions, there are no significant shifts in the positive longitudes. While, the blueshift for the negative longitude case is large, ~ 0.48 keV for $-20^\circ < l < 0^\circ$ and up to 0.9 keV for $-40^\circ < l < -20^\circ$. This asymmetry of the line energy shift may imply the Bar structure exists in the Galactic center region (Figure 3.14, Englmaier and Gerhard 1999). In the inner Galactic region $|l| < 30^\circ$, a rapidly rotation bar will affect the dynamics of gases and stars. The large

non-circular motions have been seen in HI and CO observations [Mulder and Liem, 1986, Gerhard and Vietri, 1986], and also from the NIR light distribution [Binney et al., 1997], source count asymmetries [Nikolaev and Weinberg, 1997] and gas dynamics [Englmaier and Gerhard, 1999]. The non-circular motions in the inner ring and a position angle $\sim 25^\circ$ of the bar (Englmaier and Gerhard 1999, also see Figure 3.14) would lead to the asymmetry of the ^{26}Al line energy line shifts in the inner Galaxy.

Blueshifts at positive longitudes are higher than the expectation of Galactic rotation [Kretschmer et al., 2003]. Especially for the case of $-40^\circ < l < -20^\circ$, a blueshift of 0.9keV cannot be explained by the present Galactic rotation models [Kretschmer et al., 2003, Kretschmer, 2007]. If Galactic rotation leads to a blueshift of 0.3 keV , an additional shift of $\sim$ 0.6 keV comes from other Doppler shifts of ^{26}Al sources with a bulk-motion velocity of ~ 100 km s^{-1} toward us. This bulk motions of ^{26}Al could originate in local star-formation regions, e.g., the nearest part of the Siguttarius-Carina arm (Figure 3.14), or the Gould Belt which is suggested to be active in star formations in about last 30 Myr [Grenier, 2000] and include a large amount of local star-formation complexes [Perrot and Grenier, 2003]. Contributions of these local ^{26}Al sources would affect the ^{26}Al line shapes toward this direction of the Galactic plane. This issue will be studied and discussed in §3.7.

3.6.3 ^{26}Al emission in small longitude intervals

Detections of ^{26}Al line shapes for the $\sim 10^\circ$-longitude-bin intervals of the inner Galaxy are not significant yet by the present SPI observations (see Figures 3.19 and 3.20). So direct probe of ^{26}Al line shapes in smaller regions is not possible. However, SPI has an angular resolution of $\sim 2.7^\circ$ for imaging at 1.8 MeV (Figure 3.15). Then it is possible to study the changes of ^{26}Al spectra for longitude intervals with increase or shift of longitude bins of input sky maps by a step as small as $\sim 2.7^\circ$ using model fitting. The significant differences of ^{26}Al spectra may not be found due to the changes of small scales (large error bars, or other reasons), but this would be a good test for the SPI ability of ^{26}Al imaging.

Multiple model fitting jobs should be carried out to probe the differences of ^{26}Al spectra with changes of longitude intervals by a step of several degrees. Statistical uncertainties may be a little different for various jobs of model fittings. But the same database, same background models and same sky models (sub-maps of a homogenous disk model) are applied in model fittings, so the changes of ^{26}Al spectra should not result from biases except for statistical uncertainties.

The Galactic center region $|l| < 15^\circ$

Figure 3.26 shows changes of ^{26}Al spectra for the different longitude intervals in the Galactic center region ($|b| < 10^\circ$): from $|l| < 2.5^\circ$ to $|l| < 15^\circ$ with a step of 2.5°. ^{26}Al emission is brightest in the Galactic center ($|l| < 2.5^\circ$ and $|l| < 5^\circ$), and the line centroid energy is well consistent with the laboratory value within uncertainties.

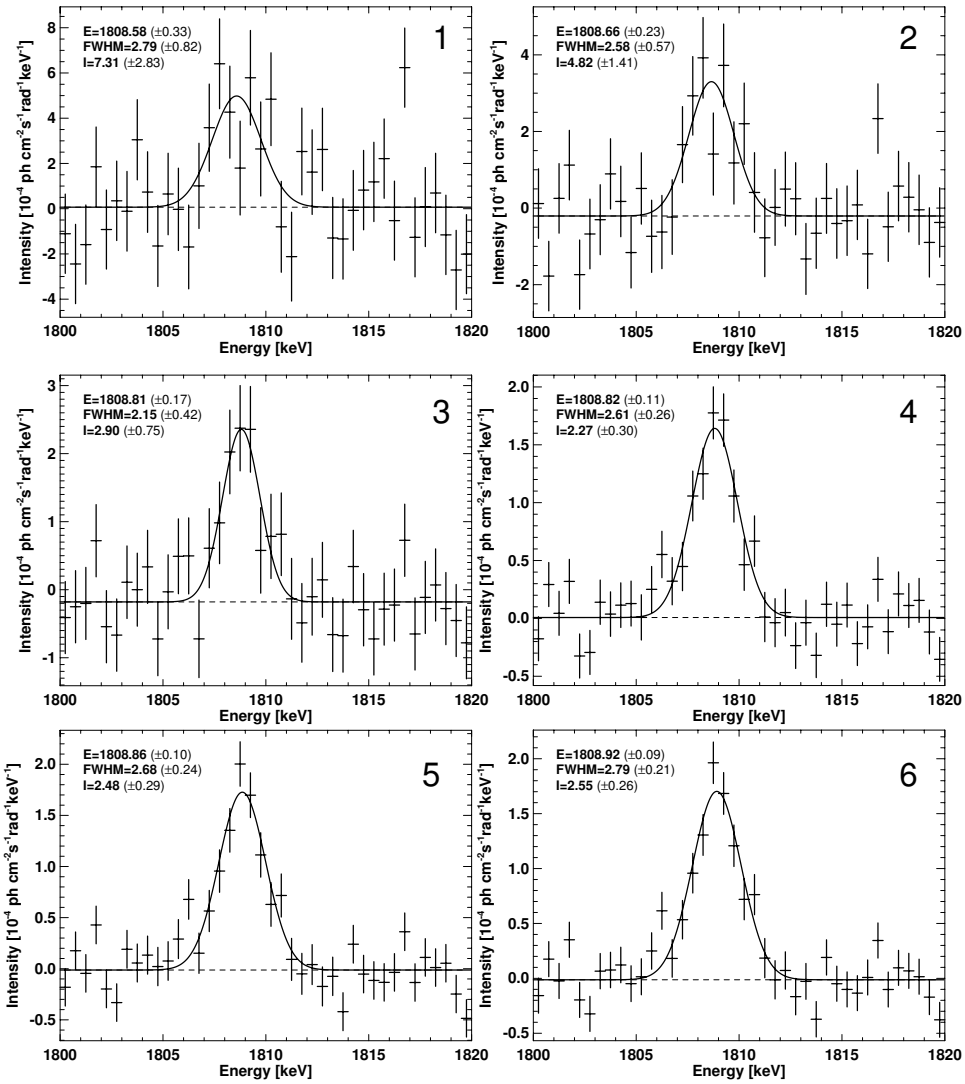

Figure 3.26: Comparison of ^{26}Al spectra in the Galactic center region for six different longitude intervals ($-10^\circ < b < 10^\circ$): 1. $-2.5^\circ < l < 2.5^\circ$, 2. $-5^\circ < l < 5^\circ$, 3. $-7.5^\circ < l < 7.5^\circ$, 4. $-10^\circ < l < 10^\circ$, 5. $-12.5^\circ < l < 12.5^\circ$, 6. $-15^\circ < l < 15^\circ$.

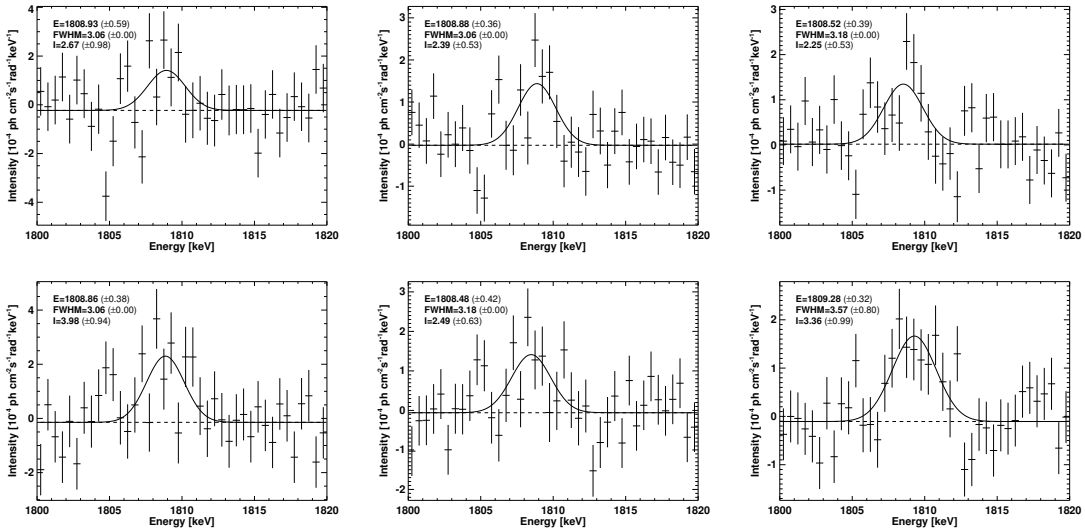

Figure 3.27: Comparison of ^{26}Al spectra with changes of longitude intervals by a step of 2.5° for the left part (upper, $l > 0°$) and right part (below, $l < 0°$) of the Galactic center: $0° < |l| < 10°$ (left), $0° < |l| < 12.5°$ (middle), $0° < |l| < 15°$ (right).

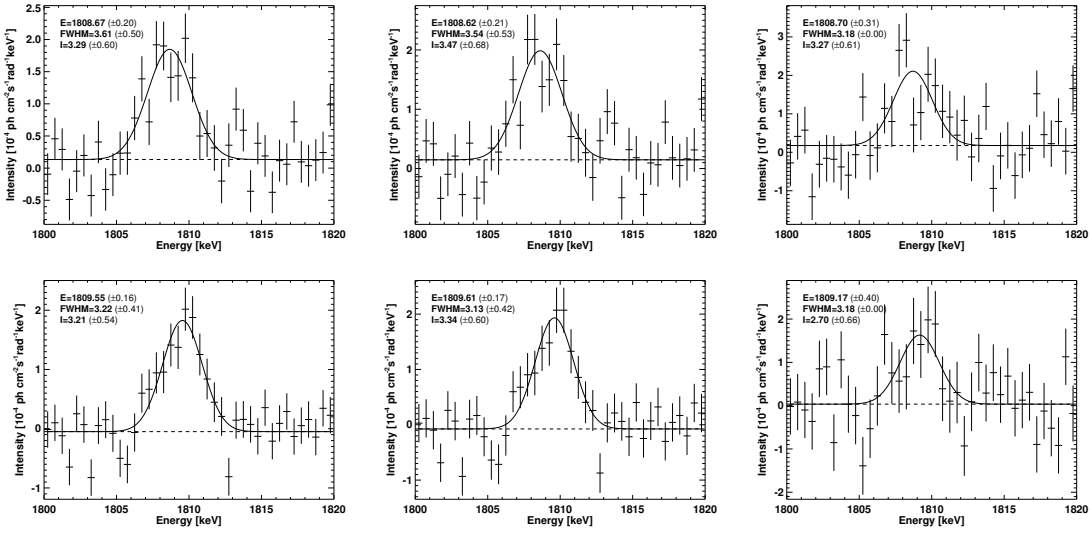

Figure 3.28: Comparison of ^{26}Al spectra with changes of longitude intervals by a step of 2.5° for the positive (upper) and negative (below) longitudes: $10° < |l| < 30°$ (left), $12.5° < |l| < 30°$ (middle), $15° < |l| < 30°$ (right).

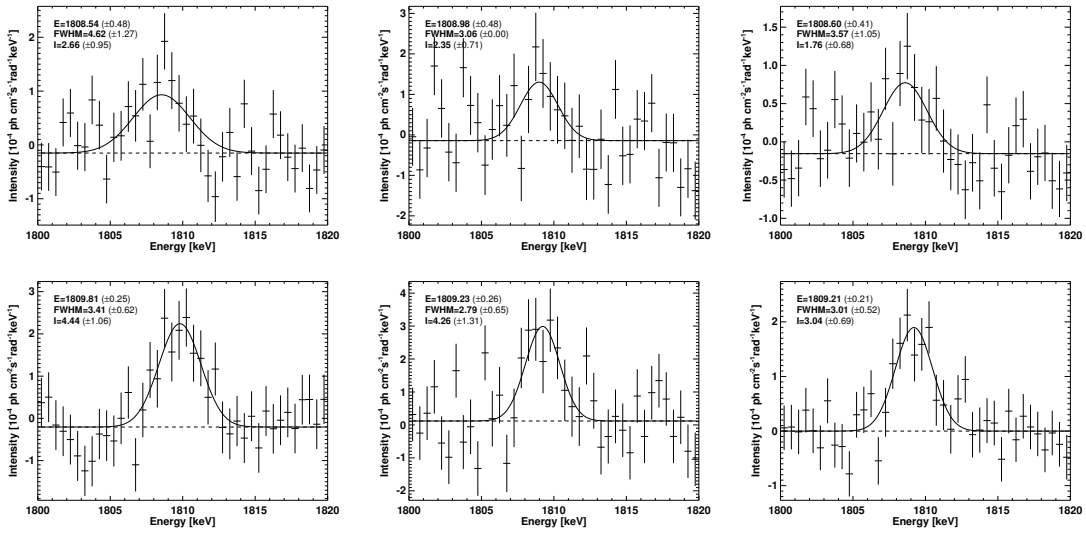

Figure 3.29: Comparison of ^{26}Al spectra with changes of longitude intervals by a step of 5° for the positive (upper) and negative (below) longitudes: $25° < |l| < 40°$ (left), $30° < |l| < 40°$ (middle), $30° < |l| < 45°$ (right).

In the regions of $|l| < 7.5°$ and $|l| < 10°$, the brightness decreases by a factor of 2 relative to the Galactic center, which suggests that ^{26}Al emission could be weak in the directions of $5° < |l| < 10°$. Extending to the larger regions of $|l| < 12.5°$ and $|l| < 15°$, the detections of ^{26}Al are quite significant ($> 10\sigma$), and the ^{26}Al brightness does not change (brighter than the average brightness for $|l| < 10°$). So significant ^{26}Al emission exists in the directions of $10° < |l| < 15°$, with an average brightness of $\sim 2.5 \times 10^{-4}$ ph cm^{-2} s^{-1}rad^{-1}. The ^{26}Al line centroids with a minor blueshift are detected from $|l| \geq 7.5°$. One possible reason may be the asymmetries of ^{26}Al emission in the positive and negative longitudes. The negative longitude is brighter than the positive one, then due to Galactic rotation, the blueshift could be observed as a whole behavior. Another possibility may be due to the bulk velocities of ^{26}Al sources in local star-formation systems toward us. We will further discuss this problem in the following sections.

^{26}Al spectra with changes of longitude intervals for the left and right parts of the Galactic center region are also studied separately. The longitude bin increases from $l = 10°$ to $l = 15°$ by a step of 2.5° for both sides. We compare the six spectra in Figure 3.27. The detections of ^{26}Al for these longitude intervals are not significant except the region of $-15° < l < 0°$. Though large error bars exists, the brightness of ^{26}Al for the negative longitudes is systematically higher than that for the positive ones ($|l| < 15°$).

$10° < |l| < 30°$

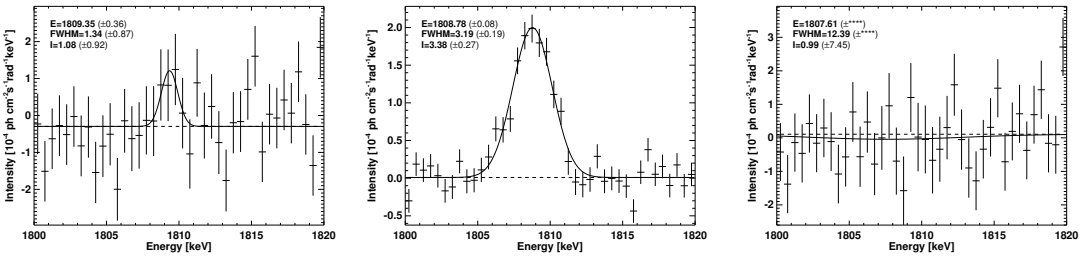

Figure 3.30: ^{26}Al spectra for three Galactic latitude intervals ($-60^\circ < l < 60^\circ$): $5^\circ < b < 20^\circ$ (left), $-5^\circ < b < 5^\circ$ (middle), $-20^\circ < b < -5^\circ$ (right).

Furthermore, we study ^{26}Al spectra with small longitude changes for the outer parts of the inner Galaxy. In Figure 3.28, we present the comparison of ^{26}Al spectra with changes of longitude intervals by a step of 2.5° for both the positive and negative longitudes of $10^\circ < |l| < 30^\circ$. Significant blueshifts of the ^{26}Al line are detected for the negative parts, but small redshifts for the positive regions. For $10^\circ < l < 30^\circ$, the ^{26}Al line brightness is nearly constant with a level of $\sim 3.3 \times 10^{-4}$ ph cm^{-2} s^{-1}rad^{-1}. The negative part is not brighter than the positive one. And the region of $-30^\circ < l < -15^\circ$ is significantly darker than $-30^\circ < l < -12.5^\circ$. This implies that ^{26}Al emission for $-15^\circ < l < -12.5^\circ$ should be higher than the average level of $\sim 3.4 \times 10^{-4}$ ph cm^{-2} s^{-1}rad^{-1}.

$25^\circ < |l| < 45^\circ$

Figure 3.29 displays the comparison of ^{26}Al spectra with changes of longitude intervals by a step of 5° for both the positive and negative longitudes of $25^\circ < |l| < 45^\circ$. The significant energy blueshifts of the^{26}Al line centroid are also detected for the negative longitudes. The ^{26}Al line centroid for $-40^\circ < l < -25^\circ$ has a large blueshift of ~ 1.1 keV relative to the laboratory value, and only ~ 0.6 keV for $-40^\circ < l < -30^\circ$. This different blueshifts imply that in the direction of $-30^\circ < l < -25^\circ$, ^{26}Al sources located in nearby star-formation complexes have a high mean bulk velocity toward us. The brightness of ^{26}Al for the negative longitudes is systematically higher than that for the positive ones, with a flux ratio of near 1.7. The region of $-40^\circ < l < -25^\circ$ is the brightest one with an average flux level of $\sim 4.4 \times 10^{-4}$ ph cm^{-2} s^{-1}rad^{-1}. It is interesting that we compare ^{26}Al spectra for the regions between $30^\circ < |l| < 40^\circ$ and $30^\circ < |l| < 45^\circ$. The brightness of $30^\circ < |l| < 45^\circ$ drops significantly relative to $30^\circ < |l| < 40^\circ$ by a factor of ~ 1.35, suggesting that ^{26}Al emission for $|l| > 40^\circ$ is very weak, which is consistent with the results in Figure 3.18.

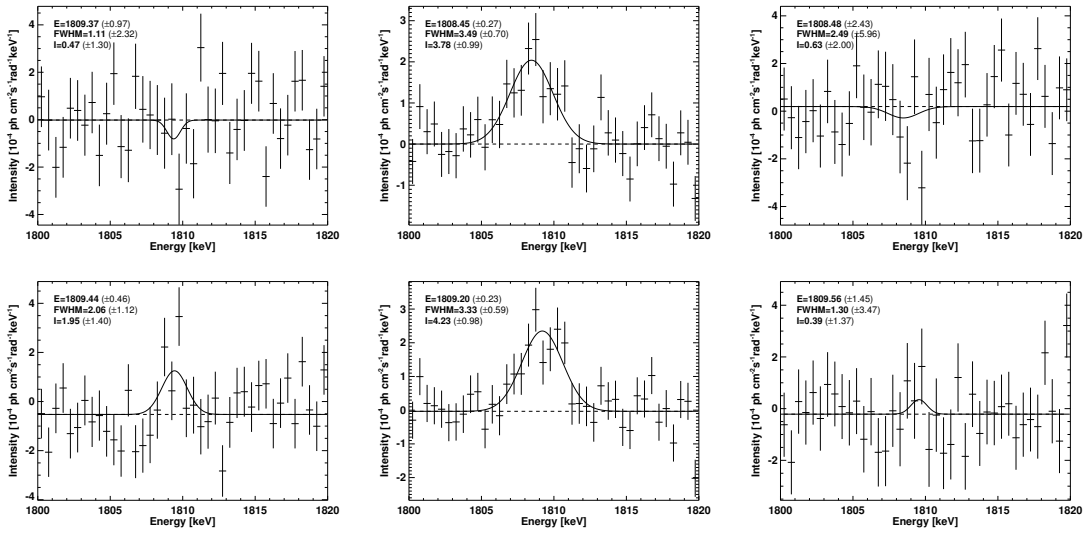

Figure 3.31: ^{26}Al spectra for different latitude intervals of the 1st (upper) and 4th (below) quadrants : $5^\circ < b < 20^\circ$ (left), $-5^\circ < b < 5^\circ$ (middle), $-20^\circ < b < -5^\circ$ (right).

3.7 Latitude studies of ^{26}Al emission

Both the ^{26}Al imaging by COMPTEL or SPI, and ^{26}Al spectra in different longitudes obtained by SPI cannot directly probe the distance information of ^{26}Al sources. The detected ^{26}Al signals in the sky could originate from the local star-formation complexes ($\sim$ 100 pc), or from the nearest part of the Siguttarius-Carina arm ($1-2$ kpc), or from the Galactic center region ($\sim$ 8 kpc), or even from the other side of the Galaxy ($>$ 10 kpc).

In this section, we try a possible way to resolve the ^{26}Al signals for the local complexes from the large scales of the Galactic plane. We split the homogenous disk model into sub-maps along Galactic latitudes, and derive ^{26}Al spectra for the different latitudes using model fitting. We have splitted the sky map into three parts along low latitudes, $-5^\circ < b < 5^\circ$, and intermediate latitudes $5^\circ < b < 20^\circ$ and $-20^\circ < b < -5^\circ$. ^{26}Al emission for low latitudes ($|b| < 5^\circ$) would be dominated by the large-scale origin in the Galactic disk. While ^{26}Al sources for high latitudes ($|b| > 5^\circ$) should originate from local star-formation systems in the Gould Belt. This definition is also similar to pulsar population studies [Wang et al., 2005b, Cheng et al., 2004]. The Gould Belt appears as an ellipsoidal shaped ring with semi-major and minor axes equal to $\sim$ 500 pc and 340 pc, respectively [Perrot and Grenier, 2003]. The Sun is displaced from the center of the Gould Belt about 200 pc towards $l = 130^\circ$ [Guillout et al., 1998]. The Vela region is located near the boundary of the Gould Belt towards $l \sim -90^\circ$. The

nearby Sco-Cen region also belongs to the Gould Belt, extending from $(l, b) = (0^\circ, 20^\circ)$ towards $(l, b) = (-30^\circ, 0^\circ)$ [Sartori et al., 2003].

Figure 3.30 displays three ^{26}Al spectra with Galactic latitudes ($|l| < 60^\circ$). No ^{26}Al signal is detected in the negative latitude region ($-20^\circ < b < -5^\circ$). And weak ^{26}Al emission is detected in the positive latitude region ($\sim 2\sigma$, $5^\circ < b < 20^\circ$). It is quite interesting that the line centroid has a significant blueshift of 0.7 ± 0.4 keV. The ^{26}Al emission for the low latitudes ($|b| < 5^\circ$) is brightest as expected, with a narrow line feature, and line centroid energy of 1808.78 ± 0.08 keV. The blueshift relative to the laboratory value is not significant yet (compared to the results in Table 3.1). Then we have explanation of the large blueshift of the ^{26}Al line centroid in Table 3.1: the large blueshift cannot originate in spiral arms and the possible asymmetry of ^{26}Al emission in the Galactic plane, but mainly comes from intermediate latitude regions where there exist nearby ^{26}Al sources with bulk velocities toward us.

We further split each latitude interval into two parts: the 1st and 4th quadrants. Then we carry out the model fitting and derive six spectra shown in Figure 3.31. No ^{26}Al signals are detected for two intermediate latitude regions of the 1st quadrant. While in the 4th quadrant, ^{26}Al emission is still clearly detected in the latitude region of $5^\circ < b < 20^\circ$, with the significant blueshift of the line centroid, 0.8 ± 0.5 keV. Additionally, a very weak ^{26}Al signal may be hinted toward the latitude region of $-60^\circ < l < 0^\circ$, $-20^\circ < b < -5^\circ$, which need a further check in future. In the low latitude cases, as an expectation, relative to the laboratory value, the ^{26}Al line centroid shows a redshift of 0.21 ± 0.27 keV for the 1st quadrant, and a blueshift of 0.54 ± 0.23 keV for the 4th quadrant, which is consistent with the explanation of Galactic rotation. The ^{26}Al spectra for the 1st and 4th quadrants also show the narrow line features, and the asymmetry of ^{26}Al brightness for two parts is also detected (a flux ratio of 1.12), though the error bars are large for both spectra.

In §3.6.2, we have studied the Galactic rotation effect on ^{26}Al spectra for three longitude intervals: $10^\circ < l < 40^\circ$, $-10^\circ < l < 10^\circ$, $-40^\circ < l < -10^\circ$. But the spectra obtained in §3.6.2 possibly includes the contributions from high latitudes. To avoid the contaminations from high latitudes, we re-study the ^{26}Al spectra for these three longitude intervals only in the low latitudes ($|b| < 5^\circ$) using the model fitting.

Figure 3.32 presents the ^{26}Al spectra of three segments along the Galactic plane. For the low latitude cases, energy shifts of the ^{26}Al line are observed along the plane. Similar to Figure 3.22, a redshift of 0.11 ± 0.35 keV is not significant, while a large blueshift of 0.75 ± 0.27 keV is still inconsistent with the expect of Galactic rotation. So the dynamics of the bar structure in the bulge may affect the ^{26}Al line shifts in positive longitudes, and in negative longitudes, motions of nearby ^{26}Al sources in the plane direction ($|b| < 5^\circ$) towards us would partly contribute to this line blueshift.

The line centroid energy for the center region ($|b| < 5^\circ$, $|l| < 10^\circ$) is determined at 1808.65 ± 0.27 keV, well within the laboratory value. Compared with the ^{26}Al spectrum for the Galactic center ($|b| < 10^\circ$, $|l| < 5^\circ$) in Figure 3.24 and spectra in high latitudes in Figure 3.31, we conclude that nearby ^{26}Al sources located in the direction

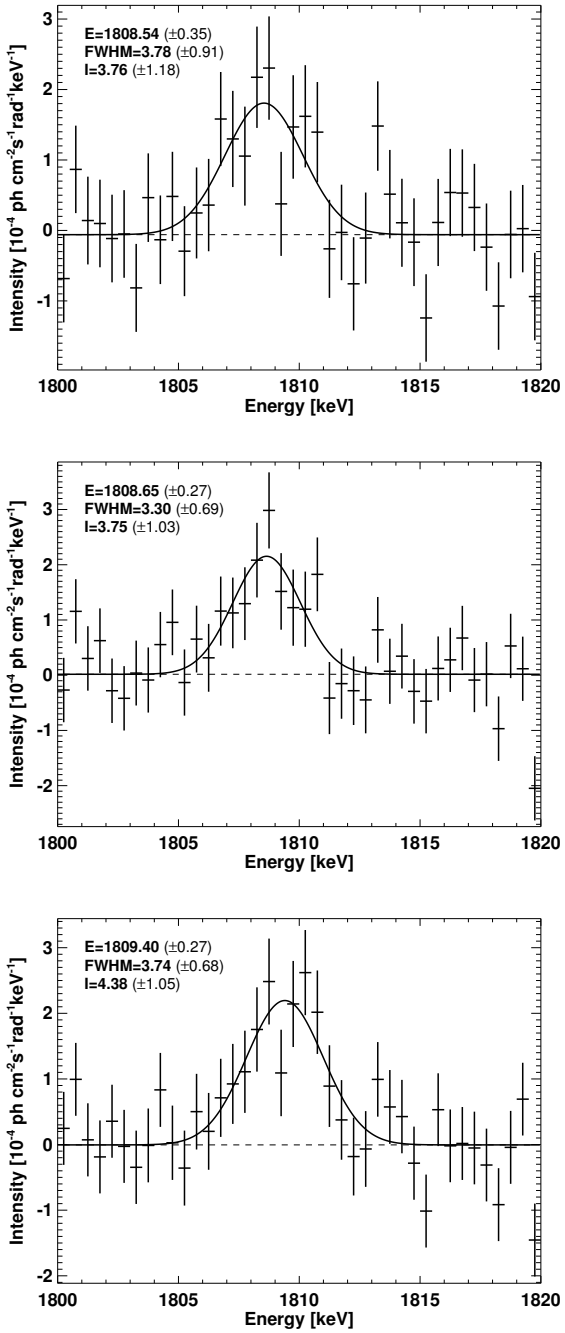

Figure 3.32: ^{26}Al spectra of three segments along the Galactic plane ($-5^\circ < b < 5^\circ$): $10^\circ < l < 40^\circ$ (top), $-10^\circ < l < 10^\circ$ (middle) , $-40^\circ < l < -10^\circ$ (down). Similar to Figure 3.22, energy shifts of the ^{26}Al line centroid are observed along the plane. And the line centroid energy for the center region ($|l| < 10^\circ$) is determined at 1808.65 ± 0.27 keV, consistent with the laboratory value.

of $b > 5^\circ$, $l < -5^\circ$, possible the Sco-Cen region in the Gould Belt, have high velocities towards us, inducing the observed ^{26}Al line blueshifts for the inner Galaxy region (e.g., the ^{26}Al spectra in Figure 3.26). We will study the possible ^{26}Al emission for the Sco-Cen region in the next Chapter.

3.8 1809 keV emission in the inner Galaxy: simulations versus observations

We have done analyses of ^{26}Al line shapes for the different longitudes along the Galactic plane with the SPI data. The different appearances of ^{26}Al emission in the 1st and 4th quadrants, and the line centroid energy shifts along the longitudes in large scales are detected. These large-scale characteristics of ^{26}Al emission should be correlated to the spiral-arm structures of the Galaxy, where ^{26}Al source candidates are most probably located. Therefore, if we know the distribution of ^{26}Al source tracers in the Galaxy, we can simulate the ^{26}Al intensity and line shape diagnostics along the plane. This simulated results can be directly compared with the SPI results on ^{26}Al line shapes (see above).

Kretschmer et al. [2003] have simulated the line shape diagnostics of Galactic ^{26}Al . Their results showed the Galactic rotation effect on ^{26}Al line shapes in large scales along the inner Galactic plane. Here we will update the simulations of ^{26}Al emission features in the inner Galaxy using some updated observations recently [Kretschmer, 2007], e.g., a three-dimensional model for the space density of free electrons by Cordes and Lazio [2002] instead of the older one by Taylor and Cordes [1993], also new observational results on the Galactic rotation curve [Avedisova, 2005].

3.8.1 Models of Galactic ^{26}Al

The space distribution of Galactic ^{26}Al should correlate with the distribution of star-formation complexes in the Galaxy. This distribution can be well traced by observations on ionization (H_α or free-free emission), molecular clouds, free electrons, and so on (see comparison among the different tracers of ^{26}Al sources §3.4). Therefore, in simulations, we adopt a three-dimensional model for the space density of free electrons based on pulsar dispersion measurements [Cordes and Lazio, 2002] as the parent distribution of Galactic ^{26}Al . A cut through this model along the Galactic plane can be found in Figure 3.33 [Kretschmer, 2007]. We have used three combinations of several different components of free electron density: (1) all components ; (2) all except the thick disk and the Galactic center ; (3) only the thin disk and spiral arms. These three combinations as ^{26}Al source distribution models will be applied in simulations separately for a comparison.

We take an approximate formula of the Galactic rotation curve in the inner Galactic disk [Olling and Merrifield, 2000] for the IAU standard value $R_0 = 8.5$ kpc, and $\Theta_0 =$

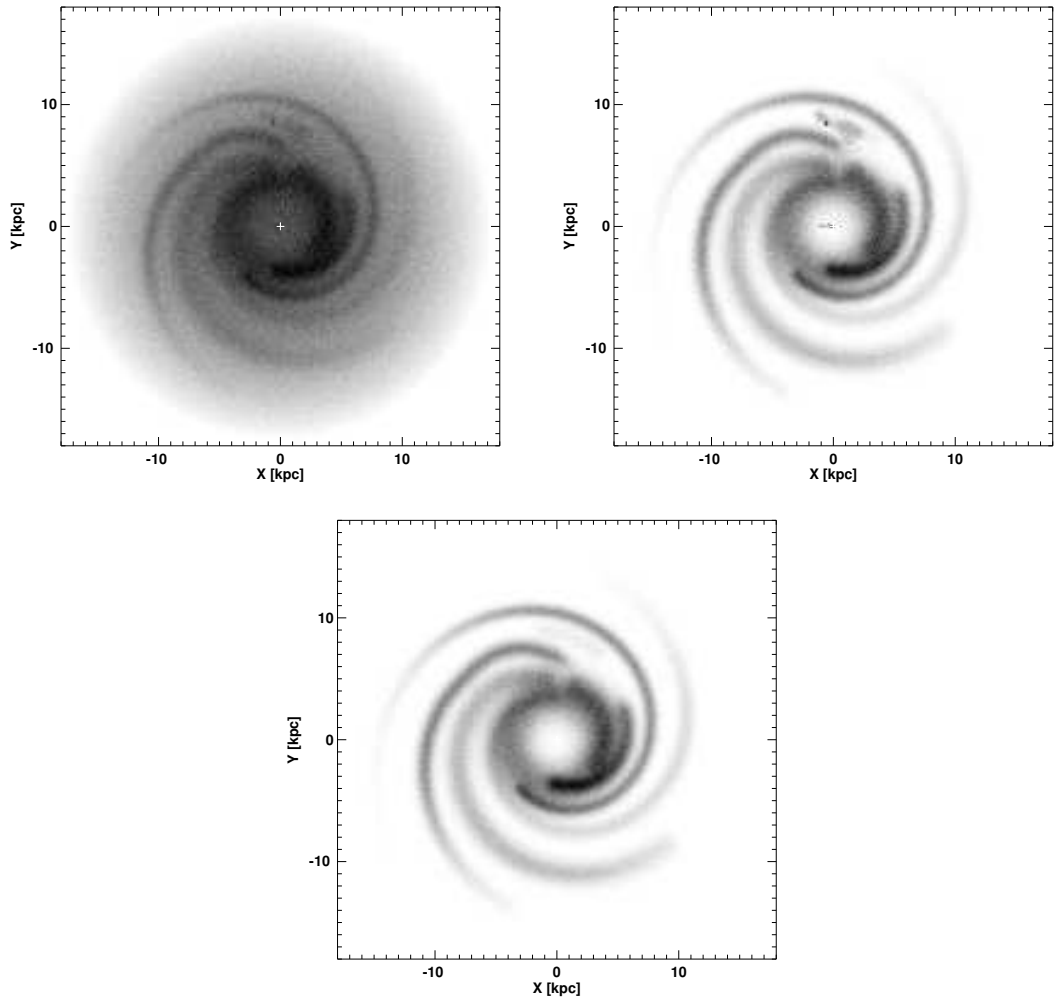

Figure 3.33: Area density models of supernovae obtained from the free-electron distribution from pulsar dispersion measurements (NE2001, Cordes and Lazio 2002). Three combinations of several different components of density are presented here (from Kretschmer 2007): all components (upper-left); all except the thick disk and the Galactic center (upper-right); only the thin disk and spiral arms (down).

220 km s^{-1} with the radial dependence is given by:

$$|v|(R) = 220[1 - \exp(-R/1\ \mathrm{kpc})]\mathrm{km\ s^{-1}}. \quad (3.2)$$

The velocity vector is parallel to the plane and perpendicular to the vector pointing from the Galactic center to the source location.

The kinematics of ^{26}Al sources in the local interstellar medium and the whole Galactic disk must be considered in our model. Dominated Galactic ^{26}Al is ejected by stellar winds of massive stars and supernova explosions. So the Galactic rotation in large scales is superimposed on the motion of freshly synthesized radioactive ^{26}Al due to the supernova explosion or ejecting Wolf-Rayet star wind and its slowed-down motion in the ISM before decay, i.e., within $\sim 10^6$ years [Kretschmer et al., 2003].

Recent hydrodynamic simulations of Type II supernovae [Kifonidis et al., 2003] find that the expansion of bulk of nucleosynthetic SN products such as ^{26}Al may be at velocities of $\sim$ 1200 km s^{-1} . Thus, in our model we allow ^{26}Al to expand freely with a velocity of 1500 km s^{-1} until it reaches the radius of the SN reverse shock formed by circumstellar interaction. After this point, we expand ^{26}Al at the velocity of the blast wave shock. This provides us a conservative estimate because ^{26}Al is probably to move slower than the forward shock. For our model for SNR dynamics from circumstellar interaction, we adopt the values of Kepler's supernova remnant shock positions and velocities given by McKee and Truelove [1995].

Type Ib/Ic supernovae and WR stars would eject matter at similar or even higher speeds than Type II SNe [Prinja et al., 1990, Garcia-Segura et al., 1996, Mellema and Lundqvist, 2002]. In addition, the interaction of ejected matter with the surrounding medium depends on the star formation history of the source region, where bubbles forming around groups of young massive stars play a potentially large role. Cavities extending over several hundred pc have been observed in galaxies [Oey and Clarke, 1996], and the Eridanus cavity presents us with a nearby example of such a cavity, extending from the Orion star formation region to very near the Sun [Burrows et al., 1993]. Matter ejected into such a low-density bubble could expand almost freely until reaching the boundary whereas typically assumed ISM densities, e.g., $n_{\mathrm{H}} \sim 1$ $\mathrm{cm^{-3}}$ would slow it down rapidly.

With the above assumptions, the ejected ^{26}Al moves freely for nearly 2 kyr, and then decelerates with the SNR's shell. The shell reaches a radius where it dissolves in the ISM at an age comparable to the lifetime of ^{26}Al , when a significant fraction has therefore already decayed. Since the expansion velocity drops below the characteristic rotational velocity of 220 km s^{-1} at about 40 kyr, when 96% of ^{26}Al is still left, the contribution from expansion to the overall ^{26}Al line width will be rather small in the model [Kretschmer et al., 2003].

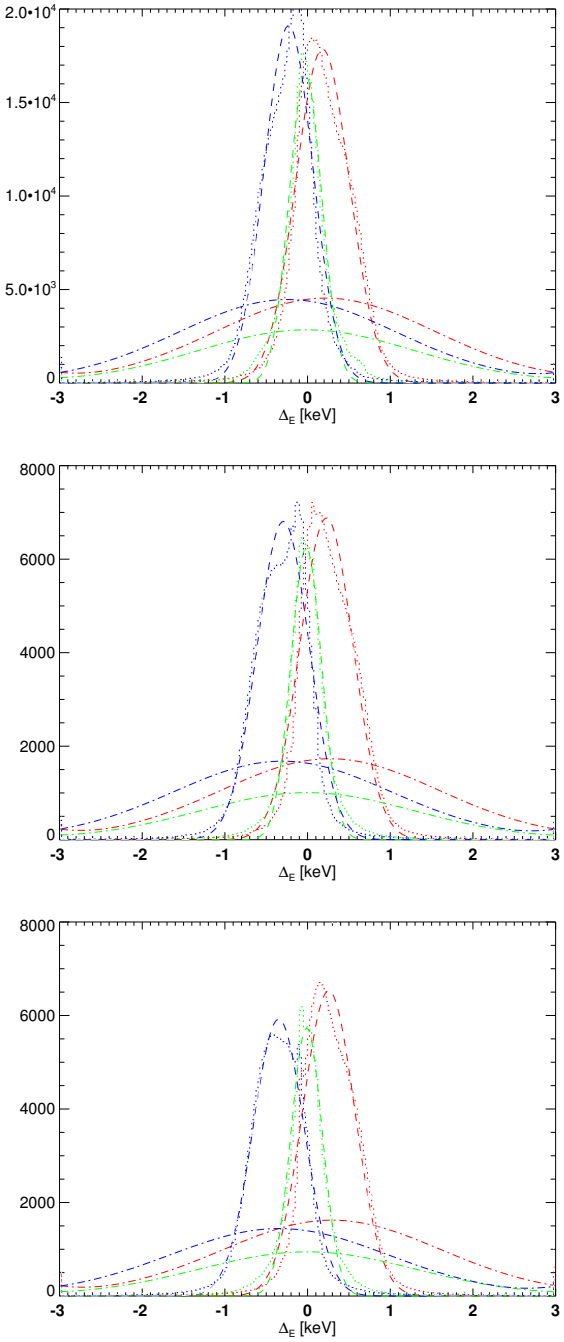

Figure 3.34: Illustrations of lines from different Galactic regions for three models separately (from Kretschmer 2007): all components (top); all except the thick disk and the Galactic center (middle); only the thin disk and spiral arms (down). The histograms in each figure show the spectra of the different parts of the inner galactic region: the Galactic center ($|l| < 5°$, green), the eastern part ($5° < l < 40°$, blue), the western part ($-40° < l < -5°$, red). The dotted lines represent the ^{26}Al source spectrum, the dashed lines are the best-fitting Gaussian, and the dash-dotted lines result from a convolution with a 3.0 keV FWHM Gaussian adopted for instrumental resolution of the measuring detector.

3.8.2 ^{26}Al intensity and line shapes: simulations versus observations

We obtain simulated sky ^{26}Al intensity and spectra from a Monte Carlo scheme: ^{26}Al source locations are chosen randomly from a spatial distribution proportional to the free electron density (Figure 3.33, Cordes and Lazio 2002, Kretschmer 2007), distributing candidate source positions within a volume centered on the Galaxy and extending 25 kpc in the plane and 7.5 kpc perpendicular to the plane. For each nucleosynthesis event, a random age is chosen within the interval $[0,\ 2 \times 10^7$ yr$]$. From this we evaluate the intrinsic velocity distribution and size of the ^{26}Al source, following the above expansion model. The age of the nucleosynthesis event thus determines extent and intrinsic velocity of its ejecta, as well as their 1.809 MeV luminosity. We represent each event by 2^{10} mass elements to reflect its spatial extent [Kretschmer, 2007].

Assuming $R_0 = 8.5$ kpc, and $\Theta_0 = 220$ km s^{-1}, we obtain viewing direction and radial velocity of ^{26}Al sources. Direction and radial velocity give us the coordinates of the ^{26}Al source mass element in a data space of ^{26}Al decay luminosity as a function of longitude, latitude and photon energy [Kretschmer et al., 2003, Kretschmer, 2007]. Simulations have been carried out using three combinations of the free electron density model respectively (Figure 3.33).

In order to compare with the SPI results, we integrate our simulated sky map of line energies and intensities over a region of interest and obtain a resulting spectrum corresponding to an observation of this region with perfect spectral resolution. The integrated ^{26}Al spectra from our models for three parts of the inner Galaxy region ($-5^\circ < l < 5^\circ$, $5^\circ < l < 40^\circ$, $-40^\circ < l < -5^\circ$, respectively) are presented in Figure 3.34. Our model spectra (dotted lines) show the deviation from a fitted Gaussian shape (dashed lines). For the realistic SPI measurements, Ge detectors have instrumental resolution 3.0 keV FWHM around 1.8 MeV (see Figure 2.9). This instrumental resolution convolution with the instrument response suppresses the difference between the measured flux and a Gaussian by a factor of ≈ 2000 (see dash-dotted lines in Figure 3.34).

The simulated ^{26}Al line shapes can be determined and compared with the SPI measurements. The ^{26}Al lines for three parts of the inner Galaxy show narrow line features, which is well consistent with our SPI constraints. When we fit Gaussians to these spectra, we obtain a line width of ~ 0.3 keV for the Galactic center (green lines, $|l| < 5^\circ$), and $\sim 0.8 - 0.9$ keV for the left and right parts of the inner Galaxy (blue and red lines, $5^\circ < |l| < 40^\circ$).

There are no ^{26}Al line centroid shifts for the Galactic center ($|l| < 5^\circ$) in all three distribution models, which is also consistent with the observed spectrum by SPI (see Figure 3.24). But the ^{26}Al line centroid energies for the left and right parts of the inner Galaxy ($5^\circ < |l| < 40^\circ$) are shifted by a significantly offset relative to the central region ($|l| < 5^\circ$). And the shifts are symmetrical for the positive and negative longitudes. The shifted values are a little different for three models. For the model of all components, the ^{26}Al line shift due to Galactic rotation is ~ 0.2 keV, while ~ 0.3 keV for the model of all except the thick disk and the Galactic center and ~ 0.4 keV for the model of only

the thin disk and spiral arms. Compared to our SPI results on ^{26}Al line centroid shifts along the Galactic plane (see Figure 3.25), a redshift for positive longitudes of ~ 0.1 keV is lower than the prediction of models, while a blueshift for negative longitudes of ≤ 0.5 keV is higher than the Galactic rotation expectation in simulations even for the model of only the thin disk and spiral arms. Asymmetry of ^{26}Al line centroid shifts for positive and negative longitudes is inconsistent with the explanation of Galactic rotation.

We also compare the ^{26}Al intensities for the left ($5^\circ < l < 40^\circ$) and right ($-40^\circ < l < -5^\circ$) parts of the inner Galaxy. For the model of all components, the ^{26}Al intensity for the left part is a little higher than that for the right part, which is not consistent with our SPI results in §3.6.1. For the model of all except the thick disk and the Galactic center, the ^{26}Al intensity of each part is similar, the significant asymmetry does not appear. But for the model of only the thin disk and spiral arms, the ^{26}Al intensity for $-40^\circ < l < -5^\circ$ is significantly higher than that for $5^\circ < l < 40^\circ$, with a flux ratio of ~ 1.15. This asymmetry has been detected in ^{26}Al spectroscopy for the 1st and 4th quadrants (see Figure 3.16, 3.17 and 3.22). In our SPI observations, we have reported a flux ratio of ~ 1.3 for $|l| < 60^\circ$, ~ 1.2 for $|l| < 30^\circ$ and ~ 1.14 for $10^\circ < |l| < 40^\circ$. Therefore, we conclude that the free-electron density model of only the thin disk and spiral arms reflects the real distribution of Galactic ^{26}Al , which is also consistent with the expectation of the massive star dominated origin of ^{26}Al sources in the Galaxy.

4 ^{26}Al sources and line shapes in star formation regions

The COMPTEL 1809 keV all sky maps (i.e., maximum entropy and MREM maps, see Figures 1.6 and 1.7, Plüschke 2001) attributed to radioactive decay of Galactic ^{26}Al have confirmed the diffuse emission along the inner Galaxy. Several significant features of the reconstructed intensity pattern are flux enhancements in the directions of nearby star-formation regions, e.g., the Cygnus region [del Rio et al., 1996], the Vela region [Diehl et al., 1995b], the Carina region [Plüschke, 2001]. A possible feature above the Galactic center (in high latitudes) has been also reported, which is attributed to the nearby Sco-Cen region [Plüschke, 2001]in the Gould Belt. The ^{26}Al map obtained by the three-year SPI observations (Figure 3.15, Halloin et al. 2007, in preparation) also confirmed the bright emission from the Cygnus region.

These nearby star-formation regions are very young (several Myr), and contain a wealth of massive stars, and recent supernova remnants. Detections of ^{26}Al in these regions strongly support the hypothesis of massive stars and their descendent supernovae being the dominant sources of interstellar ^{26}Al . ^{26}Al near these young populations may be located the different medium environment from the large scales in inner Galaxy, e.g. high turbulent velocities of interstellar medium in these star-formation regions due to stellar winds and supernova explosions.

The INTEGRAL/SPI is a powerful spectrometer to probe the ^{26}Al line shapes. So spectral studies of ^{26}Al line in these star-formation regions can provide new information of ^{26}Al sources and their environments.

In this Chapter, we will study ^{26}Al line shapes of three nearby star-formation regions: Cygnus, Vela and Sco-Cen, with the four-year SPI database (same with that in §3). Model fittings are also carried out to derive the ^{26}Al spectra using the specified sky maps for each region:

(1) split the sky distribution model map into two independent submaps, one map covering the defined star-formation region (Cygnus, Vela or Sco-Cen) and the rest of the sky;

(2) model fitting is applied with two independent submaps to fit the data;

(3) two spectra for the defined star-formation region and the rest part respectively are derived simultaneously using model fitting.

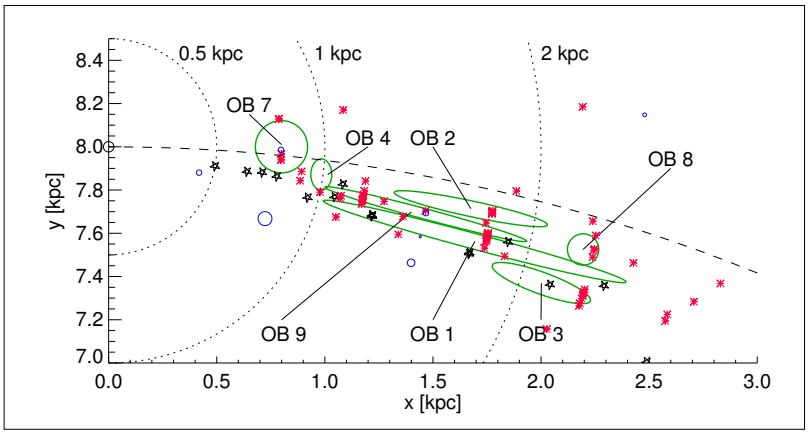

Figure 4.1: Distribution of O and WR stars (red and black stars) as well as SNR (blue circles) and OB associations (green ellipses) in the direction of Cygnus as viewed from above the galactic plane (from Plüschke 2001). The sun is allocated along the y-axis at 8.0 kpc.

4.1 Cygnus region

The Cygnus region is one of the most active nearby star forming regions in the Galaxy with a mean age of $\sim$ 3 Myr [Plüschke, 2001]. The region as defined by the Cygnus 1.8 MeV emission feature contains numerous massive stars. The Cygnus region and its ^{26}Al emission have been studied and discussed detailedly in Plüschke's thesis (2001). Here, we will summarized some main features which are related to ^{26}Al sources in Cygnus.

The galactic O star catalogue lists 96 O stars in this field [Garmany et al., 1982]. In addition, one finds 23 Wolf-Rayet stars in this region of which 14 are of WN-type, 8 of WC-type and one is classified as WO-star [van der Hucht, 2001]. Between 5 and 10 of these WR stars are believed to be members of OB associations in this area of the sky.

In the past million years, supernova explosions were also active in the Cygnus region. The Galactic SNR Catalogue lists 19 remnants in this region, for 9 of those age and distance have been estimated with sufficient accuracy [Green, 2006].

Beside numerous open clusters, the region contains nine OB associations [Alter et al., 1970, Plüschke, 2001]. Meanwhile two of those (OB 5 & 6) are thought to be *artificial* association due to projection and selection effects [Garmany and Stencel, 1992].

Figure 4.1 shows the distribution of O and WR stars, SNRs and OB associations in the direction of Cygnus as viewed from above the galactic plane [Plüschke, 2001]. For SNRs the given size of the circle represents the appearance at the sky, whereas the ellipses marking the OB association have a twofold meaning. The minor axis represents the appearance in a longitude-latitude projection and major axis gives the distance uncertainty for each association.

Optical population studies towards the Cygnus region are largely hampered by a

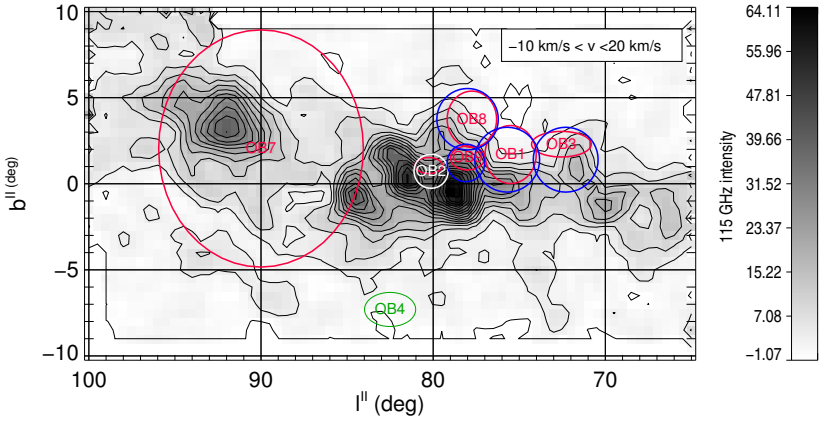

Figure 4.2: The 115 GHz CO emission towards Cygnus [Dame et al., 2001]. The ellipses mark the positions of the Cygnus OB associations.

giant molecular cloud complex lying at a distance of 500 – 1000 pc [Dame et al., 2001]. Figure 4.2 shows a velocity integrated intensity image of CO 115 GHz emission towards the Cygnus region reflecting the large angular extent of the Cygnus Molecular Rift [Dame et al., 2001]. By analyzing the 2MASS NIR data of a field centered on Cygnus OB2, Knödlseder [2000] has found a factor of three more O stars than determined from optical observations. Even more, Cyg OB2 now is the most massive conglomerate of the stars known in the Milky Way and resembles more like a young globular cluster than a typical OB association. Knödlseder [2000] has found 120 ± 20 O star and 2600 ± 400 OB star members. The slope of the mass distribution was found to be $\Gamma = 1.6 \pm 0.1$ and total mass of the stellar group is of the order of 10^5 $M_\odot$. The overall large differences of the inferred properties of Cygnus OB2 depending more or less on the impact of the molecular clouds in front of the association let one expect similar effects for the other OB associations found in Cygnus.

The ^{26}Al flux from the Cygnus region has been reported from the COMPTEL and INTEGRAL/SPI observations. From two years of COMPTEL data, del Rio et al. [1996] derived a flux of $(7.0 \pm 1.4) \times 10^{-5}$ph cm^{-2} s^{-1} from a sky region defined as $73^\circ < l < 93^\circ$, $-9^\circ < b < 9^\circ$, corresponding to a detection significance of 5σ. From the analysis of 9 years of COMPTEL data, Plüschke [2001] found a flux of $(10.3 \pm 2.0) \times 10^{-5}$ph cm^{-2} s^{-1} from a slightly larger region covering $70^\circ < l < 96^\circ$, $-9^\circ < b < 25^\circ$. With early SPI data, we presented first results of ^{26}Al line emission from the Cygnus region, and observed a 1809 keV line flux of $(7.3 \pm 1.8) \times 10^{-5}$ph cm^{-2} s^{-1} from a sky region defined as $73^\circ < l < 93^\circ$, $|b| < 9^\circ$ at a significance level of 4σ [Knödlseder et al., 2004]. The ^{26}Al line from Cygnus appears moderately broadening, with an intrinsic FWHM of (3.3 ± 1.3) keV. But this broad feature is still in dispute, and needs further

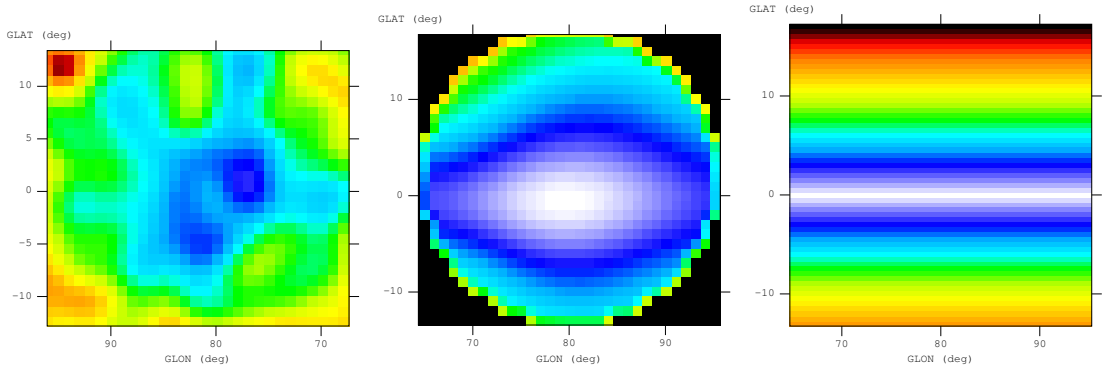

Figure 4.3: Three different sky models for the Cygnus region ($65^\circ < l < 95^\circ$, $-13^\circ < b < 17^\circ$) used in model fitting: the COMPTEL maximum entropy map (left), the COMPTEL MREM map (middle), the homogenous disk model (right).

studies.

Here we re-analyzed the ^{26}Al line line shape from the Cygnus region with a large SPI database. In the real analysis, we derive two ^{26}Al spectra simultaneously using model fitting with two sky maps, one covering the Cygnus region, and the other covering the rest of the sky (including the inner Galaxy). Three different sky models as tracers of ^{26}Al in Cygnus are used in model fittings to obtain the ^{26}Al spectra. Comparison among the ^{26}Al spectra from different sky models is a consistent check for the ^{26}Al line shapes and flux in the Cygnus region.

Figure 4.3 displays three different sky maps for the Cygnus region ($65^\circ < l < 95^\circ$, $-13^\circ < b < 17^\circ$) to obtain ^{26}Al spectra using model fittings: the COMPTEL maximum entropy map, the COMPTEL MREM map, and a homogenous disk model employed for the Cygnus region. Three ^{26}Al spectra for Cygnus derived from model fittings with these three different sky models are shown in Figure 4.4. We detect ^{26}Al line emission from Cygnus with a significance level of $\sim 6\sigma$. The reported ^{26}Al flux does not vary significantly with the different models: $(7.3 \pm 1.1) \times 10^{-5}$ph cm^{-2} s^{-1} for the COMPTEl MaxEnt map; $(7.2 \pm 1.2) \times 10^{-5}$ph cm^{-2} s^{-1} for the COMPTEL MREM map; $(6.6 \pm 1.2) \times 10^{-5}$ph cm^{-2} s^{-1} for the homogenous disk model. These flux values are still consistent with previous results reported by COMPTEL and the early SPI data analysis.

^{26}Al line shapes obtained from three different models are also similar. The line width value is near the instrumental line width value (FWHM, $\sim$ 3.1 keV). We also derive the intrinsic ^{26}Al line width by fitting the spectra deconvolved with the SPI spectral response (see §3.2), and find an intrinsic FWHM 0.93 ± 0.82 keV for the COMPTEL MaxEnt map, 0.59 ± 0.53 keV for the MREM map. So the ^{26}Al line from Cygnus is also intrinsically narrow, with a typical ISM turbulent velocity of ≤ 200 km s^{-1} in this region. Fast-expanding bubbles are not the dominating ISM components in Cygnus.

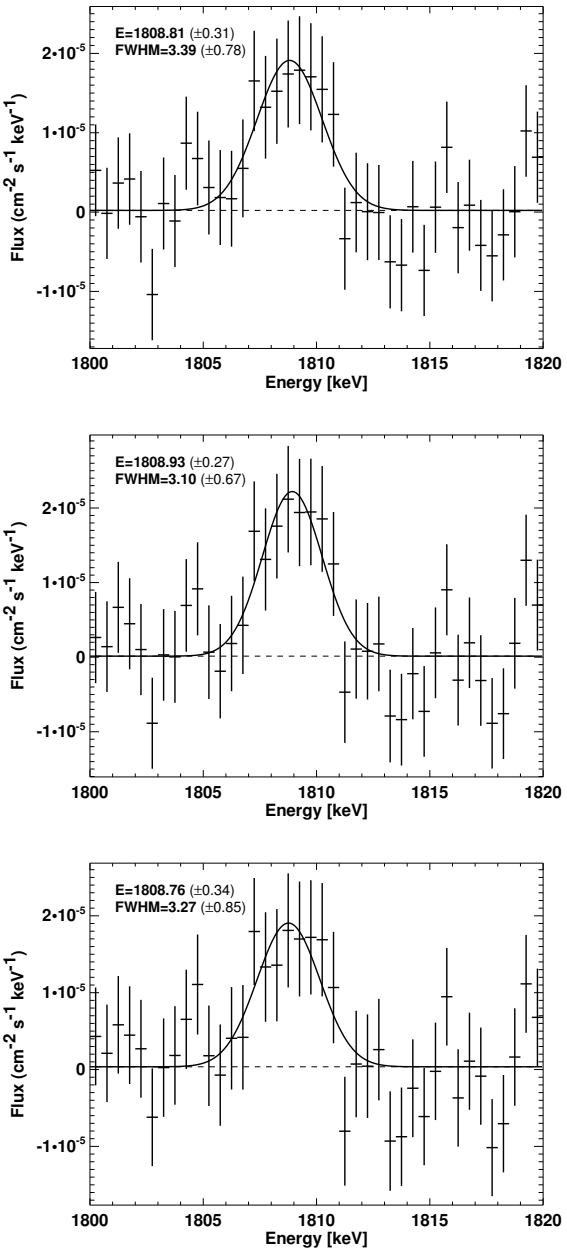

Figure 4.4: ^{26}Al spectra for Cygnus derived from model fittings using three different sky models: the COMPTEL MaxEnt model (top), with the derived ^{26}Al flux $F \sim (7.3 \pm 1.1) \times 10^{-5}$ph cm^{-2} s^{-1} for the region of $65^\circ < l < 95^\circ$, $-13^\circ < b < 17^\circ$; the COMPTEL MREM map (middle), $F \sim (7.2 \pm 1.2) \times 10^{-5}$ph cm^{-2} s^{-1}; the homogenous disk model (down), $F \sim (6.6 \pm 1.2) \times 10^{-5}$ph cm^{-2} s^{-1}.

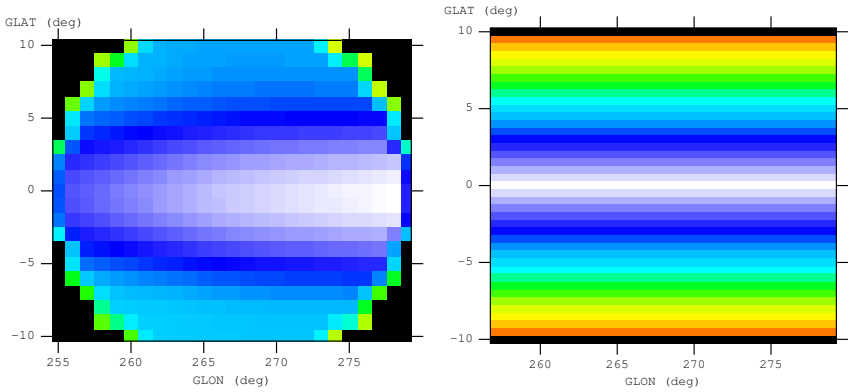

Figure 4.5: Two different sky models for the Vela region ($-104^\circ < l < -82^\circ$, $-10^\circ < b < 10^\circ$) used in model fitting: the COMPTEL MREM map (left), the homogenous disk model (right).

Even considering uncertainties of the FWHM, the broad line feature with an intrinsic FWHM of $\sim$ 3.3 keV reported by the early SPI data analysis is not held up by present results.

The value of the ^{26}Al line centroid energy in Cygnus is consistent with the laboratory value. For the case of the MREM model, a small blueshift of $\sim$ 0.27 keV may be indicated, but the energy shift is still well within the uncertainties (0.27 keV) of the measurements. Therefore, we conclude from present observations that there are no bulk motions of ^{26}Al sources in Cygnus toward or forward us.

4.2 Vela region

In the direction toward the Vela region, there exists a huge extended structure of H_α emission centered at $l \sim -100^\circ$, $b \sim -2^\circ$, the Gum Nebula, with an angular diameter of $\sim 36^\circ$ [Chanot and Sivan, 1983]. The mean distance of the nebula is approximately 300 – 450 pc [Brandt et al., 1971, Franco, 1990]. The Gum Nebula may be an interstellar bubble blown by stellar winds of the bright O5 Ia star ζ Puppis and the γ^2 Velorum system inside the nebula [Weaver et al., 1977], or an expanding SNR with an age of 1 Myr [Reynolds, 1976].

The most prominent structure toward the sky of the Gum Nebula is the Vela SNR (G263.9-3.3). This SNR is a remnant of a core-collapse supernova explosion about $\sim 10^4$ years ago estimated by the spin-down rate of the Vela pulsar [Manchester and Taylor, 1981], with a distance of $\sim 200 - 400$ pc [Cha et al., 1999, Green, 2006]. The soft X-ray observations by ROSAT revealed that the angular diameter of the Vela SNR is at least 7.3° [Aschenbach, 1993]. This nearby core-collapse SNR is the most promising ^{26}Al source toward the Vela region.

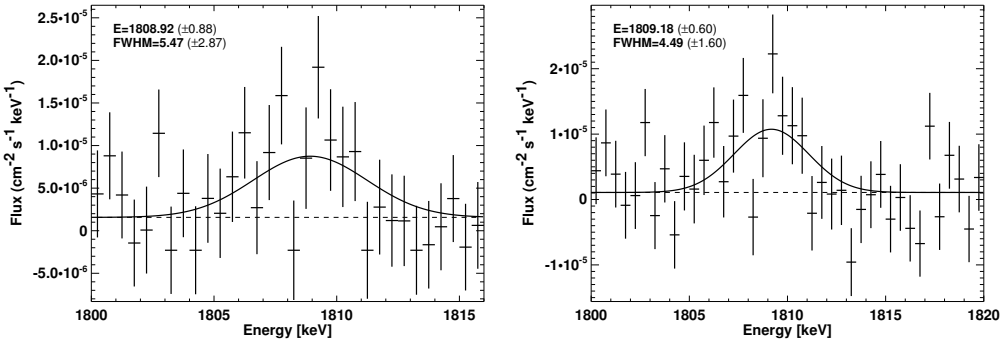

Figure 4.6: ^{26}Al spectra for Vela derived from model fittings using two different sky models: the COMPTEL MREM map (left), $F \sim (4.1 \pm 2.7) \times 10^{-5}$ph cm^{-2} s^{-1} for the region of $-104^\circ < l < -82^\circ$, $-10^\circ < b < 10^\circ$; the homogenous disk model (right), $F \sim (3.9 \pm 2.2) \times 10^{-5}$ph cm^{-2} s^{-1}.

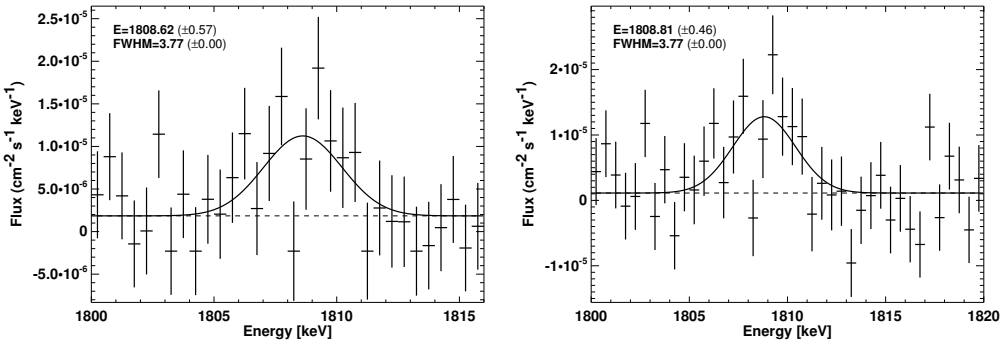

Figure 4.7: ^{26}Al spectra fitted with fixed Gaussian width for Vela derived from model fittings using two different sky models: the COMPTEL MREM map (left), $F \sim (3.7 \pm 1.2) \times 10^{-5}$ph cm^{-2} s^{-1} for the region of $-104^\circ < l < -82^\circ$, $-10^\circ < b < 10^\circ$; the homogenous disk model (right), $F \sim (4.1 \pm 1.2) \times 10^{-5}$ph cm^{-2} s^{-1}.

Besides the large Vela SNR, several small SNRs are also detected in the Vela region, e.g. Puppis A (G260.4-3.4), G261.9+5.5, and G272.2-3.2. The distance to Puppis A is about 2 kpc based on observations of radial velocities and proper motions of optical filaments [Winkler et al., 1988], which may be also a core-collapse SNR [Hui and Becker, 2006]. G261.9+5.5 is quite faint one with an estimated distance of $\sim 2.9 - 4.8$ kpc [Colomb and Dubner, 1980]. G272.2-3.2 discovered by ROSAT is a possible very young SNR (an estimated age $\sim$ 1800 years) with a distance of about 1.8 kpc. The discovery of the nearest young supernova remnant RX J0852.0-4622 / GRO J0852-4642 in the Galaxy toward the direction of the Vela region by ROSAT and COMPTEL has also been reported [Iyudin et al., 1994, Aschenbach et al., 1999]. Age and distance are estimated to be $\sim$ 680 years and $\sim$ 0.2 kpc by the X-ray diameter and the gamma-ray line flux of radioactive ^{44}Ti [Aschenbach et al., 1999]. These recent core-collapse supernova are also good candidate ^{26}Al sources in the Vela region. In addition, there are possible unresolved SNRs inside the giant molecular clouds toward the direction, so-called the Vela Molecular Ridge [Murphy and May, 1991] which is the most massive structure in this direction at a distance of $\sim 1 - 1.5$ kpc, also with a large number of O stars, IR sources, dust emission, and the brightest HII region of the southern sky.

An OB association Vel OB2 exists in this region, including many young stars with a mean distance of $\sim$ 410 pc [de Zeeuw et al., 1999]. The massive star binary system γ^2 Velorum in this group contains WR 11, the nearest known Wolf-Rayet star at $d \sim 260$ pc [van der Hucht et al., 1997].

In a word, the Vela region includes some active nearby star formation regions. ^{26}Al emission can be detected toward this region [Oberlack et al., 1994]. COMPTEL has detected the 1809 keV gamma-ray line emission from the Vela region, which may be associated with the Vela SNR [Diehl et al., 1995b] or γ^2 Velorum [Oberlack et al., 2000]. The measured ^{26}Al flux is $(3.6 \pm 1.2) \times 10^{-5}$ph cm^{-2} s^{-1}.

Here we study the spectral information of ^{26}Al line in the Vela region with SPI. The ^{26}Al source candidates described above, e.g., the Vela SNR, WR 11, other SNRs, are located in the direction of $-104^\circ < l < -82^\circ$, $-10^\circ < b < 10^\circ$. So we split the sky model into two parts, one covering the Vela region ($-104^\circ < l < -82^\circ$, $|b| < 10^\circ$) and the rest. Then we can derive the two ^{26}Al spectra of Vela and the inner Galaxy by model fitting using two sky maps simultaneously.

Two different sky models for the Vela region have been used in model fitting for a comparison (see Figure 4.5): the COMPTEL MREM map and the homogenous disk model. ^{26}Al spectra for the Vela region derived from model fitting using two different sky models are shown in Figures 4.6 and 4.7.

In Figure 4.6, we fit the ^{26}Al spectra with a flat continuum background plus a Gaussian line profile with free parameters of line position and width. The detection is not significant ($\sim 2\sigma$), and the measured ^{26}Al flux for Vela is $(4.1 \pm 2.7) \times 10^{-5}$ph cm^{-2} s^{-1} for the COMPTEL MREM map, and is $(3.9 \pm 2.2) \times 10^{-5}$ph cm^{-2} s^{-1} for the homogenous disk model. The derived ^{26}Al flux for Vela by SPI is still consistent with that obtained by COMPTEL [Diehl et al., 1995b] though the ^{26}Al signal for Vela is weak

with the present observations. The Gaussian FWHM is determined at $\sim 4.5 - 5.4$ keV, if taking the instrumental line width FWHM= 3.18 keV [Kretschmer, 2007], the derived intrinsic ^{26}Al line width is FWHM$>$ 3 keV. It could be a broad line feature though the signal is weak with large error bars for width in fit.

To reduce the effect of the large error bars for the line width on the ^{26}Al flux in Gaussian fit, we can let the line width be a fixed parameter in Gaussian fit to line profiles. In Figure 4.7, we present the ^{26}Al spectra fitted with fixed Gaussian width (FWHM = 3.77 keV) plus the flat continuum, where we assume the intrinsic ^{26}Al width in Vela as FWHM $\sim$ 2 keV. The derived ^{26}Al line flux is $(3.7 \pm 1.2) \times 10^{-5}$ph cm^{-2} s^{-1} for the COMPTEL MREM map, and is $(4.1 \pm 1.2) \times 10^{-5}$ph cm^{-2} s^{-1} for the homogenous disk model, with a significance level of $\sim 3\sigma$. The flux is consistent with COMPTEL results, but is lower than the reported value by the early analysis of SPI data [Schanne et al., 2007]. The ^{26}Al line centroid energy is well within the laboratory value.

We have assumed an intrinsic ^{26}Al line width of 2 keV for the Vela region in the line fit. The broad ^{26}Al line feature for the Vela region indicates that the environment and kinematics of ^{26}Al sources in Vela can be quite different from those in large scales of the inner Galaxy. In the Vela region, several recent supernova explosions, and stellar winds from WR 11 could lead to expanding bubbles which probably dominate the interstellar medium of ^{26}Al sources from present observation limits on the line profile. Then average turbulent velocities of ^{26}Al sources may reach $\sim 200 - 300$ km s^{-1} in the Vela region. Anyway, this issue need the further studies with more SPI data.

4.3 Sco-Cen region

The nearest site of massive star formation, the Scorpius-Centaurus-Lupus region(hereafter the Sco-Cen region), is about 100 – 150 pc from the Sun. Nearby young stars are seen mostly in the Southern Hemisphere, which is related to recent massive star formation in Sco-Cen OB association that consists of three sub-regions: Upper Scorpius (US), Upper Centaurus Lupus (UCL), and Lower Centaurus Crux (LCC), each distinguishable by different sky positions, age [de Geus et al., 1989], and kinematics (de Zeeuw et al. 1999, see Figure 4.8).

The closest of the three sub-regions is Lower Centaurus-Crux (LCC) with an estimated distance of $\sim$ 120 pc [de Zeeuw et al., 1999]. The age of LCC is thought to be 10– 20 Myr [de Geus et al., 1989]. LCC is located toward the direction of the Galactic plane ($-70^\circ < l < -40^\circ$), and may contribute to ^{26}Al line emission observed by COMPTEL and SPI in the plane (see §3.6).

US and UCL are located at latitudes above the Galactic plane. The mean distance of UCL is $\sim$ 140 pc, with an age of $\sim$ 10 Myr [de Zeeuw et al., 1999, de Geus et al., 1989]. UC is the youngest one with an age of $\sim 5 - 10$ Myr. Its mean distance is $\sim$ 145 pc [de Zeeuw et al., 1999, de Geus et al., 1989]. The rho Ophiuchus star forming region is located near the center of this group (Figure 4.8). UC is just located in the

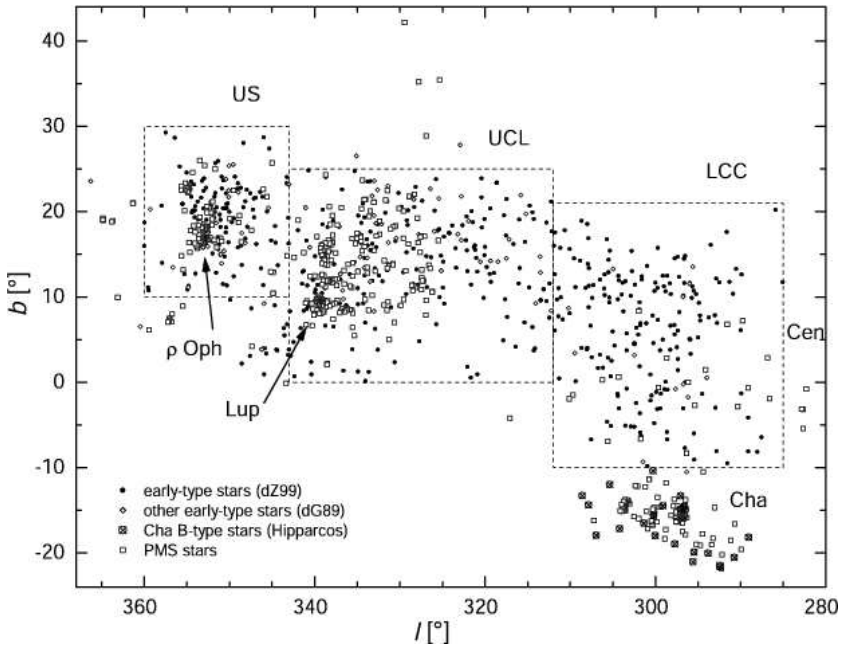

Figure 4.8: Distribution of young stars including pre-main sequence stars (PMS) and young early-type stars in Sco-Cen region (from Sartori et al. 2003). Three sub-groups, UC, UCL and LCC are notified with the dashed-line boxes. The Chamaeleon OB association could be an extension of the Sco-Cen one. The positions of the rho Ophiuchus active star formation region and the Lupus cloud complex are also marked.

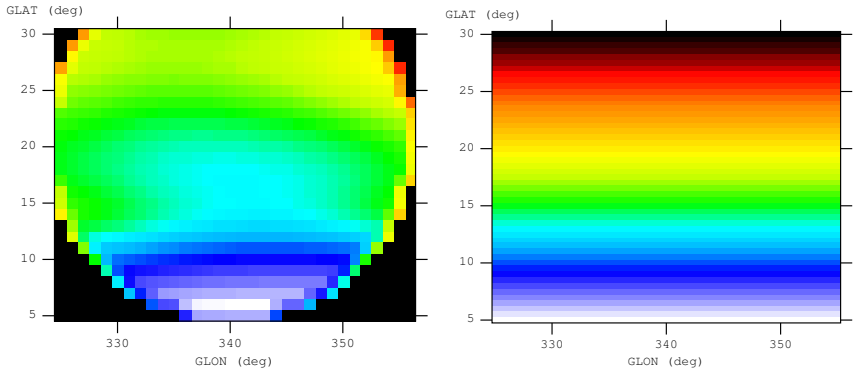

Figure 4.9: Two different sky models for the Sco-Cen region ($-35° < l < -5°$, $5° < b < 30°$) used in model fitting: the COMPTEL MREM map (left), the homogenous disk model (right).

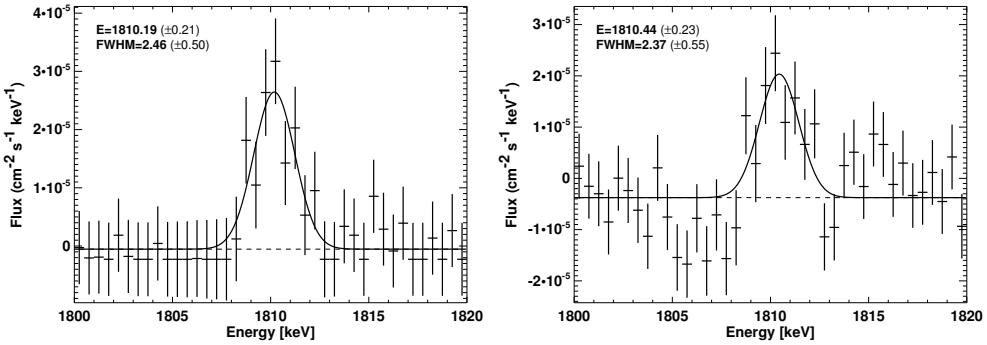

Figure 4.10: ^{26}Al spectra for Sco-Cen derived from model fittings using two different sky models: the COMPTEL MREM map (left), $F \sim (6.7 \pm 2.0) \times 10^{-5}$ph cm^{-2} s^{-1} for the region of $-35^\circ < l < -5^\circ$, $5^\circ < b < 30^\circ$; the homogenous disk model (right), $F \sim (6.0 \pm 1.9) \times 10^{-5}$ph cm^{-2} s^{-1} . Both spectra have shown the significant blueshifts of ~ 1.5 keV relative to the ^{26}Al line centroid in laboratory.

direction above the Galactic center ($l \sim -5^\circ, b \sim 18^\circ$), so the ^{26}Al emission structure in this direction observed by COMPTEL (see Figure 1.6, Plüschke 2001) is most probably attributed to the UC OB association.

Tachihara et al. [2001] have surveyed more than 500 deg^2 around the Sco-Cen region in ^{12}CO, and revealed the molecular gas distribution in this region. A total mass of $\sim 10^4$ $M_\odot$ and ~ 100 of small clouds have been detected as the Lupus cloud complex. In addition, there is an expanding HI shell centered in Upper-Sco, and the Lupus cloud complex exists between the shell and the Upper-Cen-Lup. The young star clusters are located at the edge of the shell, which suggests triggered star formation.

Here, we will study the spectral information of ^{26}Al sources toward the Sco-Cen region with SPI. The studied region concentrates on two groups, US and UCL, located in latitudes of $b > 5^\circ$, which could be resolved from the ^{26}Al contributions of the Galactic disk. To derive the ^{26}Al spectra of Sco-Cen in model fittings, we use two submaps: one for Sco-Cen defined as $-35^\circ < l < -5^\circ$, $5^\circ < b < 30^\circ$ and the rest of the sky to fit the data. Two sky distribution models are applied: the COMPTEL MREM map and the homogenous disk model (Figure 4.9). The ^{26}Al spectra for Sco-Cen from two sky models are presented in Figure 4.10. We have detected ^{26}Al from Sco-Cen with a significance level of $\sim 4\sigma$. The measured flux is $(6.7 \pm 2.0) \times 10^{-5}$ph cm^{-2} s^{-1} for the COMPTEL MREM map and $(6.0 \pm 1.9) \times 10^{-5}$ph cm^{-2} s^{-1} for the homogenous disk model. The ^{26}Al line detected toward the latitude region of $-60^\circ < l < 0^\circ, 5^\circ < b < 20^\circ$ in Figure 3.31 (§3.7) would be attributed to Sco-Cen.

Both the ^{26}Al spectra from two sky models show the significant blueshifts. The line centroid has a blueshift of $\sim 1.5 - 1.7$ keV relative to the laboratory value. This shift reflects the quite interesting dynamics of the ^{26}Al ejecta in the Sco-Cen region. The ^{26}Al

sources in Sco-Cen are dominated by the component of ^{26}Al ejecta with a bulk velocity of 200 ± 120 km s^{-1} toward us. Our studies imply that the very nearby ^{26}Al sources have a quite different behavior in dynamics from the large scale feature in the inner Galaxy. These nearby ^{26}Al sources are strongly affected by stellar winds of massive stars and ejecta of supernova explosions, and are also relatively easily been detected and resolved by the present observations.

5 Diffuse ^{60}Fe emission in the Galaxy by SPI

^{60}Fe is an unstable nucleus whose terrestrial half-life is $\simeq 1.5 \times 10^6$ years, and it is located at the neutron rich side of the "valley of stable isotopes" (also see Figure 1.11). The ^{60}Fe isotope is synthesized in neutron capture reactions from the ^{56}Fe isotope which is abundant from former equilibrium nucleosynthesis of ^{56}Ni and its decay, Such *s*-process is expected to occur in stellar regions with efficient neutron-liberating reactions, e.g., ^{13}C and ^{20}Ne α captures, hence in the O/Ne burning shell and bottom of He burning shell of core-collapse supernovae, and the He burning shell inside massive stars (more details in §1.7).

The decay chains of ^{60}Fe are shown in Figure 5.1. ^{60}Fe firstly decays to ^{60}Co, with emitting γ-ray photons at 59 keV, and then decays to ^{60}Ni, with emitting γ-ray photons at 1173 and 1333 keV. The gamma-ray efficiency of the 59 keV transition is only $\sim 2\%$ of those at 1173 and 1333 keV, so the gamma-ray flux at 59 keV is much lower than the fluxes of the high energy lines. The 59 keV gamma-ray line is very difficult to be detected with present missions. Measurements of the two high energy lines have been the main scientific target to study the radioactive ^{60}Fe isotope in the Galaxy.

^{60}Fe has been found to be part of meteorites formed in the early solar system [Shukolyukov and Lugmair, 1993]. The inferred ^{60}Fe /^{56}Fe ratio for these meteorites exceeded the interstellar-medium estimates from nucleosynthesis models, which led to suggestion that the late supernova ejection of ^{60}Fe occurred before formation of the solar system [Tachibana and Huss, 2003, Tachibana et al., 2006]. Yet, this is a proof for cosmic ^{60}Fe production, accelerator-mass spectroscopy of seafloor crust material from the southern Pacific ocean has revealed an ^{60}Fe excess in a crust depth corresponding to an age of 2.8 Myr [Knie et al., 2004]. From this interesting measurement, it is concluded that a supernova explosion event near the solar system occurred about 3 Myr ago, depositing some of its debris directly in the earth's atmosphere. All these measurements based on material samples demonstrate that ^{60}Fe necleosynthesis does occur in nature. It is now interesting to search for current ^{60}Fe production in the Galaxy through detecting radioactive-decay γ-ray lines.

Many experiments and efforts were made (also see Table 5.2) to measure the ^{60}Fe gamma-ray emission. The first detection of ^{60}Fe lines was provided by HEAO-3, the ^{60}Fe flux from the inner Galaxy region ($-30^\circ < l < 30^\circ$) is $\sim (5.3 \pm 4.3) \times 10^{-5}$ ph cm^{-2} s^{-1} rad^{-1} [Mahoney et al., 1982]. The SMM Gamma-Ray Spectrometer reported a ^{60}Fe flux of 2.9 ± 2.5 10^{-5} ph cm^{-2} s^{-1} rad^{-1} [Leising and Share, 1994]. OSSE aboard the COMPTON Observatory gave a ^{60}Fe flux of 6.3 ± 4.5 10^{-5} ph cm^{-2} s^{-1} rad^{-1} [Harris et al., 1994, 1997]. And COMPTEL aboard the COMPTON Obser-

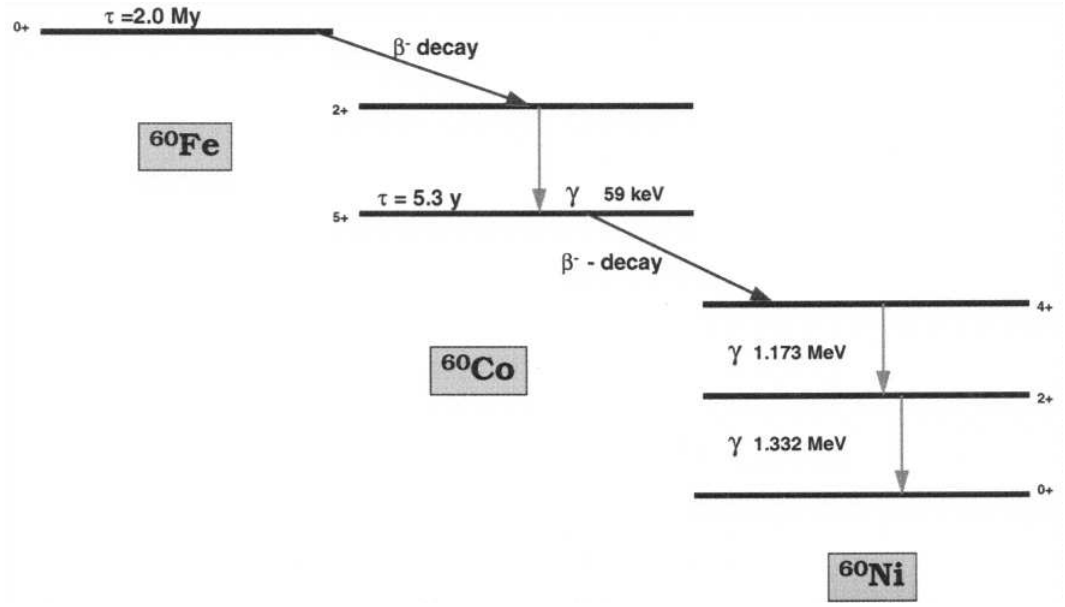

Figure 5.1: The decay scheme of ^{60}Fe . The mean lifetime is 2×10^6 years. The gamma-ray flux at 59 kev line is $\sim$ 2% of those at 1173 and 1333 keV.

vatory also reported a ^{60}Fe flux limit of $1.2\times\ 10^{-4}$ ph cm^{-2} s^{-1} rad^{-1} (2σ, Diehl et al. 1997). The Gamma-Ray Imaging Spectrometer (GRIS) reported an upper limit for the ^{60}Fe flux of $6.8\times\ 10^{-5}$ ph cm^{-2} s^{-1} rad^{-1} (2σ, Naya et al. 1998). Recently, RHESSI reported observations of the gamma-ray lines from ^{60}Fe with a signal of 2.6 σ significance, and an average flux of $(3.6 \pm 1.4) \times 10^{-5}$ph cm^{-2} s^{-1} [Smith, 2004b] from the inner Galaxy. The analysis of the first year of data from the SPI spectrometer on INTEGRAL spacecraft resulted in a similarly marginally-significant detection of these γ-ray lines from ^{60}Fe ($\sim$ 3σ, Harris et al. 2005), with an average line flux of $(3.7 \pm\ 1.1) \times 10^{-5}$ph cm^{-2} s^{-1} from the inner Galaxy.

SPI has accumulated more data since then, here we analyze 3 years of data, aiming at a consolidation of the INTEGRAL/SPI measurement of two ^{60}Fe gamma-rays at 1173 and 1333 keV.

5.1 Data preparation and analysis

As described in Chapter 2, we establish databases for single and multiple events (SE and ME), in spectral ranges with 1 keV bin size in $\sim$ 20 keV bands around each of the ^{60}Fe lines, and in adjacent energy bands for determination of instrumental background. For the science analyses of two ^{60}Fe lines, we use the data with the energy ranges around the two γ-ray lines extend from 1153 - 1193 keV and 1313 - 1359 keV. The raw

data spectra around two lines are presented in Figure 5.2. Strong instrumental lines dominate the raw spectra.

For the background modelling from the adjacent continuum, we use 1163 - 1169 keV plus 1177 - 1184 keV, and 1318 - 1328 keV plus 1336 - 1349 keV energy bands, respectively. For the case of 1333 keV line, since the strong instrumental line at 1337 keV blends with the ^{60}Fe line, we have include two strong instrumental lines (at 1337 and 1347 keV, both produced by ^{69}Ge electron captures, see Figure 5.2) in the selected adjacent energy bands. Our aims are to reduce the contamination of the instrumental line at 1337 keV. From orbits 17 to 359, a total observation time of $\sim$ 24 Ms is thus obtained, with a data set consisting of 14623 pointings with one spectrum per each detector and event type.

In background modelling, first the detector-by-detector count rates in the four continuum bands are fitted by the GEDSAT time series to construct an 'adjacent-energies' background template for each ^{60}Fe line. Other components modelling the instrumental line contribution are also required.

The most important radioactive background line component for our analysis is the emission from ^{60}Co decay inside the instrument, whose two lines at 1173 and 1333 keV are actually part of the celestial ^{60}Fe decay chain we want to measure. The convolution of the GEDSAT CR source tracer with an exponential function e^{-t/τ_0} (see §2.3), in which the decay time τ_0 is that of ^{60}Co (7.6 yr), is expected to give a good background model for energy bins containing contributions from these lines, i.e. around 1173 and 1333 keV. A second possible radioactive contaminant may be the strong ^{69}Ge K-shell electron capture line (1337 keV) which blends into the 1333 keV ^{60}Fe line; its lifetime is 2.35 days. Because the decay time is short, the convolution of the GEDSAT tracer with the exponential function ($\tau_0 = 2.35$ days) is similar to the GEDSAT tracer itself, therefore we just take the GEDSAT rates as a background component tracer for this strong instrumental line feature.

Then the set of detector-by-detector spectra per pointing in 1 keV bins covering the $\sim$ 20 keV intervals around and including the ^{60}Fe lines are fitted to the sum of adjacent continuum template, plus the radioactivity template for ^{60}Co, plus an additional GEDSAT template to capture an additional prompt background. Finally, we orthogonalize the three different background model components for an improved convergence of the fitting (see §2.3). We display examples of three background-component spectra for both the 1173 keV line and the 1333 keV cases (Figure 5.3). All these three background spectra show significant line features around the ^{60}Fe line energy ranges, confirming new and independent contribution of each background component to the model fitting.

Separate model fittings are made for each of the Fe lines and for SE and ME, respectively. The residuals after the model fitting are shown in Figure 5.4 (residuals with the time) and Figure 5.5 (with the energies) for each of the two lines. Representing our data sets with background-models only, we then obtain reduced χ^2 values of 1.185 and 1.194 for the 1173 and 1332 keV line bands (SE, 277824 *d.o.f*), and 0.665 and 0.663 for

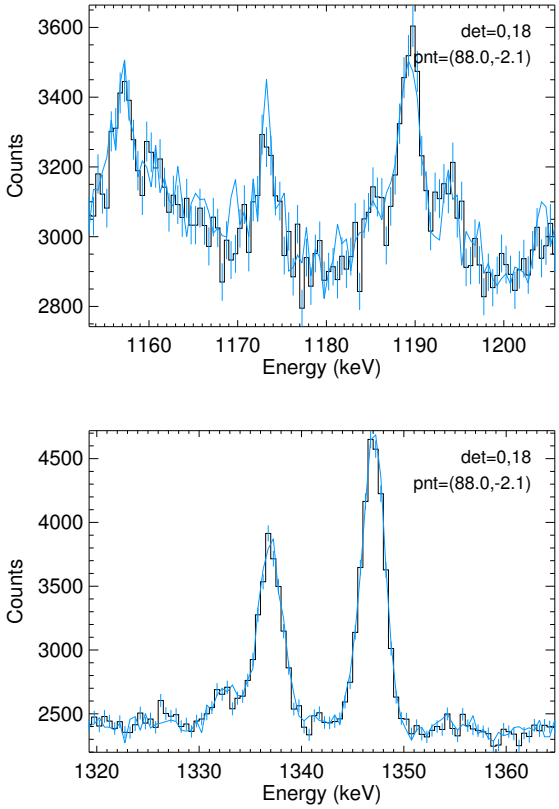

Figure 5.2: Raw data spectra around the energies of two ^{60}Fe lines in one-INTEGRAL-orbit observations (3 days), representing the instrumental lines and continuum background. For the 1173 keV case (above), three strong instrumental lines are obvious: ^{44}Sc (1157 keV), ^{60}Co (1172.9 keV), ^{182}Ta (189.4 keV), and the ^{60}Co line blends with the ^{60}Fe line [Weidenspointner et al., 2003]. For the 1333 keV case (below), the ^{60}Co background line (1332.5 keV) and the other strong instrumental line of ^{69}Ge (1336.8 keV) blend with the ^{60}Fe line, a instrumental line at 1347 keV also comes from ^{69}Ge electron captures [Weidenspointner et al., 2003].

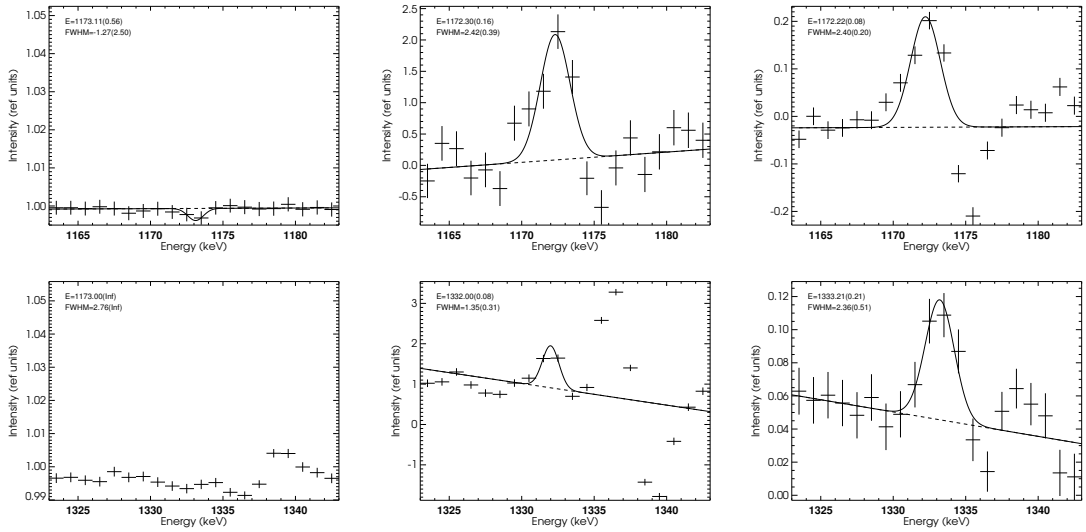

Figure 5.3: Spectra of three background components for the 1173 keV line and the 1333 keV cases: adjacent- energy-band template (left); GEDSAT tracer(middle): ^{60}Co radioactivity build-up (right). The line intensity is given in relative units (coefficients in fittings).

the 1173 and 1333 keV line bands (ME, 615038 *d.o.f.*), respectively. Note that for the low number of counts in ME spectra, χ^2 statistics does not apply here. Therefore, in our model fitting approach (both for SE and ME cases, see §2.5), we have used Poissonion statistics and the likelihood function.

These fits produce sky brightness amplitudes per energy bin. If background models are adequate, the continuum energy bins outside the ^{60}Fe lines should show sky amplitudes statistically consistent with zero sky brightness. Non-zero sky brightness should show up in the form of lines with a shape conforming to the instrumental line width, possibly broader if the celestial line energy is broadened already (as had been discussed for ^{26}Al, see Chapter 3 and Diehl et al. 2006c). Due to the low intensity of expected ^{60}Fe emission, we do not attempt to derive line shape information at all, and rather derive the ^{60}Fe line amplitude by fitting a Gaussian with fixed instrumental width to the *spimodfit* result spectra, determining amplitudes and line centroids in this way. From strong nearby instrumental lines (e.g. the instrumental line at 1107 keV), we determine that a Gaussian with a width of 2.76 keV is an adequate model for narrow lines in the regime of the ^{60}Fe lines; we use this shape to determine ^{60}Fe line parameters from the *spimodfit* result spectra. For a consistent celestial signal from ^{60}Fe, the lines should be around the ^{60}Fe decay energies of 1173 and 1333 keV and equal (within errors) in amplitudes for all four data sets.

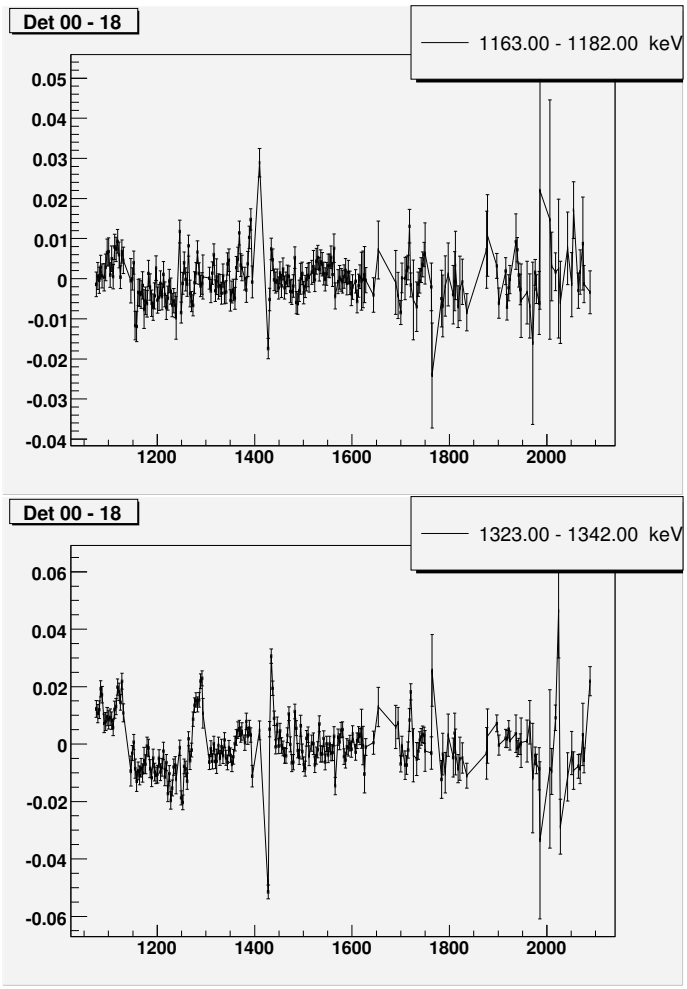

Figure 5.4: Residuals of counts after fitting in different projections for SE databases (in units of counts s^{-1}). The upper (1173 keV) and lower (1333 keV) figures show the residuals versus time (days of the Julian Date, starts at 1 Jan 2000), where counts per pointing have been re-binned into 3-day intervals for clarity. Residuals around zero confirm that our background models are adequate, with $\chi^2/d.o.f.$ in model fittings: 1.182 (SE) and 0.670 (ME) for the 1173 keV line; 1.191 (SE) and 0.667 (ME) for the 1333 keV line.

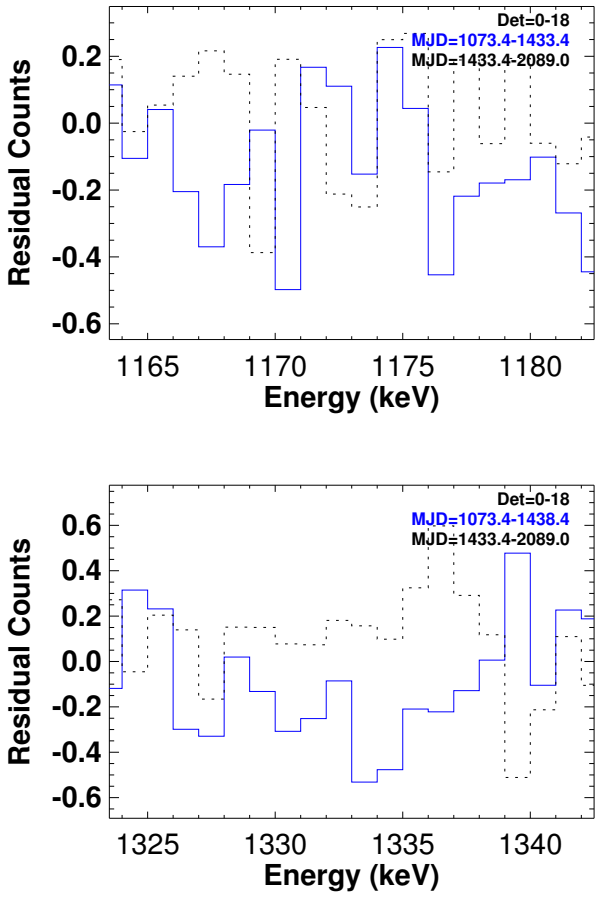

Figure 5.5: The upper (1173 keV) and lower (1333 keV) figures present the residuals (in units of counts s^{-1} keV^{-1}) projected with the energy for SE cases. For the 1333 keV line case, because of the strong instrumental ^{69}Ge line at 1337 keV, there still exist the large residuals around 1337 keV. The solid line represents residuals for the early data (e.g., from the Julian Date 1074 – 1434), and the dashed line for the recent data (from the Julian Date 1434 – 2089).

5.2 Observations of two ^{60}Fe lines at 1173 and 1333 keV in the Galaxy

5.2.1 Detections of ^{60}Fe from the inner Galaxy

^{26}Al and ^{60}Fe would share at least some of the same production sites, i.e. massive stars and supernovae (also see §1.6 and §1.7). In addition both are long-lived radioactive isotopes, so we have good reasons to believe their gamma-ray distributions are similar as well. Therefore we can adopt the sky distribution of ^{26}Al gamma-rays as our best model for celestial ^{60}Fe gamma-ray distribution. Thus, our fitted model consists of the sky intensity distribution of ^{26}Al from 9-year COMPTEL observations as a standard model (maximum entropy image, Plüschke et al. 2001), together with the background model based on measurements in energy bands adjacent to the ^{60}Fe lines and on background tracers (see above). From independently fitting the SE and ME data sets at 1 keV-wide energy bins in the energy ranges of the two lines of ^{60}Fe emission (1173 keV and 1333 keV), we obtain the four spectra from *spimodfit* (§2.5) shown in Figure 5.6 . We find excess amplitudes for the celestial component in each of the four spectra.

Residual background imperfections are small except for the instrumental line at 1337 keV. The continuum flux levels are close to zero within 10^{-5}ph cm^{-2} s^{-1} rad^{-1} keV^{-1}, without apparent energy dependence. Adding a linear slope to our spectral fit function does not improve the fit. Furthermore, the diffuse gamma-ray continuum emission around ^{60}Fe line energies in the inner Galaxy is $\sim 2 \times 10^{-6}$ph cm^{-2} s^{-1} rad^{-1} keV^{-1} from COMPTEL measurements [Strong et al., 1999], which is well below the error bars of spectral fluxes in Figure 5.6.

The ^{69}Ge line at 1337 keV has also been eliminated rather well, though not completely (about a fact of 4 compared with Harris et al. 2005). However, this strong instrumental line still leads to a spectral signal which is recognized clearly as an artifact and thus not confused with the celestial line.

We then determine the ^{60}Fe line parameters in these spectra fitting a continuum and Gaussians representing the SPI spectral response (§2.4). The width of the Gaussian profiles has been fixed at 2.76 keV. We thus obtain ^{60}Fe line positions and intensities from fitting the four spectra of Figure 5.6, where the total line flux for each line in the inner Galaxy region (e.g. $-30^\circ < l < 30^\circ$ and $-10^\circ < b < 10^\circ$) is determined from the intensity of our fitted Gaussians and from the normalization of the input sky map. We present line fluxes of two ^{60}Fe lines for the SE and ME data in Table 5.1, respectively. All line flux values are consistent within uncertainties. An average ^{60}Fe flux of these four spectra is about 4.6×10^{-5} ph cm^{-2} s^{-1} rad^{-1}.

A superposition of the four spectra of Figure 5.6 is shown in Figure 5.7. Line energies of the ^{60}Fe lines in the laboratory are 1173.23 and 1332.49 keV. Since the energy bin for the ^{60}Fe data is 1 keV, we cannot superpose two lines with the line centroid energies exactly at the laboratory values. For this superposition, we therefore define the zero of the relative energy axis at 1173 and 1333 keV, to derive the summed spectrum of

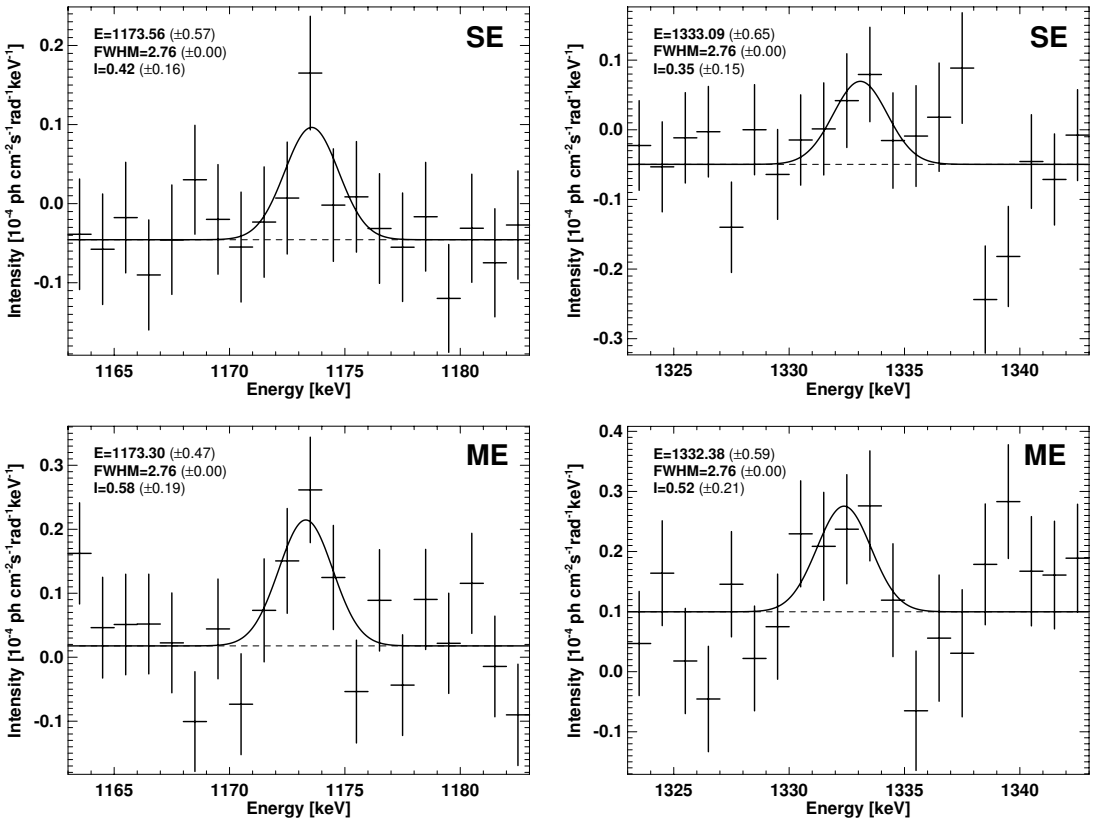

Figure 5.6: The spectra of two gamma-ray lines of ^{60}Fe from the inner Galaxy: 1173 keV and 1333 keV (from Wang et al. 2007). We have shown the results both from SE and ME databases. The data points are fitted with Gaussian profiles of fixed instrumental width (2.76 keV), and fixed continuum slope (flat), with $\chi^2/d.o.f.$ of fits: 1.06 (SE) and 1.09 (ME) for the 1173 keV line and 1.16 (SE) and 1.11 (ME) for the 1333 keV line. For the SE database, we find a line flux of $(4.2 \pm 1.6) \times 10^{-5}$ph cm^{-2} s^{-1} rad^{-1} for the 1173 keV line and $(3.5 \pm 1.5) \times 10^{-5}$ph cm^{-2} s^{-1} rad^{-1} for the 1333 keV line. For the ME database, the line flux is $(5.8 \pm 1.9) \times 10^{-5}$ph cm^{-2} s^{-1} rad^{-1} for the 1173 keV line and $(5.2 \pm 2.1) \times 10^{-5}$ph cm^{-2} s^{-1} rad^{-1} for the 1333 keV line (also see Table 5.1).

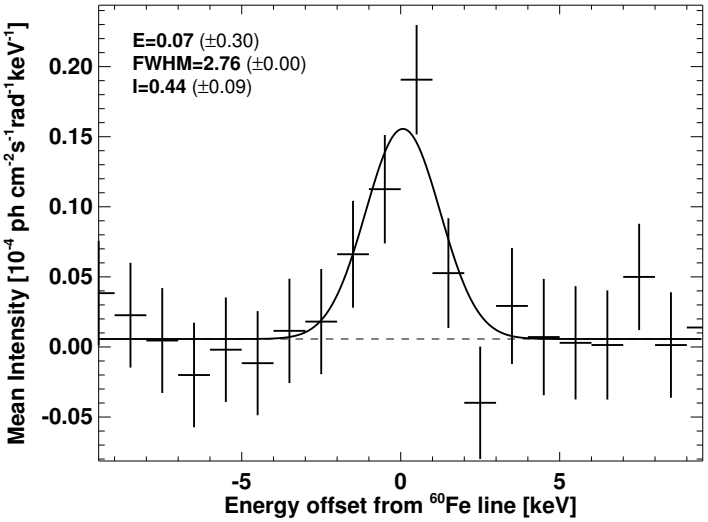

Figure 5.7: The combined spectrum of the ^{60}Fe signal in the inner Galaxy, superimposing the four spectra of Figure 5.7 (from Wang et al. 2007. In the laboratory, the line energies are 1173.23 and 1332.49 keV; here superimposed bins are zero at 1173 and 1333 keV. We find a detection significance of 4.9σ. The solid line represents a fitted Gaussian profile of fixed instrumental width (2.76 keV), and a flat continuum. The average line flux is estimated as $(4.4 \pm 0.9) \times 10^{-5}$ph cm^{-2} s^{-1} rad^{-1}.

Table 5.1: ^{60}Fe intensity in the inner Galaxy

	Flux (10^{-5} ph cm^{-2} s^{-1} rad^{-1})
1173 keV (SE)	4.2 ± 1.6
1173 keV (ME)	5.8 ± 1.9
1333 keV (SE)	3.5 ± 1.5
1333 keV (ME)	5.2 ± 2.1

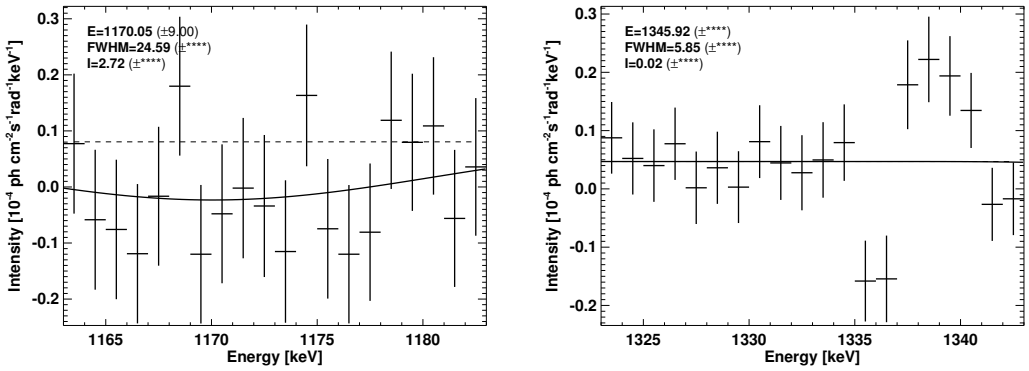

Figure 5.8: Spectra derived from model fitting using the sky distribution model of the COMPTEL ^{26}Al map with zero in the inner region of $-40^\circ < l < 40^\circ$, $-10^\circ < b < 10^\circ$. No flux excesses are found near the ^{60}Fe line energies (1173 and 1333 keV).

all ^{60}Fe signals. The energy deviation of 0.23/0.5 keV does not affect the superposed spectrum and derived ^{60}Fe flux. The line flux estimated from the combined spectrum is $(4.4 \pm 0.9) \times 10^{-5}$ph cm^{-2} s^{-1} rad^{-1}. Our significance estimate for the combined spectrum is $\sim 4.9\sigma$, adding uncertainties of the individual spectra in quadrature. This improves upon earlier ^{60}Fe signal reports from RHESSI [Smith, 2004a,b] and the first year of SPI data [Harris et al., 2005].

The signal of celestial ^{60}Fe is very weak, and marginally significant ($< 3\sigma$) in each of our four spectra. Therefore we cannot evaluate line shape information. The lines in our spectra appear well represented by Gaussians with instrumental widths (Figures 5.6 and 5.7), suggesting that the celestial ^{60}Fe lines are intrinsically-narrow lines. This would imply that broadening of ^{60}Fe lines from astrophysical processes is not significant; most of the ^{60}Fe may be distributed in a rather normal interstellar medium with turbulent velocities below $\sim$300 km s^{-1}. If we assume a line broadening of 1 keV, line fluxes would increase by $\sim 6\%$.

From our model-fitting approach (§2.5 & §5.1), in principle, the spectral result depends on the input sky map (also see Eq. 3.1). We do not know the real distribution of ^{60}Fe sources in the Galaxy, but we need a realistic model for these sources to derive correct spectra and line intensity. We use the COMPTEL ^{26}Al maximum entropy map as the standard sky model applied in the model fittings. While the maximum entropy map includes some structures and patches in the Galactic plane, we also used the COMPTEL ^{26}Al MREM map (Plüschke et al. 2001), a smoother one, in model fittings . As an alternative to the COMPTEL ^{26}Al maximum entropy and MREM sky maps, we also tried a different sky map: an exponential-disk model with scale radius 4 kpc, and scale height 180 pc. This should also be a good first-order representation of

^{26}Al emission from the inner Galaxy, and avoids the fine structure of the COMPTEL image which may partly arise from instrumental or analysis imperfections. We find that different input sky maps do not change the line profiles and intensities significantly (variations of the line fluxes are within 10% of the quoted values, i.e. below the uncertainties). If we use quite different and scientifically implausible sky distribution models, e.g., a point source at $\pm l = 20^\circ$, a bulge model (a Gaussian profile in the Galactic center), or the COMPTEL ^{26}Al map with zero in the inner region of $-60^\circ < l < 60^\circ$, $-10^\circ < b < 10^\circ$) in model fittings, and no flux excesses are found near the ^{60}Fe line energies (see examples in Figure 5.8).

5.2.2 Searching for ^{60}Fe signal from Cygnus and Vela

The Cygnus region is one of the most active nearby star formation regions in our Galaxy (see §4.1). The Vela region in the southern sky includes even more nearby massive stars, and several recent core-collapse supernova remnant (§4.2). The 1809 keV line emission of ^{26}Al from the Cygnus and Vela regions have been detected with SPI data (see details in Chapter 4). Hence, these two star-formation regions should be also good candidates for gamma-ray line emission from ^{60}Fe. Since the majority of Cygnus region star-clusters are young ($\sim$ 3 Myr), from population synthesis studies of the massive stars in the Cygnus region it has been suggested that the ^{60}Fe production is low, consistent with the small number of recent supernova events inferred for this region ($F(1173\ \mathrm{keV}) \sim 2 \times 10^{-6}$ph cm^{-2} s^{-1}, see Knödlseder et al. 2002).

We search for ^{60}Fe signal from these two regions using the similar methods described in Chapter 4. Splitting the model sky map (the MREM image of the Galactic 1809 keV emission, see Figure 1.7) into independent two components (the Cygnus region and the rest map, or the Vela region and the rest map) to fit the data, we do not see significant contributions from two regions. Our estimated upper limits for ^{60}Fe gamma-rays from the Cygnus ($65^\circ < l < 95^\circ$, $-13^\circ < b < 17^\circ$) and Vela ($256^\circ < l < 278^\circ$, $-10^\circ < b < 10^\circ$) regions are $\sim 1.1 \times 10^{-5}$ph cm^{-2} s^{-1} (2σ).

5.3 The ratio of ^{60}Fe /^{26}Al

^{26}Al and ^{60}Fe would share at least some of the same production sites, i.e. massive stars and supernovae (Timmes et al. 1995; Limongi and Chieffi 2006, also see Chapter 1). In addition both are long-lived radioactive isotopes, so we have good reasons to believe their gamma-ray distributions are similar as well. Therefore we adopt the sky distribution of ^{26}Al gamma-rays as our best model for celestial ^{60}Fe gamma-ray distribution. And we use an ^{26}Al distribution obtained in direct observations, from the 9-year COMPTEL data [Plüschke et al., 2001].

Different theoretical models have predicted the ratio of ^{60}Fe/^{26}Al [Timmes et al., 1995, Prantzos, 2004, Limongi and Chieffi, 2006]. Gamma-ray observations could de-

Table 5.2: Different measurements of ^{60}Fe flux from the inner Galaxy and ^{60}Fe/^{26}Al flux ratio

Experiments	^{60}Fe flux (10^{-5} ph cm^{-2} s^{-1} rad^{-1})	$F(^{60}\mathrm{Fe})/F(^{26}\mathrm{Al})$	references
HEAO-3	5.3 ± 4.3	0.09 ± 0.08	Mahoney et al. 1982
SMM	2.9 ± 2.5	0.1 ± 0.08	Leising & Share 1994
OSSE	6.3 ± 4.5	0.21 ± 0.15	Harris et al. 1997
COMPTEL	$< 12(2\sigma)$	0.17 ± 0.135	Diehl et al. 1997
GRIS	$< 6.8(2\sigma)$	$< 0.14(2\sigma)$	Naya et al. 1998
RHESSI	6.3 ± 5.0	0.16 ± 0.13	Smith 2004a
RHESSI	3.6 ± 1.4	0.10 ± 0.04	Smith 2004b
SPI	3.7 ± 1.1	0.11 ± 0.07	Harris et al. 2005
SPI	4.4 ± 0.9	0.148 ± 0.06	this work

tect these two isotopes and report the flux ratio of ^{60}Fe/^{26}Al which can be directly compared with theories. Therefore, the measurement of the gamma-ray flux ratio ^{60}Fe/^{26}Al is important for discussions of the astrophysical origins of the two radioactive isotopes, and the nuclear physics involved in models for their production (addressing the uncertain nuclear reaction cross sections and half-lives). For this purpose, we apply the same analysis method on the ^{26}Al data from the same observations, analyzing the 1785 — 1826 keV energy band (1 keV bins). We again generate a specific background model (from adjacent energy bands and the GEDSAT background intensity tracer), and apply the same input sky map (the 9-year COMPTEL ^{26}Al maximum entropy map) in model fitting the SE data. This produces a flux ratio of ^{60}Fe/ ^{26}Al in a self-consistent way, and yields $F(^{60}\mathrm{Fe})/F(^{26}\mathrm{Al}) = (14.8 \pm 6.0)\%$. Here, the uncertainty has been estimated from the respective model-fitting uncertainties of the two SE databases. Alternatively, from the combined spectrum of ^{60}Fe lines (Figure 5.7), and adopting the ^{26}Al intensity measured with SPI before ($F(^{26}\mathrm{Al}) = (3.04 \pm 0.31) \times 10^{-4}$ph cm^{-2} s^{-1} rad^{-1} for the inner Galaxy, see Diehl et al. 2006c), we obtain $F(^{60}\mathrm{Fe})/F(^{26}\mathrm{Al}) = (14.5 \pm 4.0)\%$.

Many experiments and efforts were made (see Table 5.2 and Figure 5.9) to measure the ^{60}Fe/^{26}Al flux ratio that was predicted by theory – we now provide the most significant detection to date. In Figure 5.9, we show the previous constraints on the flux ratio of ^{60}Fe/ ^{26}Al together with the result of this work, and compare the observational results with different theoretical predictions. The earliest observational limit was given from HEAO-3, $F(^{60}\mathrm{Fe})/F(^{26}\mathrm{Al}) = 0.09 \pm 0.08$, an upper limit being 0.27 [Mahoney et al., 1982] (in Figure 5.8, we chose to give limits at 2σ for all reported values below a significance of 3σ). Another limit was obtained with the SMM Gamma-Ray Spectrometer, a flux ratio of 0.1 ± 0.08, the upper limit being ~ 0.27 [Leising and Share,

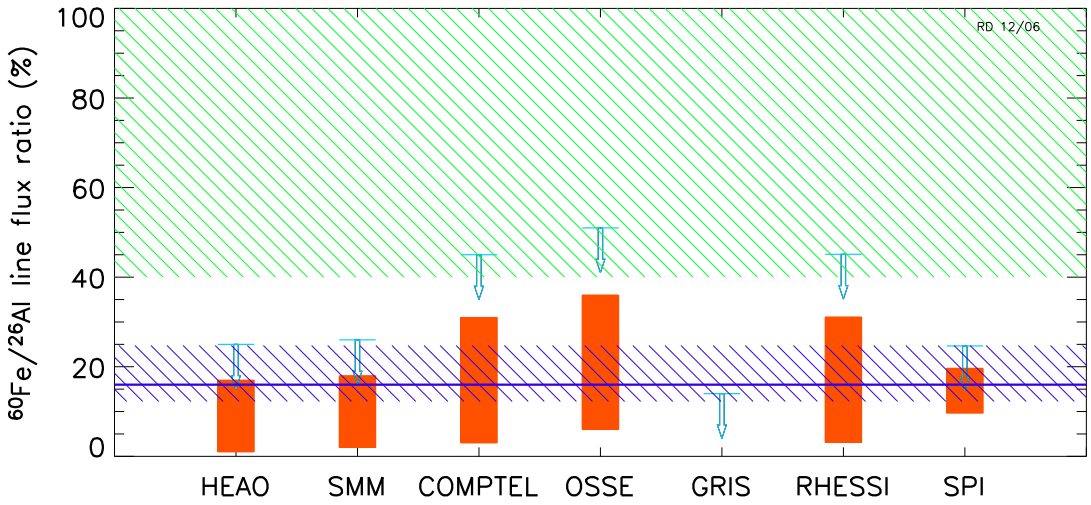

Figure 5.9: Flux ratio of the gamma-ray lines from the two long-lived radioactive isotopes ^{60}Fe/^{26}Al from several observations, including our SPI result (also see Table 5.2, from Wang et al. 2007), with upper limits shown at 2σ for all reported values, and comparison with the recent theoretical estimates (the upper hatched region from Prantzos 2004; the straight line taken from Timmes et al. 1995; the lower hatched region, see Limongi & Chieffi 2006). Our present work finds the line flux ratio to be $(14.8 \pm 6.0)\%$. See more details in the text.

1994]. OSSE aboard the COMPTON Observatory gave a flux ratio of 0.21 ± 0.15, and the upper limit is ~ 0.51 [Harris et al., 1994, 1997]. COMPTEL aboard the COMPTON Observatory also found ^{60}Fe gamma-rays, and reported a flux ratio value of ^{60}Fe/^{26}Al of 0.17 ± 0.135, which translates into an upper limit ~ 0.44 [Diehl et al., 1997]. The Gamma-Ray Imaging Spectrometer (GRIS) reported an upper limit for the ratio of < 0.14 (2σ, Naya et al. 1998). RHESSI has reported the first detection of ^{60}Fe gamma-ray lines, and gave a flux ratio 0.16 ± 0.13 for two-year data [Smith, 2004a]. The first year data of SPI gave a flux ratio 0.11 ± 0.07 [Harris et al., 2005], and the present analysis of the 3-year SPI data finds a flux ratio 0.148 ± 0.06 (also see Wang et al. 2007).

Theoretical predictions of the ratio of ^{60}Fe/ ^{26}Al have undergone some changes since Timmes et al. [1995] published the first detailed theoretical prediction. In their paper, they combine a model for ^{26}Al and ^{60}Fe nucleosynthesis in supernova explosions with a model of chemical evolution, to predict that the steady production rates are $(2.0 \pm 1.0) M_\odot$ Myr^{-1} for ^{26}Al, and $(0.75 \pm 0.4) M_\odot$ Myr^{-1} for ^{60}Fe, which corresponds to a gamma-ray flux ratio $F(^{60}\mathrm{Fe})/F(^{26}\mathrm{Al}) = 0.16 \pm 0.12$. This prediction would be consistent with our present measurements. Since 2002, theoreticians have improved various aspects of the stellar-evolution models, including improved stellar

wind models and the corresponding mass loss effects on stellar structure and evolution, of mixing effects from rotation, and also updated nuclear cross sections in the nucleosynthesis parts of the models. As a result, predicted flux ratios ^{60}Fe/ ^{26}Al rather fell into the range 0.8 ± 0.4 (see Prantzos 2004, based on, e.g. Rauscher et al. 2002, Limongi & Chieffi 2003) – such high values would be inconsistent with several observational limits and our SPI result (but see Woosley and Heger 2007 for comments on nuclear reaction rate updates). Recently, new ^{26}Al and ^{60}Fe yield models are presented [Limongi and Chieffi, 2006, Woosley and Heger, 2007], for stars of solar metallicity ranging in mass from $(11 - 120)M_{\odot}$. Limongi & Chieffi (2006) then combined their models of full stellar evolution up to and including the supernova with an adopted mass function to obtain a new prediction with latest nuclear reaction rate inputs. Their calculations yield a lower prediction for the ^{60}Fe/ ^{26}Al flux ratio of 0.185 ± 0.0625, which is again consistent with the observational constraints (see Figure 5.9).

In summary, uncertainties still exist, both in models and measurements of ^{60}Fe. On the theory side, stellar evolution in late stages is complex, nuclear reactions include neutron capture on unstable Fe isotopes, and explosive nucleosynthesis adds yet another complex ingredient. On the experimental side, cosmic ray induced ^{60}Co radioactivity in the instrument and spacecraft and the limitations of spatial resolutions and sensitivity are issues reflected in the substantial uncertainties in experimental values. With more INTEGRAL/SPI data to come, and also with the development of next-generation gamma-ray spectrometers/telescopes, gamma-ray observations hopefully can help with an independent view on the astrophysical model components.

6 Summary and perspectives

In this thesis, we have studied the long-lived radioactive sources, ^{26}Al and ^{60}Fe in the Galaxy with the INTEGRAL spectrometer (SPI). SPI has a high spectral resolution of 2.5 keV at 1 MeV, suitable for detections and studies of individual gamma-ray lines of radioactive isotopes, ^{26}Al and ^{60}Fe , and their line shapes. Details of line shapes help us to understand the dynamics of the ejected isotopes in the interstellar medium (e.g., nearby star formation regions, Knödlseder et al. 2004) and in large scales of the Galaxy [Diehl et al., 2006a,c].

^{26}Al and ^{60}Fe have similar astrophysical origins in the Galaxy. Their nucleosynthesis and ejection into the interstellar medium are dominated by massive stars, their evolution, winds, and their subsequent core-collapse supernova explosions. With its much longer half-life ($\sim 10^6$ years), ^{26}Al may propagate over significant distances of $\simeq$ few hundred pc, and accumulates in the interstellar medium from many stars and supernovae until injection and β-decay are in balance in the ISM. ^{26}Al emission appears as a diffuse Galaxy-wide glow [Mahoney et al., 1982, Plüschke et al., 2001]. The behavior of ^{60}Fe would follow that of ^{26}Al, since its half-life is similar, $\sim 2.2 \times 10^6$ years.

Large-scale characteristics of ^{26}Al emission in the inner Galaxy

Studying ^{26}Al line shape details in the Galaxy is one of the main goals in the SPI scientific analyses. With 4 years of SPI data, we detect ^{26}Al in the inner Galaxy ($|l| < 30^\circ$, $|b| < 10^\circ$) with a high significance level of $\sim 30\sigma$ (see §3.2). The measured ^{26}Al flux for the inner Galaxy is $(3.0 \pm 0.2) \times 10^{-4}$ ph cm^{-2} s^{-1} rad^{-1}. The ^{26}Al line centroid energy from the whole inner Galaxy is determined at 1809.0 ± 0.2 keV, which is still somewhat higher than the laboratory value for the ^{26}Al line of 1808.65 ± 0.07 keV. The ^{26}Al line for the inner Galaxy appears a narrow feature, with an intrinsic width value of 0.5 ± 0.4 keV. This measured line width of ^{26}Al from the inner Galaxy is consistent with expectation of Galactic rotation and modest interstellar-medium turbulence around the sources of ^{26}Al (turbulent velocities < 200 km s^{-1}). Our results are consistent with the previous reports by HEAO-C [Mahoney et al., 1982], RHESSI [Smith, 2003]. But a very broad line with a width ~ 5.4 keV as reported by GRIS [Naya et al., 1996] is clearly ruled out by our SPI measurement.

For our model-fitting approach to derive the spectra from SPI data (Eq. 3.1), the pre-assumed sky distribution models may affect the ^{26}Al flux and line shapes. As a consistent check and in order to estimate systematic uncertainties, we have compared ^{26}Al line spectra determined from the different tracers of ^{26}Al sources in the Galaxy in model fittings (see Table 3.1). Fifteen different sky maps (Figure 3.11) as

the distribution models of Galactic ^{26}Al have been used to derive ^{26}Al spectra. Using these different tracer maps, the fitted parameters of derived ^{26}Al spectra for the inner Galaxy: line centroid, flux and width, are all consistent with each other within error bars. Therefore, different sky distribution models do not affect ^{26}Al intensity and line shapes for the inner Galaxy significantly.

We can converse the determined ^{26}Al intensity into ^{26}Al mass in the Galaxy using assumed geometrical source distribution models. With the measured ^{26}Al flux of $\sim 3 \times 10^{-4}$ ph cm^{-2} s^{-1} rad^{-1} for the inner Galaxy, we obtain a Galactic ^{26}Al mass of $(2.7 \pm 0.6)\ M_{\odot}$, where we have taken the distance of the Sun to the Galactic center $R_0 =$ 8.5 kpc. This derived ^{26}Al mass leads to an isotopic ratio ^{26}Al /^{27}Al of $\sim 8.1 \times 10^{-6}$ in the interstellar medium. The derived ^{26}Al mass can be used to estimate the core-collapse supernova rate (SNRate) or the star formation rate (SFR) in the Galaxy. So we obtain a core-collapse supernova rate of $SNRate = 1.90 \pm 0.95$, corresponding to a SFR rate of $SFR = (3.8 \pm 1.9)\ M_{\odot}$ yr^{-1}, which is well consistent with the value derived by other methods (McKee and Williams 1997, also see Diehl et al. 2006a and references therein).

^{26}Al emission along longitudes

SPI can probe the spectral information toward parts of sky using multiple sub-maps covering these specified regions, which is the new scientific target for ^{26}Al studies. Studying the ^{26}Al line shapes for different parts of the sky is the main project in my thesis. Hence, we have carried out model fittings to obtain ^{26}Al spectra along the Galactic longitudes (§3.6) and along latitudes (§3.7), and for different nearby star-formation regions (see §4).

We first studied the ^{26}Al spectra for the 1st ($0^{\circ} < l < 60^{\circ}$) and 4th ($-60^{\circ} < l < 0^{\circ}$) quadrants. Brightness asymmetries for the two quadrants are found, and the flux ratio of the 4th quadrant to the 1st one is ~ 1.3 for the parts of $|l| < 60^{\circ}$ (Figure 3.16), and ~ 1.2 for the parts of $|l| < 30^{\circ}$ (Figure 3.17). The ^{26}Al line centroid energies show the shifts relative to the centroid energy of ^{26}Al line in the laboratory, 1808.66 keV: a minor redshift (~ 0.1 keV) in the 1st quadrant and a significant blueshift (~ 0.6 keV) in the 4th quadrant. We splitted the inner Galaxy ($|l| < 60^{\circ}$) into six 20°-bin parts along longitudes, and derive the ^{26}Al spectrum for each part. ^{26}Al line spectra can be still detected significantly for four 20° bin regions of $-40^{\circ} < l < 40^{\circ}$, and line energy shifts are also detected along the plane. The ^{26}Al line for the region $20^{\circ} < l < 40^{\circ}$ (the Sagittarius arm) shows a possible broad line feature. ^{26}Al fluxes for two outside regions ($40^{\circ} < |l| < 60^{\circ}$) are much lower than those of the inner regions.

Line energy shifts along the Galactic plane would be attributed to Galactic rotation. We have obtained ^{26}Al spectra along the longitudes including the Galactic center region to determine the line energy shifts of the left and right parts relative to the Galactic center for probing the Galactic rotation effect on ^{26}Al line centroid. ^{26}Al spectra for three regions are simultaneously determined ($|b| < 10^{\circ}$): $-40^{\circ} < l < -10^{\circ}$, $-10^{\circ} < l < 10^{\circ}$, $10^{\circ} < l < 40^{\circ}$. The ^{26}Al line centroid energy from the central interval

$-10^\circ < l < 10^\circ$ is not exactly at the laboratory value. Taking the ^{26}Al spectrum from $-10^\circ < l < 10^\circ$ as a reference, the line centroid energy shifts of ~ -0.16 keV ($10^\circ < l < 40^\circ$) and $\sim +0.62$ keV ($-40^\circ < l < -10^\circ$) are clearly observed (Figures 3. 22 and 3.23). In addition, we obtained the ^{26}Al spectrum for the Galactic center ($-5^\circ < l < 5^\circ, -10^\circ < b < 10^\circ$, Figure 3.24), with the line centroid determined at 1808.66 ± 0.23 keV. Then we used the ^{26}Al spectra derived from 6 segments in 20° longitude bins along the plane (Figure 3.18) to show the line energy shifts relative to the reference spectrum for the Galactic center (Figure 3.25). We have found a low redshift of ~ 0.1 keV for positive longitudes ($0^\circ < l < 40^\circ$) and a high blueshift of ~ 0.48 keV for $-20^\circ < l < 0^\circ$ and 0.9 keV for $-40^\circ < l < -20^\circ$. This asymmetry of energy shifts is not consistent with the present Galactic rotation models (Kretschmer et al. 2003, also see §3.8).

Significant ^{26}Al spectra are detected for the 20°-bin longitude intervals of the inner Galaxy ($|l| < 40^\circ$), and our model fitting could also allow for probing the spectra in the smaller regions. So we have tried to derive the ^{26}Al spectra for eight 10°-bin longitude intervals of 10° of the inner Galaxy simultaneously (Figures 3.19 and 3.20), however, the detection of the spectra for each region is not significant. Because the field view of SPI is wider than the scales of these sub-maps, contaminations between adjacent sub-maps could affect the spectra in model fittings, which leads to fluctuations of the fitted coefficients in off-line spectra and detections of ^{26}Al for each sub-map in low significance levels. One possible way to probe the ^{26}Al line properties in smaller scales is comparing the spectra with changes of longitude intervals by a step of 2.5° or 5°. The preliminary results on comparison of ^{26}Al line properties with changes of longitude sizes are presented (Figures 3.26–3.29) and discussed in §3.6.3. The implications are interesting and require further studies with more SPI data.

^{26}Al emission along latitudes

We have also derived ^{26}Al spectra along Galactic latitudes with SPI ($|l| < 60^\circ$). Possible ^{26}Al emission at latitudes of $|b| > 5^\circ$ should originate from local star-formation systems in the Gould Belt, while ^{26}Al at latitudes of $|b| < 5^\circ$ would be dominated by the large-scale origin in the Galactic disk/spiral arms. Weak ^{26}Al emission is detected in the positive latitude region of $5^\circ < b < 20^\circ$ with the line centroid blueshift of 0.7 ± 0.4 keV, but no ^{26}Al signal is detected in the negative latitude region of $-20^\circ < b < -5^\circ$ (see Figure 3.30). Further analysis of the latitude interval $5^\circ < b < 20^\circ$ found that no ^{26}Al is detected for the 1st quadrant, and ^{26}Al line emission for the 4th quadrant is significantly detected, with the blueshift of 0.8 ± 0.5 keV (Figure 3.31). This ^{26}Al emission could be attributed to the nearby Sco-Cen OB association. ^{26}Al emission for low latitudes ($|b| < 5^\circ$) is significantly detected as expected. The ^{26}Al line for the whole plane shows a narrow feature, with the line centroid energy of 1808.78 ± 0.08 keV. The asymmetry of ^{26}Al brightness for the 1st and 4th quadrants is also detected, and the ^{26}Al line centroid shows a redshift of 0.21 ± 0.27 keV for the 1st quadrant, and a blueshift of 0.54 ± 0.23 keV for the 4th quadrant, which is consistent with the expla-

nation of Galactic rotation. To probe the Galactic rotation effect on ^{26}Al spectra along the plane without contaminations of ^{26}Al emission from high latitudes, we derived ^{26}Al spectra for three longitude intervals of only low latitudes ($|b| < 5^\circ$): $10^\circ < l < 40^\circ$, $-10^\circ < l < 10^\circ$, $-40^\circ < l < -10^\circ$. The line centroid energy for the center region ($|l| < 10^\circ$) is determined at 1808.65 ± 0.27 keV, well within the laboratory value. Energy shifts of ^{26}Al line centroids are also observed: a small redshift of 0.11 ± 0.35 keV plus a large blueshift of 0.75 ± 0.27 keV. The asymmetry of energy shifts along the disk plane is still inconsistent with the expectation of Galactic rotation (Kretschmer et al. 2003, Kretschmer 2007, see §3.8), may be induced by other effects, e.g., the Bar structure or the contribution of nearby ^{26}Al sources.

^{26}Al emission of the Galaxy: simulations versus observations

SPI observations of ^{26}Al spectra in the Galaxy firstly confirm the dominant ^{26}Al origin in massive stars and supernovae, and also probe the dynamics of ^{26}Al ejecta from stellar winds and supernova explosions, and Galactic rotation effect on ^{26}Al line shapes. ^{26}Al intensity and line shapes can be simulated with the known distribution models of ^{26}Al sources in the Galaxy [Kretschmer, 2007]. Comparison between the simulated results and SPI observations will be a good constraint on ^{26}Al origin and distribution in the Galactic disk.

We have adopted a three-dimensional model for the space density of free electrons based on pulsar dispersion measurements [Cordes and Lazio, 2002] as the parent distribution of Galactic ^{26}Al , which also includes three different distribution models [Kretschmer, 2007]: (1) all components ; (2) all except the thick disk and the Galactic center ; (3) only the thin disk and spiral arms. The kinematics of ^{26}Al sources from stellar winds and supernova explosions in the local interstellar medium superimposed on Galactic rotation is considered in our simulations.

For comparison between simulations and SPI results, we integrate our simulated sky map of line energies and intensities over a region of interest, and then obtain resulting spectra for three longitude intervals of the inner Galaxy: $-5^\circ < l < 5^\circ$, $5^\circ < l < 40^\circ$, $-40^\circ < l < -5^\circ$ (see Figure 3.34, Kretschmer 2007). Simulated ^{26}Al spectra for the inner Galaxy show the narrow line features, with an intrinsic width value < 0.9 keV, which is consistent with the SPI constraints. No line centroid shifts for the Galactic center ($|l| < 5^\circ$) in all three distribution models are consistent with the SPI result. ^{26}Al line energy shifts due to Galactic rotation are symmetrical for positive and negative longitudes, the expected shift value is ~ 0.2 keV for the model of all components, ~ 0.3 keV for the model of all except the thick disk and the Galactic center and ~ 0.4 keV for the model of only the thin disk and spiral arms. However, the observed line centroid shifts of positive and negative longitudes is asymmetrical, ~ 0.1 keV for positive longitudes, and $\sim 0.5 - 0.9$ keV for negative ones. Inconsistence between the Galactic rotation expect and SPI observations suggested that some effects not considered in our simulations lead to the ^{26}Al line shift asymmetry, e.g., the Bar structure, and dynamics of nearby ^{26}Al sources. The ^{26}Al intensity ratio of the 4th

quadrant to the 1st one of the inner Galaxy can be obtained in simulations to compare with the SPI observation. For the model of all components and that of all except the thick disk and the Galactic center, ^{26}Al intensities for the 1st and 4th quadrants are nearly symmetrical, which is not consistent with our SPI results in §3.6.1. But for the model of only the thin disk and spiral arms, significant asymmetry appears, with a ^{26}Al intensity ratio of ~ 1.15 which meets the present observed limits. So the free-electron density model of only the thin disk and spiral arms would reflect the real distribution of Galactic ^{26}Al .

^{26}Al emission from star-formation regions

Detections of ^{26}Al from nearby star-formation regions are the good probe for the massive star origin of Galactic ^{26}Al and kinematics of ^{26}Al ejecta in ISM. We studied ^{26}Al spectra from these regions using model fittings with two sky maps covering the star-formation region and the rest. Then we have obtained ^{26}Al spectra from three nearby star-formation regions with the present SPI data (§4): Cygnus, Vela and Sco-Cen.

We derived the ^{26}Al spectrum for Cygnus ($65^\circ < l < 95^\circ$, $-13^\circ < b < 17^\circ$) with a significance level of $\sim 6\sigma$. A reported ^{26}Al flux is $\sim (7.0 \pm 1.2) \times 10^{-5}$ph cm^{-2} s^{-1}, which is consistent with the COMPTEL result. No shift of the line centroid is observed, and the ^{26}Al line shows the narrow feature, with an intrinsic line width < 2 keV. A typical ISM turbulent velocity is ≤ 200 km s^{-1} in the Cygnus region.

^{26}Al detection for the Vela region ($-104^\circ < l < -82^\circ$, $-10^\circ < b < 10^\circ$ is not significant ($< 3\sigma$). The ^{26}Al flux is determined at $(4.0 \pm 1.2) \times 10^{-5}$ph cm^{-2} s^{-1} which is consistent with the COMPTEL result. The ^{26}Al line in Vela appears a broad feature, without a line centroid shift. A Gaussian with the instrumental line width cannot fit the spectrum well, so we fit the spectrum with fixed Gaussian width (FWHM = 3.77 keV) after assuming the intrinsic ^{26}Al width in Vela as FWHM ~ 2 keV. A possible broad ^{26}Al line feature of Vela should require the further studies with more SPI data.

Sco-Cen is the nearest star-formation region from the sun. We obtain the ^{26}Al spectrum for Sco-Cen $-35^\circ < l < -5^\circ$, $5^\circ < b < 30^\circ$ with a significance level of $\sim 4\sigma$. A reported ^{26}Al flux for Sco-Cen is $(6.3 \pm 2.0) \times 10^{-5}$ph cm^{-2} s^{-1}. Importantly, The ^{26}Al spectrum shows a significant blueshift of ~ 1.5 keV relative to the laboratory value. This shift implies that ^{26}Al sources in Sco-Cen are dominated by the component of ^{26}Al ejecta with a bulk velocity of ~ 200 km s^{-1} toward us.

Diffuse ^{60}Fe emission in the Galaxy

Finally, We have reported the detection of ^{60}Fe decay gamma-ray lines in the Galaxy from 3 years of SPI observations. With our new measurements we detect both the 1173 keV and 1333 keV line of ^{60}Fe from SPI single and multiple-detector events. Combining our four spectra from independent model fits we obtain an ^{60}Fe signal from the Galaxy with a significance of 4.9σ. This improves upon our previous measurements (see Harris et al. 2005). The average ^{60}Fe line flux from the inner Galaxy region is $(4.4 \pm 0.9) \times 10^{-5}$ph cm^{-2} s^{-1} rad^{-1}, assuming intrinsically narrow lines and a sky

distribution equal to that of ^{26}Al as measured by COMPTEL (Plüschke et al. 2001). From the same observations and analysis procedure applied to ^{26}Al, we find a flux ratio of ^{60}Fe/ ^{26}Al of (14.8 ± 6.0)%. The ^{60}Fe signals are too weak to determine line shape details; it appears that a Gaussian with the width of the instrumental resolution can fit the data well. This would imply that broadening of ^{60}Fe lines from astrophysical processes is not significant; most of the ^{60}Fe may be distributed in a rather normal interstellar medium with turbulent velocities below $\sim$300 km s^{-1}. In order to investigate the variations over the Galaxy, we search for ^{60}Fe emission from the Cygnus and Vela regions, and do not find ^{60}Fe signals.

In this thesis, we have used the four-year SPI data for spectral analyses of ^{26}Al and ^{60}Fe in the Galaxy. INTEGRAL/ SPI will continue to accumulate more data for several years, which would cover more sky regions. With more SPI data, we could improve spectral resolution of ^{26}Al in the inner Galaxy and ^{26}Al spectra along the plane, and then confirm ^{26}Al line shapes for Cygnus, Vela and Sco-Cen, further obtain ^{26}Al spectra from some other nearby star-formation regions, like Orion and Carina. For ^{60}Fe studies, the significance level of detections for the inner Galaxy will be pushed forwards again, and possible differences of ^{60}Fe signals for the 1st and 4th quadrants can be probed with more SPI data. Finally, we can search for the ^{60}Fe gamma-ray signal from the 59 keV line using INTEGRAL/ IBIS data and SWIFT data, which might be a self-consistent check for ^{60}Fe studies.

SPI aboard INTEGRAL has a high spectral resolution but a very limited sensitivity over 0.1 – 2 MeV (see Figure 6.1). Presently the GLAST mission [Michelson, 2001], a third generation (after SAS-2/COS-B Bignami et al. 1975 and EGRET Kanbach et al. 1988) pair-creation telescope sensitive above 20 MeV, is scheduled to be launched in October 2007. In Figure 6.1, the point source sensitivity, i.e. the minimum detectable flux, for past, present (e.g., instruments aboard INTEGRAL), and future instruments in the low through high-energy regimes is shown. The lack of a sensitive instrument from 0.3 – 10 MeV is obvious. Therefore, it is timely to develop a second-generation γ-ray telescope in the Compton energy range to maintain the overall multi-wavelength sensitivity, which is so important for a full understanding of high-energy astrophysics.

Astronomy in the low- to medium-energy γ-ray range has always challenged the most advanced experimental techniques for two main reasons: (1) photon interaction cross-sections in the MeV range go through a minimum in their transition from the photoelectric effect ($\sim$ 100 keV) to pair creation ($\sim$ 10 MeV). In this so-called Compton range, the interactions are characterized by small energy deposits and long-range secondary radiation. It is therefore necessary to build a *deep* detector to achieve a reasonable efficiency and to finely segment the detector in order to record and trigger widely separated interactions of the scattered photons. (2) The nuclear energy levels of all detector and structural materials lie in the MeV range and are therefore easily excited by energetic particles. The result of this systematic *radio-activation* in orbit is a prolific γ-ray background of local origin which must be effectively discriminated against to achieve a useful sensitivity for astronomical targets.

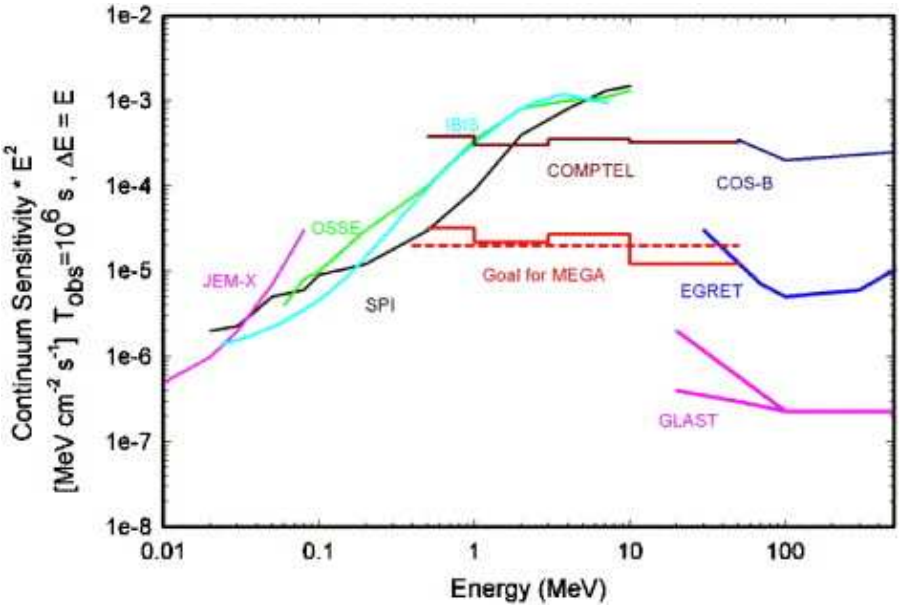

Figure 6.1: Sensitivity levels for selected hard X- and gamma-ray telescopes (10 keV – GeV). The lack of a present sensitive instrument from 300 keV – 10 MeV is evident. The goal for MEGA is set to be about one order of magnitude improvement over COMPTEL (dashed line). The histogram for MEGA shows preliminary results of a simulation for a MEGA space mission [Kanbach et al., 2005].

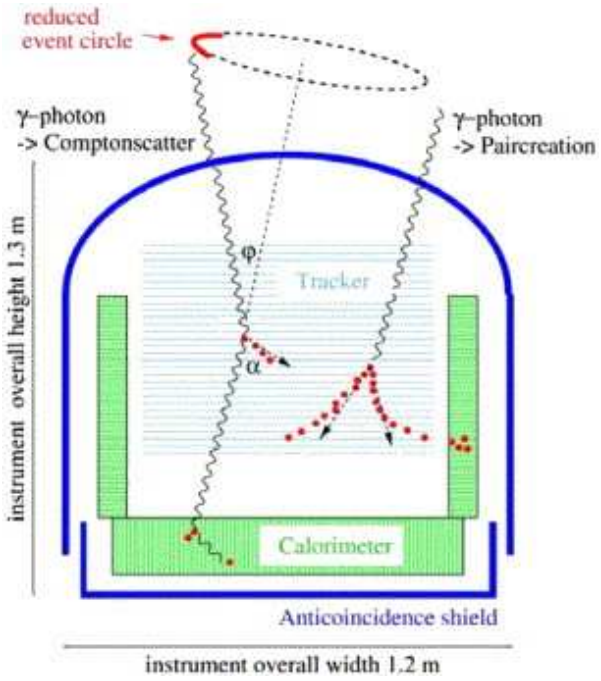

Figure 6.2: Schematic of the MEGA instrument (from Kanbach et al. 2005) and kinematics of gamma-ray interactions: Compton scatter or pair conversion of γ-ray photons.

Telescopes based on the detection of Compton- and pair-creation interactions have intrinsically large fields-of-view and are well suited as sky survey monitors and to map large-scale extended emissions. These extended sources of high-energy photons arise partly from interactions of cosmic-rays with interstellar gas, from dispersed radioactive isotopes (mainly ^{26}Al , ^{60}Fe , β^+-decay with following annihilation radiation), and possibly from the decay of dark matter in a galactic halo.

The sensitivity goal for the next MeV spacecraft mission should fall into an intermediate level, between the COMPTEL/INTEGRAL sensitivities and the extension of the GLAST sensitivity into the MeV range. It will likely revolutionize MeV astronomy in the manner that EGRET revolutionized astronomy at 100 MeV. To accomplish these goals with a medium-sized mission requires new designs beyond that of COMPTEL and EGRET. A new Compton/low-energy pair telescope for Medium Energy Gamma-ray Astronomy (MEGA) in the energy band 0.4 – 50 MeV, has been in development and test. MEGA functions in some ways similar to COMPTEL and EGRET, but also differs in many aspects. MEGA uses a stack of double-sided silicon strip detectors (DSSD) as a scattering and conversion tracking detector and finely pixelated CsI/PIN diode scintillation detectors for the absorption of the scattered radiation [Kanbach et al., 2005]. A schematic of the basic MEGA design is shown in Figure 6.2. Since MEGA has a small size and may still be an insufficient step for the future γ-ray line astronomy, other visionary MeV telescopes have also been proposed.

A visionary Advanced Compton Telescope (ACT) covering the energy range of 0.4 – 50 MeV has a goal sensitivity of $\sim 10^{-6}$MeV cm^{-2} s^{-1} in 10^6 s for continuum, corresponding to GLAST above 100 MeV, and a sensitivity for narrow lines of $\sim 10^{-7}$ph cm^{-2} s^{-1} in 10^6 s (Figure 6.3). ACT has a design principle similar to MEGA shown in Figure 6.2 with a larger size, then would have higher energy resolution [Boggs et al., 2003]. Another visionary European Gamma-Ray Imager (GRI) mission based on Laue lenses (the Bragg diffraction from crystals in transmission configuration) from 50 keV – 2 MeV is now under study for the ESA plan Cosmic Vision 2015-2025 [Knödlseder, 2006]. GRI has an angular resolution of $\sim$ 1 arcmin, and a high energy resolution of $E/\Delta E \sim 500$ at 1 MeV. The goal sensitivity for narrow lines is $\sim 10^{-7}$ph cm^{-2} s^{-1} in 10^6 s (also see Figure 6.3).

These next-generation MeV gamma-ray telescopes will greatly improve γ-ray line astronomy. Present and past instruments, e.g. SPI and COMPTEL, can detect the 511 keV annihilation line, ^{60}Fe lines from the inner Galaxy, ^{56}Co line at 847 keV from extragalactic Type Ia SNe within 20 Mpc (broad line, SN 1991T in NGC 4527, $\sim$ 17 Mpc, Morris et al. 1995), ^{44}Ti in Cas A (broad line), ^{26}Al in the inner Galaxy and nearby active star-formation regions. While many potential γ-ray line sources: the 511 keV line from Galactic novae and nearby supernova remnants; ^{60}Fe from the Vela SNR; ^{56}Co from SN Ia at a distance up to 80 Mpc; ^{44}Ti from more young SNRs, e.g. Tycho, Kepler, SN 1987A; ^{26}Al from individual sources, like the Vela SNR, the closest Wolf-Rayet star WR 11 in the Vela star-formation region, even from Crab and Cas A; and the nuclear exciting lines in ISM from C and O (see Figure 6.3), are well below the

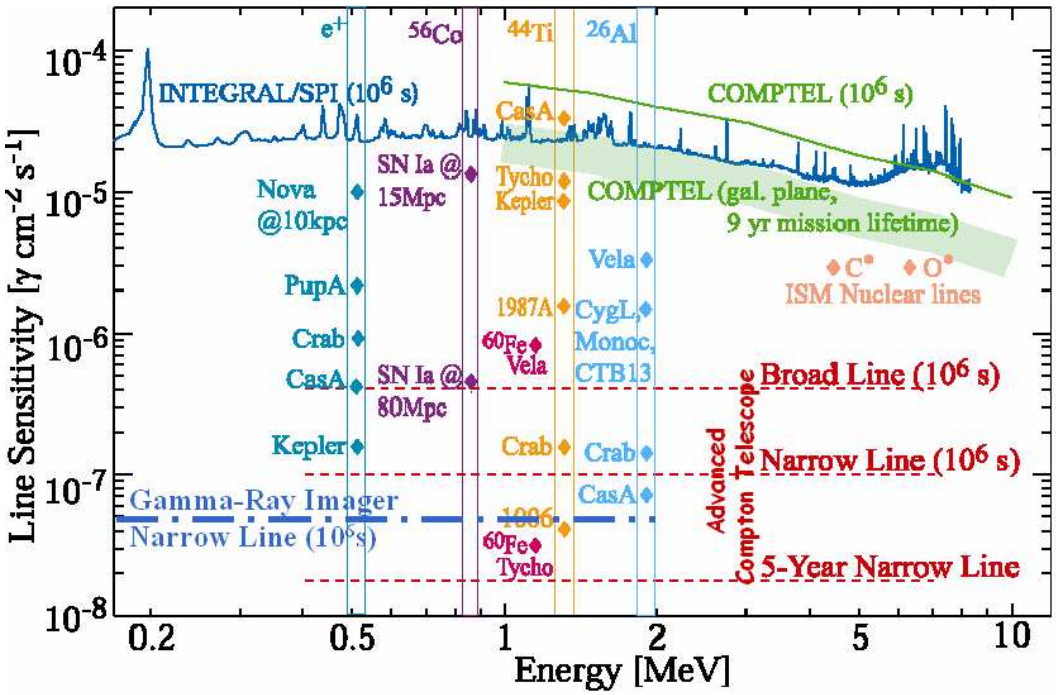

Figure 6.3: Future goals for γ-ray line astronomy (0.2 – 10 MeV): next-generation instruments (e.g., Advanced-Compton Telescope, Gamma-Ray Imager) and potential candidate γ-ray line sources for e^-e^+ annihilation line, ^{56}Co, ^{44}Ti, ^{60}Fe and ^{26}Al (from Boggs et al. 2003). Sensitivities of SPI and COMPTEL are also shown here for comparison.

sensitivity limits of present missions, but could be detected by the future advanced γ-ray telescopes, i.e., ACT and GRI (Figure 6.3). Detections of the 511 keV line, ^{44}Ti, ^{26}Al and ^{60}Fe from some individual SNRs will put the connection with yields of these radioactivity isotopes from stellar nucleosynthesis on solid ground. Era for accurate γ-ray line astronomy may come near with the launch of next-generation MeV γ-ray missions.

Bibliography

S. J. Allen. *Phys. Rev.*, 34:296, 1911.

G. Alter, B. Balazs, J. Ruprecht, and J. Vanysek. *Catalogue of star clusters and associations*. Budapest: Akademiai Kiado, 1970, 2nd ed., edited by G. Alter, B. Balazs, J. Ruprecht, 1970.

W. D. Arnett. In M. D. Papagiannis, editor, *Eight Texas Symposium on Relativistic Astrophysics*, pages 90–+, 1977.

W. D. Arnett. Supernovae and Nucleosynthesis . *Princeton University, Princeton, NJ*, 1996.

Z. Arzoumanian, D. F. Chernoff, and J. M. Cordes. *ApJ*, 568:289–301, March 2002.

B. Aschenbach. X-ray emission from supernova remnants observed with ROSAT. *Advances in Space Research*, 13:45, December 1993.

B. Aschenbach, A. F. Iyudin, and V. Schönfelder. *A&A*, 350:997–1006, October 1999.

M. Asplund, N. Grevesse, and A. J. Sauval. In T. G. Barnes, III and F. N. Bash, editors, *ASP Conf. Ser. 336: Cosmic Abundances as Records of Stellar Evolution and Nucleosynthesis*, pages 25–+, September 2005.

D. Attié, B. Cordier, M. Gros, P. Laurent, S. Schanne, G. Tauzin, P. von Ballmoos, L. Bouchet, P. Jean, J. Knödlseder, P. Mandrou, P. Paul, J.-P. Roques, G. Skinner, G. Vedrenne, R. Georgii, A. von Kienlin, G. Lichti, V. Schönfelder, A. Strong, C. Wunderer, C. Shrader, S. Sturner, B. Teegarden, G. Weidenspointner, J. Kiener, M.-G. Porquet, V. Tatischeff, S. Crespin, S. Joly, Y. André, F. Sanchez, and P. Leleux. *A&A*, 411: L71–L79, November 2003.

V. S. Avedisova. *Astronomy Reports*, 49:435–445, June 2005.

H. Becquerel. *Compt. Rend.*, 130:809, 1900.

H. Becquerel. *Compt. Rend.*, 122:420, 1896.

K. Belczynski and R. E. Taam. *ApJ*, 616:1159–1166, December 2004.

C. L. Bennett, A. J. Banday, K. M. Gorski, G. Hinshaw, P. Jackson, P. Keegstra, A. Kogut, G. F. Smoot, D. T. Wilkinson, and E. L. Wright. *ApJ*, 464:L1+, June 1996.

G. F. Bignami, G. Boella, J. J. Burger, B. G. Taylor, P. Keirle, J. A. Paul, H. A. Mayer-Hasselwander, E. Pfeffermann, L. Scarsi, and B. N. Swanenburg. *Space Science Instrumentation*, 1:245–268, August 1975.

J. Binney, O. Gerhard, and D. Spergel. *MNRAS*, 288:365–374, June 1997.

H. Bloemen, W. Hermsen, B. N. Swanenburg, C. P. de Vries, R. Diehl, V. Schoenfelder, H. Steinle, A. W. Strong, A. Connors, M. McConnell, D. Morris, G. Stacy, K. Bennett, and C. Winkler. *ApJS*, 92:419–423, June 1994.

C. Boehm, D. Hooper, J. Silk, M. Casse, and J. Paul. *Physical Review Letters*, 92(10): 101301, March 2004.

S. E. Boggs, M. S. Amman, P. Jean, S. Amrose, W. Coburn, R. P. Lin, D. M. Smith, P. N. Luke, N. W. Madden, M. Burks, E. L. Hull, P. von Ballmoos, W. W. Craig, and K. Ziock. In J. E. Truemper and H. D. Tananbaum, editors, *X-Ray and Gamma-Ray Telescopes and Instruments for Astronomy. Edited by Joachim E. Truemper, Harvey D. Tananbaum. Proceedings of the SPIE, Volume 4851, pp. 1221-1227 (2003).*, volume 4851 of *Presented at the Society of Photo-Optical Instrumentation Engineers (SPIE) Conference*, pages 1221–1227, March 2003.

J. Brand and L. Blitz. *A&A*, 275:67–+, August 1993.

J. C. Brandt. *Sol. Phys.*, 6:171–+, 1969.

J. C. Brandt, T. P. Stecher, D. L. Crawford, and S. P. Maran. *ApJ*, 163:L99+, February 1971.

E. M. Burbidge, G. R. Burbidge, W. A. Fowler, and F. Hoyle. *Reviews of Modern Physics*, 29:547–650, 1957.

D. N. Burrows, K. P. Singh, J. A. Nousek, G. P. Garmire, and J. Good. *ApJ*, 406:97–111, March 1993.

R. W. Bussard, R. Ramaty, and R. J. Drachman. *ApJ*, 228:928–934, March 1979.

M. Cassé, B. Cordier, J. Paul, and S. Schanne. *ApJ*, 602:L17–L20, February 2004.

G. R. Caughlan and W. A. Fowler. *Atomic Data and Nuclear Data Tables*, 40:283–+, 1988.

A. N. Cha, K. R. Sembach, and A. C. Danks. *ApJ*, 515:L25–L28, April 1999.

A. Chanot and J. P. Sivan. *A&A*, 121:19–25, May 1983.

W. Chen, N. Gehrels, and R. Diehl. *ApJ*, 440:L57–L60, February 1995.

W. Chen, R. Diehl, N. Gehrels, D. Hartmann, M. Leising, J. E. Naya, N. Prantzos, J. Tueller, and P. von Ballmoos. In C. Winkler, T. J.-L. Courvoisier, and P. Durouchoux, editors, *ESA SP-382: The Transparent Universe*, pages 105–+, 1997.

K. S. Cheng, L. Zhang, P. Leung, and Z. J. Jiang. *ApJ*, 608:418–426, June 2004.

K. S. Cheng, D. O. Chernyshov, and V. A. Dogiel. *ApJ*, 645:1138–1151, July 2006.

L. X. Cheng, M. Leventhal, D. M. Smith, W. R. Purcell, J. Tueller, A. Connors, D. Dixon, R. L. Kinzer, and J. G. Skibo. *ApJ*, 481:L43+, May 1997.

X. Chi, K. S. Cheng, and E. C. M. Young. *ApJ*, 459:L83+, March 1996.

E. Churazov, R. Sunyaev, S. Sazonov, M. Revnivtsev, and D. Varshalovich. *MNRAS*, 357:1377–1386, March 2005.

D. D. Clayton. *Nature*, 368:222–+, March 1994.

F. R. Colomb and G. M. Dubner. *A&A*, 82:244–248, February 1980.

A. H. Compton. *Naturwissenschaften*, 17:507, 1929.

J. M. Cordes and T. J. W. Lazio. NE2001. *ArXiv Astrophysics e-prints (astro-ph/0207156)*, July 2002.

T. J.-L. Courvoisier, R. Walter, V. Beckmann, A. J. Dean, P. Dubath, R. Hudec, P. Kretschmar, S. Mereghetti, T. Montmerle, N. Mowlavi, S. Paltani, A. Preite Martinez, N. Produit, R. Staubert, A. W. Strong, J.-P. Swings, N. J. Westergaard, N. White, C. Winkler, and A. A. Zdziarski. *A&A*, 411:L53–L57, November 2003.

T. M. Dame, H. Ungerechts, R. S. Cohen, E. J. de Geus, I. A. Grenier, J. May, D. C. Murphy, L.-A. Nyman, and P. Thaddeus. *ApJ*, 322:706–720, November 1987.

T. M. Dame, D. Hartmann, and P. Thaddeus. *ApJ*, 547:792–813, February 2001.

H. de Boer and et. al. In V. Di Gesu and et. al., editors, *Data Analysis in Astronomy IV*, volume 59, page 241, 1991.

E. J. de Geus, P. T. de Zeeuw, and J. Lub. *A&A*, 216:44–61, June 1989.

P. T. de Zeeuw, R. Hoogerwerf, J. H. J. de Bruijne, A. G. A. Brown, and A. Blaauw. *AJ*, 117:354–399, January 1999.

E. del Rio, P. von Ballmoos, K. Bennett, H. Bloemen, R. Diehl, W. Hermsen, J. Knoedlseder, U. Oberlack, J. Ryan, V. Schoenfelder, and C. Winkler. *A&A*, 315: 237–242, November 1996.

J. M. Dickey and F. J. Lockman. *ARA&A*, 28:215–261, 1990.

R. Diehl and F. X. Timmes. *PASP*, 110:637–659, June 1998.

R. Diehl, C. Dupraz, K. Bennett, H. Bloemen, W. Hermsen, J. Knoedlseder, G. Lichti, D. Morris, J. Ryan, V. Schoenfelder, H. Steinle, A. Strong, B. Swanenburg, M. Varendorff, and C. Winkler. *A&A*, 298:445–+, June 1995a.

R. Diehl, K. Bennett, H. Bloemen, C. Dupraz, W. Hermsen, J. Knoedlseder, G. Lichti, D. Morris, U. Oberlack, J. Ryan, V. Schoenfelder, H. Steinle, M. Varendorff, and C. Winkler. *A&A*, 298:L25+, June 1995b.

R. Diehl, U. Wessolowski, U. Oberlack, H. Bloemen, R. Georgii, A. Iyudin, J. Knodlseder, G. Lichti, W. Hermsen, D. Morris, J. Ryan, V. Schonfelder, A. Strong, P. von Ballmoos, and C. Winkler. In C. D. Dermer, M. S. Strickman, and J. D. Kurfess, editors, *AIP Conf. Proc. 410: Proceedings of the Fourth Compton Symposium*, pages 1109–+, November 1997.

R. Diehl, N. Baby, V. Beckmann, P. Connell, P. Dubath, P. Jean, J. Knödlseder, J.-P. Roques, S. Schanne, C. Shrader, G. Skinner, A. Strong, S. Sturner, B. Teegarden, A. von Kienlin, and G. Weidenspointner. *A&A*, 411:L117–L121, November 2003a.

R. Diehl, J. Knödlseder, G. G. Lichti, K. Kretschmer, S. Schanne, V. Schönfelder, A. W. Strong, A. von Kienlin, G. Weidenspointner, C. Winkler, and C. Wunderer. *A&A*, 411:L451–L455, November 2003b.

R. Diehl, K. Kretschmer, G. Lichti, V. Schönfelder, A. W. Strong, A. von Kienlin, J. Knödlseder, P. Jean, V. Lonjou, G. Weidenspointner, J.-P. Roques, G. Vedrenne, S. Schanne, N. Mowlavi, C. Winkler, and C. Wunderer. In V. Schoenfelder, G. Lichti, and C. Winkler, editors, *ESA SP-552: 5th INTEGRAL Workshop on the INTEGRAL Universe*, pages 27–+, October 2004.

R. Diehl, H. Halloin, K. Kretschmer, G. G. Lichti, V. Schönfelder, A. W. Strong, A. von Kienlin, W. Wang, P. Jean, J. Knödlseder, J.-P. Roques, G. Weidenspointner, S. Schanne, D. H. Hartmann, C. Winkler, and C. Wunderer. *Nature*, 439:45–47, 2006a.

R. Diehl, N. Prantzos, and P. von Ballmoos. *Nuclear Physics A*, 777:70–97, October 2006b.

R. Diehl, H. Halloin, K. Kretschmer, A. W. Strong, W. Wang, P. Jean, G. G. Lichti, J. Knödlseder, J.-P. Roques, S. Schanne, V. Schönfelder, A. von Kienlin, G. Weidenspointner, C. Winkler, and C. Wunderer. *A&A*, 449:1025–1031, April 2006c.

C. Dupraz, H. Bloemen, K. Bennett, R. Diehl, W. Hermsen, A. F. Iyudin, J. Ryan, and V. Schoenfelder. *A&A*, 324:683–689, August 1997.

P. Durouchoux, P. Wallyn, C. Chapuis, J. Matteson, B. Bowman, M. Pelling, L. Peterson, G. Vedrenne, P. von Ballmoos, I. Malet, M. Niel, R. Lin, P. Feffer, D. Smith, and K. Hurley. *A&AS*, 97:185–187, January 1993.

C. D. Ellison, C. F. Jones, and R. Ramaty. In *International Cosmic Ray Conference*, pages 68–+, 1990.

P. Englmaier and O. Gerhard. *MNRAS*, 304:512–534, April 1999.

R. B. Firestone and L. B. Ekstrüm. http://ie.lbl.gov/toi/. 2004.

G. A. P. Franco. *A&A*, 227:499–514, January 1990.

C. Fransson and C. Kozma. *New Astronomy Review*, 46:487–492, July 2002.

G. Gamow. *Physical Review*, 70:572–573, October 1946.

G. Garcia-Segura, N. Langer, and M.-M. Mac Low. *A&A*, 316:133–146, December 1996.

C. D. Garmany and R. E. Stencel. *A&AS*, 94:211–244, August 1992.

C. D. Garmany, P. S. Conti, and C. Chiosi. *ApJ*, 263:777–790, December 1982.

N. Gehrels and W. Chen. *A&AS*, 120:C331+, December 1996.

O. Gerhard. In *ASP Conf. Ser. 273: The Dynamics, Structure & History of Galaxies: A Workshop in Honour of Professor Ken Freeman*, pages 73–+, 2002.

O. E. Gerhard and M. Vietri. *MNRAS*, 223:377–+, November 1986.

P. Goldreich and W. H. Julian. *ApJ*, 157:869–+, August 1969.

J. N. Goswami, K. K. Marhas, and S. Sahijpal. *ApJ*, 549:1151–1159, March 2001.

M. Gounelle, F. H. Shu, H. Shang, A. E. Glassgold, K. E. Rehm, and T. Lee. *ApJ*, 640: 1163–1170, April 2006.

D. A. Green. Catalogue of Galactic Supernova Remnants, URL: http://www.mrao.cam.ac.uk/surveys/snrs/. 2006.

I. A. Grenier. *A&A*, 364:L93–L96, December 2000.

P. Guillout, M. F. Sterzik, J. H. M. M. Schmitt, C. Motch, and R. Neuhaeuser. *A&A*, 337:113–124, September 1998.

M. J. Harris, W. R. Purcell, D. A. Grabelsky, M. P. Ulmer, W. N. Johnson, R. L. Kinzer, J. D. Kurfess, M. S. Strickman, M. D. Leising, and G. V. Jung. In *Bulletin of the American Astronomical Society*, pages 968–+, May 1994.

M. J. Harris, W. R. Purcell, K. McNaron-Brown, R. J. Murphy, J. E. Grove, W. N. Johnson, R. L. Kinzer, J. D. Kurfess, G. H. Share, and G. V. Jung. In C. D. Dermer, M. S. Strickman, and J. D. Kurfess, editors, *AIP Conf. Proc. 410: Proceedings of the Fourth Compton Symposium*, pages 1079–+, November 1997.

M. J. Harris, J. Knödlseder, P. Jean, E. Cisana, R. Diehl, G. G. Lichti, J.-P. Roques, S. Schanne, and G. Weidenspointner. *A&A*, 433:L49–L52, April 2005.

C. G. T. Haslam, C. J. Salter, H. Stoffel, and W. E. Wilson. *Astronomy Data Image Library*, pages 1–+, December 1995.

A. Heger, C. L. Fryer, S. E. Woosley, N. Langer, and D. H. Hartmann. *ApJ*, 591:288–300, July 2003.

M. Herant and S. E. Woosley. *ApJ*, 425:814–828, April 1994.

W. Hillebrandt and F.-K. Thielemann. *ApJ*, 255:617–623, April 1982.

C. Ho. *MNRAS*, 221:523–536, August 1986.

C. Y. Hui and W. Becker. *A&A*, 454:543–552, August 2006.

S. D. Hunter, D. L. Bertsch, J. R. Catelli, T. M. Dame, S. W. Digel, B. L. Dingus, J. A. Esposito, C. E. Fichtel, R. C. Hartman, G. Kanbach, D. A. Kniffen, Y. C. Lin, H. A. Mayer-Hasselwander, P. F. Michelson, C. von Montigny, R. Mukherjee, P. L. Nolan, E. Schneid, P. Sreekumar, P. Thaddeus, and D. J. Thompson. *ApJ*, 481:205–+, May 1997.

A. F. Iyudin, R. Diehl, H. Bloemen, W. Hermsen, G. G. Lichti, D. Morris, J. Ryan, V. Schoenfelder, H. Steinle, M. Varendorff, C. de Vries, and C. Winkler. *A&A*, 284: L1–L4, April 1994.

A. F. Iyudin, R. Diehl, G. G. Lichti, V. Schönfelder, A. W. Strong, H. Bloemen, W. Hermsen, J. Ryan, K. Bennett, and C. Winkler. In C. Winkler, T. J.-L. Courvoisier, and P. Durouchoux, editors, *ESA SP-382: The Transparent Universe*, pages 37–+, 1997.

A. F. Iyudin, V. Schonfelder, K. Bennett, H. Bloemen, R. Diehl, W. Hermsen, G. G. Lichti, R. D. van der Meulen, J. Ryan, and C. Winkler. *Nature*, 396:142–144, 1998.

F. A. Iyudin, V. Schönfelder, K. Bennett, H. Bloemen, R. Diehl, W. Hermsen, J. Knödlseder, G. G. Lichti, U. Oberlack, J. Ryan, W. A. Strong, and C. Winkler. *Astrophysical Letters Communications*, 38:383–+, 1999.

P. Jean, G. Vedrenne, J. P. Roques, V. Schönfelder, B. J. Teegarden, A. von Kienlin, J. Knödlseder, C. Wunderer, G. K. Skinner, G. Weidenspointner, D. Attié, S. Boggs, P. Caraveo, B. Cordier, R. Diehl, M. Gros, P. Leleux, G. G. Lichti, E. Kalemci, J. Kiener, V. Lonjou, P. Mandrou, P. Paul, S. Schanne, and P. von Ballmoos. *A&A*, 411:L107–L112, November 2003.

P. Jean, J. Knödlseder, W. Gillard, N. Guessoum, K. Ferrière, A. Marcowith, V. Lonjou, and J. P. Roques. *A&A*, 445:579–589, January 2006.

P. L. Jensen, K. Clausen, C. Cassi, F. Ravera, G. Janin, C. Winkler, and R. Much. *A&A*, 411:L7–L17, November 2003.

W. N. Johnson, III and R. C. Haymes. *ApJ*, 184:103–126, August 1973.

J. Jose, M. Hernanz, and A. Coc. *ApJ*, 479:L55+, April 1997.

G. Kanbach, D. L. Bertsch, C. E. Fichtel, R. C. Hartman, S. D. Hunter, D. A. Kniffen, B. W. Hughlock, A. Favale, R. Hofstadter, and E. B. Hughes. *Space Science Reviews*, 49:69–84, 1988.

G. Kanbach, R. Andritschke, A. Zoglauer, M. Ajello, M. L. McConnell, J. R. Macri, J. M. Ryan, P. Bloser, S. Hunter, G. Dicocco, J. Kurfess, and V. Reglero. *Nuclear Instruments and Methods in Physics Research A*, 541:310–322, April 2005.

A. I. Karakas and J. C. Lattanzio. *Publications of the Astronomical Society of Australia*, 20: 279–293, 2003.

K. Kifonidis, T. Plewa, H.-T. Janka, and E. Müller. *A&A*, 408:621–649, September 2003.

K. Knie, G. Korschinek, T. Faestermann, E. A. Dorfi, G. Rugel, and A. Wallner. *Physical Review Letters*, 93(17):171103, October 2004.

J. Knödlseder. *A&A*, 360:539–548, August 2000.

J. Knödlseder. In M. J. L. Turner and G. Hasinger, editors, *Space Telescopes and Instrumentation II: Ultraviolet to Gamma Ray. Edited by Turner, Martin J. L.; Hasinger, Günther. Proceedings of the SPIE, Volume 6266, pp. 626623 (2006).*, volume 6266 of *Presented at the Society of Photo-Optical Instrumentation Engineers (SPIE) Conference*, July 2006.

J. Knödlseder. *ApJ*, 510:915–929, January 1999.

J. Knödlseder, D. Dixon, K. Bennett, H. Bloemen, R. Diehl, W. Hermsen, U. Oberlack, J. Ryan, V. Schönfelder, and P. von Ballmoos. *A&A*, 345:813–825, May 1999a.

J. Knödlseder, K. Bennett, H. Bloemen, R. Diehl, W. Hermsen, U. Oberlack, J. Ryan, V. Schönfelder, and P. von Ballmoos. *A&A*, 344:68–82, April 1999b.

J. Knödlseder, M. Cerviño, J.-M. Le Duigou, G. Meynet, D. Schaerer, and P. von Ballmoos. *A&A*, 390:945–960, August 2002.

J. Knödlseder, M. Valsesia, M. Allain, S. Boggs, R. Diehl, P. Jean, K. Kretschmer, J.-P. Roques, V. Schönfelder, G. Vedrenne, P. von Ballmoos, G. Weidenspointner, and C. Winkler. In V. Schoenfelder, G. Lichti, and C. Winkler, editors, *ESA SP-552: 5th INTEGRAL Workshop on the INTEGRAL Universe*, pages 33–+, October 2004.

J. Knödlseder, P. Jean, V. Lonjou, G. Weidenspointner, N. Guessoum, W. Gillard, G. Skinner, P. von Ballmoos, G. Vedrenne, J.-P. Roques, S. Schanne, B. Teegarden, V. Schönfelder, and C. Winkler. *A&A*, 441:513–532, October 2005.

B. Kozlovsky, R. E. Lingenfelter, and R. Ramaty. *ApJ*, 316:801–818, May 1987.

K. Kretschmer. PhD thesis, Technische Universität München, 2007.

K. Kretschmer, R. Diehl, and D. H. Hartmann. *A&A*, 412:L47–L51, December 2003.

P. Kroupa. *Science*, 295:82–91, January 2002.

B. M. Kuzhevskij, S. N. Kuznetsov, and E. V. Troitskaia. *Advances in Space Research*, 22: 1141–1147, 1998.

M. Lang. Dipl. Thesis, Technische Universität München. 2006.

N. Langer. *A&A*, 220:135–143, August 1989.

N. Langer, H. Braun, and J. Fliegner. *Ap&SS*, 224:275–278, February 1995.

T. N. LaRosa, N. E. Kassim, T. J. W. Lazio, and S. D. Hyman. *AJ*, 119:207–240, January 2000.

T. N. LaRosa, C. L. Brogan, S. N. Shore, T. J. Lazio, N. E. Kassim, and M. E. Nord. *ApJ*, 626:L23–L27, June 2005.

R. Launhardt, R. Zylka, and P. G. Mezger. *A&A*, 384:112–139, March 2002.

M. D. Leising and G. H. Share. *ApJ*, 424:200–207, March 1994.

P. Leleux, F. Albernhe, V. Borrel, B. Cordier, R. Coszach, S. Crespin, J. M. Denis, P. Duhamel, P. Frabel, W. Galster, J.-S. Graulich, P. Jean, B. Kandel, J. P. Meulders, G. Tauzin, J. Vanhorenbeeck, G. Vedrenne, and P. von Ballmoos. *A&A*, 411:L85–L90, November 2003.

M. Leventhal, C. J. MacCallum, and P. D. Stang. *ApJ*, 225:L11–L14, October 1978.

M. Limongi and A. Chieffi. *ApJ*, 592:404–433, July 2003.

M. Limongi and A. Chieffi. *ApJ*, 647:483–500, August 2006.

R. E. Lingenfelter and G. J. Hueter. In S. E. Woosley, editor, *American Institute of Physics Conference Series*, pages 558–+, 1984.

R. E. Lingenfelter and R. Ramaty. In R. Ramaty, editor, *AIP Conf. Proc. 101: Positron-Electron Pairs in Astrophysics*, pages 267–272, 1983.

C. J. MacCallum, A. F. Huters, P. D. Stang, and M. Leventhal. *ApJ*, 317:877–880, June 1987.

K. Maeda and K. Nomoto. *ApJ*, 598:1163–1200, December 2003.

W. A. Mahoney, J. C. Ling, A. S. Jacobson, and R. E. Lingenfelter. *ApJ*, 262:742–+, November 1982.

W. A. Mahoney, J. C. Ling, W. A. Wheaton, and A. S. Jacobson. *ApJ*, 286:578–585, November 1984.

R. N. Manchester and J. H. Taylor. Observed and derived parameters for 330 pulsars. *AJ*, 86:1953–1973, December 1981.

A. Mastichiadis, R. J. Protheroe, and S. A. Stephen. In D. O'Sullivan, editor, *22d Int. Cosmic-Ray Conf.*, page 2, 1991.

H. A. Mayer-Hasselwander, D. L. Bertsch, B. L. Dingus, A. Eckart, J. A. Esposito, R. Genzel, R. C. Hartman, S. D. Hunter, G. Kanbach, D. A. Kniffen, Y. C. Lin, P. F. Michelson, A. Muecke, C. von Montigny, R. Mukherjee, P. L. Nolan, M. Pohl, O. Reimer, E. J. Schneid, P. Sreekumar, and D. J. Thompson. *A&A*, 335:161–172, July 1998.

M. McConnell, S. Fletcher, K. Bennett, H. Bloemen, R. Diehl, W. Hermsen, J. Ryan, V. Schonfelder, A. Strong, and R. van Dijk. In C. D. Dermer, M. S. Strickman, and J. D. Kurfess, editors, *AIP Conf. Proc. 410: Proceedings of the Fourth Compton Symposium*, pages 1099–+, November 1997.

C. F. McKee and J. K. Truelove. *Phys. Rep.*, 256:157–172, May 1995.

C. F. McKee and J. P. Williams. *ApJ*, 476:144–+, February 1997.

G. Mellema and P. Lundqvist. *A&A*, 394:901–909, November 2002.

G. Meynet, M. Arnould, N. Prantzos, and G. Paulus. *A&A*, 320:460–468, April 1997.

P. F. Michelson. In S. Ritz, N. Gehrels, and C. R. Shrader, editors, *Gamma 2001: Gamma-Ray Astrophysics*, volume 587 of *American Institute of Physics Conference Series*, pages 713–+, 2001.

G. E. Miller and J. M. Scalo. *ApJS*, 41:513–547, November 1979.

P. A. Milne, J. D. Kurfess, M. D. Leising, and D. D. Dixon. In *Bulletin of the American Astronomical Society*, pages 1253–+, October 2000.

P. A. Milne, J. D. Kurfess, R. L. Kinzer, M. D. Leising, and D. D. Dixon. In A. Gimenez, V. Reglero, and C. Winkler, editors, *ESA SP-459: Exploring the Gamma-Ray Universe*, pages 145–148, September 2001.

D. J. Morris, K. Bennett, H. Bloemen, W. Hermsen, G. G. Lichti, M. L. McConnell, J. M. Ryan, and V. Schönfelder. In H. Böhringer, G. E. Morfill, and J. E. Trümper, editors, *Seventeeth Texas Symposium on Relativistic Astrophysics and Cosmology*, volume 759 of *New York Academy Sciences Annals*, pages 397–+, 1995.

N. Mowlavi and G. Meynet. *A&A*, 361:959–976, September 2000.

W. A. Mulder and B. T. Liem. *A&A*, 157:148–158, March 1986.

M. P. Muno, F. K. Baganoff, M. W. Bautz, W. N. Brandt, P. S. Broos, E. D. Feigelson, G. P. Garmire, M. R. Morris, G. R. Ricker, and L. K. Townsley. *ApJ*, 589:225–241, May 2003.

D. C. Murphy and J. May. *A&A*, 247:202–214, July 1991.

S. Nagataki, M.-A. Hashimoto, K. Sato, and S. Yamada. *ApJ*, 486:1026–+, September 1997.

J. E. Naya, S. D. Barthelmy, L. M. Bartlett, N. Gehrels, M. Leventhal, A. Parsons, B. J. Teegarden, and J. Tueller. *Nature*, 384:44–46, November 1996.

J. E. Naya, S. D. Barthelmy, L. M. Bartlett, N. Gehrels, A. Parsons, B. J. Teegarden, J. Tueller, and M. Leventhal. Gamma-Ray Limits on Galactic 60Fe Nucleosynthesis and Implications on the Origin of the 26Al Emission. *ApJ*, 499:L169+, June 1998.

S. Nikolaev and M. D. Weinberg. *ApJ*, 487:885–+, October 1997.

I. Nofar, G. Shaviv, and S. Starrfield. *ApJ*, 369:440–450, March 1991.

T. Nugis and H. J. G. L. M. Lamers. *A&A*, 360:227–244, August 2000.

U. Oberlack. PhD thesis, Technische Universität München, 1997.

U. Oberlack, R. Diehl, T. Montmerle, N. Prantzos, and P. von Ballmoos. *ApJS*, 92: 433–439, June 1994.

U. Oberlack, K. Bennett, H. Bloemen, R. Diehl, C. Dupraz, W. Hermsen, J. Knoedlseder, D. Morris, V. Schoenfelder, A. Strong, and C. Winkler. *A&AS*, 120:C311+, December 1996.

U. Oberlack, U. Wessolowski, R. Diehl, K. Bennett, H. Bloemen, W. Hermsen, J. Knödlseder, D. Morris, V. Schönfelder, and P. von Ballmoos. *A&A*, 353:715–721, January 2000.

M. S. Oey. *ApJ*, 467:666–+, August 1996.

M. S. Oey and C. J. Clarke. *Bulletin of the American Astronomical Society*, 28:857–+, May 1996.

R. P. Olling and M. R. Merrifield. *MNRAS*, 311:361–369, January 2000.

A. Palacios, G. Meynet, C. Vuissoz, J. Knödlseder, D. Schaerer, M. Cerviño, and N. Mowlavi. *A&A*, 429:613–624, January 2005.

C. A. Perrot and I. A. Grenier. *A&A*, 404:519–531, June 2003.

E. Pfahl, S. Rappaport, and P. Podsiadlowski. *ApJ*, 571:L37–L40, May 2002.

S. Plüschke. PhD thesis, Technische Universität München, 2001.

S. Plüschke, R. Diehl, V. Schönfelder, H. Bloemen, W. Hermsen, K. Bennett, C. Winkler, M. McConnell, J. Ryan, U. Oberlack, and J. Knödlseder. In A. Gimenez, V. Reglero, and C. Winkler, editors, *ESA SP-459: Exploring the Gamma-Ray Universe*, pages 55–58, September 2001.

M. Politano, S. Starrfield, J. W. Truran, A. Weiss, and W. M. Sparks. *ApJ*, 448:807–+, August 1995.

N. Prantzos. *A&A*, 420:1033–1037, June 2004.

N. Prantzos and R. Diehl. *Phys. Rep.*, 267:1–69, March 1996.

R. K. Prinja, M. J. Barlow, and I. D. Howarth. *ApJ*, 361:607–620, October 1990.

W. R. Purcell, L.-X. Cheng, D. D. Dixon, R. L. Kinzer, J. D. Kurfess, M. Leventhal, M. A. Saunders, J. G. Skibo, D. M. Smith, and J. Tueller. *ApJ*, 491:725–+, December 1997.

R. Ramaty. *A&AS*, 120:C373+, December 1996.

R. Ramaty and R. E. Lingenfelter. *ApJ*, 213:L5–L7, April 1977.

R. Ramaty and R. E. Lingenfelter. *Nature*, 278:127–132, March 1979.

R. Ramaty, B. Kozlovsky, and R. E. Lingenfelter. *ApJS*, 40:487–526, July 1979.

T. Rauscher, A. Heger, R. D. Hoffman, and S. E. Woosley. *ApJ*, 576:323–348, September 2002.

B. C. Reed. *AJ*, 130:1652–1657, October 2005.

M. J. Reid. *ARA&A*, 31:345–372, 1993.

M. Renaud, F. Lebrun, J. Ballet, A. Decourchelle, R. Terrier, and N. Prantzos. In V. Schoenfelder, G. Lichti, and C. Winkler, editors, *ESA SP-552: 5th INTEGRAL Workshop on the INTEGRAL Universe*, pages 81–+, October 2004.

M. Renaud, J. Vink, A. Decourchelle, F. Lebrun, P. R. d. Hartog, R. Terrier, C. Couvreur, J. Knödlseder, P. Martin, N. Prantzos, A. M. Bykov, and H. Bloemen. *ApJ*, 647:L41–L44, August 2006.

R. J. Reynolds. *ApJ*, 206:679–684, June 1976.

A. C. Robin, C. Reylé, S. Derrière, and S. Picaud. *A&A*, 409:523–540, October 2003.

C. E. Rolfs and W. S. Rodney. Cauldrons in the Cosmos. *University of Chicago Press*, 1994.

J. P. Roques, S. Schanne, A. von Kienlin, J. Knödlseder, R. Briet, L. Bouchet, P. Paul, S. Boggs, P. Caraveo, M. Cassé, B. Cordier, R. Diehl, P. Durouchoux, P. Jean, P. Leleux, G. Lichti, P. Mandrou, J. Matteson, F. Sanchez, V. Schönfelder, G. Skinner, A. Strong, B. Teegarden, G. Vedrenne, P. von Ballmoos, and C. Wunderer. *A&A*, 411:L91–L100, November 2003.

M. Ruderman. *ApJ*, 366:261–269, January 1991.

M. A. Ruderman and P. G. Sutherland. *ApJ*, 196:51–72, February 1975.

D. Russeil. *A&A*, 397:133–146, January 2003.

E. Rutherford. Radio-activity. *Cambridge: Cambridge Univ. Press*, 1905.

E. Rutherford. *Phil. Mag.*, 47:109, 1899.

M. J. Sartori, J. R. D. Lépine, and W. S. Dias. *A&A*, 404:913–926, June 2003.

S. Schanne, P. Sizun, D. Maurin, B. Cordier, A. von Kienlin, and C. Hamadache. *ArXiv Astrophysics e-prints (astro-ph/0701640)*, January 2007.

V. Schoenfelder and M. Varendorff. In P. Durouchoux and N. Prantzos, editors, *AIP Conf. Proc. 232: Gamma-Ray Line Astrophysics*, pages 101–115, 1991.

V. Schoenfelder, H. Aarts, K. Bennett, H. de Boer, J. Clear, W. Collmar, A. Connors, A. Deerenberg, R. Diehl, A. von Dordrecht, J. W. den Herder, W. Hermsen, M. Kippen, L. Kuiper, G. Lichti, J. Lockwood, J. Macri, M. McConnell, D. Morris, R. Much, J. Ryan, G. Simpson, M. Snelling, G. Stacy, H. Steinle, A. Strong, B. N. Swanenburg, B. Taylor, C. de Vries, and C. Winkler. *ApJS*, 86:657–692, June 1993.

V. Schönfelder, K. Bennett, J. J. Blom, H. Bloemen, W. Collmar, A. Connors, R. Diehl, W. Hermsen, A. Iyudin, R. M. Kippen, J. Knödlseder, L. Kuiper, G. G. Lichti, M. McConnell, D. Morris, R. Much, U. Oberlack, J. Ryan, G. Stacy, H. Steinle, A. Strong, R. Suleiman, R. van Dijk, M. Varendorff, C. Winkler, and O. R. Williams. *A&AS*, 143: 145–179, April 2000.

G. H. Share, R. L. Kinzer, J. D. Kurfess, D. J. Forrest, E. L. Chupp, and E. Rieger. *ApJ*, 292:L61–L65, May 1985.

A. Shukolyukov and G. W. Lugmair. *Science*, 259:1138–1142, February 1993.

G. Skinner and P. Connell. *A&A*, 411:L123–L126, November 2003.

D. M. Smith. *ApJ*, 589:L55–L58, May 2003.

D. M. Smith. *New Astronomy Review*, 48:87–91, February 2004a.

D. M. Smith. In V. Schoenfelder, G. Lichti, and C. Winkler, editors, *ESA SP-552: 5th INTEGRAL Workshop on the INTEGRAL Universe*, pages 45–+, October 2004b.

S. Starrfield, J. W. Truran, M. Politano, W. M. Sparks, I. Nofar, and G. Shaviv. *Phys. Rep.*, 227:223–234, 1993.

A. W. Strong. *A&A*, 411:L127–L129, November 2003.

A. W. Strong and et. al. In V. Di Gesu and et. al., editors, *Data Analysis in Astronomy IV*, volume 59, page 251, 1991.

A. W. Strong, J. B. G. M. Bloemen, T. M. Dame, I. A. Grenier, W. Hermsen, F. Lebrun, L.-A. Nyman, A. M. T. Pollock, and P. Thaddeus. *A&A*, 207:1–15, December 1988.

A. W. Strong, H. Bloemen, R. Diehl, W. Hermsen, and V. Schönfelder. *Astrophysical Letters Communications*, 39:209–+, 1999.

A. W. Strong, L. Bouchet, R. Diehl, P. Mandrou, V. Schönfelder, and B. J. Teegarden. *A&A*, 411:L447–L450, November 2003.

A. W. Strong, R. Diehl, H. Halloin, V. Schönfelder, L. Bouchet, P. Mandrou, F. Lebrun, and R. Terrier. *A&A*, 444:495–503, December 2005.

S. J. Sturner and J. E. Naya. *ApJ*, 526:200–206, November 1999.

S. J. Sturner, C. R. Shrader, G. Weidenspointner, B. J. Teegarden, D. Attié, B. Cordier, R. Diehl, C. Ferguson, P. Jean, A. von Kienlin, P. Paul, F. Sánchez, S. Schanne, P. Sizun, G. Skinner, and C. B. Wunderer. *A&A*, 411:L81–L84, November 2003.

P. A. Sturrock. *ApJ*, 164:529–+, March 1971.

S. Tachibana and G. R. Huss. *ApJ*, 588:L41–L44, May 2003.

S. Tachibana, G. R. Huss, N. T. Kita, G. Shimoda, and Y. Morishita. *ApJ*, 639:L87–L90, March 2006.

K. Tachihara, R. Neuhäuser, S. Toyoda, T. Onishi, A. Mizuno, and Y. Fukui. In E. R. Schielicke, editor, *Astronomische Gesellschaft Meeting Abstracts*, pages 72–+, 2001.

J. H. Taylor and J. M. Cordes. *ApJ*, 411:674–684, July 1993.

B. J. Teegarden, S. D. Barthelmy, N. Gehrels, J. Tueller, M. Leventhal, and C. J. MacCallum. *ApJ*, 375:L9–L12, July 1991.

B. J. Teegarden, K. Watanabe, P. Jean, J. Knödlseder, V. Lonjou, J. P. Roques, G. K. Skinner, P. von Ballmoos, G. Weidenspointner, A. Bazzano, Y. M. Butt, A. Decourchelle, A. C. Fabian, A. Goldwurm, M. Güdel, D. C. Hannikainen, D. H. Hartmann, A. Hornstrup, W. H. G. Lewin, K. Makishima, A. Malzac, J. Miller, A. N. Parmar, S. P. Reynolds, R. E. Rothschild, V. Schönfelder, J. A. Tomsick, and J. Vink. *ApJ*, 621:296–300, March 2005.

O. V. Terekhov, R. A. Syunyaev, A. V. Kuznetsov, C. Barat, R. Talon, G. Trottet, and N. Vilmer. *Astronomy Letters*, 19:65–68, March 1993.

F.-K. Thielemann, K. Nomoto, and M.-A. Hashimoto. *ApJ*, 460:408–+, March 1996.

F. X. Timmes, S. E. Woosley, D. H. Hartmann, R. D. Hoffman, T. A. Weaver, and F. Matteucci. *ApJ*, 449:204–+, August 1995.

P. Ubertini, F. Lebrun, G. Di Cocco, A. Bazzano, A. J. Bird, K. Broenstad, A. Goldwurm, G. La Rosa, C. Labanti, P. Laurent, I. F. Mirabel, E. M. Quadrini, B. Ramsey, V. Reglero, L. Sabau, B. Sacco, R. Staubert, L. Vigroux, M. C. Weisskopf, and A. A. Zdziarski. *A&A*, 411:L131–L139, November 2003.

K. A. van der Hucht. The VIIth catalogue of galactic Wolf-Rayet stars. *New Astronomy Review*, 45:135–232, February 2001.

K. A. van der Hucht, B. Hidayat, A. G. Admiranto, K. R. Supelli, and C. Doom. *A&A*, 199:217–234, June 1988.

K. A. van der Hucht, H. Schrijver, B. Stenholm, I. Lundstrom, A. F. J. Moffat, S. V. Marchenko, W. Seggewiss, D. Y. A. Setia Gunawan, W. Sutantyo, E. P. J. van den Heuvel, J.-P. de Cuyper, and A. E. Gomez. *New Astronomy*, 2:245–250, August 1997.

G. Vedrenne, J.-P. Roques, V. Schönfelder, P. Mandrou, G. G. Lichti, A. von Kienlin, B. Cordier, S. Schanne, J. Knödlseder, G. Skinner, P. Jean, F. Sanchez, P. Caraveo, B. Teegarden, P. von Ballmoos, L. Bouchet, P. Paul, J. Matteson, S. Boggs, C. Wunderer, P. Leleux, G. Weidenspointner, P. Durouchoux, R. Diehl, A. Strong, M. Cassé, M. A. Clair, and Y. André. *A&A*, 411:L63–L70, November 2003.

J. Vink, J. M. Laming, J. S. Kaastra, J. A. M. Bleeker, H. Bloemen, and U. Oberlack. *ApJ*, 560:L79–L82, October 2001.

J. S. Vink and A. de Koter. *A&A*, 442:587–596, November 2005.

P. von Ballmoos, R. Diehl, and V. Schoenfelder. *ApJ*, 318:654–663, July 1987.

G. Wallerstein, I. J. Iben, P. Parker, A. M. Boesgaard, G. M. Hale, A. E. Champagne, C. A. Barnes, F. Käppeler, V. V. Smith, R. D. Hoffman, F. X. Timmes, C. Sneden, R. N. Boyd, B. S. Meyer, and D. L. Lambert. *Reviews of Modern Physics*, 69:995–1084, 1997.

W. Wang. *Chin. J. Astron. Astrophys. Supplement, ArXiv Astrophysics e-prints (astro-ph/0510461)*, 6:268–272, December 2006.

W. Wang, Z. J. Jiang, and K. S. Cheng. *MNRAS*, 358:263–269, March 2005a.

W. Wang, Z. J. Jiang, C. S. J. Pun, and K. S. Cheng. *MNRAS*, 360:646–654, June 2005b.

W. Wang, C. S. J. Pun, and K. S. Cheng. *A&A*, 446:943–948, February 2006.

W. Wang, M. J. Harris, R. Diehl, H. Halloin, B. Cordier, A. W. Strong, K. Kretschmer, J. Knoedlseder, P. Jean, G. G. Lichti, J. P. Roques, S. Schanne, A. von Kienlin, G. Weidenspointner, and C. Wunderer. *A&A*, 469:1005–1012, July 2007.

R. A. Ward and W. A. Fowler. *ApJ*, 238:266–286, May 1980.

G. J. Wasserburg, R. Gallino, and M. Busso. *ApJ*, 500:L189+, June 1998.

R. Weaver, R. McCray, J. Castor, P. Shapiro, and R. Moore. *ApJ*, 218:377–395, December 1977.

T. A. Weaver and S. E. Woosley. *Phys. Rep.*, 227:65–96, 1993.

G. Weidenspointner, J. Kiener, M. Gros, P. Jean, B. J. Teegarden, C. Wunderer, R. C. Reedy, D. Attié, R. Diehl, C. Ferguson, M. J. Harris, J. Knödlseder, P. Leleux, V. Lonjou, J.-P. Roques, V. Schönfelder, C. Shrader, S. Sturner, V. Tatischeff, and G. Vedrenne. *A&A*, 411:L113–L116, November 2003.

C. Weidner and P. Kroupa. *ApJ*, 625:754–762, June 2005.

A. Weiss and J. W. Truran. *A&A*, 238:178–186, November 1990.

S. Wheelock, J. Chillemi, N. Gautier, D. Gregorich, D. Kester, H. McCallon, C. Oken, J. White, and T. Chester. In *Bulletin of the American Astronomical Society*, pages 908–+, March 1991.

M. Wiescher, J. Gorres, F.-K. Thielemann, and H. Ritter. *A&A*, 160:56–72, May 1986.

C. Winkler, T. J.-L. Courvoisier, G. Di Cocco, N. Gehrels, A. Giménez, S. Grebenev, W. Hermsen, J. M. Mas-Hesse, F. Lebrun, N. Lund, G. G. C. Palumbo, J. Paul, J.-P. Roques, H. Schnopper, V. Schönfelder, R. Sunyaev, B. Teegarden, P. Ubertini, G. Vedrenne, and A. J. Dean. *A&A*, 411:L1–L6, November 2003.

P. F. Winkler, J. H. Tuttle, R. P. Kirshner, and M. J. Irwin. In R. S. Roger and T. L. Landecker, editors, *IAU Colloq. 101: Supernova Remnants and the Interstellar Medium*, pages 65–+, 1988.

S. E. Woosley. In J. Audouze, C. Chiosi, and S. E. Woosley, editors, *Saas-Fee Advanced Course 16: Nucleosynthesis and Chemical Evolution*, pages 1–+, 1986.

S. E. Woosley. *ApJ*, 476:801–+, February 1997.

S. E. Woosley and A. Heger. *to appear in Physics Reports, Bethe Centennial Volume, ArXiv Astrophysics e-print (astro-ph/0702176)*, 2007.

S. E. Woosley and T. A. Weaver. *ApJS*, 101:181–+, November 1995.

S. E. Woosley, W. D. Arnett, and D. D. Clayton. The Explosive Burning of Oxygen and Silicon. *ApJS*, 26:231–+, November 1973.

S. E. Woosley, D. Hartmann, and P. A. Pinto. *ApJ*, 346:395–404, November 1989.

S. E. Woosley, D. H. Hartmann, R. D. Hoffman, and W. C. Haxton. *ApJ*, 356:272–301, June 1990.

L. Zhang and K. S. Cheng. *A&A*, 398:639–646, February 2003.

Acknowledgements

I firstly would like to thank my advisor Dr. habil. Roland Diehl very much for his careful and intensive guidance in three years of study at MPE. He bring me to a completely new scientific field for me before I came here: gamma-ray line astronomy. The progress of my knowledge and now the finish of my PhD work should be attributed to Roland's help.

I want to thank Prof. Günther Hasinger for representing this thesis to the Technische Universität München.

I also thank Karsten Kretschmer, the first people I met at MPE three years ago. His warm welcome made me feel that I came back home. Thank Karsten very much for his help in my study for three years.

Thanks a lot to Zhang Xiao-Ling for her friendship and assistance in my study and life.

I should be very grateful to Jochen Greiner, Andrew Strong, Gottfried Kanbach, Giselher Lichti, Andreas von Kienlin, Werner Collmar, Hubert Halloin, Michael Lang, and the other people in the Gamma Group for their help in my studies.

I am grateful to some colleagues in other institutes, M. J. Harris, J. Knödlseder, P. Jean, J. P. Roques, S. Schanne, B. Cordier, G. Weidenspointner, C. Wunderer for their collaboration in my research work.

Many thanks to my Chinese friends in the Garching campus, Fan Yi, Zhang Yu-Ying, Wang Jie, Wang Lan, Xiang Fei, Regina Huang, David Hui, Guo Qi, Li Yang-Fang, Gao Hong, Zhang Chen and the people in the Garching CSSU for their friendship and help during the last three years.

I am also grateful to the Max-Planck-Institut für extraterrestrische Physik to provide me the good chance of study and research for three years in Germany. The excellent academic environment in MPE and the campus of Garching makes me very enjoyable during my PhD studies.

The INTEGRAL project is supported by government grants in all member states of the hardware teams. The SPI project has been completed under responsibility and leadership of CNES. I am grateful to ASI, CEA, CNES, DLR, ESA, INTA, NASA, and OSTC for support.

Finally, special thanks to encouragement and support from my family in China. For love of my mother, my sister, and my wife, I can successfully finish my research work and the PhD thesis.